Physics of Atomic Nuclei, Vol. 67, No. 11, 2004, pp. 1931–1941. From Yadernaya Fizika, Vol. 67, No. 11, 2004, pp. 1957–1966.
Original English Text Copyright © 2004 by Bednyakov.

DARK MATTER

Aspects of Spin-Dependent Dark Matter Search*

V. A. Bednyakov**

Joint Institute for Nuclear Research, Dubna, Moscow oblast, 141980 Russia

Received November 4, 2003

Abstract—The Weakly Interacting Massive Particle (WIMP) is the main candidate for the relic dark matter. A set of exclusion curves currently obtained for cross sections of spin-dependent WIMP—proton and WIMP—neutron interaction is given. A two-orders-of-magnitude improvement of the sensitivity of the dark matter experiment is needed to reach the SUSY predictions for relic neutralinos. It is noted that new experiments with the high-spin isotope ^{73}Ge can yield a new important constraint on the neutralino—neutron effective coupling and the SUSY parameter space. *© 2004 MAIK "Nauka/Interperiodica".*

1. INTRODUCTION

Nowadays, the main efforts in the direct dark matter search experiments are concentrated in the field of so-called spin-independent (or scalar) interaction of a dark matter particle or the Weakly Interacting Massive Particle (WIMP) with a nucleus. The lightest supersymmetric (SUSY) particle (LSP) neutralino is assumed here as the best WIMP candidate. It is believed that this spin-independent (SI) interaction of dark matter (DM) particles with nuclei makes a dominant contribution to the expected event rate of detection of these particles. The reason for this is the strong (proportional to the squared mass of the target nucleus) enhancement of SI WIMP—nucleus interaction. The results currently obtained in the field are usually presented in the form of exclusion curves (see, for example, Fig. 1). For the fixed mass of the WIMP, the values of the cross section due to scalar elastic WIMP—nucleon interaction located above these curves are already excluded experimentally. There is also the DAMA closed contour, which corresponds to the first claim for evidence for the dark matter signal due to the positive annual modulation effect [5].

In this paper we consider some aspects of the spin-dependent (or axial-vector) interaction of the DM WIMP with nuclei. There are at least three reasons to think that this spin-dependent (SD) interaction could also be very important. First, contrary to the only constraint for SUSY models available from scalar WIMP—nucleus interaction, the spin WIMP—nucleus interaction supplies us with two such constraints (see, for example, [6] and formulas below). Second, one can notice [1, 7] that even with a very accurate DM detector (say, with sensitivity 10^{-5} events/d/kg) which is sensitive only to the WIMP—nucleus scalar interaction (with spinless target nuclei) one can, in principle, miss a DM signal. To safely avoid such a situation, one should have a spin-sensitive DM detector, i.e., a detector with spin-nonzero target nuclei. Finally, there is a complicated (and theoretically very interesting) nucleus spin structure, which possesses the so-called long q-tail form factor behavior for heavy targets and heavy WIMP. Therefore, the SD efficiency needed to detect a DM signal is much higher than the SI efficiency, especially for the heavy target nucleus and WIMP masses [8].

2. ZERO MOMENTUM TRANSFER

A dark matter event is elastic scattering of a relic neutralino χ (or $\tilde{\chi}$) from a target nucleus A producing a nuclear recoil E_R that can be detected by a suitable detector. The differential event rate, with respect to the recoil energy, is the subject of experimental measurements. The rate depends on the distribution of the relic neutralinos in the solar vicinity $f(v)$ and the cross section of neutralino—nucleus elastic scattering [9—16]. The differential event rate per unit mass of the target material has the form

$$\frac{dR}{dE_R} = N\frac{\rho_\chi}{m_\chi}\int\limits_{v_{\min}}^{v_{\max}} dv f(v) v \frac{d\sigma}{dq^2}(v, q^2). \qquad (1)$$

The nuclear recoil energy $E_R = q^2/(2M_A)$ is typically about $10^{-6}m_\chi$, and $N = \mathcal{N}/A$ is the number density of the target nuclei, where $\mathcal{N}$ is the Avogadro number and A is the atomic mass of the nuclei with mass M_A. The neutralino—nucleus elastic scattering cross section for spin-nonzero ($J \neq 0$) nuclei contains coherent (spin-independent, or SI) and axial

---

*This article was submitted by the author in English.

**e-mail: `Vadim.Bednyakov@jinr.ru`

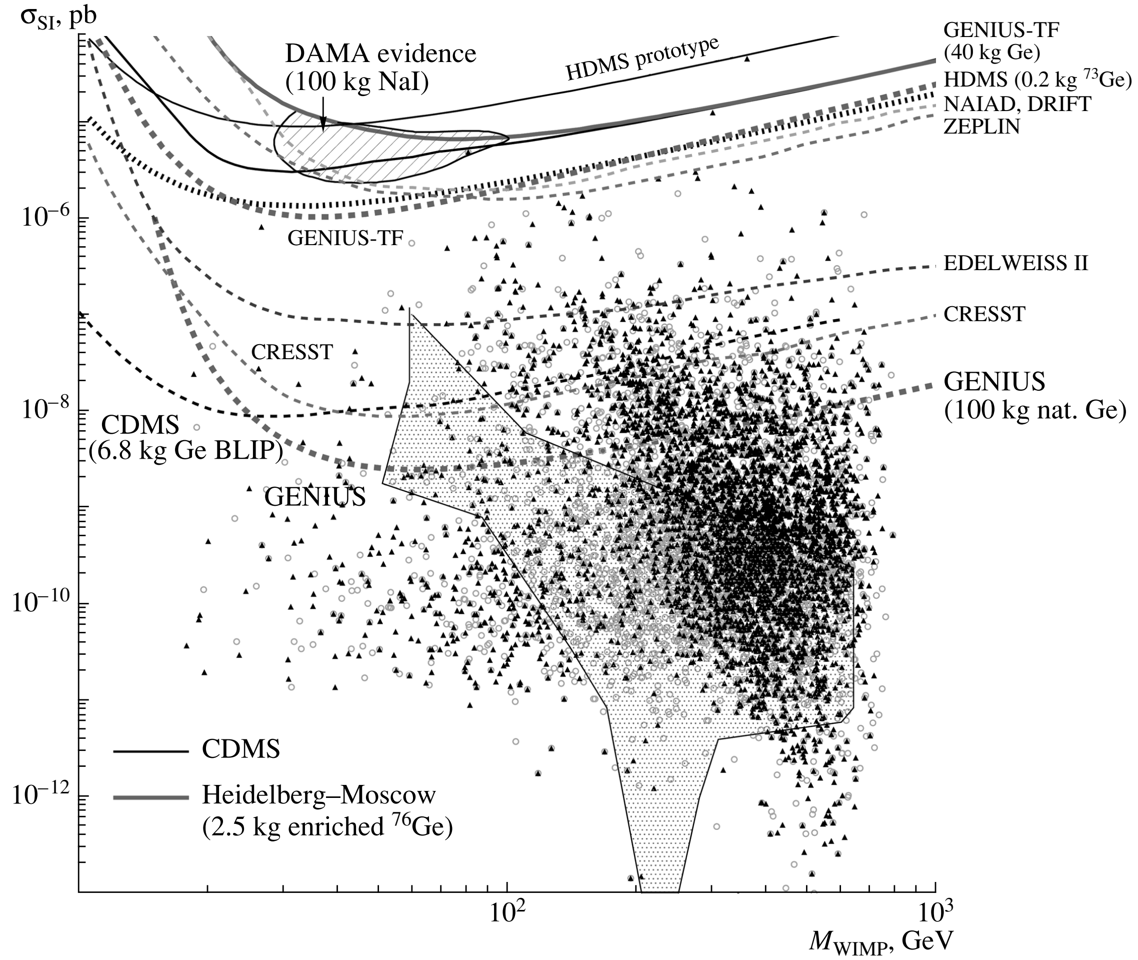

Fig. 1. WIMP–nucleon cross section limits for scalar (spin-independent) interactions as a function of the WIMP mass. Shown are contour lines of the present experimental limits (solid curve) and of projected experiments (dashed curve). Also shown is the region of evidence published by DAMA. The theoretical expectations are shown by scatter plots (circles and triangles are from [1, 2]) and by the grey closed region [3]. (From [4].)

(spin-dependent, or SD) terms [8, 17, 18]:

$$\frac{d\sigma^A}{dq^2}(v,q^2) = \frac{\sum|\mathcal{M}|^2}{\pi v^2(2J+1)} = \frac{S^A_{\rm SD}(q^2)}{v^2(2J+1)} \tag{2}$$

$$+ \frac{S^A_{\rm SI}(q^2)}{v^2(2J+1)} = \frac{\sigma^A_{\rm SD}(0)}{4\mu_A^2 v^2}F^2_{\rm SD}(q^2) + \frac{\sigma^A_{\rm SI}(0)}{4\mu_A^2 v^2}F^2_{\rm SI}(q^2).$$

The normalized nonzero-momentum-transfer nuclear form factors

$$F^2_{\rm SD,SI}(q^2) = \frac{S^A_{\rm SD,SI}(q^2)}{S^A_{\rm SD,SI}(0)} \tag{3}$$

$$(F^2_{\rm SD,SI}(0) = 1)$$

are defined via nuclear structure functions [8, 17, 18]

$$S^A_{\rm SI}(q) = \sum_{L\ \rm even} |\langle J||\mathcal{C}_L(q)||J\rangle|^2 \tag{4}$$

$$\simeq |\langle J||\mathcal{C}_0(q)||J\rangle|^2,$$

$$S^A_{\rm SD}(q) = \sum_{L\ \rm odd} \big(|\langle N||\mathcal{T}^{\rm el5}_L(q)||N\rangle|^2 \tag{5}$$

$$+ |\langle N||\mathcal{L}^5_L(q)||N\rangle|^2\big).$$

The transverse electric $\mathcal{T}^{\rm el5}(q)$ and longitudinal $\mathcal{L}^5(q)$ multipole projections of the axial vector current operator, scalar function $\mathcal{C}_L(q)$ are given in the form

$$\mathcal{T}^{\rm el5}_L(q) = \frac{1}{\sqrt{2L+1}}\sum_i \frac{a_0 + a_1\tau_3^i}{2}$$

$$\times\Big[-\sqrt{L}M_{L,L+1}(q\mathbf{r}_i) + \sqrt{L+1}M_{L,L-1}(q\mathbf{r}_i)\Big],$$

$$\mathcal{L}^5_L(q) = \frac{1}{\sqrt{2L+1}}\sum_i\Big(\frac{a_0}{2} + \frac{a_1 m_\pi^2\tau_3^i}{2(q^2+m_\pi^2)}\Big)$$

$$\times \left[\sqrt{L+1}M_{L,L+1}(q\mathbf{r}_i)+\sqrt{L}M_{L,L-1}(q\mathbf{r}_i)\right],$$

$$\mathcal{C}_L(q)=\sum_{i,\text{nucleons}} c_0 j_L(qr_i)Y_L(\hat{r}_i),$$

$$\mathcal{C}_0(q)=\sum_i c_0 j_0(qr_i)Y_0(\hat{r}_i),$$

where $a_{0,1}=a_n\pm a_p$ (see (10)) and $M_{L,L'}(q\mathbf{r}_i)=j_{L'}(qr_i)[Y_{L'}(\hat{r}_i)\boldsymbol{\sigma}_i]^L$ [8, 17, 18]. The nuclear SD and SI cross sections at $q=0$ (in (2)) have the forms

$$\sigma^A_{\rm SI}(0)=\frac{4\mu_A^2 S_{\rm SI}(0)}{(2J+1)}=\frac{\mu_A^2}{\mu_p^2}A^2\sigma^p_{\rm SI}(0), \tag{6}$$

$$\sigma^A_{\rm SD}(0)=\frac{4\mu_A^2 S_{\rm SD}(0)}{(2J+1)}=\frac{4\mu_A^2}{\pi}\frac{(J+1)}{J} \tag{7}$$
$$\times\left\{a_p\langle\mathbf{S}^A_p\rangle+a_n\langle\mathbf{S}^A_n\rangle\right\}^2=\frac{\mu_A^2}{\mu_{p,n}^2}\frac{(J+1)}{3J}$$
$$\times\left\{\sqrt{\sigma^p_{\rm SD}(0)}\langle\mathbf{S}^A_p\rangle+\mathrm{sgn}(a_pa_n)\sqrt{\sigma^n_{\rm SD}(0)}\langle\mathbf{S}^A_n\rangle\right\}^2.$$

Here,

$$\mu_A=m_\chi M_A/(m_\chi+M_A) \tag{8}$$

is the reduced neutralino–nucleus mass. The zero-momentum-transfer proton and neutron SI and SD cross sections

$$\sigma^p_{\rm SI}(0)=4\frac{\mu_p^2}{\pi}c_0^2, \tag{9}$$
$$c_0\equiv c_0^{(p,n)}=\sum_q \mathcal{C}_q f_q^{(p,n)};$$

$$\sigma^{p,n}_{\rm SD}(0)=12\frac{\mu_{p,n}^2}{\pi}a^2_{p,n}, \tag{10}$$
$$a_n=\sum_q\mathcal{A}_q\Delta_q^{(p)},\quad a_p=\sum_q\mathcal{A}_q\Delta_q^{(n)}$$

depend on the effective neutralino–quark scalar $\mathcal{C}_q$ and axial-vector $\mathcal{A}_q$ couplings from the effective Lagrangian

$$\mathcal{L}_{\rm eff}=\sum_q\left(\mathcal{A}_q\cdot\bar{\chi}\gamma_\mu\gamma_5\chi\cdot\bar{q}\gamma^\mu\gamma_5 q+\mathcal{C}_q\cdot\bar{\chi}\chi\cdot\bar{q}q\right)+\ldots \tag{11}$$

and on the spin ($\Delta_q^{(p,n)}$) and mass ($f_q^{(p,n)}$) structure of nucleons. The factors $\Delta_q^{(p,n)}$ parametrize the quark spin content of the nucleon and are defined by the relation $2\Delta_q^{(n,p)}s^\mu\equiv\langle p,s|\bar{\psi}_q\gamma^\mu\gamma_5\psi_q|p,s\rangle_{(p,n)}$. The total nuclear spin (proton, neutron) operator is defined as follows

$$\mathbf{S}_{p,n}=\sum_i^A\mathbf{s}_{p,n}(i), \tag{12}$$

where i runs over all nucleons. Further, the convention is used that all angular momentum operators are evaluated in their z projection in the maximal M_J state, e.g.,

$$\langle\mathbf{S}\rangle\equiv\langle N|\mathbf{S}|N\rangle\equiv\langle J,M_J=J|S_z|J,M_J=J\rangle. \tag{13}$$

Therefore, $\langle\mathbf{S}_{p(n)}\rangle$ is the spin of the proton (neutron) averaged over all nucleons in the nucleus A. The cross sections at zero momentum transfer show strong dependence on the nuclear structure of the ground state [19–21].

The relic neutralinos in the halo of our Galaxy have a mean velocity of $\langle v\rangle\simeq 300$ km/s $=10^{-3}c$. When the product $q_{\rm max}R\ll 1$, where R is the nuclear radius and $q_{\rm max}=2\mu_A v$ is the maximum momentum transfer in the $\tilde{\chi}A$ scattering, the matrix element for the spin-dependent $\tilde{\chi}A$ scattering reduces to a very simple form (zero momentum transfer limit) [20, 21]:

$$\mathcal{M}=C\langle N|a_p\mathbf{S}_p+a_n\mathbf{S}_n|N\rangle\cdot\mathbf{s}_{\tilde{\chi}} \tag{14}$$
$$=C\Lambda\langle N|\mathbf{J}|N\rangle\cdot\mathbf{s}_{\tilde{\chi}}.$$

Here, $\mathbf{s}_\chi$ is the spin of the neutralino, and

$$\Lambda=\frac{\langle N|a_p\mathbf{S}_p+a_n\mathbf{S}_n|N\rangle}{\langle N|\mathbf{J}|N\rangle} \tag{15}$$
$$=\frac{\langle N|(a_p\mathbf{S}_p+a_n\mathbf{S}_n)\cdot\mathbf{J}|N\rangle}{J(J+1)}.$$

It is seen that the χ couples to the spin carried by the protons and the neutrons. The normalization C involves the coupling constants, the masses of the exchanged bosons, and various LSP mixing parameters, which have no effect upon the nuclear matrix element [22]. In the limit of zero momentum transfer $q=0$, the spin structure function (5) reduces to

$$S^A_{\rm SD}(0)=\frac{2J+1}{\pi}\Lambda^2J(J+1). \tag{16}$$

Perhaps, the first model to estimate the spin content in the nucleus for the dark matter search was the independent single-particle shell model (ISPSM) used originally by Goodman and Witten [23] and later in [11, 24, 25]. The ground state value of the nuclear total spin J can be described by those of one extra nucleon interacting with the effective potential of the nuclear core.

There are nuclear structure calculations (including non-zero-momentum approximation) for spin-dependent neutralino interaction with helium ^{3}He [26]; fluorine ^{19}F [19, 26, 27]; sodium ^{23}Na [19, 20, 26, 27]; aluminum ^{27}Al [21]; silicon ^{29}Si [17, 19, 27]; chlorine ^{35}Cl [17]; potassium ^{39}K [21]; germanium ^{73}Ge [17, 28]; niobium ^{93}Nb [29]; iodine ^{127}I [20]; xenon ^{129}Xe [20] and ^{131}Xe [8, 20, 30];

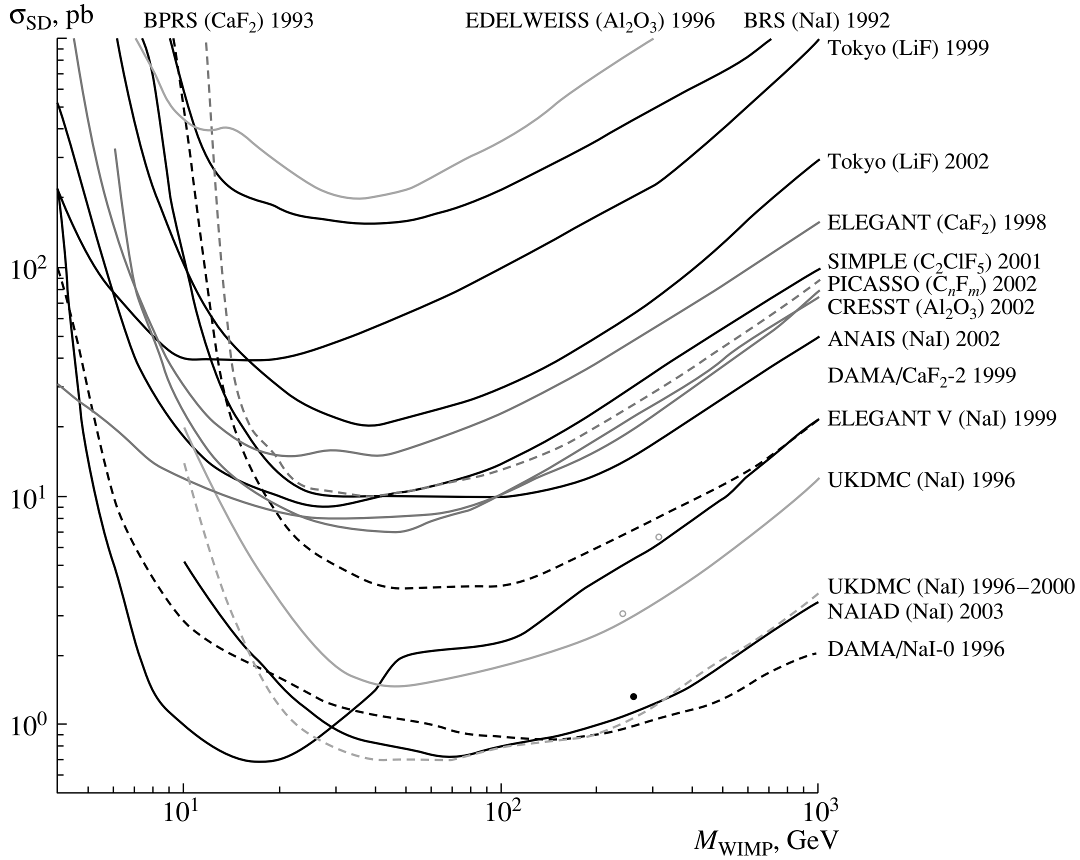

Fig. 2. Full set of currently available exclusion curves for spin-dependent WIMP–proton cross sections (σ^p_{SD} as a function of WIMP mass). The curves are obtained from [36–59].

tellurium ^{123}Te [30] and ^{125}Te [20]; and lead ^{208}Pb [26, 31]. The zero-momentum case is also investigated for Cd, Cs, Ba, and La in [30, 32, 33].

There are several approaches to more accurate calculation of the nuclear structure effects relevant to dark matter detection. To the best of our knowledge, an almost complete list of the models includes the Odd Group Model (OGM) of Engel and Vogel [34] and their extended OGM (EOGM) [18, 34]; the Interacting Boson Fermion Model (IBFM) of Iachello, Krauss, and Maino [33]; the Theory of Finite Fermi Systems (TFFS) of Nikolaev and Klapdor-Kleingrothaus [35]; the Quasi Tamm–Dancoff Approximation (QTDA) of Engel [8]; the different shell model treatments (SM) by Pacheco and Strottman [32], by Engel, Pittel, Ormand, and Vogel [29] and Engel, Ressell, Towner, and Ormand [21], by Ressell *et al.* [17] and Ressell and Dean [20], by Kosmas, Vergados, *et al.* [19, 26, 31]; the so-called "hybrid" model of Dimitrov, Engel, and Pittel [28]; and the perturbation theory (PT) based on calculations of Engel *et al.* [21].

3. SPIN CONSTRAINTS

For the spin-zero nuclear target, the experimentally measured event rate (1) of direct DM particle detection via formula (2) is connected with the zero-momentum WIMP–proton (for the neutron, the cross section is the same) cross section (7). The zero momentum scalar WIMP–proton (neutron) cross section $\sigma^p_{\mathrm{SI}}(0)$ can be expressed through effective neutralino–quark couplings $\mathcal{C}_q$ (11) by means of expression (9). These couplings $\mathcal{C}_q$ (as well as $\mathcal{A}_q$) can be directly connected with the fundamental parameters of a SUSY model such as $\tan\beta$, $M_{1,2}$, μ, masses of sfermions and Higgs bosons, etc. Therefore, experimental limitations on the spin-independent neutralino–nucleon cross section supply us with a constraint on the fundamental parameters of an underlying SUSY model.

In the case of the spin-dependent WIMP–nucleus interaction from measured differential rate (1), one first extracts limitation for $\sigma^A_{\mathrm{SD}}(0)$ and, therefore, has in principle two constraints [6] for the neutralino–proton a_p and neutralino–neutron a_n spin effective

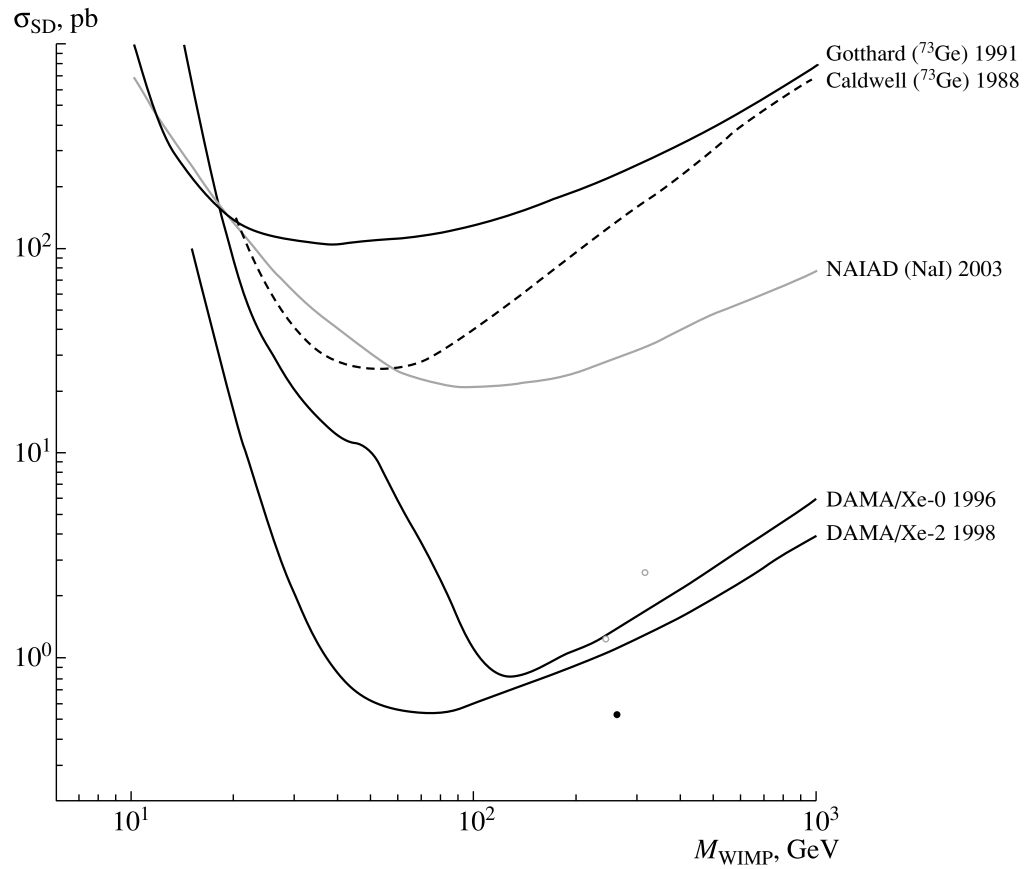

Fig. 3. Full set of currently available exclusion curves for spin-dependent WIMP–neutron cross sections (σ^n_{SD} versus WIMP mass). The curves are obtained from [36–59]. Note that the NAIAD curve corresponds to the subdominant contribution extracted from the p-odd nucleus Na (compare with the relevant NAIAD curve in Fig. 2).

couplings, as follows from relation (7). From (7), one can also see that contrary to the spin-independent case (6), there is no factorization of the nuclear structure for $\sigma^A_{SD}(0)$. Both proton $\langle \mathbf{S}^A_p \rangle$ and neutron $\langle \mathbf{S}^A_n \rangle$ spin contributions simultaneously enter formula (7) for the SD WIMP–nuclear cross section $\sigma^A_{SD}(0)$.

In the earlier considerations based on the OGM [18, 34], one assumed that the nuclear spin is carried by the "odd" unpaired group of protons or neutrons, and only one of either $\langle \mathbf{S}^A_n \rangle$ or $\langle \mathbf{S}^A_p \rangle$ is nonzero (the same is true in the ISPSM [11, 23–25]. In this case, all possible target nuclei can naturally be classified into n-odd and p-odd groups. The current experimental situation for the spin-dependent WIMP–proton cross section is given in Fig. 2. The data are taken from experiments BRS (NaI, 1992) [36, 37], BPRS (CaF_2, 1993) [38], EDELWEISS (sapphire, 1996) [39], DAMA (NaI, 1996) [40], DAMA (CaF_2, 1999) [41, 42], UKDMC (NaI, 1996) [43–46], ELEGANT (CaF_2, 1998) [47], ELEGANT (NaI, 1999) [48, 49], Tokio (LiF, 1999, 2002) [50–54], SIMPLE (C_2ClF_5, 2001) [55], CRESST (Al_2O_3, 2002) [56], PICASSO (C_nF_m, 2002) [57], ANAIS (NaI, 2002) [58], and NAIAD (NaI, 2003) [59]. The current experimental situation for the spin-dependent WIMP–neutron cross section is given in Fig. 3. The data are taken from the first experiments with natural Ge (1988, 1991) [60, 61], xenon (DAMA/Xe-0,2) [62–64], and sodium iodide (NAIAD) [59]. In the future one can also expect exclusion curves for the SD cross section, for example, from the EDELWEISS and CDMS experiments with natural germanium bolometric detectors.

From Fig. 4, one can conclude that an about two-orders-of-magnitude improvement of the current DM experiment sensitivities is needed to reach the SUSY predictions for the σ^p_{SD} provided the LSP is the best WIMP particle candidate. There is the same situation for the σ^n_{SD}.

Further, more accurate calculations of [8, 17, 19–21, 26, 28, 29, 31–33] demonstrate that contrary to the simplified odd-group approach both $\langle \mathbf{S}^A_p \rangle$ and

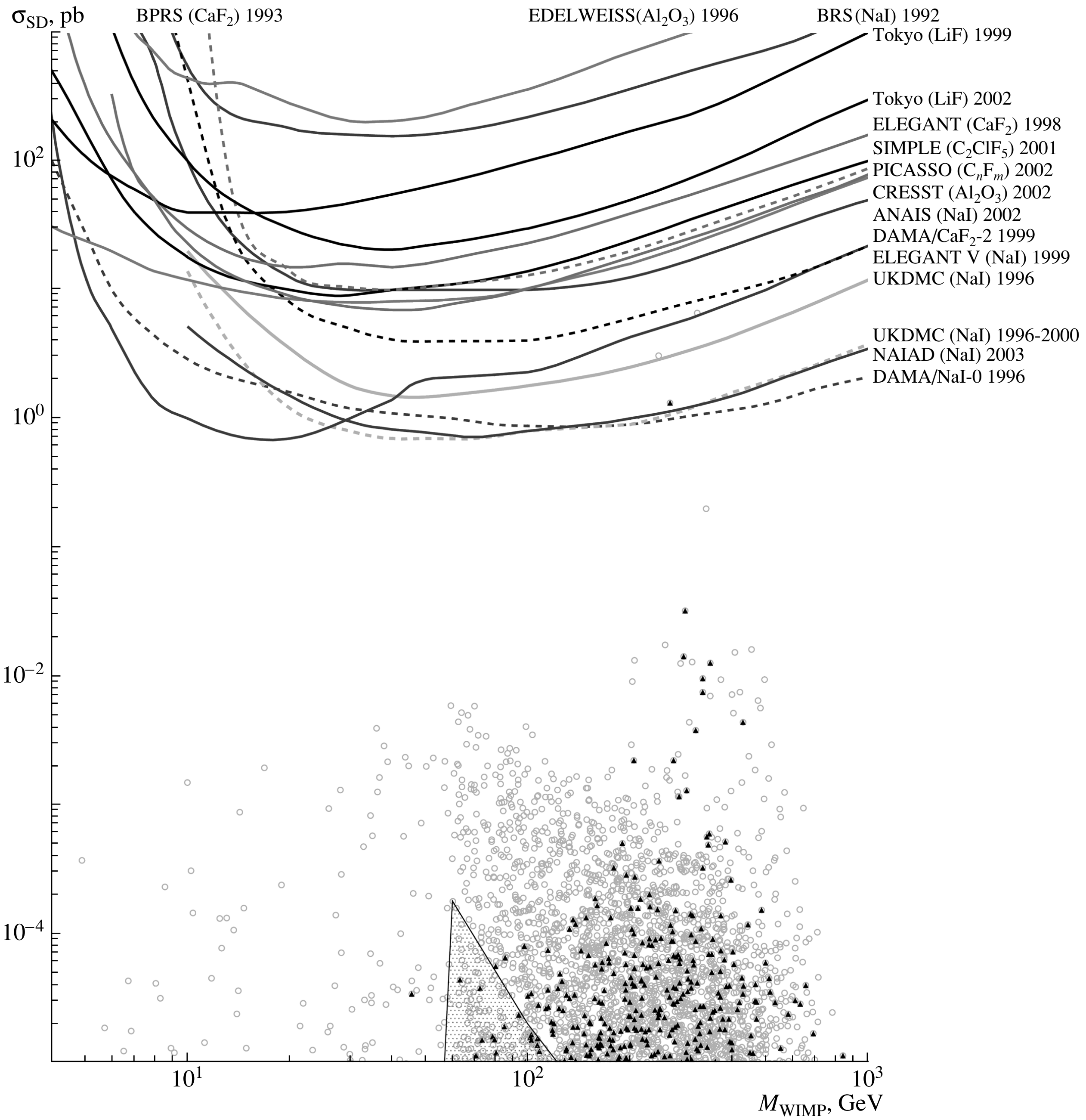

Fig. 4. The same as in Fig. 2, but with the theoretical scatter plot from [2], obtained in the effMSSM with all coannihilation channels included (circles) and with $0.1 < \Omega h^2 < 0.3$ (black triangles). The triangle-like shaded area is taken from [3].

$\langle \mathbf{S}_n^A \rangle$ differ from zero, but nevertheless one of these spin quantities always dominates ($\langle \mathbf{S}_p^A \rangle \ll \langle \mathbf{S}_n^A \rangle$ or $\langle \mathbf{S}_n^A \rangle \ll \langle \mathbf{S}_p^A \rangle$). If, together with dominance like $\langle \mathbf{S}_{p(n)}^A \rangle \ll \langle \mathbf{S}_{n(p)}^A \rangle$, one would have WIMP–proton and WIMP–neutron couplings of the same order of magnitude (not $a_{n(p)} \ll a_{p(n)}$), the situation could look like that in the odd-group model. Nevertheless, it was shown in [65] that in the general SUSY model one can meet a case when $a_{n(p)} \ll a_{p(n)}$. To solve the problem (to separate the SD proton and neutron constraints), at least two new approaches were proposed. As the authors of [65] claimed, their method has the advantage that the limits on individual WIMP–proton and WIMP–neutron SD cross sections for a given WIMP mass can be combined to give a model-

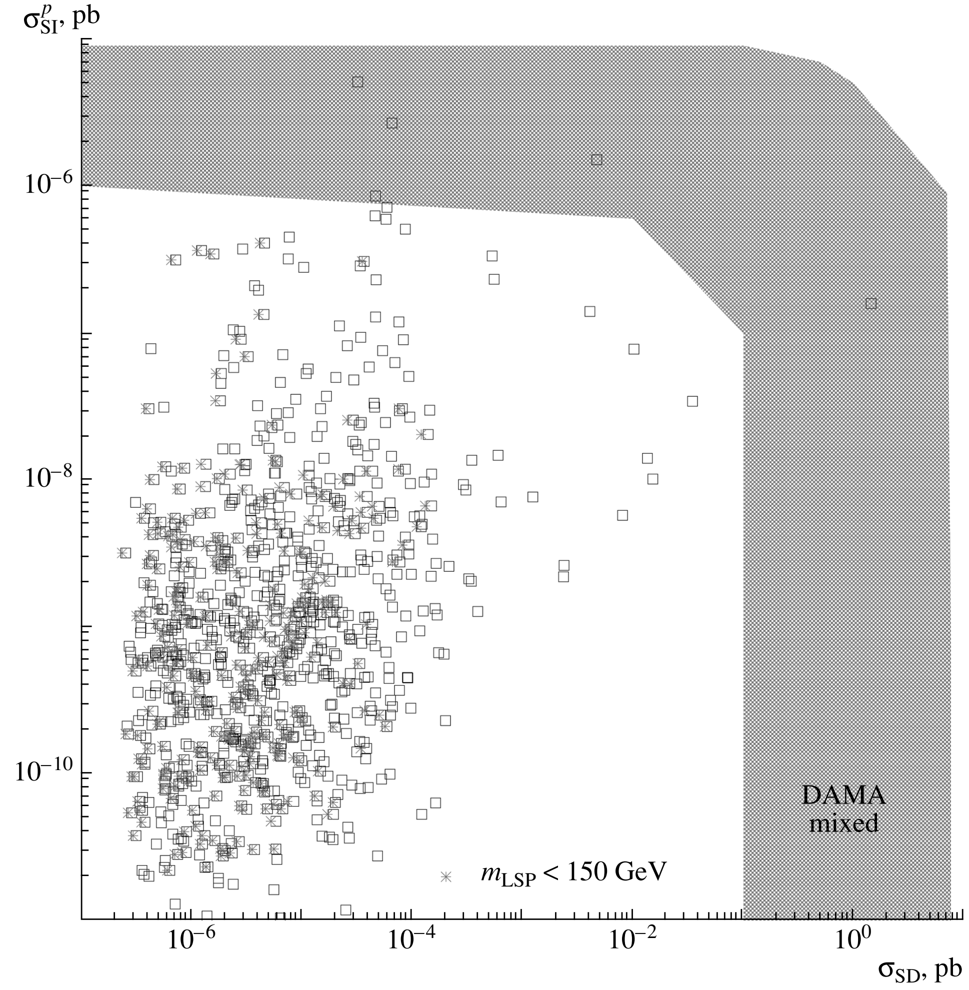

Fig. 5. The DAMA/NaI region from the WIMP annual modulation signature in the $(\xi\sigma_{\rm SI}, \xi\sigma_{\rm SD})$ space [66]. Scatter plots give correlations between $\sigma_{\rm SI}^{p}(0)$ and $\sigma_{\rm SD}$ in effMSSM with the requirement for neutralino relic density $0.1 < \Omega h^2 < 0.3$ [2]. Stars correspond to an assumption that $m_{\rm LSP} < 150$ GeV.

independent limit on the properties of WIMP scattering from both protons and neutrons in the target nucleus. The method relies on the assumption that the WIMP–nuclear SD cross section can be presented in the form $\sigma_{\rm SD}^{A}(0) = \left(\sqrt{\sigma_{\rm SD}^{p}|_A} \pm \sqrt{\sigma_{\rm SD}^{n}|_A}\right)^2$, where $\sigma_{\rm SD}^{p}|_A$ and $\sigma_{\rm SD}^{n}|_A$ are auxiliary quantities not directly connected with measurements. Furthermore, to extract, for example, a constraint on the subdominant WIMP–proton spin contribution, one should assume the proton contribution dominance for a nucleus whose spin is almost completely determined by the neutron-odd group. It may seem useless, especially, because these subdominant constraints are always much weaker than the relevant constraints obtained directly with a proton-odd group target.

Another approach of [66] is based on introduction of another auxiliary quantity $\sigma_{\rm SD} = 12\frac{\mu_p^2}{\pi}(a_p^2 + a_n^2)$, where $\tan\theta = a_n/a_p$. With these definitions the SD WIMP–proton and WIMP–neutron cross section can be given in the form $\sigma_{\rm SD}^{n(p)}(0) = \sigma_{\rm SD}\sin^2\theta(\cos^2\theta)$. In Fig. 5 the WIMP–nucleon spin-mixed and scalar couplings allowed by the annual modulation signature from the 100-kg DAMA/NaI experiment (57 986 kg d) are given by filled region. The region (at 3σ C.L.) in the $(\xi\sigma_{\rm SI}, \xi\sigma_{\rm SD})$ space for $40 < m_{\rm WIMP} < 110$ GeV covers all four particular couplings ($\theta = 0$, $\theta = \pi/4$, $\theta = \pi/2$ and $\theta = 2.435$ rad) reported in [66]. Scatter plots give $\sigma_{\rm SI}^{p}(0)$ versus $\sigma_{\rm SD}$ in effMSSM with $0.1 < \Omega h^2 < 0.3$ and all coannihilation channels included from [2] under the assumption of $\xi = 1$. Red stars correspond to the same calculations but with

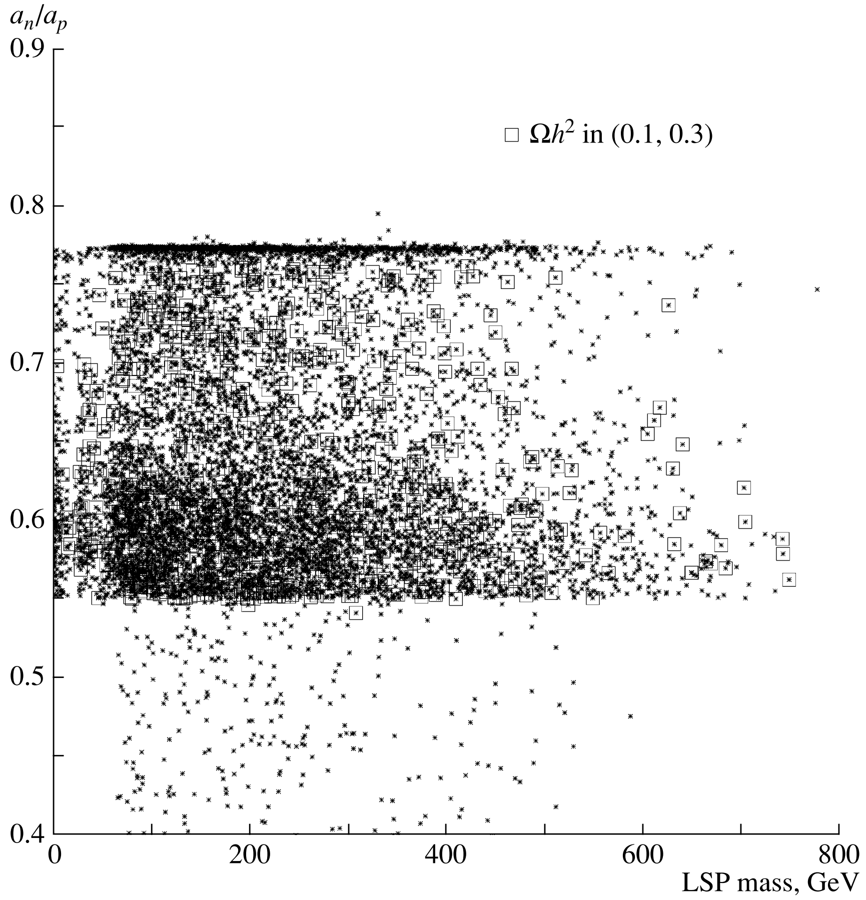

Fig. 6. The scatter plot (dots) gives the ratio of the neutralino–neutron a_n and neutralino–proton a_p spin couplings in the effMSSM [2]. Boxes correspond to the relic neutralino density constraint $0.1 < \Omega h^2 < 0.3$.

$m_{\rm LSP} < 150$ GeV. In this mixed case, the limits for the spin couplings depend on assumptions about the scalar coupling, and the relevant exclusion curve for the spin-dependent WIMP–proton cross section (not given in Fig. 2) cannot be simply extracted from these mixed results of [67].

4. THE ROLE OF THE ^{73}Ge ISOTOPE

Comparing the number of exclusion curves in Figs. 2 and 3, one can easily see that there are many measurements with p-odd nuclei and there is a lack of data for n-odd nuclei, i.e., for $\sigma^n_{\rm SD}$. Therefore, measurements with n-odd nuclei are needed. From our point of view, this lack of $\sigma^n_{\rm SD}$ measurements can be filled with new data expected from the HDMS experiment with the high-spin isotope ^{73}Ge [68]. This isotope looks, with good accuracy, like an almost pure n-odd group nucleus with $\langle \mathbf{S}_n \rangle \gg \langle \mathbf{S}_p \rangle$ (the table). The variation of the $\langle \mathbf{S}_p \rangle$ and $\langle \mathbf{S}_n \rangle$ in the table reflects the level of inaccuracy and complexity of the current nuclear structure calculations.

On the other hand, Fig. 6 shows that for the ratio of a_n to a_p one can have the bounds $0.55 < |a_n/a_p| < 0.8$. The scatter plots in Fig. 6 were obtained in effMSSM [2] when all coannihilation channels were included. The open squares (black points) were calculated with (without) the relic neutralino density constraint $0.1 < \Omega h^2 < 0.3$. Therefore, in the model, the couplings are almost the same, and one can safely neglect the $\langle \mathbf{S}^A_p \rangle$-spin contribution in the analysis of the DM data with the ^{73}Ge target (for which $\langle \mathbf{S}^A_p \rangle \ll \langle \mathbf{S}^A_n \rangle$).

We would like to advocate the old odd-group-like approach for experiments with germanium detectors. Of course, from measurements with ^{73}Ge, one can extract not only the dominant constraint for WIMP–nucleon coupling a_n (or $\sigma^n_{\rm SD}$) but also the constraint for the subdominant WIMP–proton coupling a_p (or $\sigma^p_{\rm SD}$) using the approach of [65]. Nevertheless, the

Zero-momentum spin structure (and predicted magnetic moments μ) of the ^{73}Ge nucleus in different nuclear models (the experimental value of the magnetic moment given in the brackets was used as input in the calculations)

^{73}Ge ($L_J = G_{9/2}$)	$\langle \mathbf{S}_p \rangle$	$\langle \mathbf{S}_n \rangle$	μ (in μ_N)
ISPSM, Ellis–Flores [24, 69]	0	0.0	−1.913
OGM, Engel–Vogel [34]	0	0.23	$(-0.879)_{\rm exp}$
IBFM, Iachello *et al.* [33] and [17]	−0.009	0.469	−1.785
IBFM (quenched), Iachello *et al.* [33] and [17]	−0.005	0.245	$(-0.879)_{\rm exp}$
TFFS, Nikolaev–Klapdor-Kleingrothaus [35]	0	0.34	–
SM (small), Ressell *et al.* [17]	0.005	5.596	−1.468
SM (large), Ressell *et al.* [17]	0.011	0.468	−1.239
SM (large, quenched), Ressell *et al.* [17]	0.009	0.372	$(-0.879)_{\rm exp}$
"Hybrid" SM, Dimitrov *et al.* [28]	0.030	0.378	−0.920

latter constraint will be much weaker in comparison with the constraints from p-odd group nuclear targets, like ^{19}F or NaI. This fact illustrates the NAIAD (NaI, 2003) curve in Fig. 3, which corresponds to the subdominant WIMP–neutron spin contribution extracted from the p-odd nucleus Na.

5. FINITE MOMENTUM TRANSFER

As $m_{\tilde{\chi}}$ becomes larger, the product qR ceases to be negligible and the finite momentum transfer limit must be considered. With the isoscalar coupling constant $a_0 = a_n + a_p$ and the corresponding isovector coupling constant $a_1 = a_p - a_n$, one splits $S^A_{\rm SD}(q)$ into a pure isoscalar, S_{00}, a pure isovector, S_{11}, and an interference term, S_{01} [17, 20]:

$$S^A_{\rm SD}(q) = a_0^2 S^A_{00}(q) + a_1^2 S^A_{11}(q) + a_0 a_1 S^A_{01}(q). \quad (17)$$

The differential SD event rate has the form

$$\frac{dR^A_{\rm SD}}{dq^2} = \frac{\rho}{m_{\tilde{\chi}} m_A} \int v dv f(v) \frac{8G_F^2}{(2J+1)v^2} S^A_{\rm SD}(q). \quad (18)$$

Comparing the differential rate (18), together with the spin structure functions of (17), with the observed recoil spectra for different targets (Ge, Xe, F, NaI, etc.), one can directly and simultaneously restrict both isoscalar and isovector neutralino–nucleon effective couplings $a_{0,1}$. These constraints will impose the most model-independent restrictions on the MSSM parameter space free from any assumption of [65, 66]. Perhaps, it would be best to fit all the data directly [65] in terms of the neutralino proton and neutron effective spin couplings $a_{0,1}$ or $a_{p,n}$ (see, for example, analysis of [54]) and not to use such spin quantities as $\sigma^{p,n}_{\rm SD}$ and $\sigma_{\rm SD}$.

Another attractive feature of spin-dependent WIMP–nucleus interaction is the q-dependence of the SD structure function (17). One knows that the ratio of SD to SI rate in the ^{73}Ge detector grows with the WIMP mass [1, 7]. The growth is much greater for heavy target isotopes like xenon. The reason is the different behavior of the spin and scalar structure functions with increasing momentum transfer. For example, the xenon SI structure function vanishes for $q^2 \approx 0.02$ GeV, but the SD structure function is a nonzero constant in the region. As noted by Engel in [8], the relatively long tail of the SD structure function is caused by nucleons near the Fermi surface, which do the bulk of the scattering. The core nucleons, which dominate the SI nuclear coupling, contribute much less at large q. Therefore, the SD efficiency for detection of a DM signal is higher than the SI efficiency, especially for very heavy neutralinos.

6. CONCLUSION

The idea of this review paper is to attract attention to the role of the spin-dependent WIMP–nucleus interaction in dark matter search experiments. The importance of this interaction is discussed. The fullest possible set of currently available exclusion curves for spin-dependent WIMP—proton and WIMP—neutron cross sections is given in Figs. 2 and 3. Nowadays, about two-orders-of-magnitude improvement of the current DM experiment sensitivities is needed to reach the SUSY predictions for the $\sigma_{\rm SD}^{p,n}$. It is noted that a near-future experiment like HDMS [68], with the high-spin isotope ^{73}Ge being an almost pure n-odd nucleus, can fill in this gap and supply us with new important constraints for SUSY models.

ACKNOWLEDGMENTS

The author thanks Prof. H.V. Klapdor-Kleingrothaus for collaboration, Profs. V.A. Kuzmin and V.A. Rubakov for their interest in this work, and Drs. V.A. Kuzmin and F. Simkovic for helpful discussions.

This work was supported by the Russian Foundation for Basic Research, project no. 02-02-04009.

REFERENCES

1. V. A. Bednyakov and H. V. Klapdor-Kleingrothaus, Phys. Rev. D **63**, 095005 (2001).
2. V. A. Bednyakov, H. V. Klapdor-Kleingrothaus, and V. Gronewold, Phys. Rev. D **66**, 115005 (2002).
3. J. R. Ellis, A. Ferstl, and K. A. Olive, Phys. Lett. B **481**, 304 (2000).
4. I. V. Krivosheina, Yad. Fiz. **65**, 2228 (2002) [Phys. At. Nucl. **65**, 2165 (2002)].
5. R. Bernabei *et al.*, Phys. Lett. B **480**, 23 (2000).
6. V. A. Bednyakov, H. V. Klapdor-Kleingrothaus, and S. G. Kovalenko, Phys. Lett. B **329**, 5 (1994).
7. V. A. Bednyakov, Yad. Fiz. **66**, 518 (2003) [Phys. At. Nucl. **66**, 490 (2003)].
8. J. Engel, Phys. Lett. B **264**, 114 (1991).
9. G. Jungman, M. Kamionkowski, and K. Griest, Phys. Rep. **267**, 195 (1996).
10. J. D. Lewin and P. F. Smith, Astropart. Phys. **6**, 87 (1996).
11. P. F. Smith and J. D. Lewin, Phys. Rep. **187**, 203 (1990).
12. V. A. Bednyakov and H. V. Klapdor-Kleingrothaus, Yad. Fiz. **62**, 1033 (1999) [Phys. At. Nucl. **62**, 966 (1999)].
13. V. A. Bednyakov, H. V. Klapdor-Kleingrothaus, and S. G. Kovalenko, Yad. Fiz. **59**, 1777 (1996) [Phys. At. Nucl. **59**, 1718 (1996)].
14. V. A. Bednyakov, H. V. Klapdor-Kleingrothaus, and S. G. Kovalenko, Phys. Rev. D **55**, 503 (1997).
15. V. A. Bednyakov, S. G. Kovalenko, H. V. Klapdor-Kleingrothaus, and Y. Ramachers, Z. Phys. A **357**, 339 (1997).
16. V. A. Bednyakov, H. V. Klapdor-Kleingrothaus, and S. Kovalenko, Phys. Rev. D **50**, 7128 (1994).
17. M. T. Ressell *et al.*, Phys. Rev. D **48**, 5519 (1993).
18. J. Engel, S. Pittel, and P. Vogel, Int. J. Mod. Phys. E **1**, 1 (1992).
19. P. C. Divari, T. S. Kosmas, J. D. Vergados, and L. D. Skouras, Phys. Rev. C **61**, 054612 (2000).
20. M. T. Ressell and D. J. Dean, Phys. Rev. C **56**, 535 (1997).
21. J. Engel, M. T. Ressell, I. S. Towner, and W. E. Ormand, Phys. Rev. C **52**, 2216 (1995).
22. K. Griest, Phys. Rev. D **38**, 2357 (1988).
23. M. W. Goodman and E. Witten, Phys. Rev. D **31**, 3059 (1985).
24. J. R. Ellis and R. A. Flores, Nucl. Phys. B **307**, 883 (1988).
25. A. K. Drukier, K. Freese, and D. N. Spergel, Phys. Rev. D **33**, 3495 (1986).
26. J. D. Vergados, J. Phys. G **22**, 253 (1996).
27. J. D. Vergados, Yad. Fiz. **66**, 509 (2003) [Phys. At. Nucl. **66**, 481 (2003)].
28. V. Dimitrov, J. Engel, and S. Pittel, Phys. Rev. D **51**, 291 (1995).
29. J. Engel, S. Pittel, E. Ormand, and P. Vogel, Phys. Lett. B **275**, 119 (1992).
30. M. A. Nikolaev and H. V. Klapdor-Kleingrothaus, Z. Phys. A **345**, 183 (1993).
31. T. S. Kosmas and J. D. Vergados, Phys. Rev. D **55**, 1752 (1997).
32. A. F. Pacheco and D. Strottman, Phys. Rev. D **40**, 2131 (1989).
33. F. Iachello, L. M. Krauss, and G. Maino, Phys. Lett. B **254**, 220 (1991).
34. J. Engel and P. Vogel, Phys. Rev. D **40**, 3132 (1989).
35. M. A. Nikolaev and H. V. Klapdor-Kleingrothaus, Z. Phys. A **345**, 373 (1993).
36. C. Bacci *et al.*, Nucl. Phys. B (Proc. Suppl.) **35**, 159 (1994).
37. C. Bacci *et al.*, Phys. Lett. B **293**, 460 (1992).
38. C. Bacci *et al.*, Astropart. Phys. **2**, 117 (1994).
39. A. de Bellefon *et al.*, Astropart. Phys. **6**, 35 (1996).
40. R. Bernabei *et al.*, Phys. Lett. B **389**, 757 (1996).
41. R. Bernabei *et al.*, Astropart. Phys. **7**, 73 (1997).
42. P. Belli *et al.*, Nucl. Phys. B **563**, 97 (1999).
43. M. L. Sarsa *et al.*, Phys. Lett. B **386**, 458 (1996).
44. P. F. Smith *et al.*, Phys. Lett. B **379**, 299 (1996).
45. T. J. Sumner *et al.*, Nucl. Phys. B (Proc. Suppl.) **70**, 74 (1999).
46. N. J. C. Spooner *et al.*, Phys. Lett. B **473**, 330 (2000).
47. I. Ogawa *et al.*, Nucl. Phys. A **663**, 869 (2000).
48. K. Fushimi *et al.*, Astropart. Phys. **12**, 185 (1999).
49. S. Yoshida *et al.*, Nucl. Phys. B (Proc. Suppl.) **87**, 58 (2000).
50. W. Ootani *et al.*, Astropart. Phys. **9**, 325 (1998).
51. M. Minowa, Yad. Fiz. **61**, 1217 (1998) [Phys. At. Nucl. **61**, 1117 (1998)].
52. W. Ootani *et al.*, Phys. Lett. B **461**, 371 (1999).
53. W. Ootani *et al.*, Nucl. Instrum. Methods Phys. Res. A **436**, 233 (1999).
54. K. Miuchi *et al.*, Astropart. Phys. **19**, 135 (2003).
55. J. I. Collar *et al.*, astro-ph/0101176.
56. G. Angloher *et al.*, Astropart. Phys. **18**, 43 (2002).
57. N. Boukhira *et al.*, Nucl. Phys. B (Proc. Suppl.) **110**, 103 (2002).

58. S. Cebrian *et al.*, Nucl. Phys. B (Proc. Suppl.) **114**, 111 (2003).
59. B. Ahmed *et al.*, hep-ex/0301039.
60. D. O. Caldwell *et al.*, Phys. Rev. Lett. **61**, 510 (1988).
61. D. Reusser *et al.*, Phys. Lett. B **255**, 143 (1991).
62. P. Belli *et al.*, Nuovo Cimento C **19**, 537 (1996).
63. P. Belli *et al.*, Nucl. Phys. B (Proc. Suppl.) **48**, 62 (1996).
64. R. Bernabei *et al.*, Phys. Lett. B **436**, 379 (1998).
65. D. R. Tovey, R. J. Gaitskell, P. Gondolo, *et al.*, Phys. Lett. B **488**, 17 (2000).
66. R. Bernabei *et al.*, Phys. Lett. B **509**, 197 (2001).
67. R. Bernabei *et al.*, astro-ph/0305542.
68. H. V. Klapdor-Kleingrothaus *et al.*, Astropart. Phys. **18**, 525 (2003).
69. J. R. Ellis and R. A. Flores, Phys. Lett. B **263**, 259 (1991).

Physics of Atomic Nuclei, Vol. 67, No. 11, 2004, pp. 1942–1947. From Yadernaya Fizika, Vol. 67, No. 11, 2004, pp. 1967–1972.
Original English Text Copyright © 2004 by Popov.

NEUTRINO PHYSICS

Final Results on the Search for $\nu_\mu \to \nu_e$ Oscillations in the NOMAD Experiment[*]

B. A. Popov[**]
(for the NOMAD Collaboration)

Dzhelepov Laboratory of Nuclear Problems, Joint Institute for Nuclear Research,
Dubna, Moscow oblast, 141980 Russia

Received January 20, 2004

Abstract—The results of the search for $\nu_\mu \to \nu_e$ oscillations in the NOMAD experiment at CERN are presented. The experiment looked for the appearance of ν_e in a predominantly ν_μ wideband neutrino beam at the CERN SPS. No evidence for oscillations was found. The 90% confidence limits obtained are $\Delta m^2 <$ 0.4 eV^2 for maximal mixing and $\sin^2(2\theta) < 1.4 \times 10^{-3}$ for large Δm^2. This result excludes the LSND allowed region of oscillation parameters with $\Delta m^2 \gtrsim 10$ eV^2. *© 2004 MAIK "Nauka/Interperiodica".*

1. INTRODUCTION

The NOMAD experiment was designed to search for ν_τ appearance from neutrino oscillations [1] in the CERN wideband neutrino beam produced by the 450-GeV proton synchrotron (SPS). The detector was optimized to identify efficiently electrons from $\tau^- \to e^-\nu_e\nu_\tau$ decays and therefore could also be used to look for ν_e appearance in a predominantly ν_μ beam by detecting their charged current (CC) interactions $\nu_e N \to e^- X$. The main motivation for this search was the evidence for $\bar{\nu}_\mu \to \bar{\nu}_e$ and $\nu_\mu \to \nu_e$ oscillations found by the LSND experiment [2]. For $\nu_\mu \to \nu_e$ oscillations with $\Delta m^2 \gtrsim 10$ eV^2 and with the probability of 2.6×10^{-3} observed by LSND, a signal should be seen in the NOMAD data. The sensitivity of the NOMAD experiment to lower values of Δm^2 is limited by its L/E_ν ratio of ~0.025 km/GeV, where L is the average source-to-detector distance and E_ν is the average neutrino energy.

Preliminary results of the search for $\nu_\mu \to \nu_e$ oscillations in NOMAD were presented earlier [3]. In this paper, the final results of a "blind" analysis [4] are reported.

2. NOMAD DETECTOR AND NEUTRINO BEAM

A detailed description of the NOMAD detector and its performance is given in [5]. The detector consisted of a large dipole magnet delivering a field of 0.4 T and housing several subdetectors, starting with an active target composed of 132 planes of large 3 × 3-m drift chambers (DC) [6]. The walls of the chambers provided a low average density (0.1 g/cm^3) target with a mass of 2.7 t. The density of the chambers was low enough to allow an accurate measurement of the momenta of the charged particles produced in the neutrino interactions. The chambers were followed by nine transition radiation detector (TRD) modules [7] each consisting of a polypropylene radiator and a plane of straw tubes operated with an 80% xenon and 20% methane gas mixture. An electromagnetic calorimeter (ECAL) [8] consisting of 875 lead glass blocks provided a measurement of the energies of electrons and photons with a resolution of $\sigma(E)/E = 3.2\%/\sqrt{E(\mathrm{GeV})} + 1\%$. The ECAL was preceded by a lead-proportional tube preshower for better photon localization. A hadron calorimeter (HCAL) was located just beyond the magnet coil and was followed by two muon stations consisting of large-area DC, the first station located after 8 and the second one after 13 interaction lengths of iron.

The CERN West Area Neutrino Facility (WANF) neutrino beam [9] was produced by impinging 450-GeV protons extracted from the SPS onto a target consisting of beryllium rods adding up to a total thickness of 110 cm. The secondary particles emerging from the target were focused into a nearly parallel beam by two magnetic lenses (the horn and the reflector) providing toroidal magnetic fields. When running in neutrino mode, positively charged particles were focused. The focused particles then traversed a 290-m-long decay tunnel followed by an iron and earth shield. Neutrinos originating from the decay of these

---

[*] This article was submitted by the author in English.

[**] e-mail: `popov@nusun.jinr.dubna.su`

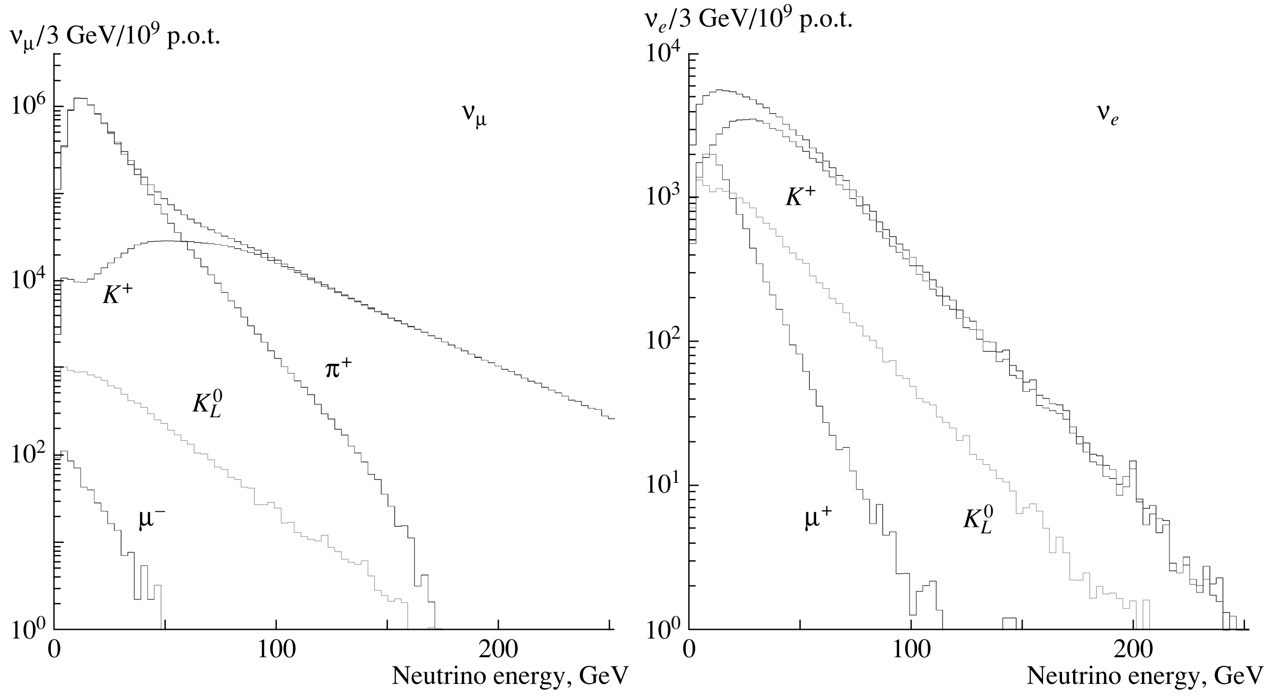

Fig. 1. Composition of the ν_μ and ν_e energy spectra at NOMAD, within a transverse fiducial area of 260 × 260 cm, as predicted by the NOMAD simulation of the neutrino beam line.

particles traveled on average a distance of 625 m before reaching the NOMAD detector.

Since the oscillation search implies a direct comparison between the measured and expected ratios of the number of ν_e CC to ν_μ CC interactions, an accurate prediction of the neutrino fluxes and spectra is crucial. They are computed with a detailed Monte Carlo simulation of the neutrino beam, referred to as NUBEAM and thoroughly described in [10]. This is implemented in three steps. First, the yields of the secondary particles from the interactions of 450-GeV protons with the Be target are calculated with the 2000 version of FLUKA [11], a generator of hadronic interactions. These yields are then modified in order to agree with all measurements currently available in the relevant energy and angular range, namely, the SPY/NA56 [12] and NA20 [13] results. Finally, the propagation of the secondary particles is described by a simulation program based on GEANT3 [14].

The resulting energy spectra of ν_μ and ν_e, and of their components, are shown in Fig. 1. The ν_μ flux is predominantly due to decays of π^+ up to 60-GeV neutrino energy and to those of K^+ above this energy. The bulk of the ν_e flux comes from the decays of K^+, with K_L^0 contributing at the level of about 18% and μ^+ at the level of about 14%. The composition of the beam is shown in the table.

The neutrino fluxes generated by NUBEAM were used as an input to the NOMAD event generator to produce interactions of ν_μ, $\bar{\nu}_\mu$, ν_e, and $\bar{\nu}_e$. Deep-inelastic scattering events were simulated with a modified version of the LEPTO 6.1 event generator [15], with Q^2 and W^2 cutoffs removed. Quasielastic [16] and resonance production [17] events were generated as well. The GRV-HO parametrization [18] of the parton density functions and the nucleon Fermi motion distribution of [19], truncated at 1 GeV/c, were used along with JETSET 7.4 [20] to treat the fragmentation.

The secondary particles produced in these interactions were then propagated through a full GEANT3 [14] simulation of the NOMAD detector.

Average energies and relative abundances of the fluxes and charged current events of the four principal neutrino flavors at NOMAD, within a transverse fiducial area of 260 × 260 cm

Flavor	Flux		CC interactions	
	$\langle E_\nu \rangle$, GeV	rel. abund.	$\langle E \rangle$, GeV	rel. abund.
ν_μ	24.3	1.0	47.5	1.0
$\bar{\nu}_\mu$	17.2	0.068	42.0	0.024
ν_e	36.4	0.010	58.2	0.015
$\bar{\nu}_e$	27.6	0.0027	50.9	0.0015

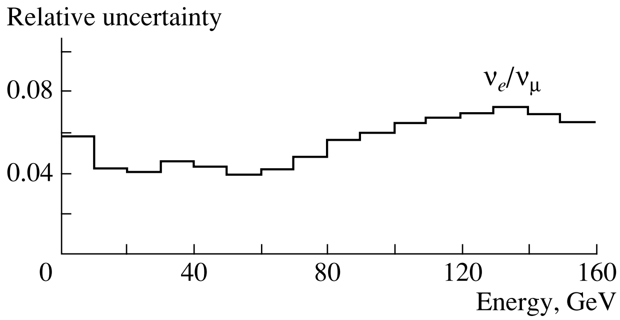

Fig. 2. Energy-dependent uncertainty in the prediction of the $R_{e\mu}$ ratio.

3. DATA COLLECTION AND EVENT RECONSTRUCTION

The NOMAD experiment collected data from 1995 to 1998. Most of the run, a total exposure of 5.1×10^{19} protons on target (p.o.t.), was in neutrino mode and yielded 1.3×10^6 ν_μ CC interactions in the fiducial volume of the detector.

The trajectories of charged particles are reconstructed from the hits in the DC and, from these trajectories, momenta are computed using the Kalman filter technique [21], which accounts for energy loss along the trajectory. As a first step, the energy-loss model used is that for pions, resulting in a momentum estimate, p_π, at the beginning of the track. Particles later identified as electrons or positrons are refitted [22] with an additional average energy loss due to bremsstrahlung, resulting in a new estimate, p_e, of the momentum. Energy clusters in the ECAL not associated to charged particles are assumed to be due to photons.

Vertices are reconstructed from the trajectories of charged particles. The energy of the incident neutrino, E_ν, is approximated by the total (visible) energy of an event computed from the sum of the energies of all observed primary particles and of photons.

Since the electron radiates bremsstrahlung photons in traversing the DC, in order to have an accurate measure of its energy, these photons must be identified and their energy added to the energy of the ECAL cluster at the end of the electron trajectory. Because of the curvature of the electron trajectory in the magnetic field, these photons are located in a vertical band. The energy of photons in the ECAL and of photon conversions in the DC found in this region is included, resulting in a measure of the electron energy, E_{brem}, with an average resolution of 2.1%.

4. PRINCIPLES OF OSCILLATION SEARCH

The $\nu_\mu \to \nu_e$ oscillation signal should manifest itself as an excess in the number of ν_e CC events over that expected for an intrinsic ν_e contamination in the beam (about 1% of ν_μ). In order to reduce systematic uncertainties associated with absolute flux predictions and selection efficiencies, we study the ratio $R_{e\mu}$ of the number of ν_e CC to ν_μ CC interactions. Due to different energy and radial distributions of incident electron and muon neutrinos, the contribution of the intrinsic ν_e component is smaller at low ν_e energies, E_ν, where a low-Δm^2 oscillation signal is expected, and at small radial distances from the beam axis, r. Thus, the sensitivity of the search is increased by taking into account the dependence of $R_{e\mu}$ on E_ν and r.

The presence or absence of $\nu_\mu \to \nu_e$ oscillations is established by comparing the measured $R_{e\mu}$ with the one expected in the absence of oscillations. In order to avoid biases, we adopted a "blind analysis" strategy: the comparison of the measured to the predicted $R_{e\mu}$ is not made until the accuracy of the flux predictions and the robustness of the data analysis have been demonstrated and until all selection criteria are fixed. It should be noted that no-oscillation signal is expected to be measurable in $\bar{\nu}_e$ since the intrinsic ratio of $\bar{\nu}_\mu/\bar{\nu}_e$ in the beam is 4 times smaller than the intrinsic ν_μ/ν_e ratio and the antineutrino statistics are limited.

5. EVENT SELECTION

In order to calculate $R_{e\mu}$, pure samples of ν_e CC and ν_μ CC interactions are selected. A detailed description of the selection criteria is given in [4]. The initial data sample for ν_e CC interactions is complementary to that used in the ν_μ CC selection described below; i.e., it consists only of those events that include no muon (identified with looser criteria than in the ν_μ CC selection). The basic requirement is the presence of a track associated with the neutrino interaction vertex, pointing to an energy deposition in the ECAL and identified as an electron in the TRD and ECAL.

Electrons from conversions and Dalitz decays are rejected by requiring (1) that the first point on the candidate track be within 15 cm of the primary vertex and (2) that no positively charged track, either identified as a positron in the TRD or missing the TRD, when taken together with the candidate electron, results in the combination being consistent with a conversion. The criteria used are the invariant mass and the angle between the plane containing the trajectories of the two tracks and the vertical.

In order to reduce further the background from neutral current and charged current events in which the muon was not identified, kinematic cuts are also

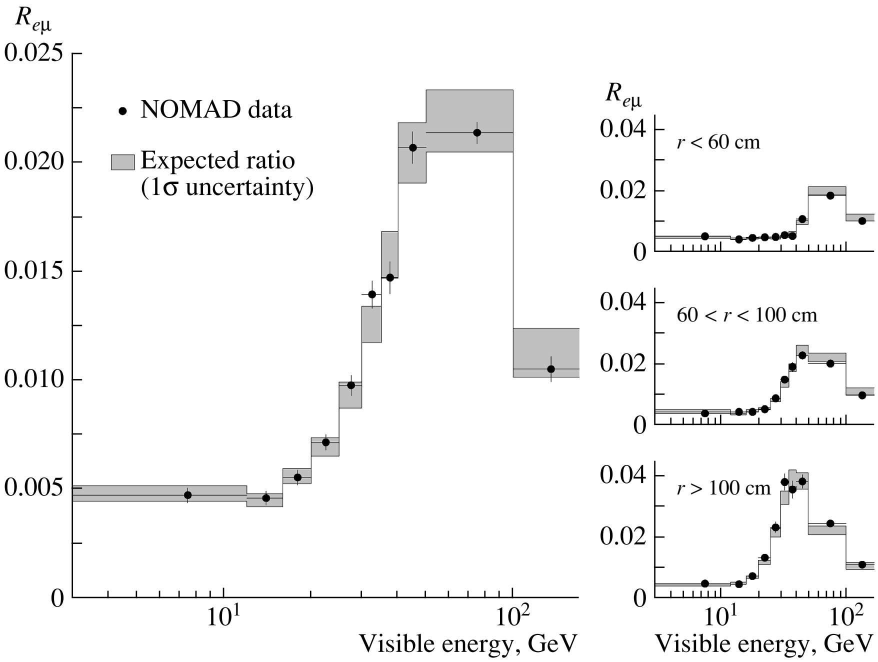

Fig. 3. The $R_{e\mu}$ ratio as a function of the visible energy for the data (points) and for the Monte Carlo prediction assuming no oscillations (filled bands), for the full radial acceptance (left) and in the three radial bins (right). The upper and lower boundaries of the bands correspond to the predictions with $\pm 1\sigma$ uncertainty, where σ includes both the normalization and the energy-dependent systematic uncertainties added in quadrature.

applied requiring the isolation of the electron from the hadronic jet.

Finally, only events with $p_e > 2.5$ GeV/c and $E_\nu < 300$ GeV are retained. These selection criteria result in an efficiency for ν_e CC, estimated from the Monte Carlo, of 43.9%. The surviving background contribution to the ν_e CC sample is estimated, from the Monte Carlo and its comparison with the data for a class of background e^+ events, to be 2.3%.

Charged current interactions of ν_μ are characterized by the presence of a primary muon in the final state, which had to penetrate 13 interaction lengths of absorber material to reach both muon stations in order to be identified. In addition, to minimize the differences between selection efficiencies of ν_μ CC and ν_e CC events, we apply kinematic criteria identical to those used in the ν_e CC selection, although they are not needed for the background suppression. The resulting ν_μ CC data sample has a negligible background contamination, while the average selection efficiency is 60%.

The geometrical and kinematical distributions of both types of events are well reproduced by the Monte Carlo simulation, with the exception of the distribution of interaction vertices along z, the beam direction. The origin of this difference is due mostly to a cut introduced during the reconstruction of events: events with a very high density of hits in the DC were not reconstructed due to a prohibitive reconstruction CPU time. Since the data has on average a higher density of hits than the Monte Carlo, the effect of this cut is different on the two samples. Furthermore, since electrons radiate photons in traversing the DC and some of these photons convert, the density of hits in ν_e CC events is large, thus enhancing the effect of the density cut for these events. The reprocessing of a sample of data and Monte Carlo events without this density cut resulted in z distributions that were in much better agreement. We therefore decided to restrict the analysis to events occurring in the 72 downstream planes of DC by requiring $z > 184$ cm. It should be noted that oscillation effects could not manifest themselves over the 4-m longitudinal dimension of the detector since the point of origin of the neutrinos is spread over more than 300 m.

A total of 5584 ν_e CC and 472378 ν_μ CC events were retained for the final analysis.

6. SYSTEMATIC UNCERTAINTIES

The single largest uncertainty in this oscillation search is the uncertainty in the prediction of the fraction and the energy spectrum of intrinsic ν_e present in the beam. The computation of this uncertainty is described in detail in [10]. The overall uncertainty arising from the knowledge of the beam composition

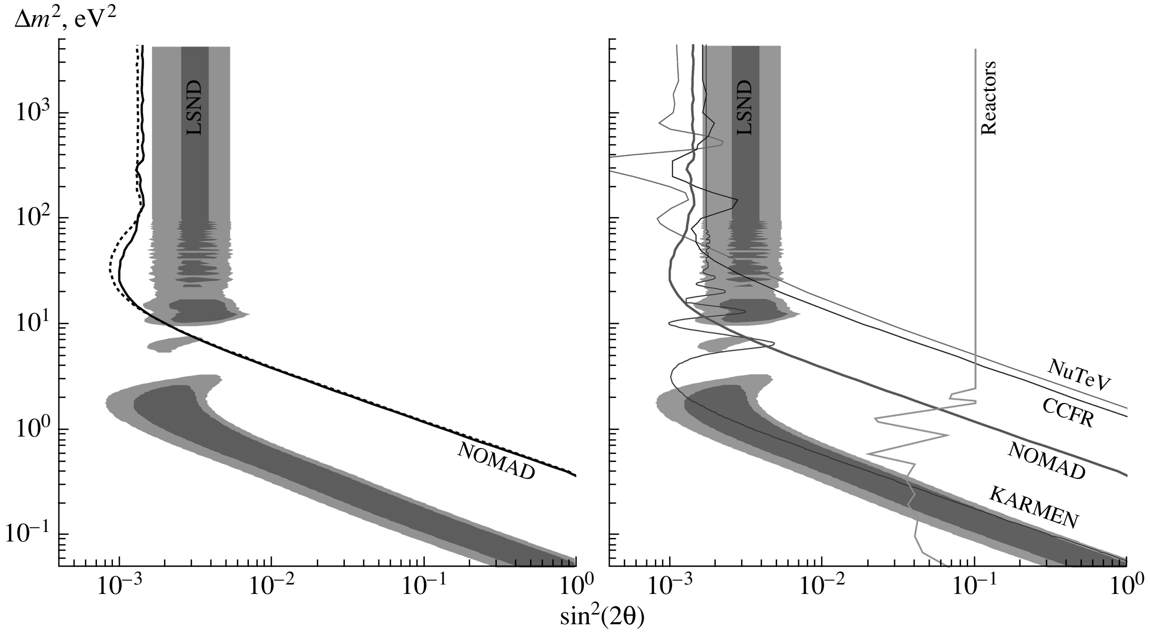

Fig. 4. The resulting NOMAD exclusion curve (solid) and the sensitivity (dashed) of the experiment (left). The 90% C.L. exclusion region in the (Δm^2, $\sin^2(2\theta)$) plane from this analysis superimposed on the results of other experiments (right).

is divided into an energy-independent, or normalization, uncertainty and an energy-dependent one. The normalization uncertainty on $R_{e\mu}$ is 4.2%, while the energy-dependent uncertainty, shown in Fig. 2, varies from 4 to 7%.

The contributions to systematic uncertainties from different sources can be summarized in the following way: particle production contributes ~5%; beam transport, ~3%; electron efficiency (identification and reconstruction), 1.0%; fragmentation and reinteraction model, up to 2%; electron energy scale, <1.0%. Contributions from the relative efficiency of kinematic selection and from “nonprompt” background (both amount and shape) are negligible.

7. RESULTS

The $R_{e\mu}$ distribution as a function of the visible energy obtained from the data is shown in Fig. 3 for the full radial acceptance (left) and in three radial bins (right). It is in good agreement with the Monte Carlo prediction under the no-oscillation hypothesis, also shown in the figure as $\pm 1\sigma$ uncertainty bands: $\chi^2 = 37.1/30$ d.o.f. is obtained when the data are analyzed and compared to the simulation in the ten energy bins and the three radial bins shown in Fig. 3 (incorporating both statistical and systematic uncertainties). The best fit to $\nu_\mu \to \nu_e$ oscillations, in the two-family approximation, gives a similar χ^2 value, $\chi^2_{\min} = 37.0/28$ d.o.f.

We use a frequentist approach [23] to set a 90% confidence upper limit on the oscillation parameters. The resulting exclusion region is shown in Fig. 4, together with results of other accelerator experiments, LSND [2], KARMEN [24], CCFR [25], and NuTeV [26], and the combined limit of Bugey [27] and Chooz [28] reactor experiments. Values of $\Delta m^2 > 0.4$ eV^2 for maximal mixing and $\sin^2(2\theta) > 1.4 \times 10^{-3}$ for large Δm^2 are excluded at 90% C.L. For comparison, the sensitivity [23] of the experiment is found to be $\Delta m^2 > 0.4$ eV^2 for maximal mixing and $\sin^2(2\theta) > 1.3 \times 10^{-3}$ at large Δm^2. Our result rules out the interpretation of the LSND measurements in terms of $\nu_\mu \to \nu_e$ oscillations with $\Delta m^2 \gtrsim 10$ eV^2.

8. CONCLUSION

The results of a search for $\nu_\mu \to \nu_e$ neutrino oscillations in the NOMAD experiment at CERN have been presented. The experiment looked for the appearance of ν_e in a predominantly ν_μ wideband neutrino beam at the CERN SPS. No evidence for oscillations was found. The 90% confidence limits obtained are $\Delta m^2 < 0.4$ eV^2 for maximal mixing and $\sin^2(2\theta) < 1.4 \times 10^{-3}$ for large Δm^2. This result excludes the high-Δm^2 region of oscillation parameters favored by the LSND experiment.

ACKNOWLEDGMENTS

It is a pleasure to thank the organizers of the NANP’03 conference for giving me a chance to present the results reported in this article. Crucial help from Slava Valuev in preparation of this contribution is very much appreciated.

REFERENCES

1. P. Astier *et al.* (NOMAD Collab.), Nucl. Phys. B **611**, 3 (2001).
2. C. Athanassopoulos *et al.* (LSND Collab.), Phys. Rev. Lett. **77**, 3082 (1996); **81**, 1774 (1998); A. Aguilar *et al.*, Phys. Rev. D **64**, 112007 (2001).
3. V. Valuev, in *Proceedings of the International EPS Conference on High-Energy Physics, Budapest, Hungary, 2001*, Ed. by D. Horvath, P. Levai, and A. Patkos, JHEP Proceedings Section, PRHEP-hep2001/190; http://jhep.sissa.it/
4. P. Astier *et al.* (NOMAD Collab.), Phys. Lett. B **570**, 19 (2003).
5. J. Altegoer *et al.* (NOMAD Collab.), Nucl. Instrum. Methods Phys. Res. A **404**, 96 (1998).
6. M. Anfreville *et al.*, Nucl. Instrum. Methods Phys. Res. A **481**, 339 (2002).
7. G. Bassompierre *et al.*, Nucl. Instrum. Methods Phys. Res. A **403**, 363 (1998); **411**, 63 (1998).
8. D. Autiero *et al.*, Nucl. Instrum. Methods Phys. Res. A **372**, 556 (1996); **373**, 358 (1996); **387**, 352 (1997); **411**, 285 (1998); **425**, 188 (1999).
9. G. Acquistapace *et al.*, CERN-ECP 95-14 (1995).
10. P. Astier *et al.* (NOMAD Collab.), hep-ex/0306022; CERN–EP/2003-032; Nucl. Instrum. Methods Phys. Res. A **515**, 800 (2003).
11. A. Fassò, A. Ferrari, P. R. Sala, and J. Ranft, in *Proceedings of the Monte Carlo 2000 Conference,* Ed. by A. Kling *et al.* (Springer, Berlin, 2001), p. 955.
12. G. Ambrosini *et al.* (SPY Collab.), Eur. Phys. J. C **10**, 605 (1999).
13. H. W. Atherton *et al.*, CERN Yellow Report 80-07 (1980).
14. R. Brun and F. Carminati, *GEANT—Detector Description and Simulation Tool,* CERN Program Library Long Writeup W5013 (1993).
15. G. Ingelman, in *Proceedings of the HERA Workshop,* Ed. by W. Buchmüller and G. Ingelman (DESY, Hamburg, 1992), p. 1336.
16. C. H. Llewellyn Smith, Phys. Rep. **3**, 261 (1972).
17. D. Rein and L. M. Sehgal, Ann. Phys. (N.Y.) **133**, 79 (1981).
18. M. Glück, E. Reya, and A. Vogt, Z. Phys. C **53**, 127 (1992).
19. A. Bodek and J. Ritchie, Phys. Rev. D **23**, 1070 (1981).
20. T. Sjöstrand, Comput. Phys. Commun. **39**, 347 (1986); T. Sjöstrand and M. Bengtsson, Comput. Phys. Commun. **43**, 367 (1987); T. Sjöstrand, Comput. Phys. Commun. **82**, 74 (1994).
21. R. Frühwirth, Nucl. Instrum. Methods Phys. Res. A **262**, 444 (1987).
22. P. Astier *et al.*, Nucl. Instrum. Methods Phys. Res. A **450**, 138 (2000).
23. G. J. Feldman and R. D. Cousins, Phys. Rev. D **57**, 3873 (1998).
24. B. Armbruster *et al.* (KARMEN Collab.), Phys. Rev. D **65**, 112001 (2002).
25. A. Romosan *et al.* (CCFR Collab.), Phys. Rev. Lett. **78**, 2912 (1997).
26. S. Avvakumov *et al.* (NuTeV Collab.), Phys. Rev. Lett. **89**, 011804 (2002).
27. B. Achkar *et al.*, Nucl. Phys. B **434**, 503 (1995).
28. M. Apollonio *et al.*, Eur. Phys. J. C **27**, 331 (2003).

Physics of Atomic Nuclei, Vol. 67, No. 11, 2004, pp. 1948–1952. From Yadernaya Fizika, Vol. 67, No. 11, 2004, pp. 1973–1976.
Original English Text Copyright © 2004 by Beda, Brudanin, Demidova, Egorov, Gavrilov, Kornoukhov, Starostin, Vylov.

NEUTRINO PHYSICS

Status of the Experiment on the Measurement of the Neutrino Magnetic Moment with the Spectrometer GEMMA*

A. G. Beda, V. B. Brudanin[1], E. V. Demidova, V. G. Egorov[1], M. G. Gavrilov, V. N. Kornoukhov, A. S. Starostin, and C. Vylov[1]**

Institute of Theoretical and Experimental Physics,
Bol'shaya Cheremushkinskaya ul. 25, Moscow, 117259 Russia

Received April 16, 2004

Abstract—The investigation of the background structure of the spectrometer GEMMA was carried out in a low-background laboratory in ITEP. GEMMA is destined for measurement of the neutrino magnetic moment near the core of a nuclear power plant (NPP) reactor. The results of the investigation in ITEP and measurement of the background in the experimental hall at the Kalininskaya NPP proved that GEMMA is ready for the start of the experiment at the reactor. Now the preparation of the experimental hall for the measurement is completed and an assembling of the setup is in progress. © *2004 MAIK "Nauka/Interperiodica"*.

INTRODUCTION

The magnetic moment is a fundamental parameter of the neutrino and its measurement in a laboratory experiment may lead to results beyond the standard concepts of elementary particle physics and astrophysics. In the Minimal Extension Standard Model, the magnetic moment of the neutrino (MMN) does not exceed $10^{-19}\mu_{\rm B}$ (where $\mu_{\rm B}$ is the Bohr magneton, $\mu_{\rm B} = eh/(2m_e)$). Some time ago, the hypothesis was put forward that the neutrino can have an anomalously large magnetic moment of order $10^{-11}\mu_{\rm B}$ [1, 2]. Now the experimental limitation on MMN is $\mu_\nu < 1.3 \times 10^{-10}\ \mu_{\rm B}$ [3, 4]. Stronger limits of the order of $(0.01–0.1) \times 10^{-10}\mu_{\rm B}$ can be derived from analysis of astrophysical data [5]. However, such estimates rely on model-dependent assumptions. So, an improvement in sensitivity of laboratory MMN measurements by an order of magnitude would make it possible to verify the hypothesis that the neutrino has an anomalously large magnetic moment (for the current MMN status, see [6]).

A laboratory measurement of the MMN, μ_ν, is based on its contribution to the antineutrino–electron scattering. As antineutrino sources, commercial water–water reactors with a heat power of the order of 3 GW are used. They provide a flux of $2 \times 10^{13}\ \nu/(\text{cm}^2\ \text{s})$ at a distance of ∼15 m from the center of the core. For nonzero MMN, the differential over kinetic energy T of the recoil electron cross section $d\sigma/dT$ is given by the sum of the standard weak interaction (W) and the electromagnetic (EM) one. At small recoil energy ($T \ll E_\nu$, E_ν being the neutrino energy), the W component of the differential cross section, $(d\sigma/dT)_{\rm W}$, is virtually constant, while the EM one, $(d\sigma/dT)_{\rm EM}$, increases as $1/T$ with decreasing scattered electron energy. Therefore, the most effective way to improve sensitivity to μ_ν is to decrease the energy threshold of the detector.

It was proposed to measure the MMN with a low-background germanium spectrometer similar in performance to facilities for searching for 2β decay and dark matter [7]. In the above experiments, energy thresholds of 2–15 keV were attained and good experience in providing an extremely low background was gained. If such parameters could be achieved for a shallow setup, then the sensitivity to μ_ν would be significantly improved. For example, with a background of 0.3 events/(keV kg d) and an antineutrino flux of $2 \times 10^{13}\nu/(\text{cm}^2\ \text{s})$, a germanium detector with an energy threshold of 2–3 keV weighing only 2 kg may have a sensitivity as good as $\sim(3–4) \times 10^{-11}\mu_{\rm B}$.

The basic challenge of the experiment on the measurement of MMN with the use of a low-background germanium spectrometer is to decrease the level of the background for a shallow setup down to the level of 0.3 event/(keV kg d), comparable with the background achieved for deep underground setups. Taking into account this goal, we have chosen the construction of a low-background setup including NaI active

---

*This article was submitted by the authors in English.

[1] Joint Institute for Nuclear Research, Dubna, Moscow oblast, 141980 Russia.

**e-mail: `starostin@itep.ru`

shielding since it allows maximum reduction of all background components under conditions of strong cosmic radiation (CR) [7].

SPECTROMETER GEMMA

The spectrometer GEMMA (Germanium Experiment on the measurement of Magnetic Moment of Antineutrino) includes an array of four Ge(Li) detectors of total mass above 2 kg within NaI(Tl) active shielding (AS). The Ge(Li) detectors and NaI AS are surrounded with combined multilayer passive shielding. The NaI(Tl) is viewed by nine photomultiplying tubes (PMTs) through bent light guides. This design allows PMTs, dividers, and cables to be kept outside the passive shielding and thus the intrinsic radiation background of the spectrum to be considerably decreased. At the top, the spectrometer is closed with a 120 × 120 × 4 cm plastic scintillator counter. To protect the spectrometer against ^{222}Rn, nitrogen is blown through the air-tight cavity around the detector and forced ventilation with outside air is provided in the laboratory (a more detailed description is presented in [7, 8]).

CAMAC and NIM electronic modules are used to control the spectrometer and for data acquisition. The spectrometric part of the electronic equipment comprises preamplifiers, amplifiers, analog-to-digital converters, a CAMAC controller, an interface, and a computer. Electronic logic modules serve to shape and sum PMT signals and to allow passage of spectrometric signals. The entire information of selection and data acquisition is controlled by special programs. Analog signals from each of the four germanium detectors can be written as a separate energy spectrum if they are not accompanied by inhibiting signals from the active shielding or other detectors. In addition, signals are selected according to frequency characteristics, which allows microphone and electron noise and mains interference to be isolated and eliminated.

TEST RESULTS OF THE SPECTROMETER

Tests were carried out at the ITEP low-background laboratory (l.b.l.), where concrete overhead covers serve as CR shielding equivalent to 4 mwe. The results of measurement are presented in the figure, which displays the spectrometer background in the energy range from 10 to 4000 keV. Histograms *1* and *2* are the backgrounds for the unshielded detector and the detector with passive shielding, respectively; histogram *3* is the background of the spectrometer connected in anticoincidence with the NaI AS and upper scintillation counter; histogram *4* is the result of suppressing noise and mains interference by software. The star (*5*) marks off the background level that is planned to be obtained at the reactor facility.

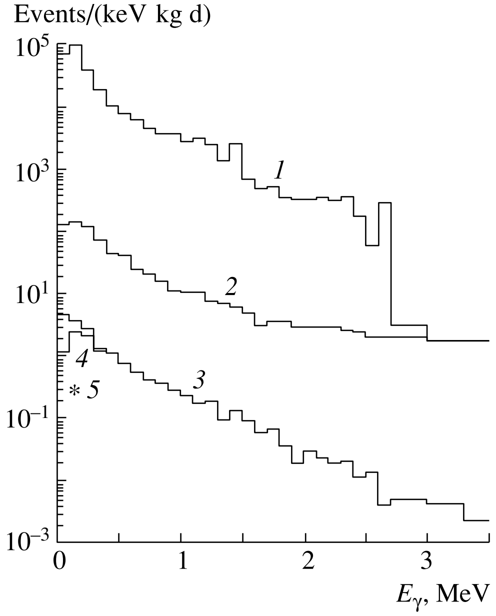

Histogram data taken under different shielding conditions: (*1*) unshielded detector, (*2*) detector with passive shielding, (*3*) detector with passive and active shielding, (*4*) software suppression is activated; (*5*) the background level that is planned to be obtained at the reactor facility.

It follows from the data in the figure that the total background suppression effect for all energy ranges is larger than four orders of magnitude. The NaI AS decreases the background by eliminating the charged component of the CR and suppressing the Compton scattering of gamma quanta. With the upper scintillation counter on, the background of gamma quanta and neutrons resulting from interaction of secondary muons with passive shielding is suppressed. The software filtration of signals is most effective at low energies because, as was stated above, the software is tuned to suppress noise and mains interference signals gathering at the beginning of the energy spectrum. Selection of signals according to frequency characteristics allowed energy thresholds to be decreased from 10–15 to 4.5–6 keV for all detectors.

ANALYSIS OF THE RESULTS

Tentative results of the GEMMA test with a single-crystal germanium detector at the energy threshold of 50 keV were given in [7]. The results of the present measurements give a better idea of the background structure and efficiency of its suppression by various shielding elements.

Table 1. Lines observed in GEMMA background spectra

Energy, keV	Source of background	Counting rate, events/(kg d)
53.4	^{72}Ge$(n,\gamma)^{73m}$Ge	5.5 ± 1.5
60.9	^{212}Bi	5.3 ± 1.9
66.7	^{72}Ge$(n,\gamma)^{73m}$Ge	7.1 ± 1.9
74.8	^{214}Pb	7.0 ± 2.1
77.1	^{214}Pb	5.1 ± 2.0
139.5	^{74}Ge$(n,\gamma)^{75m}$Ge	5.0 ± 1.1
198.3	^{70}Ge$(n,\gamma)^{71m}$Ge	7.5 ± 1.6
238.6	^{212}Pb	7.5 ± 1.6
295.2	^{214}Pb	5.7 ± 1.1
351.9	^{214}Pb	7.5 ± 0.9
511.0	Annihilation	2.5 ± 1.0
609.3	^{214}Bi	2.5 ± 0.9
911.1	^{228}Ac	>1.0
1120.3	^{214}Bi	2.0 ± 0.3
1460.8	^{40}K	4.1 ± 0.5
1764.5	^{214}Bi	1.8 ± 0.3
2204.2	^{214}Bi	1.0 ± 0.2
2614.7	^{208}Tl	0.40 ± 0.10

The main background component for an unshielded detector is virtually always a radiation background from uranium–thorium series isotopes and ^{40}K. In our case, it exceeds 99% in the energy range 10–400 keV. However, the radiation background is easily suppressed by multilayer passive shielding. Its suppression efficiency is larger than 10^4. Other background sources, in decreasing order of their contribution, are muons and secondary CR neutrons, neutrons (tertiary) and gamma quanta from muon capture in the passive shielding, electronic noise and mains interference, and finally the intrinsic radiation background of the spectrometer.

Table 1 presents lines observed in the GEMMA spectra. Their intensities allow one to judge the magnitude of the intrinsic radiation background of the spectrometer and to estimate the background component due to interaction of muons and thermal neutrons (CR derivative) with germanium nuclei. These data noticeably differ from the results of numerous surface measurements with low-background germanium spectrometers. Apart from an appreciable decrease in the integral counting of the facility, noteworthy is the absence of spectral lines corresponding to inelastic scattering of fast neutrons by germanium nuclei at 596 keV, ^{74}Ge$(n,n\gamma)^{74}$Ge, and at 691 keV, ^{72}Ge$(n,n\gamma)^{72}$Ge. This is the result of effective suppression of tertiary neutrons, which arise from muon absorption in the passive shielding and the detector.

Knowing the line intensities, efficiency of various shielding elements, and relationship among CR components, we can find the structure of the residual background and predict the spectrometer background variation with CR. Out of 1.2 events/(keV kg d) observed in the range 10–60 keV, 0.2 events/(keV kg d) is the intrinsic radiation background of GEMMA, and 0.6 and 0.4 events/(keV kg d) are the contributions from interaction of secondary and tertiary neutrons with the detector, respectively. Low-background measurements at the reactor for scientific purposes show that the layers of concrete and steel structures above the facility may have a total thickness of 20–30 mwe, which guarantees practically total absorption of secondary neutrons and a factor of 4–6 decrease in the number of tertiary neutrons. Consequently, the total background of GEMMA at the reactor should be noticeably lower than that at the ITEP l.b.l. According to our preliminary estimation, it should not be larger than 0.3–0.5 events/(keV kg d).

Thus, the parameters found during GEMMA tests allow preparation for measurements at the reactor to be started. Now it is going on in two directions.

A. The facility characteristics are being improved. The NaI AS efficiency has been increased by using light guides of a larger cross section. The four-crystal Ge(Li) detector is being replaced by a one-crystal high-purity germanium (HPGe) detector weighing about 2 kg. There are weighty reasons for this replacement. The Ge(Li) detector was made 15 years ago and all its potentialities have been exhausted. Therefore, its replacement by an HPGe crystal will guarantee reliable operation of the facility during the entire measurement period. The energy threshold of the HPGe detector is 1.5–2.0 keV, while that of the Ge(Li) detector is 5 keV. Finally, the replacement of four small crystals by one large crystal will change the response function of the detector. The calculations show that, in this case, the Compton component of the radiation background (related to a unit weight of the detector) in the range 3–50 keV will decrease by a factor of 3. Therefore, replacement of the detector will not only increase reliability of the facility but also considerably improve the sensitivity of the spectrometer.

Table 2. Comparison of the GEMMA background structure (events/(keV kg d)) in ITEP and forthcoming background in the experiment at KNPP

Sources of the background	ITEP	KNPP
Inherent radiation background	0.2	0.1*
Detector activation by thermal neutrons and μ capture	0.4	0.08
Gamma and neutrons from lead shielding at μ capture	0.3	0.06
Detector activation by secondary fast neutrons	0.3	∼0
Total count rate in the range 10–100 keV	1.2	∼0.3

* Upon change of 0.5-kg germanium detector by 2-kg one.

B. A box is prepared for installation of the facility at a distance of 14.5 m from the center of the core of one of the 3-GW reactors of the Kalininskaya Nuclear Power Plant (KNPP). The radiation, neutron, and CR background were measured at the site of the future experiment.

(a) Gamma radiation was measured with a germanium detector. Its main sources were ^{60}Co and ^{137}Cs isotopes. According to our estimation, the radiation background should not be a serious problem for the future measurements because the active and passive shielding of GEMMA is sufficient to suppress it.

(b) Neutron background was measured with ^{3}He counters enclosed in a polyethylene moderator; i.e., thermal neutrons were counted. Their number at the site of the facility turned out to be 30 times smaller than that in the laboratory room on the surface.

(c) Measurement of the charged component of the CR showed that the muon component of the CR under the reactor is 5 times smaller than that on the surface. Thus, the absorbing effect of the structural materials of the reactor at the depth of the experimental box is equivalent to 25–30 mwe. It provides practically total absorption of secondary neutrons and decreases the intensity of muons and tertiary neutrons by a factor 4–6. Thus, in the experimental box at KNPP, the level of background should be about 0.3 events/(keV kg d) (see Table 2).

The site at the KNPP is practically ready for installing the spectrometer. The box is decontaminated and the electrical equipment is installed, and systems of forced ventilation with filtration and incoming air heating are mounted. Air is taken in from outside.

Table 3. Sensitivity of the GEMMA experiment under different conditions of the measurements

Distance, m	Flux, $10^{13}\nu/(\mathrm{cm}^2\ \mathrm{s})$	Detector mass, kg	On/off	Sensitivity, $10^{-11}\ \mu_\mathrm{B}$
14.5	2.1	2	8	3.2
14.5	2.1	6	8	2.4
14.5	2.1	6	1	2.0
8.5	6.1	2	8	1.9
8.5	6.1	6	8	1.4
8.5	6.1	6	1	1.2

Note: The estimates are made for a reactor of power 3 GW, an energy interval of 3–50 keV, a background of 0.3 events/(keV kg d), and a measurement time of 2 years.

The real sensitivity of the experiment may differ from the above estimates obtained for a detector of mass 2 kg and an antineutrino flux of $2 \times 10^{13}\nu/(\mathrm{cm}^2\ \mathrm{s})$. Firstly, the design of the cryostat allows the detector mass to be increased to 6 kg. Secondly, as an antineutrino flux is determined by the position of the spectrometer with respect to the reactor core, the possibility of placing the detector at a distance of 8.5 m from the center of the reactor is examined. Table 3 shows dependence of the final measurement results on the detector mass, the antineutrino flux, and the ratio of the operation periods with the reactor *on* and *off*. As is evident from the table, the projected experiment may allow an order-of-magnitude improvement in the sensitivity compared with what is so far attained in MMN measurements. Further progress can be achieved by reducing the background, decreasing the energy threshold [9], and increasing the detector mass.

ACKNOWLEDGMENTS

We wish to thank the directorate of ITEP and JINR (Dubna) for constant support of this work. We are also grateful to the Radiation Safety Department of KNPP for help during the preparation of the experimental box.

This work was supported by the Russian Foundation for Basic Research (project no. 02-02-16111a).

REFERENCES

1. M. B. Voloshin, M. I. Vysotsky, and L. B. Okun, Zh. Éksp. Teor. Fiz. **91**, 756 (1986) [Sov. Phys. JETP **64**, 446 (1986)].
2. M. Fukugita and T. Yanagida, Phys. Rev. Lett. **58**, 1807 (1987).
3. Z. Daraktchieva *et al.* (MUNU Collab.), Phys. Lett. B **564**, 190 (2003).
4. H. B. Li *et al.* (TEXONO Collab.), hep-ex/0212003.
5. G. G. Raffelt, Phys. Rep. **320**, 319 (1999).
6. S. Pakvasa and J. W. F. Valle, hep-ph/0301061.
7. A. G. Beda, E. V. Demidova, A. S. Starostin, and M. B. Voloshin, Yad. Fiz. **61**, 72 (1998) [Phys. At. Nucl. **61**, 66 (1998)].
8. A. G. Beda, A. S. Starostin, *et al.,* Prog. Part. Nucl. Phys. **48**, 175 (2002).
9. A. S. Starostin and A. G. Beda, Yad. Fiz. **63**, 1370 (2000) [Phys. At. Nucl. **63**, 1297 (2000)]; hep-ex/0002063.

Physics of Atomic Nuclei, Vol. 67, No. 11, 2004, pp. 1953–1958. From Yadernaya Fizika, Vol. 67, No. 11, 2004, pp. 1977–1982.
Original English Text Copyright © 2004 by Titov.

NEUTRINO PHYSICS

Sensitivity and Systematics of KATRIN Experiment*

N. A. Titov**
(for the KATRIN Collaboration[1])

Institute for Nuclear Research, Russian Academy of Sciences,
pr. Shestidesyatiletiya Oktyabrya 7a, Moscow, 117312 Russia

Received January 20, 2004

Abstract—The KArlsruhe TRItium Neutrino experiment (KATRIN) will measure a "kinematical" electron antineutrino mass upper limit up to 0.2 eV/c^2. The experimental setup based on an electrostatic spectrometer with adiabatic magnetic collimation and windowless gaseous tritium source is briefly described. This sensitivity to the neutrino mass could be reached with a 10-m-diameter spectrometer after three years of data taking. Several major sources of the systematic errors are discussed. © *2004 MAIK "Nauka/Interperiodica".*

A neutrino oscillation is a well-established fact that implies a nonzero neutrino mass [1]. Oscillation data provide us with a neutrino mass spectral pattern, but not the absolute mass values. It is only possible to deduce that at least one neutrino mass eigenstate is heavier than 0.03 eV/c^2. A "kinematical" experiment based on analysis of kinematics of a weak decay is the only laboratory experiment suitable to provide an absolute neutrino mass value. Particularly, the proposed KATRIN setup will be able to set an electron-antineutrino mass upper limit at the level of 0.2 eV/c^2. Such a study makes sense because there are two neutrino mass schemes: hierarchical and quasidegenerate (Fig. 1). In the hierarchical scheme, the mass eigenstates have a different scale determined by Δm^2_{atm} and Δm^2_{sol} and the heaviest mass is about 0.05 eV/c^2. In the quasidegenerate scheme, all neutrinos have about the same mass, much larger than the mass splitting. The latter scheme is somewhat favored by the observed large mixing angles of different mass eigenstates $\sin\theta_{ij} \approx 1$ [1]. The neutrino mass in the quasidegenerate scheme has a chance to be detected in the tritium experiment (otherwise this scheme will be mostly excluded).

The tritium β decay is a superallowed transition. In the quasidegenerate regime, neutrino mass splitting can be neglected and the electron spectrum is described by the well-known formula

$$dN/dE = KF(Z,E)pE_{\text{tot}} \times (E_0 - E)^2\sqrt{(E_0-E)^2 - m_\nu^2}. \qquad (1)$$

Almost all of the spectrum data points have $(E_0 - E)^2 \gg m_\nu^2$, and the neutrino mass signature is a negative constant shift of the parabolic spectrum with respect to the background level (Fig. 2):

$$dN/dE \sim (E_0 - E)^2 - m_\nu^2/2. \qquad (2)$$

The absolute value of the statistical error bar is a linear function of the distance from the endpoint $(E_0 - E)$. The sensitivity to nonzero neutrino mass is steadily vanishing far from the spectrum endpoint, as is shown in the inset in Fig. 2.

A real experimental parameter in the tritium-decay experiment is a neutrino mass square [see (1)]. During the last 10–15 years, the experimental sensitivity to neutrino mass square was improved by about two orders of magnitude (Fig. 3). This improvement was achieved by invention of an electrostatic spectrometer with an adiabatic magnetic col-

Table 1. KATRIN parameters

WGTS	Spectrometer	Measurements
Tritium column density 5×10^{17} mol/cm^2	Diameter 10 m (effective 9 m)	Three years of data taking
Diameter 90 mm (effective 81 mm)	Resolution $\Delta E = 0.93$ eV	Optimized set of data points
Acceptance angle 51°		
Tritium purity 95%		

---

*This article was submitted by the author in English.

[1] KATRIN Collaboration: U Bonn; LNP/JINR, Dubna; FH Fulda; FZ & U Karlsruhe; U Mainz; INP, Řež; RAL; UW, Seattle; UW Swansea; INR RAS, Troitsk.

**e-mail: `titov@al20.inr.troitsk.ru`

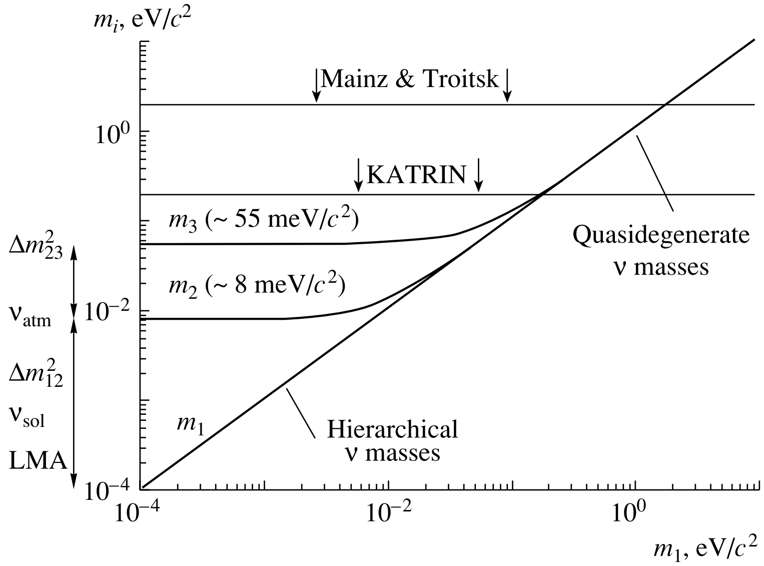

Fig. 1. Neutrino mass scheme. Hierarchical and quasidegenerate parts are shown. The current experimental mass limit [2] and that of KATRIN [3] are shown.

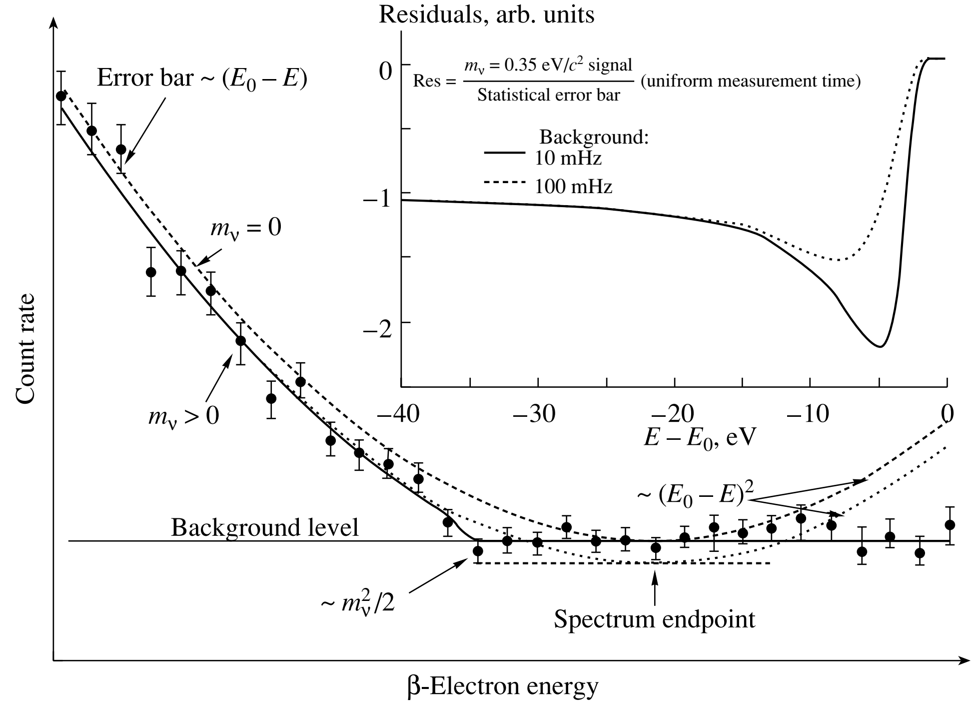

Fig. 2. The exact tritium β-electron energy spectrum and its parabolic approximation. The neutrino mass signature is a shift of the parabolic part of the spectrum. The absolute data error bar increases for high-intensity points. In the inset, the signal-to-error bar ratio is presented for different background levels.

limation (AMC). The AMC allows high-resolution and high-luminosity requirements to be decoupled. This idea was independently developed by several researchers [2]. The AMC is based on conservation (as an adiabatic invariant) of the ratio of transversal kinetic energy to magnetic field strength

$$\mu = E_t/B \qquad (3)$$

for a charged particle moving through the magnetic field. For the conservation of the adiabatic invariant, it is only required that, along the trajectory of a

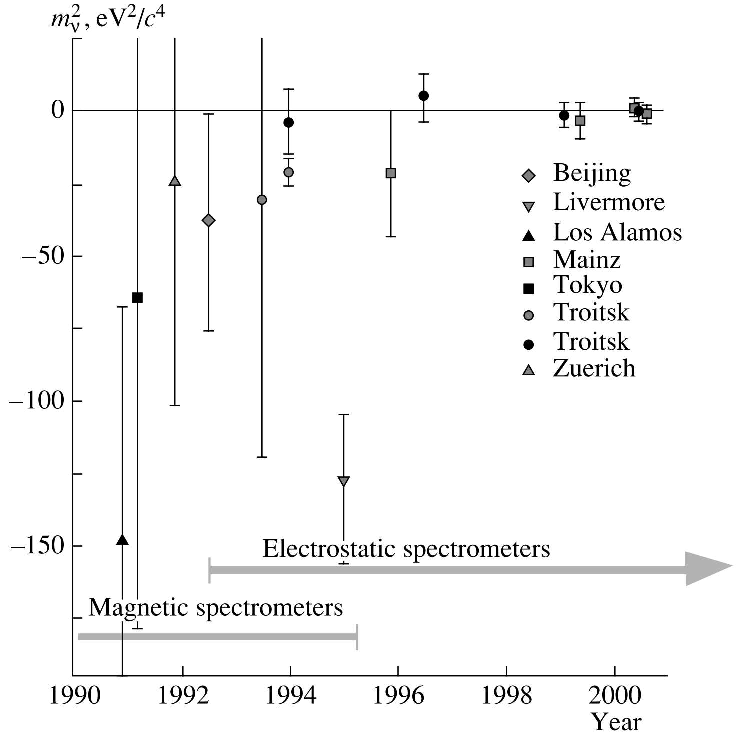

Fig. 3. The electron-antineutrino mass-square measurement summary for the previous decade.

moving particle, the magnetic field variation should be small on the time scale of one gyration. The idea of the AMS is that a tritium β decay takes place in a strong magnetic field within a large solid angle (Fig. 4). When electrons are transported to the low-magnetic-field region, their moments become aligned along the magnetic field due to the conservation of the adiabatic invariant. The aligned electron energy can be analyzed with an electrostatic spectrometer. To define the tritium decay solid angle, electrons should pass the region with magnetic field $B_{\max}$ somewhat stronger than the one in the decay region. Finally, one obtains an integral spectrometer—a high-pass filter at an electrostatic mirror potential U_0 with a full width resolution:

$$\Delta E = |eU_0|\frac{B_{\text{analys}}}{B_{\max}}. \quad (4)$$

Thus, the spectrometer resolution is only determined by the magnetic field ratio with an acceptance solid angle of the order of 1 sr and an arbitrary source diameter.

The second important invention is a windowless gaseous tritium source (WGTS), first used in the LANL experiment [4] and significantly modified later at Troitsk [5]. The WGTS provides an excellent intensity of β electrons and has high uniformity and well-controlled energy losses.

The KATRIN project united almost all experts in the field with the aim to get ultimate sensitivity to m_ν using an electrostatic spectrometer with AMC and the WGTS. The KATRIN setup is given in Fig. 5. The tritium β decay takes place inside the WGTS, surrounded by differential pumping stations. The outgoing tritium is collected, purified, and reinjected in the center of the WGTS. The decay electrons are guided by the magnetic field through the WGTS and the cryotrapping section toward the pre- and main spectrometer. In order to have a low spectrometer background, the multiple differential pumping stations and cryotrapping sections have to reduce the tritium partial pressure in the spectrometer compared

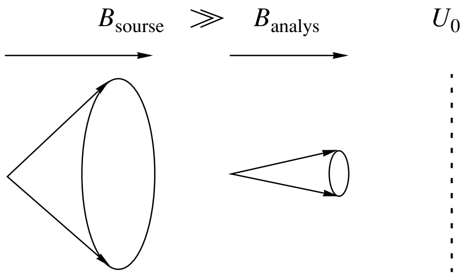

Fig. 4. The operational principle of the electrostatic spectrometer with an adiabatic magnetic collimation. Electron moments are aligned along the guiding magnetic field after transition into the low-field region and are analyzed with electrostatic barrier.

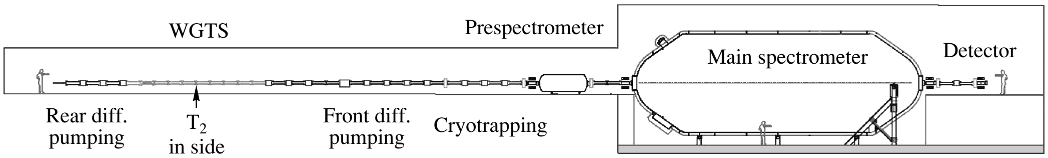

Fig. 5. The KATRIN setup general view. The tritium β decay takes place inside the windowless gaseous tritium source, surrounded by differential pumping stations. Decay electrons are guided by the magnetic field through the cryotrapping section toward the pre- and main spectrometer. After being analyzed by an electrostatic mirror, the decay electrons are recorded by a semiconductor detector.

with the WGTS by a factor of 10^{16}. Inside the pre- and main spectrometers, the decay electron energies are analyzed by the electrostatic mirror formed by a set of electrodes. After being analyzed, the decay electrons are recorded by a segmented semiconductor detector. The total setup length is up to 90 m long. Magnetic field values are 3.6 (WGTS), 6 (maximal field), and 0.0003 T (analyzing plane). The WGTS diameter is 90 mm, the main spectrometer diameter is 10 m, and the spectrometer vacuum is up to 10^{-12} mbar.

To evaluate the statistical sensitivity of the KATRIN setup, one should take into account the fact that several parameters can be further optimized but others are interrelated. The spectrometer resolution and acceptance define the magnetic field ratios and geometry of the vessels. Technical limitations are a maximal diameter of the extrahigh-vacuum spectrometer vessel (10 m) and a maximal field in the superconducting magnets (6 T). For the ultimate accuracy, only the electrons leaving the WGTS without inelastic scattering are useful (see below). The source column density and acceptance angle are selected in such a way that the nonscattering fraction of outgoing decay electrons is near saturation. The spectrometer resolution improvement below 1 eV provides no increase in sensitivity, because the effective resolution is limited by rotovibrational excitation of a recoil molecular ion $(^3\mathrm{HeT})^+$. Finally, a data point distribution was optimized to reach maximal sensitivity. A set of parameters for the sensitivity calculations is presented in Table 1. Assuming $\sigma_{\mathrm{syst}} \approx \sigma_{\mathrm{stat}}$ and a background level of 10 mHz with parameters from Table 1, one obtains the KATRIN neutrino mass upper limit to be 0.2 eV/c^2 (90% C.L.).

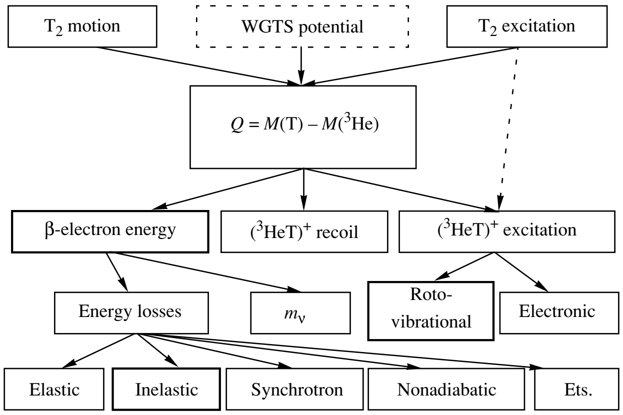

Fig. 6. Energy flow chart. First line—corrections to the released energy. Second line—the nuclear mass difference is the main source of released energy. Other lines—different energy drains.

Considering the KATRIN systematic uncertainties, one should keep in mind that the neutrino mass signature is some drain of part of the β-electron kinetic energy to the neutrino rest mass. All other competing sources of the energy drain can mimic the neutrino mass. A chart of the energy flow is presented in Fig. 6. The main source of released energy is a nuclear mass difference. The released energy is modified by the source molecule motion and excitation. A tiny effect is the influence of mother molecule excitation on the recoil ion excitation spectra shown by the dashed arrow [6, 7]. The space charge potential inside the WGTS decelerates the β electron when it leaves the source. Different energy drains are listed at the lower part of the chart. The most significant are the excitation of the recoil ion $(^3\mathrm{HeT})^+$ and the β-electron inelastic energy losses. All of them modify the endpoint energy E_0 in formulas (1) and (2). It is crucial that one should distinguish two cases of the endpoint modification: endpoint shift and endpoint broadening. In all practical cases, the tritium spectrum analysis keeps the endpoint energy as a free parameter and the endpoint shift is accounted for, leaving no damage. On the contrary, the endpoint broadening results in false m_ν^2 without any other signature. If broadening is described with a Gaussian distribution, the false m_ν^2 is determined by the distribution width [8]:

$$\delta m_\nu^2 = -2\sigma^2. \qquad (5)$$

The recoil ion $(^3\mathrm{HeT})^+$ final-state spectrum (FSS) is presented in Fig. 7. No method has yet been proposed to measure the FSS and only theoretical calculations [6, 7] are used to take the FSS into account. To reduce the FSS influence, it is proposed to perform the measurements only in the last 20–25 eV of the tritium-decay spectrum. The rotovibrational

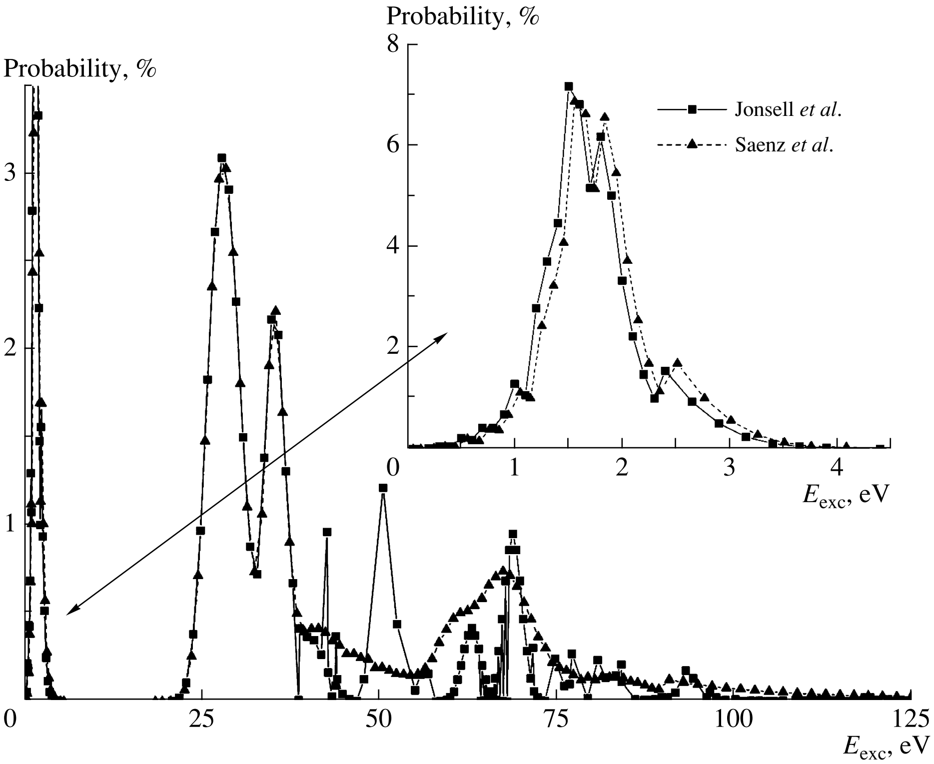

Fig. 7. Molecular ion $(^3\mathrm{HeT})^+$ excitation spectrum calculated by S. Jonsel *et al.* [6] and Saenz *et al.* [7]. In the inset, a rotovibrational part of spectrum is presented.

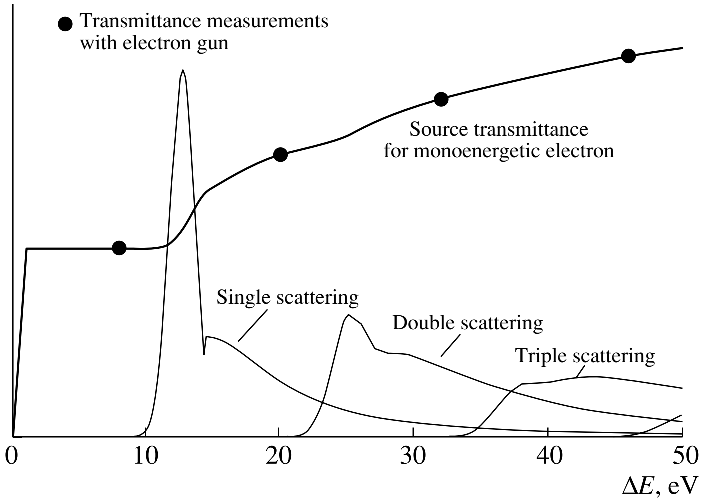

Fig. 8. Monoenergetic electron energy-loss spectra for single, double, and triple scatterings. A gaseous source transmittance function for monoenergetic electrons. Points for transmittance measurements with an electron gun.

part of the FSS cannot be excluded and it should be known very well. The two most sophisticated calculations [6, 7] provide slightly different estimates of the rotovibrational FSS, resulting in m_ν^2 ambiguity of 0.010–0.015 eV^2/c^4.

The β electron undergoes inelastic scattering in the WGTS. When the last 20–25 eV of the tritium-decay spectrum are analyzed, only single and double scattering can be accounted for (Fig. 8). The energy loss spectrum will be measured with a high accuracy with monoenergetic electrons from an electron gun placed at the rear side of the WGTS as in the existing experiments [9]. The relative probability of zero, single, and double scattering is controlled by the source

Table 2. Existing WGTS parameters

Laboratory	Magnetic field, kG	Gas temperature, K	Mean density, 10^{14} mol/cm^{-3}	Storage time, s	Ion–electron pair concentration, 10^6 pair/cm^{-3}
LANL (Los Alamos) [4]	3.1	160	0.19	0.2	0.03
LLNL (Livermore) [11]	6.0	100	1.5	0.5	1.1
INR (Troitsk) [5]	5.6/37.5	30	2.5/1.2	4.9	13/6
KATRIN	36.0	30	5.0	1.3	26

thickness, which should be known with a 0.1% accuracy (including the contribution from the non-tritium hydrogen isotopes). The required source-thickness-measurement accuracy will be achieved using frequent transmittance measurements with the electron gun. Measurements will take place at several points selected in a way to determine the source thickness with a redundancy.

The electric potential inside the WGTS is generated by a positive ion space charge left after the escape of the fast β electrons. The primary space charge value is determined by the decay rate, tritium density, and the mean time of the ion storage. The secondary ionization, electron thermalization, and recombination should be taken into account and turn out to be crucial processes [10]. A simple estimate shows that ions and electrons form a slightly ionized plasma. The comparison of properties of the existing WGTS (Table 2) shows that similar effects were present in all of them. It is expected that ion space charge will be compensated by thermalized electrons ("quasineutrality") with the accuracy limited by the electron temperature: $e(\varphi_{\text{ion}} - \varphi_e) \sim T_e$.

The electron temperature T_e defines both the scale of the potential mean value and its variation in space and time. The LANL group measured a mean WGTS potential with a 17 830-eV intrinsic K-conversion electron line of the ^{83m}Kr γ decay. Krypton was circulated alone and together with the tritium. No line shift was detected: $\Delta(e\varphi) < 0.5$ eV. The Troitsk group measured a mean potential difference for regular WGTS volume and its axial part containing 1/4 of the regular one. A tritium spectrum endpoint shift was evaluated and no difference was found: $\Delta(e\varphi) = 0.1 \pm 0.3$ eV.

The KATRIN specification is much lower and deals with smaller potential variation $\sigma(e\varphi) <$ 75 meV. A special experiment is planned at Troitsk to measure broadening of the ^{83m}Kr 17 830-eV conversion line when ^{83m}Kr is circulated together with T_2 (but at 100 K). A sensitivity to the line broadening at the level of a few hundred meV is expected.

The KATRIN project is now in the R&D phase. The Collaboration is sticking to the schedule to start the first measurements in 2007.

REFERENCES

1. K. Hagiwara *et al.* (Particle Data Group), Phys. Rev. D **66**, 010001 (2002).
2. V. M. Lobashev, Nucl. Phys. A **719**, C153 (2003).
3. KATRIN Letter of Intent, hep-ex/0109033.
4. R. G. H. Robertson *et al.*, Phys. Rev. Lett. **67**, 957 (1991).
5. V. M. Lobashev *et al.*, Phys. Lett. B **460**, 227 (1999).
6. S. Jonsell and H. J. Monkhorst, Phys. Rev. Lett. **76**, 4476 (1996).
7. A. Saenz, S. Jonsell, and P. Froelich, Phys. Rev. Lett. **84**, 242 (2000).
8. R. G. H. Robertson and D. Knapp, Annu. Rev. Nucl. Part. Sci. **38**, 185 (1988).
9. V. N. Aseev *et al.*, Eur. Phys. J. D **10**, 39 (2000).
10. F. Glueck, KATRIN Internal Report 95-TRP-1316.
11. W. Stoeffl and D. J. Decman, Phys. Rev. Lett. **75**, 3237 (1995).

Physics of Atomic Nuclei, Vol. 67, No. 11, 2004, pp. 1959–1962. From Yadernaya Fizika, Vol. 67, No. 11, 2004, pp. 1983–1986.

The Need to Measure Low-Energy Antineutrinos ($E_{\bar{\nu}} < 0.782$ MeV) from the Sun*

O. Manuel**

University of Missouri, Rolla, USA

Received January 14, 2004

Abstract—Measurements are needed of low-energy antineutrinos generated by possible neutron decay at the core of the Sun. The measurement will test the validity of a proposal that solar luminosity, solar neutrinos, and the outpouring of H^+ ions from the solar surface are the products of a chain of reactions triggered by neutron emission from the solar core. Inverse β decay of 87-d ^{35}S, induced by capture of low-energy antineutrinos on ^{35}Cl, is a likely candidate for this measurement. © *2004 MAIK "Nauka/Interperiodica"*.

Fresh debris of a supernova (SN) formed the Solar System. This is the conclusion to numerous measurements since 1960 [1]. The SN exploded about 5 Gyr ago [2]. The Sun formed on the collapsed SN core, Fe-rich material around the SN core formed iron meteorites and cores of the inner planets, and material from the outer SN layers formed the giant Jovian planets from light elements like H, He, and C [3, 4]. This sequence of events is shown in Fig. 1.

When first proposed in the mid-1970s [3, 4], the scene in Fig. 1 appeared to contradict several widely held opinions:

1. Supernovae always explode symmetrically.
2. SN debris cannot form planets surrounding the collapsed SN core.
3. Poorly mixed SN debris is inconsistent with uniform atomic weights and isotopic abundances assumed throughout the Solar System.
4. The Sun is mostly hydrogen; it could not be formed in this manner.
5. Abundant solar hydrogen is required to explain solar luminosity.

This paper suggests a measurement to test the validity of the fifth assumption. The other objections have been resolved.

Problems with the first assumption were exposed when the Hubble telescope found that asymmetric SN explosions are commonplace, for example, the explosion of SN1987A [5]. The validity of the second assumption was brought into question with the finding of two rocky, Earth-like planets and one Moon-like object orbiting a neutron star, PSR1257+12 [6]. Decay products of nuclides even shorter lived than ^{129}I and ^{244}Pu [7, 8] and linked elemental and isotopic variations in meteorites and planets [9–14] ruled out the third assumption.

The fourth assumption, that the interior of the Sun is hydrogen-filled like its surface, was invalidated by the finding that mass separation inside the Sun enriches lighter elements and the lighter isotopes of each element at the solar surface [15]. After correcting for mass fractionation, the most abundant elements in the interior of the Sun [15] were shown to be the same elements that Harkins [16] found to comprise 99% of ordinary meteorites, i.e., Fe, O, Ni, Si, Mg, S, and Ca. These elements are produced in the deep interior of highly evolved stars [17], as expected from the events in Fig. 1.

SN debris is not the only possible source for some short-lived nuclides and isotopic anomalies observed in meteorites and planets [9–14]. However, rapid neutron capture in a SN is the only viable mechanism to produce extinct ^{244}Pu [2, 8]. The validity of Fig. 1 was strengthened when Kuroda and Myers [2] combined age dating techniques based on ^{238}U, ^{235}U, and ^{244}Pu to show that a SN explosion produced these actinide nuclides at the birth of the Solar System, about 5 Gyr ago. Their results are in Fig. 2.

The present paper concerns the need for measurements to test a proposed source for luminosity in an iron-rich Sun, i.e., to test the validity of the fifth objection to events shown in Fig. 1. In layman's terms, "How can the Sun shine if it is made mostly of iron?" The answer requires the use of reduced variables, like those in van der Waals' equation of corresponding states, to look for sources of energy in properties of

---

*This article was submitted by the author in English.

**e-mail: `om@umr.edu`

1063-7788/04/6711-1959$26.00 © 2004 MAIK "Nauka/Interperiodica"

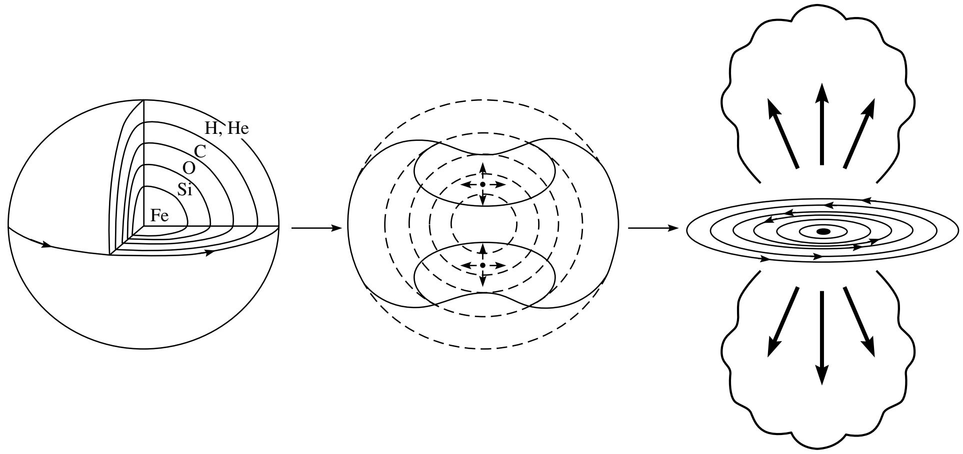

A massive spinning star becomes chemically layered near the end of its life, when asymmetric collapse occurs to conserve angular momentum.

The infall of low-*Z* elements causes an axially directed SN explosion, producing a rapidly expanding bipolar nebula with an equatorial accretion disk.

The Sun forms on the SN core; cores of inner planets form in the Fe-rich region around the SN core; Jovian planets form in the outer SN layers.

Fig. 1. Formation of the Solar System from the chemically and isotopically heterogeneous debris of a spinning supernova [3, 4]. The Sun formed on the collapsed supernova core; Fe-rich material formed iron meteorites and cores of the inner planets; and H, He, and C-rich material from the outer layers formed giant planets like Saturn and Jupiter.

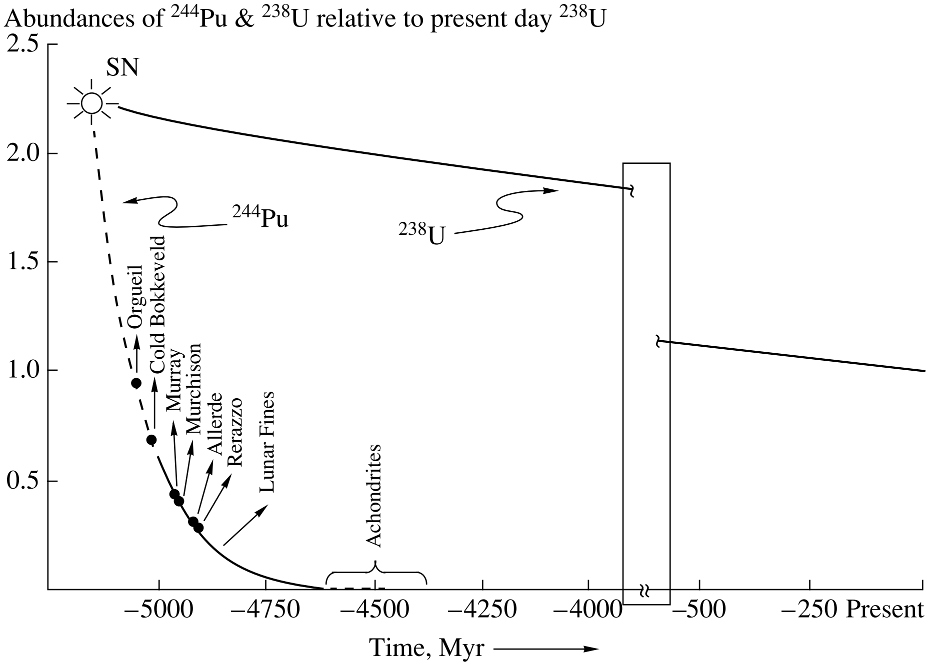

Fig. 2. Combined U–Pb and Pu–Xe age dating of the supernova explosion that occurred at the birth of the Solar System, about 5 Gyr ago [2].

the 2850 nuclides tabulated in the latest report from the National Nuclear Data Center [18].

The results are shown in Fig. 3, where data for ground states of 2850 known nuclides [18] are displayed on a three-dimensional graph of Z/A, charge per nucleon, versus M/A, mass or total potential energy per nucleon, versus A, mass number. All nuclides lie within the limits of $0 \leq Z/A \leq 1$ and $0.998 \leq M/A \leq 1.010$, and the data [18] define a cradle shaped like a trough or valley. The more stable nuclides lie along the valley, and the lowest point is ^{56}Fe.

Cross sections through Fig. 3 at any fixed value of A reveal the familiar "mass parabola." An example

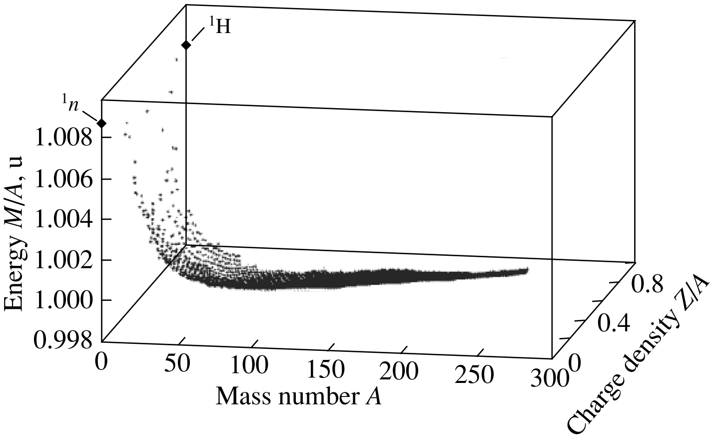

Fig. 3. The "cradle of the nuclides," a three-dimensional plot of reduced nuclear variables, Z/A (charge per nucleon) vs. M/A (mass per nucleon) vs. A (mass number) for the ground states of 2850 known nuclides [18]. The cradle provides new insight into possible sources of nuclear energy [19].

is shown in Fig. 4 at $A = 27$. Data points are also shown in Fig. 4 for unbound nucleons, ^1n on the left at $Z/A = 0$ and ^{1}H on the right at $Z/A = 1.0$. The mass parabola in Fig. 4 is defined by masses of ground-state nuclides at ^{27}F, ^{27}Ne, ^{27}Na, ^{27}Mg, ^{27}Al, ^{27}Si, ^{27}P, and ^{27}S [18]. At $Z/A = 0$, the empirical parabola yields a value of $M/A = M(^1n) + \sim 10$ MeV.

The results shown in Fig. 4 are typical of values indicated at $Z/A = 0$ from mass parabolas at each mass number A, where $A > 1$. Together, these mass parabolas [18] at all values of A suggest a driving force of $\sim$ 10–22 MeV for neutron emission from a neutron star [19]. This energy source and the following sequence of reactions thus offer a possible explanation for solar luminosity (SL), the fifth objection to the scene shown in Fig. 1:

Neutron emission from the solar core (>57% SL):

$$\langle ^1n \rangle \rightarrow {}^1n + \sim 10\text{–}22\ \text{MeV}.$$

Neutron decay or capture (<5% SL):

$$^1n \rightarrow {}^1\mathrm{H} + e^- + \bar{\nu} + 0.782\ \text{MeV}.$$

Fusion and upward migration of H$^+$ (<38% SL):

$$4^1\mathrm{H}^+ + 2e^- \rightarrow 4\mathrm{He}^+ + 2\nu + 27\ \text{MeV}.$$

Escape of excess H$^+$ in solar wind (100% SW):

$$3 \times 10^{43}\ \mathrm{H}^+/\mathrm{yr} \rightarrow \text{depart in solar wind}.$$

Thus, neutron emission from a collapsed SN core in the center of the Sun, as shown in Fig. 1, may start a chain of reactions that explain luminosity, as well as the observed outflow of solar neutrinos and H$^+$ ions from the surface of an iron-rich Sun [19]. In the first step, neutron emission may release 1.1–2.4% of the nuclear rest mass as energy. In the third step, hydrogen fusion releases about 0.7% of the rest mass as energy.

However, this paper is most concerned with the need to measure low-energy antineutrinos emitted in the second step. This measurement may confirm or deny the occurrence of the above reactions in the Sun and the historical validity of the events shown in Fig. 1.

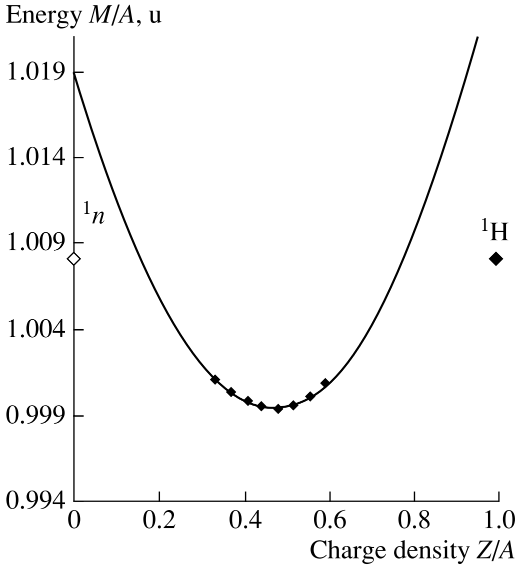

Fig. 4. A cross-sectional cut through the "cradle of the nuclides" (Fig. 3) at $A = 27$. The mass parabola is defined by masses of ground-state nuclides at ^{27}F, ^{27}Ne, ^{27}Na, ^{27}Mg, ^{27}Al, ^{27}Si, ^{27}P, and ^{27}S. For comparison, reference values are shown for unbound nucleons, ^1n on the left at $Z/A = 0$ and ^{1}H on the right at $Z/A = 1.0$.

Specifically, it is proposed to look for inverse β decay induced by low-energy antineutrinos coming from the Sun, e.g., ^{3}He → ^{3}H, ^{14}N → ^{14}C, or ^{35}Cl → ^{35}S. The latter reaction in the Homestake mine [20] might produce measurable levels of 87-d ^{35}S. Alternatively, ^{35}S might be extracted from underground deposits of salt (NaCl) and detected by counting or by AMS (accelerator mass spectrometry) measurements.

ACKNOWLEDGMENTS

This work was supported by the University of Missouri and by the Foundation for Chemical Research, Inc.

REFERENCES

1. O. Manuel and S. Friberg, in *Proceedings of SOHO 12/GONG 2002 Conference*, Ed. by H. Lacoste, ESA SP-517 SOHO/GONG (Noordwijk, The Netherlands, 2003), p. 345.
2. P. K. Kuroda and W. A. Myers, Radiochim. Acta **77**, 15 (1996).
3. O. K. Manuel and D. D. Sabu, Trans. Mo. Acad. Sci. **9**, 104 (1975).
4. O. K. Manuel and D. D. Sabu, Science **195**, 208 (1977).
5. Ph. Podsiadlowski *et al.*, Nature **354**, 43 (1991).
6. A. Wolszczan, Science **264**, 538 (1994).
7. J. H. Reynolds, Phys. Rev. Lett. **4**, 8 (1960).
8. M. W. Rowe and P. K. Kuroda, J. Geophys. Res. **70**, 709 (1965).
9. R. V. Ballad *et al.*, Nature **277**, 615 (1979).
10. D. D. Sabu and O. K. Manuel, Meteoritics **15**, 117 (1980).
11. O. K. Manuel, Geokhimiya **12**, 1776 (1981).
12. F. Begemann, in *Origins and Evolution of the Elements*, Ed. by N. Prantoz, E. Vangioni-Flam, and M. Casse (Cambridge Press, Cambridge, 1993), p. 518.
13. J. T. Lee *et al.*, Comments Astrophys. **18**, 335 (1996).
14. O. Manuel *et al.*, J. Radioanal. Nucl. Chem. **238**, 119 (1998).
15. O. Manuel and G. Hwaung, Meteoritics **18**, 209 (1983).
16. W. D. Harkins, J. Am. Chem. Soc. **39**, 856 (1917).
17. E. Burbidge *et al.*, Rev. Mod. Phys. **29**, 547 (1957).
18. J. K. Tuli, *Nuclear Wallet Cards* (National Nuclear Data Center, BNL, Upton, NY, USA, 2000).
19. O. Manuel *et al.*, J. Radioanal. Nucl. Chem. **252**, 3 (2002).
20. R. Davis *et al.*, Phys. Rev. Lett. **20**, 1205 (1968).

Physics of Atomic Nuclei, Vol. 67, No. 11, 2004, pp. 1963–1968. From Yadernaya Fizika, Vol. 67, No. 11, 2004, pp. 1987–1992.

NEUTRINO PHYSICS

Components of Antineutrino Emission in Nuclear Reactor[*]

V. I. Kopeikin, L. A. Mikaelyan, and V. V. Sinev[**]

Russian Research Centre Kurchatov Institute, pl. Kurchatova 1, Moscow, 123182 Russia

Received January 20, 2004

Abstract—New $\bar{\nu}_e e$ scattering experiments aimed at sensitive searches for the ν_e magnetic moment and projects to explore small mixing angle neutrino oscillations at reactors require a better understanding of the reactor antineutrino spectrum. Six components which contribute to the total $\bar{\nu}_e$ spectrum generated in a nuclear reactor are considered. They are beta decays of the fission fragments of ^{235}U, ^{239}Pu, ^{238}U, and ^{241}Pu and decays of beta emitters produced as a result of neutron capture in ^{238}U and in accumulated fission fragments which perturb the spectrum. For antineutrino energies of less than 3.5 MeV and for each of the four fissile isotopes, the time evolution of $\bar{\nu}_e$ spectra is given during fuel irradiation and after the irradiation is stopped. The relevant uncertainties are estimated. Small corrections to the ILL spectra are considered. *© 2004 MAIK "Nauka/Interperiodica".*

1. INTRODUCTION

One has stressed many times (see, e.g., reviews [1, 2]) the importance of having exact knowledge of the reactor antineutrino ($\bar{\nu}_e$) energy spectrum for planning and for analyzing the experiments on neutrino intrinsic properties and on searches for new physics at reactors.

In widely used pressurized water reactors (PWR, VVER in Russian abbreviation), the summed U and Pu isotope fission rate is about 3.1×10^{19}/s per 1 GW thermal power. About $N_\nu \approx 6.7\,\bar{\nu}_e$ are emitted per one fission event. There are 75% of these antineutrinos with energy $E < 1.80$ MeV, below the threshold of the inverse beta decay of the proton. The quantity N_ν receives contribution from six sources:

$$N_\nu = {}^F N + {}^U N + \delta^F N. \qquad (1)$$

Here, ${}^F N \approx 5.5\bar{\nu}_e$/fission represents the summed contribution from the beta decays of fission fragments of the four fissile isotopes ^{235}U, ^{239}Pu, ^{238}U, and ^{241}Pu, undistorted by their interaction with reactor neutrons; ${}^U N \approx 1.2\bar{\nu}_e$/fission comes from the beta decay of the $^{239}\text{U} \rightarrow {}^{239}\text{Np} \rightarrow {}^{239}\text{Pu}$ chain produced via neutron radiative capture in ^{238}U; and $\delta^F N < 0.03\bar{\nu}_e$/fission originates from the neutron capture in accumulated fission fragments and gives small but not negligible local distortions of the total energy spectrum $\bar{\nu}_e$ of the reactor.

In the following, we first present a short (and incomplete) overview of a half-century-long history which has led us to the present understanding of the reactor antineutrinos. Second, we give new results on the computed evolution of the $\bar{\nu}_e$ energy spectra corresponding to the four fissile isotopes vs. fuel irradiation time and their decay after the end of irradiation. We compare all available data and estimate relevant uncertainties. Next, data are presented on antineutrinos due to neutron radiative capture in ^{238}U and in accumulated fission fragments. Finally, we consider small corrections to the ILL spectra.

2. SHORT HISTORY

In 1949, L. Alvarez did historically the first estimation of the reactor $\bar{\nu}_e$ spectrum using the concept of fission radiation developed by Way and Wigner [3]. The next were King and Perkins in 1958 [4]. These studies were stimulated by B. Pontecorvo's proposal (in 1946) to look for Cl → Ar transitions near an atomic reactor and by the famous Reines–Cowan experiments. At that time and many years after, it was assumed that the only source of reactor antineutrinos is the decay of ^{235}U fission fragments.

In 1974–1977, the Kurchatov Institute's Rovno group noticed that, in nuclear reactors, fission of other heavy isotopes produces an antineutrino flux comparable with the flux of ^{235}U and their energy spectra can be quite different from spectra of ^{235}U, which, among other effects, would cause a time variation of the antineutrino-induced reaction cross sections (burnup effect) [5]. The calculated energy spectrum for $\bar{\nu}_e$ emitted by ^{239}Pu fission fragments was first published in [6] and for each of the four fissile isotopes was given in [7]. In 1980, Avignone III *et al.* published

---

[*] This article was submitted by the authors in English.

[**] e-mail: `sinev@polyn.kiae.su`

Table 1. Calculated $\bar{\nu}_e$ spectra (1/(MeV fission)) for ^{235}U and ^{239}Pu vs. irradiation time t_{on}

E, MeV	^{235}U				^{239}Pu			
	1 d	30 d	100 d	2 yr	1 d	30 d	100 d	2 yr
0.05	0.102	0.216	0.300	0.426	0.165	0.309	0.397	0.502
0.1	0.226	0.608	0.897	1.326	0.229	0.720	1.019	1.373
0.2	0.718	1.719	2.007	2.322	0.722	2.013	2.402	2.710
0.3	1.129	2.029	2.316	2.637	1.043	1.989	2.217	2.446
0.4	1.587	2.184	2.353	2.413	1.475	2.141	2.284	2.331
0.5	1.866	2.395	2.496	2.543	1.753	2.363	2.442	2.475
0.6	1.740	2.277	2.366	2.397	1.739	2.278	2.343	2.362
0.7	1.847	2.366	2.459	2.495	1.854	2.336	2.398	2.420
0.8	1.868	2.386	2.486	2.527	1.886	2.360	2.426	2.451
0.9	1.873	2.355	2.450	2.493	1.885	2.321	2.382	2.409
1.0	1.812	2.137	2.203	2.247	1.798	2.093	2.132	2.160
1.2	1.702	1.929	1.988	2.033	1.580	1.776	1.809	1.840
1.4	1.541	1.621	1.661	1.702	1.399	1.461	1.482	1.513
1.6	1.472	1.515	1.522	1.542	1.316	1.355	1.362	1.386
1.8	1.378	1.407	1.412	1.432	1.215	1.240	1.245	1.270
2.0	1.241	1.257	1.262	1.282	1.082	1.095	1.101	1.125
2.25	1.054	1.064	1.068	1.086	0.909	0.916	0.921	0.944
2.5	0.887	0.895	0.898	0.912	0.754	0.759	0.763	0.782
2.75	0.768	0.772	0.775	0.785	0.647	0.650	0.653	0.668
3.0	0.650	0.651	0.651	0.652	0.538	0.539	0.540	0.546
3.25	0.553	0.554	0.554	0.554	0.445	0.445	0.446	0.450
3.5	0.452	0.452	0.452	0.452	0.355	0.355	0.356	0.358

the first results on ^{238}U [8]. In 1979, Davis *et al.* [9] calculated the spectrum for ^{239}Pu, and in 1981, Vogel *et al.* [10] published results for the four fissile isotopes. In these publications, mainly "high"-energy parts ($E > 1$–1.5 MeV) of the antineutrino spectra were presented.

Quoted calculations were done in 1976–1981 [6–10] and have confirmed the idea that $\bar{\nu}_e$ spectra associated with fission of different isotopes considerably differ from one another. In comparison with the $\bar{\nu}_e$ spectrum generated in the decay of ^{235}U fission fragments, the fission of ^{238}U gives much harder spectrum, while ^{239}Pu fission produces $\bar{\nu}_e$ of lower energies. The absolute values of each of the four spectra were established, however, with large uncertainties associated with poor knowledge of the decay schemes of short-lived fission fragments, which significantly contribute to the hard part of the $\bar{\nu}_e$ spectra.

Accurate knowledge of the $\bar{\nu}_e$ spectra came from experiments in which relevant beta-electron spectra were measured. Electrons and antineutrinos come from the same beta decay and are closely related. This simple idea is used in the conversion method, in which the $\bar{\nu}_e$ spectrum can be reconstructed (at least for not overly low energies) if the spectrum of fission electrons is known. This idea was first proposed and used for ^{235}U by Muehlhause and Oleksa in 1957 [11] and by Reines' group in 1959 [12]. Later, the correlation between calculated electron and $\bar{\nu}_e$ fission spectra was analyzed in 1979–1981 [9, 10], in 1981 by K. Schreckenbach *et al.* [13], and in 1982 by the Rovno group [14]. The first measurement of the ^{235}U and ^{239}Pu fission electron spectra and the observation

Table 2. Calculated $\bar{\nu}_e$ spectra (1/(MeV fission)) for ^{238}U and ^{241}Pu vs. irradiation time $t_{\rm on}$

E, MeV	^{238}U				^{241}Pu			
	1 d	30 d	100 d	2 yr	1 d	30 d	100 d	2 yr
0.05	0.164	0.302	0.390	0.503	0.192	0.328	0.407	0.502
0.1	0.247	0.715	1.016	1.397	0.235	0.695	0.965	1.286
0.2	0.782	2.008	2.386	2.723	0.742	1.956	2.330	2.643
0.3	1.177	2.089	2.334	2.596	1.103	2.008	2.219	2.448
0.4	1.668	2.298	2.448	2.499	1.571	2.216	2.353	2.397
0.5	1.984	2.558	2.644	2.681	1.874	2.473	2.549	2.580
0.6	1.937	2.471	2.544	2.567	1.911	2.435	2.497	2.516
0.7	2.077	2.578	2.653	2.680	2.046	2.536	2.598	2.620
0.8	2.126	2.621	2.701	2.732	2.087	2.568	2.634	2.659
0.9	2.156	2.608	2.681	2.714	2.098	2.537	2.597	2.624
1.0	2.113	2.420	2.470	2.504	2.036	2.331	2.366	2.395
1.2	1.954	2.162	2.205	2.242	1.812	1.998	2.028	2.061
1.4	1.810	1.880	1.908	1.943	1.645	1.701	1.720	1.754
1.6	1.752	1.793	1.800	1.821	1.568	1.603	1.612	1.642
1.8	1.659	1.686	1.691	1.713	1.456	1.479	1.486	1.517
2.0	1.514	1.528	1.533	1.555	1.318	1.330	1.337	1.368
2.25	1.332	1.341	1.345	1.365	1.138	1.145	1.151	1.179
2.5	1.158	1.164	1.168	1.184	0.964	0.969	0.974	0.998
2.75	1.028	1.032	1.035	1.047	0.839	0.842	0.846	0.865
3.0	0.895	0.896	0.897	0.900	0.712	0.713	0.715	0.724
3.25	0.775	0.776	0.776	0.779	0.598	0.599	0.600	0.606
3.5	0.653	0.654	0.654	0.655	0.491	0.491	0.492	0.495

of their considerable difference were performed by the Rovno group in 1980–1981 [15]. The best $\bar{\nu}_e$ spectra for ^{235}U, ^{239}Pu, and ^{241}Pu thermal fission at neutrino energies $E \geq 2.0$ MeV were found by the ILL group in a number of experiments carried out in 1981–1989 [16]. The ILL group accurately measured relevant electron spectra and effectively modified the conversion procedure. These ILL spectra above 2 MeV are commonly used now. For ^{238}U, the spectrum calculated in [10] is used.

Voloshin *et al.* [17], Akhmedov [18], and Vogel and Engel [19] in 1986–1989 stimulated new efforts to search for the anomalous magnetic moment of the neutrino in $\bar{\nu}_e e$ scattering experiments at reactors and further studies of the components of the reactor $\bar{\nu}_e$ spectrum. The Moscow MEPhI group in 1989 calculated the time evolution of the $\bar{\nu}_e$ spectra emitted by U and Pu fission fragments [20]. The fifth component of the spectrum, $^{\rm U}N$, which originates from the ^{238}U(n, γ) reaction, was "discovered" only in 1996 [21]. The last component, $\delta^F N$, which comes

Table 3. Fraction $N(E)/N_{\rm tot}$ of antineutrinos emitted in the energy intervals 0–E for fuel irradiation time $t_{\rm on} = 2$ yr (absolute values of $N_{\rm tot}$ for $t_{\rm on} = 2$ yr are presented in the last row)

E, MeV	^{235}U	^{239}Pu	^{238}U	^{241}Pu
0.1	9.94(−3)	1.64(−2)	1.10(−2)	1.55(−2)
0.2	4.73(−2)	6.01(−2)	4.48(−2)	5.15(−2)
0.3	8.84(−2)	0.105	8.04(−2)	9.04(−2)
0.5	0.179	0.201	0.158	0.174
0.75	0.290	0.320	0.257	0.285
1.0	0.399	0.436	0.357	0.394
1.5	0.570	0.606	0.517	0.560
2.0	0.700	0.734	0.646	0.692
2.5	0.798	0.827	0.749	0.792
3.0	0.869	0.893	0.827	0.865
4.0	0.951	0.965	0.926	0.951
5.0	0.983	0.990	0.971	0.984
$N_{\rm tot}$, $\bar{\nu}_e$/fission	5.585	5.091	6.688	5.897

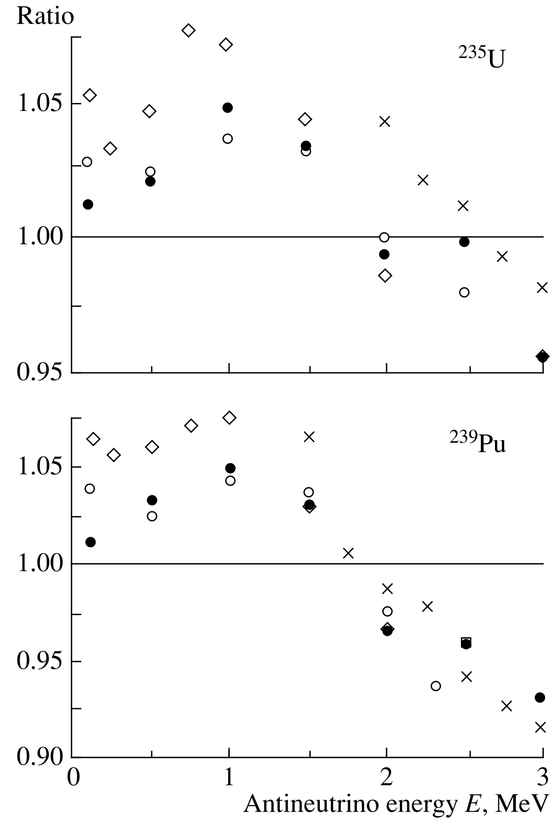

Fig. 1. Ratios of ^{235}U and ^{239}Pu fission antineutrino spectra found in [16, 19, 20] to the results of present work at various fuel irradiation times: 1.5 d (●) [20] and (×) [16]; 10^7 s (○) [20]; 2 yr (◇) [19].

from reactor neutron capture in fission fragments, was considered in [7, 21, 22].

3. MAIN RESULTS

3.1. Fission Antineutrinos from Four Fissile Isotopes

For each of four fissile isotope, we calculate the time evolution of the $\bar{\nu}_e$ spectrum during the fuel irradiation time $t_{\rm on}$ and this isotope decay as a function of time $t_{\rm off}$ after the end of irradiation. Calculations involve summation of all beta branches of 571 fission fragments. For fragment yields, we use data compiled in [23]. For the decay schemes, information accumulated in our laboratory during the past 25 years is used. Our code evaluates the spectra in the energy range 0–10 MeV (200 points per 1 MeV) for $t_{\rm on}$ and $t_{\rm off}$ intervals from 0.2 h to infinity.

The time evolution of the four spectra for $\bar{\nu}_e$ energy below 3.5 MeV is presented in Tables 1 and 2. One can see that, at 3.5 MeV, full saturation is already achieved in ~1 d after the beginning of the fission process; in the 2–3 MeV energy range, ~3% increase takes place at long irradiation times, while low energies do not reach equilibrium even in 2 yr (in typical PWR reactors, 2 yr is the average fuel irradiation time at the end of the operational run). In Table 3, one can see that, at $t_{\rm on} = 2$ yr, 50% of fission $\bar{\nu}_e$ are emitted below 1.2–1.3 MeV and approximately 30% of these antineutrinos have energy higher than 2.0 MeV.

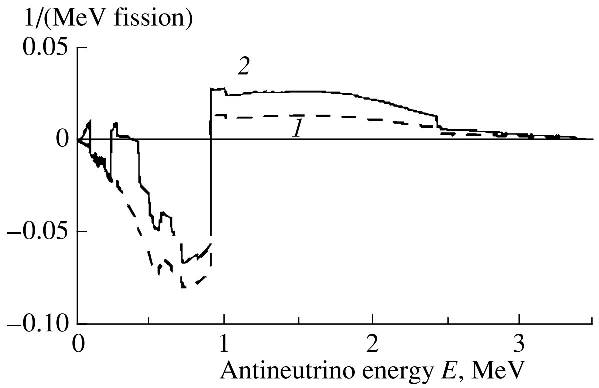

Fig. 2. Component $\delta^F N$ due to neutron capture in fission fragments: (*1*) beginning and (*2*) end of PWR reactor typical run.

The fuel continues to emit $\bar{\nu}_e$ after the irradiation is stopped (Table 4). In the softest part of the spectrum (50–500 keV), the residual $\bar{\nu}_e$ emission rate is at a level of 50–5% during the first month and does not completely vanish at $t_{\rm off} = 1$ yr.

To what extent are the calculated $\bar{\nu}_e$ spectra reliable in the energy range $E < 3$ MeV? Here, in contrast with the $E > 3$ MeV region, the contribution of well-established beta emitters amounts to 85–90%. We estimate that relative uncertainties here do not exceed 5–6% (68% C.L.). This estimate is confirmed by comparison of present results (Fig. 1) with spectra calculated earlier by Vogel and Engel [19] and by the MEPhI group [20] and with the ILL conversion spectra [16].

3.2. Antineutrinos from Neutron Capture in ^{238}U and in Fission Fragments

Nuclear fuel in PWR reactors contains 95–97% ^{238}U, which absorbs ~0.6 neutron per fission via (n, γ) reaction: $^{238}\text{U} + n \to {}^{239}\text{U}$ ($E_{\max} = 1.26$ MeV) $\to {}^{239}\text{Np}$ ($E_{\max} = 0.71$ MeV) $\to {}^{239}\text{Pu}$. This process contributes $^{U}N \sim 20\%$ to the total flux. The quantity ^{U}N is practically constant over the reactor run and is known with an uncertainty of 5%. Note that, in reactors with fuel elements of natural uranium, the $\bar{\nu}_e$ production rate in the channel considered is ~1.5 times higher.

Neutron capture in fission fragments can either increase or decrease its intensity depending on the energy of $\bar{\nu}_e$ (Fig. 2). The term $\delta^F N$ in (1) is negative

Table 4. Residual $\bar{\nu}_e$ emission: ratios of the current ^{235}U and ^{239}Pu fission antineutrino spectra vs. time after the end of fuel irradiation time $t_{\rm off}$ to that at the end of irradiation period $t_{\rm on} = 2$ yr

E, MeV	^{235}U				^{239}Pu			
	1 d	10 d	30 d	1 yr	1 d	10 d	30 d	1 yr
0.05	0.762	0.592	0.495	6.2(−2)	0.672	0.487	0.386	4.4(−2)
0.1	0.830	0.651	0.543	6.6(−2)	0.834	0.606	0.478	5.1(−2)
0.2	0.691	0.395	0.262	6.2(−2)	0.734	0.403	0.259	4.2(−2)
0.3	0.572	0.358	0.232	4.5(−2)	0.574	0.315	0.188	3.4(−2)
0.4	0.343	0.180	9.5(−2)	8.3(−3)	0.367	0.163	8.2(−2)	6.6(−3)
0.5	0.266	0.120	5.9(−2)	9.2(−3)	0.292	0.104	4.6(−2)	7.4(−3)
0.75	0.261	0.113	5.5(−2)	2.9(−3)	0.232	8.4(−2)	3.7(−2)	3.1(−3)
1.0	0.194	8.1(−2)	4.9(−2)	4.2(−3)	0.168	5.6(−2)	3.1(−2)	4.7(−3)
1.25	0.130	7.5(−2)	5.2(−2)	5.9(−3)	0.106	5.4(−2)	3.6(−2)	7.4(−3)
1.5	6.8(−2)	4.1(−2)	3.3(−2)	7.6(−3)	6.1(−2)	3.6(−2)	2.9(−2)	1.0(−2)
1.75	3.8(−2)	2.0(−2)	1.8(−2)	8.4(−3)	4.3(−2)	2.6(−2)	2.4(−2)	1.2(−2)
2.0	3.2(−2)	2.2(−2)	2.0(−2)	9.2(−3)	3.8(−2)	2.9(−2)	2.7(−2)	1.3(−2)
2.25	3.0(−2)	2.2(−2)	2.1(−2)	9.6(−3)	3.7(−2)	3.1(−2)	3.0(−2)	1.5(−2)
2.5	2.8(−2)	2.1(−2)	2.0(−2)	8.8(−3)	3.6(−2)	3.1(−2)	2.9(−2)	1.4(−2)
2.75	2.2(−2)	1.8(−2)	1.7(−2)	7.5(−3)	3.2(−2)	2.8(−2)	2.7(−2)	1.3(−2)
3.0	2.0(−3)	1.1(−3)	1.1(−3)	5.8(−4)	1.6(−2)	1.5(−2)	1.4(−2)	7.5(−3)
3.25	1.6(−3)	8.7(−4)	8.4(−4)	4.5(−4)	1.3(−2)	1.2(−2)	1.1(−2)	6.0(−3)
3.5	1.2(−3)	6.0(−4)	5.8(−4)	3.1(−4)	8.9(−3)	8.2(−3)	7.9(−3)	4.2(−3)

for energies below 0.9 MeV and positive for higher energies. It slowly changes along the reactor run and its contribution to the total flux of $\bar{\nu}_e$ does not exceed 0.3%. The negative part of $\delta^F N$ originates mainly from intensive absorption of neutrons in the fragment ^{135}Xe ($T_{1/2} = 9.1$ h, $E_{\rm max} = 0.91$ MeV), which is produced in the reactor at a rate of ~0.07/fission. Due to a very high cross section of the (n, γ) reaction (a few million barn), the majority of ^{135}Xe nuclei absorb neutrons before they decay.

Neutron interactions with reactor construction materials have been found to contribute less than 0.3% to the total flux and have been neglected at this stage of study.

3.3. Small Corrections to the ILL Spectra

The ILL spectra have been obtained after a 1–1.5 d exposure time. Their uncertainties are estimated to be 2.5%. These spectra do not contain time-dependent contributions due to decay of long-lived fission fragments (Tables 1 and 2) or due to additional radiation associated with neutron capture (Fig. 2), which affects the part of the $\bar{\nu}_e$ spectra above 1.80 MeV, the threshold of the inverse beta-decay reaction on the proton. We mention this point here because it may appear to be of some importance in searches for very small mixing angle oscillations at reactors.

4. CONCLUSIONS

In this paper, we tried to give a short story of the long process of understanding the reactor antineutrino sources and to outline the present status of the problem. New efforts to improve the accuracy could be needed in the future. So far, however, we do not feel challenges coming from current or planned experiments which could stimulate such efforts.

ACKNOWLEDGMENTS

This work is partially funded by Support of Leading Scientific Schools (grant no. 1246.2003.2) and the Russian Foundation for Basic Research (project no. 03-02-16055).

REFERENCES

1. C. Bemporad, G. Gratta, and P. Vogel, Rev. Mod. Phys. **74**, 297 (2002).
2. L. A. Mikaelyan, Yad. Fiz. **65**, 1206 (2002) [Phys. At. Nucl. **65**, 1173 (2002)].
3. K. Way and E. P. Wigner, Phys. Rev. **73**, 1318 (1948).
4. R. King and J. Perkins, Phys. Rev. **112**, 963 (1958).
5. A. A. Borovoi, L. A. Mikaelyan, and A. Y. Rumyancev, Kurchatov Institute Report No. 12-1453 (Moscow, 1974) (unpublished); L. A. Mikaelyan, in *Proceedings of the International Conference NEUTRINO'77, Baksan, 1977* (Nauka, Moscow, 1978), Vol. 2, p. 383.
6. A. A. Borovoĭ, Yu. L. Dobrynin, and V. I. Kopeĭkin, Yad. Fiz. **25**, 264 (1977) [Sov. J. Nucl. Phys. **25**, 144 (1977)].
7. V. I. Kopeikin, Yad. Fiz. **32**, 1507 (1980) [Sov. J. Nucl. Phys. **32**, 780 (1980)].
8. F. T. Avignone III and Z. D. Greenwood, Phys. Rev. C **22**, 594 (1980).
9. B. R. Davis, P. Vogel, F. M. Mann, and R. E. Schenter, Phys. Rev. C **19**, 2259 (1979).
10. P. Vogel, G. K. Schenter, F. M. Mann, and R. E. Schenter, Phys. Rev. C **24**, 1543 (1981).
11. C. O. Muehlhause and S. Oleksa, Phys. Rev. **105**, 1332 (1957).
12. R. E. Carter, F. Reines, J. J. Wagner, and M. E. Wyman, Phys. Rev. **113**, 280 (1959).
13. K. Schreckenbach *et al.*, Phys. Lett. B **99B**, 251 (1981).
14. A. A. Borovoi, V. I. Kopeikin, L. A. Mikaelyan, and S. V. Tolokonnikov, Yad. Fiz. **36**, 400 (1982) [Sov. J. Nucl. Phys. **36**, 232 (1982)].
15. A. A. Borovoi, Yu. V. Klimov, and V. I. Kopeikin, Preprint No. IAE-3465/2 (Moscow, 1981); Yad. Fiz. **37**, 1345 (1983) [Sov. J. Nucl. Phys. **37**, 801 (1983)].
16. F. Von Feilitzsch, A. A. Hahn, and K. Schreckenbach, Phys. Lett. B **118B**, 162 (1982); K. Schreckenbach, G. Colvin, W. Gelletly, and F. Von Feilitzsch, Phys. Lett. B **160B**, 325 (1985); A. A. Hahn *et al.*, Phys. Lett. B **218**, 365 (1989).
17. M. B. Voloshin, M. I. Vysotskii, and L. B. Okun', Zh. Éksp. Teor. Fiz. **91**, 754 (1986) [Sov. Phys. JETP **64**, 446 (1986)].
18. E. Kh. Akhmedov, Yad. Fiz. **48**, 599 (1988) [Sov. J. Nucl. Phys. **48**, 382 (1988)].
19. P. Vogel and J. Engel, Phys. Rev. D **39**, 3378 (1989).
20. V. G. Aleksankin, S. V. Rodichev, P. M. Rubtchov, *et al., Beta- and Antineutrino Radiation from Radioactive Nuclei* (Moscow, 1989).
21. A. M. Bakalyarov, V. I. Kopeikin, and L. A. Mikaelyan, Yad. Fiz. **59**, 1225 (1996) [Phys. At. Nucl. **59**, 1171 (1996)].
22. V. I. Kopeikin, L. A. Mikaelyan, and V. V. Sinev, Yad. Fiz. **60**, 230 (1997) [Phys. At. Nucl. **60**, 172 (1997)].
23. T. R. England and B. F. Rider, LA-UR-94-3106, ENDF-349, LANL (Los Alamos, 1994).

Physics of Atomic Nuclei, Vol. 67, No. 11, 2004, pp. 1969–1973. From Yadernaya Fizika, Vol. 67, No. 11, 2004, pp. 1993–1997.

NEUTRINO PHYSICS

Interaction of Electron Neutrinos with ^{56}Fe in the LSD for $E_{\nu_e} \leq 50$ MeV*

Yu. V. Gaponov[1], O. G. Ryazhskaya[1], and S. V. Semenov**

Russian Research Centre Kurchatov Institute, pl. Kurchatova 1, Moscow, 123182 Russia

Received January 20, 2004; in final form, May 6, 2004

Abstract—The neutrino pulses detected by the LSD (Liquid Scintillator Detector) on February 23, 1987, are analyzed on the basis of a two-stage model of supernova explosion. The number of events due to the electron-neutrino interaction with ^{56}Fe in the LSD is calculated. The obtained number of signals is in agreement with experimental data. © *2004 MAIK "Nauka/Interperiodica"*.

The study of $\nu_e{}^{56}$Fe interaction has been initialized during the last few years by developing the idea of a rotating mechanism of supernova explosion [1]. The paper [2] describes the improved rotational scenario of the process. This mechanism leads to a two-stage collapse with a phase difference of ~ 5 h. The neutrino flux during the first burst consists of electron neutrinos with a total energy $W_{\nu_e} = 8.9 \times 10^{52}$ erg. The neutrino energy spectrum is hard with an average energy of ~ 30–40 MeV. The second neutrino burst corresponds to the standard collapse theory without rotation with the formation of the neutrino sphere and with an equal energy distribution between all types of neutrinos [3].

The hypothesis of a new two-stage mechanism of supernova collapse returns us quite naturally to the data analysis due to the SN 1987A neutrino-event observation. The review and analysis of these data were presented in [4]. In the connection with this approach, a new analysis of neutrino pulses, detected by the Liquid Scintillator Detector (LSD) setup on February 23, 1987, was produced in [2]. During the analysis, attention was paid to the fact that the neutrino LSD, besides the large volume of scintillator, containing hydrogen for detection of antineutrino events in the reaction

$$\bar{\nu}_e + p \rightarrow n + e^+, \tag{1}$$

also includes a large amount of ^{56}Fe as a shielding material (about 200 t), distributed between the scintillator counters. Under the exposure of neutrino flux from a supernova, the iron nuclei should produce additional electrons and gamma quanta, which could be recorded by the detector. Due to this reason, the calculation of the partial $\nu_e{}^{56}$Fe cross section is very important.

Actually, in neutrino interaction with ^{56}Fe, the following charge-exchange reaction takes place,

$$\nu_e + {}^{56}\text{Fe} \rightarrow {}^{56}\text{Co}^* + e^-, \tag{2}$$

which leads to excitation of analog 0^+ and Gamow–Teller 1^+ giant resonances (AR and GTR, respectively) in the ^{56}Co nucleus. The excitation of the first one (AR) is connected with the Fermi transition. The ground-state quantum numbers of ^{56}Co are 4^+; therefore, the corresponding cross section with $^{56}\text{Co}_{\text{g.s}}$ in the final state is small, compared with AR and GTR excitation. The cross sections for AR and GTR can be simply estimated, if nuclear matrix elements M_{F} and M_{GT} connected with their excitation are known, according to the usual expressions:

$$\sigma_{\text{F}}(E_\nu) = \frac{G_\beta^2 m_e^2}{\pi} M_{\text{F}}^2 \pi_e \varepsilon_e F(Z_f, \varepsilon_e), \tag{3}$$

$$\sigma_{\text{GT}}(E_\nu) = \frac{G_\beta^2 m_e^2}{\pi} g_A^2 M_{\text{GT}}^2 \pi_e \varepsilon_e F(Z_f, \varepsilon_e), \tag{4}$$

where ε_e and π_e are the energy and momentum of the outgoing electron in units of m_e, $\varepsilon_e = (E_\nu - \Delta)/m_e$, Δ is the mass difference of ^{56}Co* and ^{56}Fe nuclei, and $g_A = 1.27$ is the axial-vector weak interaction constant. Fermi function $F(Z_f, \varepsilon_e)$ is a relativistic Coulomb factor which corrects the electron plane wave for the distortion caused by the nuclear Coulomb field, $Z_f = 27$, and $G_\beta^2 = 1.3255 \times 10^{-22}$ MeV^{-4} is the β-decay Fermi constant squared. For the ^{56}Co ground state, $\Delta = 4.056$ MeV. As is well known, the following qualitative estimates for AR and GTR matrix elements are valid: $M_{\text{F}}^2 = N - Z$,

---

*This article was submitted by the authors in English.

[1] Institute for Nuclear Research, Russian Academy of Sciences, pr. Shestidesyatiletiya Oktyabrya 7a, Moscow, 117312 Russia.

**e-mail: `semenov@imp.kiae.ru`

$M_{\mathrm{GT}}^2 = 3(N-Z)$, where $N-Z=4$ for the ^{56}Fe nucleus. For neutrino energies in the range of 30–50 MeV, the cross sections connected with AR and GTR excitations are on the order of 10^{-40} cm^2, although in the case of reaction (1) the cross section has a magnitude of about 10^{-41} cm^2. So the neutrino flux, generated in the new collapse model during the first stage of supernova collapse, should be recorded by the LSD even in the case when the flux is one order of magnitude smaller than the flux in the final, basic collapse stage. At the same time, the other neutrino detectors, which observed predominantly antineutrino flux according to reaction (1), should have a rather small response because at the first stage the flux consists mainly of neutrinos. This qualitative picture is rather reasonable for analysis of SN 1987A, and it points to the necessity for a more detailed study of the possibility to explain the first set of observed signals [4] in terms of the two-stage mechanism and consideration of ^{56}Fe as a neutrino detector based on reaction (2).

A simple quantitative analysis of ^{56}Co isobaric-state excitations in (ν_e, e^-) charge-exchange reactions, induced by electron-neutrino flux generated by SN 1987A, can be produced on the basis of finite Fermi system theory [5] combined with the approximate nuclear model of the states developed by one of the authors (Yu.V.G. and his coworkers) in the 1990s for description of Fermi (0^+) and GT (1^+) collective states on the basis of the broken $SU(4)$ symmetry scheme [6]. Really, in the 30–50 MeV neutrino energy region, the cross section of charge-exchange reactions for neutrino interaction with the $A(N,Z)$ nucleus is determined presumably by contributions of inverse allowed beta transitions to the $A(N-1,Z+1)$ nucleus through excitation of the isobaric 0^+ and 1^+ states in the $A(N-1,Z+1)$ nucleus. The contributions are connected with the excitation of the most collective states, first of all, AR and GTR (which is split into two components for ^{56}Co) and satellites of the GTR {Gamow–Teller satellite (GTS) and Anti-Gamow–Teller state (AGT) [6]}.

If positions of these states in the $A(N-1,Z+1)$ nucleus are known, the cross section of reaction (2) with the excitation of AR is determined by (3). Similarly, the cross section for excitation of 1^+ collective states of GTR, GTS, and AGT types is given by the following expression analogous to (4):

$$\sigma_{\mathrm{GT}_i} = \frac{G_\beta^2 m_e^2}{\pi} g_A^2 M_{\mathrm{GT}_i}^2 \pi_e \varepsilon_e F(Z_f, \varepsilon_e), \qquad (5)$$

with $\varepsilon_e = (E_\nu - E_{\mathrm{GT}_i} - \Delta)/m_e$ and $M_{\mathrm{GT}_i}^2 = e_q^2 \times 3(N-Z) \times R_i$. Here, M_{GT_i} is the matrix element of induced GT transition from the ground state of the $A(N,Z)$ nucleus to the ith GT state in $A(N-1,Z+1)$; E_{GT_i} is the corresponding excitation energy of the $A(N-1,Z+1)$ nucleus; e_q is the effective charge of GT type; and R_i is the relative contribution of the GT_i state to the GT sum rule. Indeed, according to the sum rule for Gamow–Teller matrix elements in GT transitions, there is the following relation:

$$\sum_i M_{\mathrm{GT}_i}^2(p\bar{n}) = 3(N-Z)e_q^2 + \sum_j M_{\mathrm{GT}_j}^2(n\bar{p}), \quad (6)$$

where $M_{\mathrm{GT}_i}^2(p\bar{n})$ are matrix elements of GT type for inverse β transition from the ground state of the $A(N,Z)$ nucleus to GT_i $p\bar{n}$ state localized in the $A(N-1,Z+1)$ nucleus and $M_{\mathrm{GT}_j}^2(n\bar{p})$ ones are for inverse β transition from the ground state to GT_j $n\bar{p}$ state, which belongs to the $A(N+1,Z-1)$ nucleus. Since for the simple approximation in the case of ^{56}Fe nucleus there is only one $n\bar{p}$-type transition $1f_{7/2}p \to 1f_{5/2}n$ with matrix element squared of one order smaller than the sum over all $p\bar{n}$ states in (6), it is possible to neglect the second term on the right-hand side of (6). Then, for the estimation of the ^{56}Fe$(\nu_e, e^-)^{56}$Co cross section, we need only to know the relative contributions R_i of each considered $p\bar{n}$ state in the sum rule (6). In any case, it gives the lower limit of the calculated cross sections. For effective GT charge e_q, we use $e_q = 0.8$, a value which is usually used in the finite Fermi-system theory and includes pion-mode effects [5, 6].

Let us now describe in some detail the structure of the isobaric states of the $A(N,Z)$ nucleus. For 0^+ states, there are two main types of these kinds: analog resonance (AR) and antianalog state (AAR) [6]. The former is located in the $A(N-1,Z+1)$ nucleus at a Coulomb energy higher than the ground state of the $A(N,Z)$ nucleus and belongs to the $SU(2)$ isomultiplet with $T=(N-Z)/2$. AAR is located below AR, near the ground state of the $A(N-1,Z+1)$ nucleus and belongs to the other isomultiplet with $T=(N-Z)-1$. As is well known, the isotopic invariance which is broken only by Coulomb interaction is conserved in nuclei with accuracy of about 10^{-3}–10^{-2}, so that the squared Fermi matrix element for transition from ^{56}Fe to AAR in ^{56}Co is of the same value and its contribution to the cross section of inverse beta decay does not exceed 1%. In the case of ^{56}Fe, the corresponding states in ^{56}Co are 3.59 MeV (AR) and 1.45 MeV (AAR).

The cross section calculation for the allowed Fermi transition to the isobaric AR of 3.59 MeV in ^{56}Co is produced with expression (3), $M_{\mathrm{F}}^2 = N-Z$. The relativistic Coulomb correction factor, $F(Z_f, \varepsilon)$, is written as [7]

$$F(Z_f, \varepsilon)$$

$$= \frac{4}{[\Gamma(2\gamma_1+1)]^2}(2pR_A)^{2(\gamma_1-1)}|\Gamma(\gamma_1+iy)|^2 e^{\pi y},$$

$$y = \frac{\alpha Z_f \varepsilon}{p}, \quad \gamma_1 = \sqrt{1-(Z_f\alpha)^2},$$

$$R_A = 1.2A^{1/3}\mathrm{Fm}.$$

Here, p is the electron momentum and α is the fine structure constant. The exact mathematical procedure for estimating $F(Z_f, \varepsilon)$ is taken from [8].

The structure of isobaric GT 1^+ states in ^{56}Co is more complex and depends significantly on the magnitude of the spin–orbit force potential, which for states with quantum numbers $j = l \pm 1/2$ defines their spin–orbital splitting. As was demonstrated in finite Fermi system theory, the splitting is essentially renormalized by the great spin–isospin particle–hole forces [5]. For ^{56}Fe–^{56}Co nuclei, where the $1f_{7/2}n$ shell is completely occupied, the $2p_{3/2}n$ shell is half occupied by neutrons, and $1f_{7/2}p$ is three-fourths occupied by protons, one can use for the renormalized spin–orbital splitting the following values: 7 MeV for $1f_{7/2}$–$1f_{5/2}$ and 3–4 MeV for $2p_{3/2}$–$2p_{1/2}$. The former is responsible for the 7.06-MeV 1^+-level position in ^{56}Fe, and the latter is related to the 4.54-MeV and 3.45-MeV 1^+ ones in ^{56}Fe, which can be interpreted as states formed by the transitions from the half occupied $2p_{3/2}n$ level to the $2p_{1/2}n$ and $1f_{5/2}n$ ones.

Gamow–Teller collective states of $p\bar{n}$ type take part in the charge-exchange neutrino reaction as broad resonances, formed by transitions of neutrons from the $1f_{7/2}n$ and $2p_{3/2}n$ levels into free proton ones. They include the following states:

(i) Two components of GTR: GT$_1$ and GT$_2$ caused by a mixture of $1f_{7/2}n \to 1f_{5/2}p$ and $2p_{3/2}n \to 2p_{1/2}p$ transitions which arise from spin–isospin particle–hole interaction [5]. Their energies relative to AR are determined by the renormalized spin–orbital $1f_{7/2}$–$1f_{5/2}$ and $2p_{3/2}$–$2p_{1/2}$ splittings. This leads to two resonance states of $p\bar{n}$ type about 10.6 MeV and 8.2 MeV in ^{56}Co with expected widths of about 3 MeV. Such energies are similar to expected positions in ^{56}Co for analog states of 7.6-MeV and 4.54-MeV 1^+ experimental levels of ^{56}Fe. It should be noted that such a two-component structure of the GTR is a consequence of a small neutron excess in ^{56}Fe, where $N - Z = 4$. For nuclei with large $N - Z$, the GTR usually has one collective component [6].

(ii) The 1^+ GTS state—GT$_3$, which is generated on the basis of the $2p_{3/2}n \to 1f_{5/2}p$ transition from the level partially occupied by neutrons into one free of protons. Since in this transition the orbital quantum number changes by 2, the contribution of the transition into full GT strength is strongly suppressed compared with the $2p_{3/2}n \to 2p_{1/2}p$ transition, which is included in the GTR. The position of GT$_3$ can be estimated with starting from the 3.45-MeV state of ^{56}Fe, having similar structure in the neutral excitation branch, relative to which it should be shifted approximately on the Coulomb energy. This leads to value 7.2 MeV in ^{56}Co within the same expected 3-MeV-width domain.

(iii) AGT 1^+ state—GT$_4$, which in the considered model should lie near the AAR. Actually, the 1.72-MeV 1^+ level is known in ^{56}Co and is rather close to the 1.45-MeV AAR in this nucleus. The structure of this state is defined by $1f_{7/2}n \to 1f_{7/2}p$ and $2p_{3/2}n \to 2p_{3/2}p$ transitions and the state belongs to the other $SU(4)$ supermultiplet than the GTR and $A(N, Z)$ ground state do. It means that GT matrix element of the transition from the $A(N, Z)$ ground state to AGT in $A(N-1, Z+1)$ is proportional to the magnitude of $SU(4)$ symmetry-breaking forces, so this matrix element squared can be estimated to be about 10% of the sum of GT$_1$ and GT$_2$ matrix elements squared [6].

Thus, for the calculation of neutrino–^{56}Fe charge current reaction cross section, connected with allowed $0^+ \to 1^+$ transitions into GT states of ^{56}Co by expression (5), we use the simple four-component model of GT states in ^{56}Co with the following energies: $E_{\mathrm{GT}_1} = 10.7$ MeV, $E_{\mathrm{GT}_2} = 8.2$ MeV, $E_{\mathrm{GT}_3} = 7.2$ MeV, $E_{\mathrm{GT}_4} = 1.72$ MeV. Here, we do not consider forbidden transitions.

To estimate quantitatively R_i values, describing relative contributions of GT$_i$ states to the sum rule (6), one has to use a version of the microscopic nuclear model of GT 1^+ states which allows one to determine $M^2_{\mathrm{GT}_i}$ through the energy parameters of the states, particle–hole interaction strength, and occupation numbers for neutrons and protons in the specific nucleus. The basic factor is spin–isospin interaction strength, which is supposed to have a magnitude comparable to the magnitude of isospin interaction strength in accordance with the broken $SU(4)$ symmetry model [6]. The inclusion of this interaction leads to the strong suppression of $M^2_{\mathrm{GT}_4}$ for $j \to j$, $n \to p$ transitions that is connected with the abovementioned effect of $SU(4)$ breaking. Simultaneously, it leads to a nonzero (however, small) contribution to the sum rule (6) from l-forbidden transition $2p_{3/2} \to 1f_{5/2}$ connected with $M^2_{\mathrm{GT}_3}$ for the GT$_3$ state, which has zero value in the case when the spin–isospin interaction is switched off. For the sum rule (6), the relative weights of GT$_1$ and GT$_2$, generated by $j_n \to j'_p$ ($1f_{7/2}n \to 1f_{5/2}p$ and $2p_{3/2}n \to 2p_{1/2}p$) transitions,

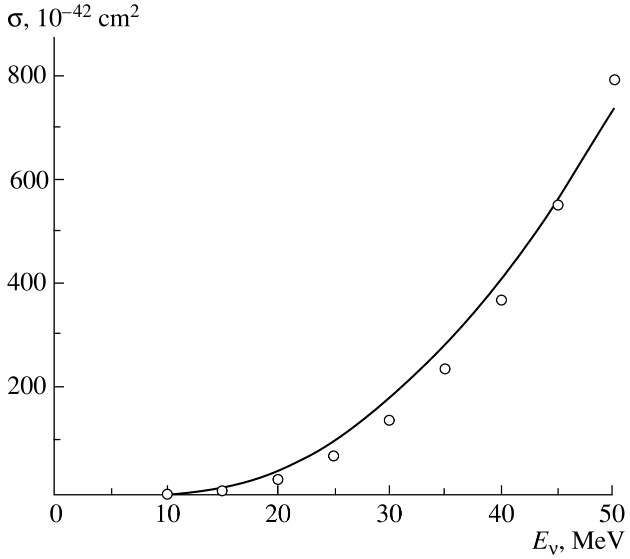

Total ^{56}Fe(ν_e, e^-)^{56}Co cross section as a function of neutrino energy. The circles are the results of calculations from [9].

are approximately proportional to the occupation factors. As has been demonstrated in a simple model [6], relative weights of a certain state generated by $j_n \to j'_p$ transition are determined by the following factors, which depend on the occupation numbers $n(j_n), n(j'_p)$:

$$F(j_n \to j'_p) = n(j_n) - n(j'_p); \quad n(j) = \frac{N(j)}{2j+1}$$

($N(j)$ is the number of the particles on the jth level). In ^{56}Fe, these factors for $M^2_{\mathrm{GT}_i} (i = 1, 2, 4)$ connected with $1f_{7/2}n \to 1f_{5/2}p$, $2p_{3/2}n \to 2p_{1/2}p$, and mixture of $1f_{7/2}n \to 1f_{7/n}p$ and $2p_{3/2}n \to 2p_{3/2}p$ transitions are correspondingly as follows: 1; 1/2; 1/4, 1/2. It means that, in a zero approximation, the $R_1 : R_2$ ratio is of order 2 : 1. For more exact estimates, we have used here the special simple model based on the finite Fermi system theory [5] in combination with the $SU(4)$ symmetry model [6]. It leads to the following results for R_i values:

$$R(\mathrm{GT}_1) = 0.60, \quad R(\mathrm{GT}_2) = 0.24,$$
$$R(\mathrm{GT}_3) = 0.04, \quad R(\mathrm{GT}_4) = 0.12.$$

The details of the model, as well as more exact calculations, will be presented in a separate publication.

Making use of these GT_i characteristics, one can calculate the energy dependence of the cross section for the interaction neutrino with the ^{56}Fe nucleus in the charge-exchange channel. It is presented in the figure, where for comparison the results of [9] for the same reaction are also shown. For the control, the total cross section for the ^{56}Fe(ν_e, e^-)^{56}Co reaction, averaged over the muon-decay-at-rest neutrino spectrum, was calculated in the considered model. It leads to the value 2.78×10^{-40} cm^2, which is in agreement with the KARMEN experiment result $(2.56 \pm 1.08(\mathrm{stat}) \pm 0.43(\mathrm{syst})) \times 10^{-40}$ cm^2 [10].

Adopting the assumption that the first neutrino pulse from supernova 1987A, which could be connected with the initial stage of the collapse in the two-stage model, had an electron-neutrino energy of about 40 MeV and the total power of neutrino radiation in it was equal to 8.9×10^{52} erg [2], one can calculate the number of neutrino events to be recorded in the LSD. Thus, we have obtained a cross section value of 4.2×10^{-40} cm^2 for 40-MeV energy and 0.5×10^{10} neutrino/cm^2 for the flux on the Earth's surface (the distance from the supernova to the Earth is 50 kPs). If the total ^{56}Fe mass in the LSD setup is 200 t, one can obtain about five interactions of electron neutrinos with ^{56}Fe only due to charge current. Taking into account $\nu_e{}^{56}$Fe neutral current interaction and $\nu_e{}^{12}$C interaction in the LSD scintillator together with the efficiency of neutrino detection by the counters, we can see that the calculated number is in good agreement with the observed number of events [2].

It should be emphasized that the LSD is a unique detector for observing the neutrino pulse connected with the first stage of the collapse in the scenario [2]. The reason is the following: the LSD is a detector which incorporates a sufficient amount of proper material for detecting, namely, the electron-neutrino pulse, but not the antineutrino one (as was expected before). As to the other detectors, including hydrogen components (e.g., IMB type), they cannot detect a pulse consisting mainly of electron neutrinos. In the same way, the number of events detected in the neutrino—electron interaction, as is in the case of the KII detector, is small because of the smallness of the cross section in the supernova neutrino energy range ($\approx 10^{-43}$ cm^2) in comparison with the neutrino—^{56}Fe one.

Thus, the estimates presented here demonstrate that the observation of two series of neutrino pulses, recorded on February 23, 1987, from supernova 1987A explosion in the Large Magellan Cloud, can be explained qualitatively and quantitatively within the new two-stage model of V.S. Imshennik. Moreover, this model allows one to assume that, during the first stage of the collapse, one has to expect the generation of electron-neutrino flux of high energy near 40—50 MeV. For its detection, one can use detectors built on the basis of large volumes of stable isotopes with large values of neutron excess $N - Z$. As is well known, the high-lying collective isobaric resonances are present in such nuclei. For this energy region, the most sufficient ones are analog and Gamow–Teller resonances and also spin–dipole resonances of 0^-, 1^-, 2^- characteristics. The excitation of these resonances in a charge-exchange reaction by electron neutrinos accompanied with high-energy electron production will cause the large cross section of this reaction. The subsequent decay of these resonances with neutron or gamma-quanta emission as well as high-energy electrons generated by neutrinos allows one to record these reactions quite reliably. An instructive example of these targets is presented by the ^{208}Pb nucleus, since there are extremely collective AR and GTR at an excitation energy of about 18 MeV in the ^{208}Bi nucleus. These states have very high cross sections and can be excited in neutrino flux coming from the first stage of supernova collapses. This example demonstrates that the employment of nuclear targets with large neutron excess $N - Z$ as neutrino detectors for supernova burst detection opens interesting perspectives and can give new information on the processes taking place during the first stage of the collapse.

ACKNOWLEDGMENTS

We are very grateful to V.S. Imshennik, S.S. Gerstein, and D.K. Nadezhin for interesting and useful discussions and to the Organizing Committee of the NANP-2003 International Conference for the invitation to present the report at the conference.

This work is supported by the Russian Foundation for Basic Research, project nos. 03-02-17266, 03-02-16414, and 03-02-16436, and the RRC Kurchatov Institute, grant no. 14 of 2003–2004 on fundamental research.

REFERENCES

1. V. S. Imshennik and D. V. Popov, Pis'ma Astron. Zh. **20**, 620 (1994) [Astron. Lett. **20**, 529 (1994)]; **24**, 251 (1998) [**24**, 206 (1998)].
2. V. S. Imshennik and O. G. Ryazhskaya, Pis'ma Astron. Zh. **30**, 17 (2004) [Astron. Lett. **30**, 14 (2004)].
3. V. S. Imshennik and D. K. Nadezhin, Itogi Nauki Tekh., Ser. Astron. **21**, 63 (1982).
4. V. L. Dadykin, G. T. Zatzepin, and O. G. Ryazhskaya, Usp. Fiz. Nauk **158**, 139 (1989) [Sov. Phys. Usp. **32**, 459 (1989)].
5. A. B. Migdal, *Theory of the Finite Fermi-Systems and Its Application to the Atomic Nuclei* (Interscience, New York, 1967).
6. Yu. V. Gaponov, D. M. Vladimirov, and J. Bang, Preprint No. 96-11, NBI (1996); Acta Phys. Hung. **3**, 189 (1996).
7. M. Doi, T. Kotani, and E. Takasugi, Prog. Theor. Phys. Suppl. **83**, 1 (1985).
8. S. V. Semenov, F. Simkovic, V. V. Khruschev, and P. Domin, Yad. Fiz. **63**, 1271 (2000).
9. E. Kolbe, K. Langanke, and G. Martinez-Pinedo, Phys. Rev. C **60**, 052801 (1999).
10. B. Zenitz, Prog. Part. Nucl. Phys. **32**, 351 (1994).

Physics of Atomic Nuclei, Vol. 67, No. 11, 2004, pp. 1974–1983. From Yadernaya Fizika, Vol. 67, No. 11, 2004, pp. 1998–2007.
Original English Text Copyright © 2004 by Zdesenko, Danevich, Tretyak.

CAMEO Project and Discovery Potential of the Future 2β-Decay Experiments*

Yu. G. Zdesenko[†], **F. A. Danevich**[**], **and V. I. Tretyak**

Institute for Nuclear Research, Kiev, Ukraine

Received December 4, 2003

Abstract—The demands on the future supersensitivity 2β-decay experiments (aiming to observe neutrinoless 2β decay or to advance restrictions on the neutrino mass to $m_\nu \leq 0.01$ eV) are considered and requirements for their discovery potential are formulated. The most realistic 2β projects are reviewed and the conclusion is obtained that only several of them with high energy resolution would completely satisfy these severe demands and requirements. At the same time, most of the recent projects (CAMEO, CUORE, DCBA, EXO, etc.) could certainly advance the limit on the neutrino mass up to $m_\nu \leq 0.05$ eV. *© 2004 MAIK "Nauka/Interperiodica".*

Recent observations of neutrino oscillations [1–4], demonstrating that neutrinos have nonzero mass (m_ν), provide important motivation for the double-beta (2β) decay experiments [5–7]. The neutrinoless (0ν) double-β decay, being forbidden in the Standard Model (SM) of electroweak theory since it violates lepton number (L) conservation, requires neutrinos to be massive Majorana particles [8]. At the same time, many extensions of the SM incorporate L-violating interactions and, thus, could lead to this process, which, if observed, will be clear evidence for new physics beyond the SM and a unique confirmation of the Majorana nature of the neutrino. The oscillation experiments are sensitive to the neutrino mass difference; therefore, only the measured $0\nu2\beta$-decay rate can give the absolute scale of the effective Majorana neutrino mass, which could allow one to test different neutrino mixing models.

Despite numerous efforts, $0\nu2\beta$ decay still remains unobserved (see the latest reviews [5–7, 9]). Recently, the impressive half-life limits for the 0ν mode were set in direct measurements with several nuclides: $T^{0\nu}_{1/2} \geq 10^{23}$ yr for ^{116}Cd [10], ^{128}Te, ^{130}Te [11], and ^{136}Xe [12], and $T^{0\nu}_{1/2} \geq 10^{25}$ yr for ^{76}Ge [13, 14]. These limits and the corresponding restrictions on the Majorana neutrino mass are given in Table 1. The m_ν constraints are determined on the basis of the nuclear matrix elements (NME) calculations of [15], which were chosen because of the most extensive list of 2β nuclei calculated in this work, allowing one to compare the sensitivity of different experiments to the m_ν bound within the same scale. In addition, two new experiments (NEMO-3 [17] and CUORICINO [18]) are running now. The NEMO-3 apparatus allows direct detection of two electrons by a tracking device (6180 drift cells) and measurement of their energies by 1940 large blocks of plastic scintillators. The energy resolution at 3 MeV is 8.8%. For a 5-yr measuring time and with a passive source of 7 kg of ^{100}Mo $\approx$ 60-mg/cm^2 thickness ($\sim$ 50 mg/cm^2 of ^{100}Mo foil itself, plus $\approx$ 10 mg/cm^2 of scintillator wrapping, gas and wires of the tracking counters), the sensitivity of the NEMO-3 detector would be about $T^{0\nu}_{1/2} \geq 5 \times 10^{24}$ yr [17], which corresponds to $m_\nu \leq 0.5$ eV. The CUORICINO setup contains 56 low-temperature bolometers made of TeO$_2$ crystals (750 g each) with a total mass of 42 kg cooled down to a temperature of $\approx$ 10 mK [18]. The projected CUORICINO sensitivity is $T^{0\nu}_{1/2} \geq 10^{24}$–$10^{25}$ yr ($m_\nu \leq 0.2$–0.7 eV), depending on what background rate at the energy 2.5 MeV will be reached (0.1–0.05 counts/(yr kg keV)) [18].

Thus, one can conclude that present (and near future) 2β-decay results have already brought the most stringent restrictions on the values of the Majorana neutrino mass ($m_\nu \leq 0.3$–2 eV), the right-handed admixture in the weak interaction ($\eta \approx 10^{-8}$, $\lambda \approx 10^{-6}$), the neutrino–Majoron coupling constant ($g_M \approx 10^{-4}$), and the R-parity-violating parameter of the minimal supersymmetric SM ($\lambda \approx 10^{-4}$) [5–7, 9].

Moreover, nowadays the 2β-decay research is entering a new era, where discovery of $0\nu2\beta$ decay has

---

[*] This article was submitted by the authors in English.

[†] Deceased.

[**] e-mail: `danevich@kinr.kiev.ua`

Table 1. The best reported $T_{1/2}^{0\nu}$ and m_ν limits from direct 2β-decay experiments

Nuclide	Experimental limit $T_{1/2}^{0\nu}$, yr		Reference	Limit on m_ν [eV] on the basis of [15]	
	68% C.L.	90% C.L.		68% C.L.	90% C.L.
^{76}Ge	3.1×10^{25}	1.9×10^{25}	[13]	0.27	0.35
	–	1.6×10^{25}	[14]	–	0.38
	$4.2 \times 10^{25*}$	$2.5 \times 10^{25*}$	[16]	0.24	0.31
^{116}Cd	2.6×10^{23}	1.7×10^{23}	[10]	1.4	1.7
^{130}Te	–	2.1×10^{23}	[11]	–	1.5
^{136}Xe	–	4.4×10^{23}	[12]	–	2.2

* Results were established [16] by analyzing the cumulative data sets of the Heidelberg–Moscow [13] and IGEX [14] experiments.

become realistic. But to do it, the present level of the experimental sensitivity should be enhanced up to $m_\nu \approx 0.01$ eV (or at least up to $m_\nu \leq 0.05$ eV). It is a great challenge and a lot of projects have been proposed in the past few years aiming to reach this goal [5–7]. As regards these projects, two points should be noted.

First, it is widely recognized now that 2β-decay searches must be performed with several candidates. This is because a reliable value (or restrictions) of the neutrino mass can be derived from experiments on the basis of the calculation of the NME of $0\nu2\beta$ decay, whose uncertainties are often unknown [19, 20].[1] Another reason is the difficulties in developing the experimental techniques. If $0\nu2\beta$ decay is finally observed in one experiment, such a discovery certainly has to be confirmed with other nuclides and by using other experimental techniques, which should be well developed by then. However, because of the superlow-background nature of the 2β studies, the corresponding development is a multistage process and consequently a rather long one. For instance, the first valuable result for the $0\nu2\beta$ decay of ^{76}Ge was obtained in 1970 as $T_{1/2}^{0\nu} \geq 10^{21}$ yr [22]. Recently, after 30 yr of strong efforts, this limit was advanced up to $T_{1/2}^{0\nu} \geq 10^{25}$ yr [13, 14].

Secondly, practically all proposals require a large mass production of enriched isotopes; thus, their costs are comparable with those of accelerator experiments. Because most of these projects need strong efforts and a long time to prove their feasibility, it is very important to choose those which will really be able to observe the $0\nu2\beta$-decay rate corresponding to neutrino mass $m_\nu \approx 0.01$ eV and could be constructed within a reasonable time. With this aim in the present paper, we consider demands on the future high-sensitivity 2β-decay experiments and formulate requirements for their discovery potential. Then, recent projects are reviewed and discussed.

As is obvious from Table 1, the present ^{76}Ge studies [13, 14] (with ≈ 10 kg of enriched HP ^{76}Ge detectors) have brought the most stringent restrictions on the neutrino mass, at the level of ≈ 0.3 eV. Other experiments offer m_ν bounds in the range of ≈ 2 eV, which is not so drastically weaker, especially if taking into account that, e.g., the ^{116}Cd result was obtained with very small ^{116}CdWO$_4$ crystal scintillators (total mass of ~ 0.3 kg) [10]. It demonstrates the importance of the right choice of 2β-decay candidate for study, which we consider next by using the formula for the $0\nu2\beta$-decay probability (right-handed contributions are neglected) [20, 23]: $\left(T_{1/2}^{0\nu}\right)^{-1} = G_{mm}^{0\nu}\,|\mathrm{NME}|^2\,\langle m_\nu\rangle^2$ (where $G_{mm}^{0\nu}$ is the phase-space integral of the $0\nu2\beta$ decay). The phase-space integral $G_{mm}^{0\nu}$ strongly depends on the available energy release, $Q_{\beta\beta}$, roughly as $Q_{\beta\beta}^5$ [20, 23]. Thus, if we skip for the moment the problem of the NME calculation, it is evident that the $Q_{\beta\beta}$ value is a very important parameter for the choice of the most sensitive 2β-decay candidates. Moreover, the larger the 2β-decay energy, the simpler, from an experimental point of view, it is to overcome background problems.[2]

Among 35 possible $2\beta^-$-decay candidates, there are only 13 nuclei with $Q_{\beta\beta}$ larger than ≈ 1.7 MeV

---

[1] See, e.g., [21]: "The nuclear structure uncertainty can be reduced by further development of the corresponding nuclear models. At the same time, by reaching comparable experimental limits in several nuclei, the chances of a severe error in the NME will be substantially reduced."

[2] Note that the background from natural radioactivity drops sharply above 2615 keV, which is the energy of the γ from ^{208}Tl decay (^{232}Th family).

Table 2. Double-β-decay candidates with $Q_{\beta\beta} \geq 1.7$ MeV

Nuclide	$Q_{\beta\beta}$, keV	Abundance δ, %	Parameter $G^{0\nu}_{mm}$, 10^{-14} yr	$T^{0\nu}_{1/2}\langle m_\nu\rangle^2$, yr eV^2 (after NME [15])
^{48}Ca	4272	0.187	6.4	–
^{76}Ge	2039	7.61	0.6	2.3×10^{24}
^{82}Se	2995	8.73	2.7	6.0×10^{23}
^{96}Zr	3350	2.80	5.7	5.3×10^{23}
^{100}Mo	3034	9.63	4.6	1.3×10^{24}
^{110}Pd	2000	11.72	–	2.0×10^{24}
^{116}Cd	2805	7.49	4.9	4.9×10^{23}
^{124}Sn	2287	5.79	2.6	1.4×10^{24}
^{130}Te	2529	34.08	4.1	4.9×10^{23}
^{136}Xe	2468	8.87	4.4	2.2×10^{24}
^{148}Nd	1929	5.7	–	1.4×10^{24}
^{150}Nd	3367	5.6	19	3.4×10^{22}
^{160}Gd	1730	21.86	–	8.6×10^{23}

[24]. They are listed in Table 2, where $Q_{\beta\beta}$, the natural abundance δ [25], and the calculated values of the phase-space integral $G^{0\nu}_{mm}$ [20, 23] and $T^{0\nu}_{1/2} \times \langle m_\nu\rangle^2$ [15] are given. Note that due to the low $Q_{\beta\beta}$ value of ^{76}Ge (2039 keV), its phase-space integral is about 7–10 times smaller as compared with those of ^{48}Ca, ^{96}Zr, ^{100}Mo, ^{116}Cd, ^{130}Te, and ^{136}Xe.

Now let us consider the experimental sensitivity, which can be expressed in terms of a lower half-life limit as follows [6, 9]: $T_{1/2} \sim \varepsilon\delta\sqrt{mt/(RB)}$. Here, ε is the detection efficiency; δ is the abundance or enrichment of candidate nuclei contained in the detector; t is the measurement time; m and R are the total mass and the energy resolution of the detector, respectively; and B is the background rate in the energy region of the $0\nu2\beta$-decay peak. First of all, it is clear from the formula that efficiency and enrichment are the most important characteristics of a setup for 2β-decay studies, because any other parameters are under the square root. Obviously, 100% enrichment is very desirable. In order to reach the sensitivity to neutrino mass of about 0.01 eV, one has to exploit enriched sources whose masses should exceed at least some 100 kg. The latter restricts the list of candidate nuclei given in Table 2 because a large mass production of enriched materials is possible only for several of them. These are ^{76}Ge, ^{82}Se, ^{100}Mo, ^{116}Cd, ^{130}Te, and ^{136}Xe, which could be produced by means of centrifugal separation. Centrifugal isotope separation requires the substances to be in gaseous form. Thus, xenon gas can be used directly. There also exist volatile germanium, selenium, molybdenum, and tellurium hexafluorides, as well as the metal to organic cadmium–dimethyl compound [26]. Note that two nuclides from Table 2 (^{130}Te and ^{160}Gd) can be used without enrichment owing to their relatively high natural abundances ($\approx 34\%$ and $\approx 22\%$, respectively).

Secondly, one would require that the detection efficiency should be close to 100%, which is possible, in fact, only for the "active" source technique. There are two classes of 2β-decay experiments—with "passive" and "active" sources. In the last case, a detector, containing 2β-decay candidate nuclei, serves as a source simultaneously. If the $0\nu2\beta$ decay occurs in the source, the sharp peak at the $Q_{\beta\beta}$ value will be observed in the electron sum energy spectrum of the detector(s). Indeed, the mass of the "passive" source can be enlarged by increasing its thickness, which in turn lowers detection efficiency due to absorption of electrons in the source, broadening and shifting of the $0\nu2\beta$-decay peak to lower energies, etc.

Thirdly, the energy resolution of the detector is an extremely important characteristic for the $0\nu2\beta$-decay quest. Foremost, with high energy resolution, it is possible to minimize the irremovable background produced by the $2\nu2\beta$-decay events. It is because, for the case of a poor resolution, the events from the high-energy tail of the 2ν distribution could run into the energy window of the 0ν peak and, thus, generate a background which cannot be discriminated from the $0\nu2\beta$-decay signal, even in principle. However, the better the energy resolution, the smaller the fraction

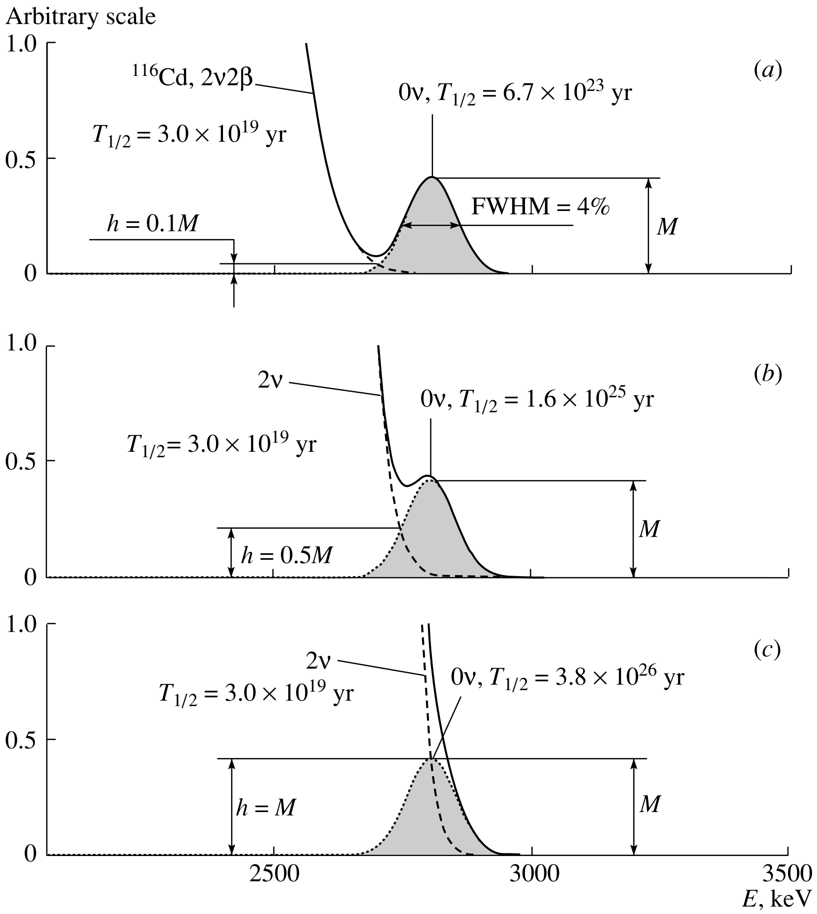

Fig. 1. Definition of the discovery potential of the 2β-decay studies. The 2ν distribution of ^{116}Cd (with $T^{2\nu}_{1/2} = 3 \times 10^{19}$ yr) overlaps the 0ν peaks with the half-life corresponding to (a) 6.7×10^{23}, (b) 1.6×10^{25}, and (c) 3.8×10^{26} yr. Correspondingly, the 0ν peak with the amplitude M (the energy resolution at 2.8 MeV is FWHM = 4%) and the 2ν spectrum meet at the relative height (a) $h/M = 0.1$, (b) $h/M = 0.5$, and (c) $h/M = 1$.

of the 2ν tail that can fall within the 0ν interval, and the irremovable background would be decreased too.

Likewise, the role of the energy resolution of the detector is even more crucial for the discovery of $0\nu2\beta$ decay. Indeed, this process manifests itself by the peak at $Q_{\beta\beta}$ energy; hence, the great advantage of $0\nu2\beta$-decay experiments is the possibility of searching for the sharp peak on the continuous background. Since the width of the $0\nu2\beta$-decay peak is determined by the energy resolution of the detector, the latter should be sufficient to discriminate this peak from the background and to recognize the effect. Practically, it would be very useful to determine the minimal level of the energy resolution which is needed to detect $0\nu2\beta$ decay with a certain $T^{0\nu}_{1/2}$ value and at a given $2\nu2\beta$-decay rate.

Aiming to make such an estimation quantitatively, let us consider Fig. 1 with three examples, in which the 2ν distribution of ^{116}Cd (with $T^{2\nu}_{1/2} = 3 \times 10^{19}$ yr) overlaps the three 0ν peaks with the half-life corresponding to (a) 6.7×10^{23}, (b) 1.6×10^{25}, and (c) 3.8×10^{26} yr. The spectrum of the sum of electron energies for $2\nu2\beta$ decay (0^+–0^+ transition, $2n$ mechanism) was obtained (as described in [27]) by integrating the theoretical two-dimensional energy distribution $\rho_{12}(t_1, t_2)$: $\rho_{1+2}(t) = \int_0^t \rho_{12}(t - t_2, t_2)\, dt_2$, where t_i is the kinetic energy of the ith electron and t is the sum of electron energies (t_i and t are in units of the electron mass m_0c^2). The basic two-dimensional distribution is taken from [28]: $\rho_{12}(t_1, t_2) = (t_1 + 1)p_1F(t_1, Z)(t_2 + 1)p_2F(t_2, Z)\,(t_0 - t_1 - t_2)^5$, where t_0 is the energy available in the 2β process ($Q_{\beta\beta}$ for decay to the ground state) and p_i is the momentum of the ith electron, $p_i = \sqrt{t_i(t_i + 2)}$ (in units of m_0c). The Fermi function is defined as [29] $F(t, Z) = \mathrm{const} \cdot p^{2s-2}e^{\pi\eta}|\Gamma(s + i\eta)|^2$, where $s = \sqrt{1 - (\alpha Z)^2}$, $\eta = \alpha Z(t + 1)/p$, $\alpha = 1/137.036$, Z is the atomic number of the daughter nucleus, and Γ is the gamma

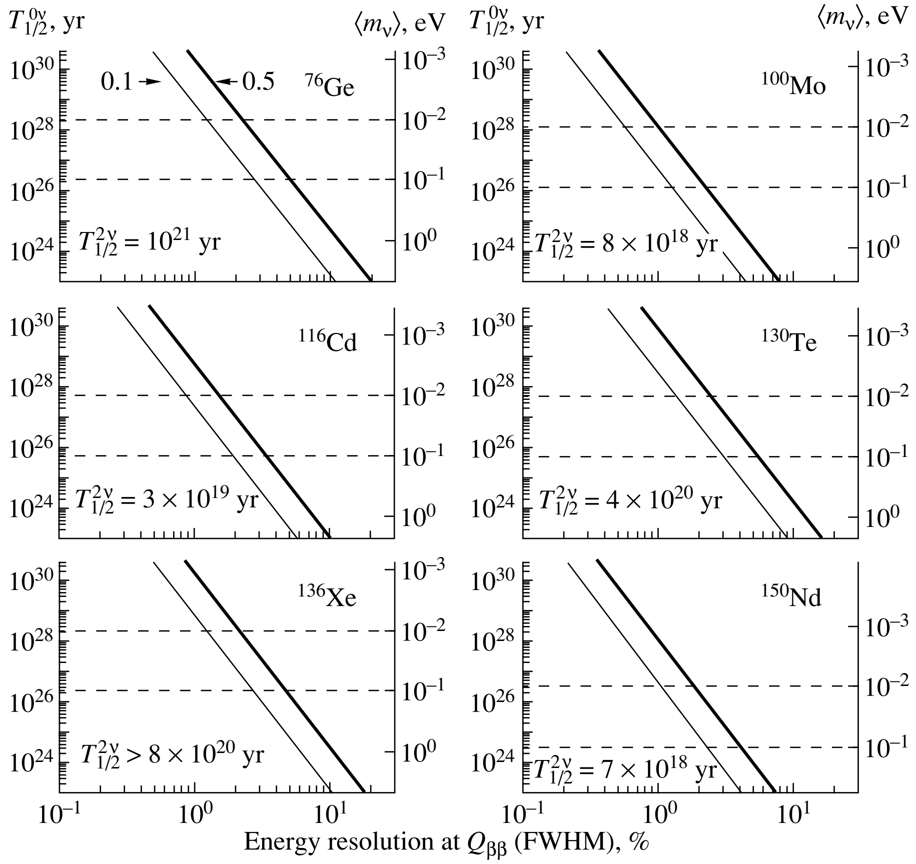

Fig. 2. The dependences of the discovery potential versus the energy resolution calculated (bold line for $h/M = 0.5$; thin line for $h/M = 0.1$) for 2β-decay candidate nuclei (^{76}Ge, ^{100}Mo, ^{116}Cd, ^{130}Te, ^{136}Xe, and ^{150}Nd). Neutrino mass scale (right) is shown in accordance with [15].

function. Then the obtained 2ν distribution for the sum of electron energies was properly convoluted with the response function of the detector, whose relative energy resolution given at $Q_{\beta\beta}$ varies as the square root of energy.

In Fig. 1*a*, the 0ν peak (with the amplitude M) and $2\nu2\beta$-decay spectrum meet at the relative height $h/M = 0.1$, and due to this, the separation of the effect is excellent. However, it seems that such a demand ($h/M = 0.1$) is too severe. At the same time, Fig. 1*c* demonstrates another extreme case (they meet at the relative height $h/M = 1$), which does not allow one to discriminate the effect at all.[3] In our opinion, the example shown in Fig. 1*b*, where the 2ν distribution and the 0ν peak meet at $h/M = 0.5$, represents the minimal requirement for recognition of the effect, which can still be reasonable in experimental practice. Therefore, if we accept the last criteria, the discovery potential of a setup with fixed energy resolution can be defined as the half-life of the $0\nu2\beta$ decay, which could be registered by satisfying this demand ($h/M = 0.5$) at a given $T_{1/2}^{2\nu}$ value. The dependences of this quantity (let us call it "the discovery potential") versus the energy resolution were determined for several 2β-decay candidate nuclei, and they are depicted in Fig. 2. Similarly, the exposures (product of detector mass and measuring time), which are needed to collect ten counts in the 0ν peak at a given $T_{1/2}^{0\nu}$ value, were calculated for each nucleus (under assumption that detection efficiency and enrichment both equal 100%), and the results are shown in Fig. 3. We will use these dependences below when discussing different projects.

In summary, on the basis of this brief analysis, we can formulate the following requirements for the future ultimate-sensitivity 2β-decay experiments:

---

[3] The discrimination of the effect and background in the case $h/M = 1$ could be, in principle, possible if (i) the theoretical shape of the $2\nu2\beta$-decay spectrum near the $Q_{\beta\beta}$ energy is known exactly; (ii) the statistics accumulated in the experiment are very high, which, however, is a great technical challenge (Fig. 3); and (iii) the contributions from the different background origins to the measured spectrum near the $Q_{\beta\beta}$ value are precisely known, which appears to be a quite unrealistic task (see discussion in [16]).

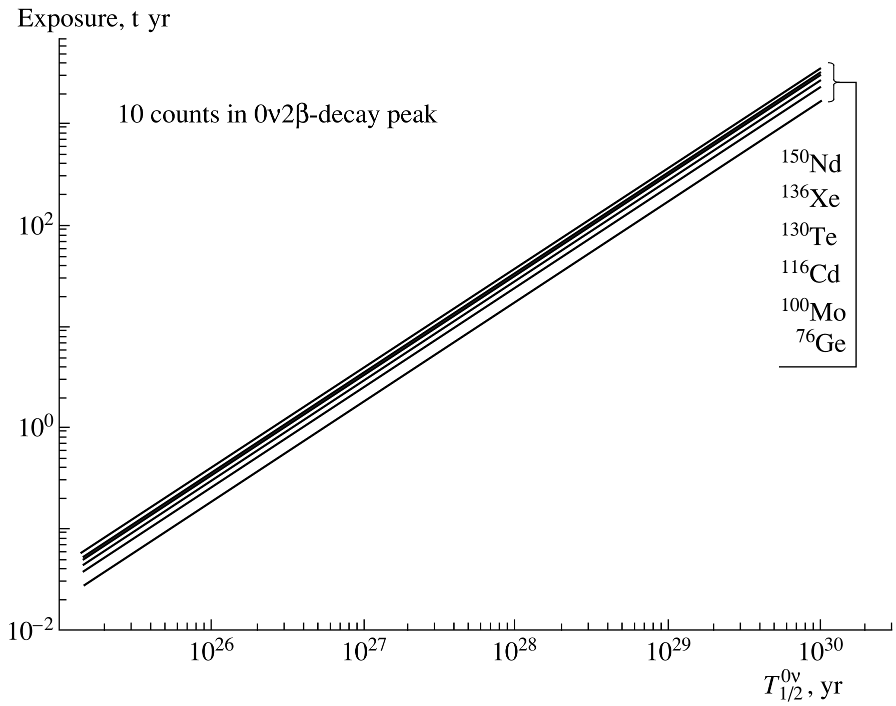

Fig. 3. The exposure (product of detector mass and measuring time) needed to collect ten counts in the 0ν peak at given $T_{1/2}^{0\nu}$ value calculated for different nuclei under the assumption that detection efficiency and enrichment both are equal to 100%.

(i) The use of highly enriched ($\delta \to 100\%$) detectors and an "active" source technique because only in this case could the total detection efficiency be close to 100%.

(ii) The energy resolution is a crucial characteristic, and its value at $Q_{\beta\beta}$ energy must correspond to the required discovery potential for a given nucleus (Fig. 2).

(iii) The exposure (mt) needed to reach a certain $T_{1/2}^{0\nu}$ value should be in accordance with Fig. 3 (20–30 t yr for $T_{1/2}^{0\nu} \approx 10^{28}$ yr).

(iv) Because of the square root dependence of the sensitivity versus source mass and measuring time, it is not enough, however, to increase the exposure alone. The background must be reduced practically to zero.

(v) The measuring time of the future experiments will be of the order of ≈ 10 yr; hence, detectors and setups should be as simple as possible to provide stable and reliable operation over such a long period.

Evidently, it could be very difficult to find the project and construct the experiment which would completely satisfy these severe requirements. However, perhaps some of the recent proposals could do it to certain extent, so let us consider them briefly.

The MOON project [30] to study the $0\nu2\beta$ decay of ^{100}Mo ($Q_{\beta\beta} = 3034$ keV) calls for the use of 34 t of natural Mo (i.e., 3.3 t of ^{100}Mo) per detector module in the form of passive foil (≈ 50 mg/cm^2). The module will be composed of ≈ 60 000 plastic scintillators (6 m × 0.2 m × 0.25 cm), the light outputs from which are collected by 866 000 wavelength shifter fibers (∅1.2 mm × 6 m), viewed through clear fibers by 6800 16-anode photomultiplier tubes (PMT). The sensitivity to the neutrino mass could be of the order of ≈ 0.05 eV [30].

The XMASS project [31] intends to use ultrapure liquid Xe scintillator with ≈ 10-t fiducial mass as a real time, low-energy solar neutrino detector. Such a detector (with ≈ 1 t of enriched ^{136}Xe) could allow a simultaneous search for the $0\nu2\beta$ decay of ^{136}Xe ($Q_{\beta\beta} = 2468$ keV) with a sensitivity to neutrino mass of ≈ 0.02 eV [32].

The DCBA project is under development in KEK (Japan) [33]. The drift chamber placed in a uniform magnetic field (0.6 kG) can measure the momentum of each β particle emitted in 2β decay and the position of the decay vertex by means of a three-dimensional reconstruction of the tracks. With 18 kg of an enriched ^{150}Nd ($Q_{\beta\beta} = 3367$ keV) passive source (50 mg/cm^2), the projected sensitivity to the Majorana neutrino mass is ≈ 0.05 eV [33].

^{160}Gd ($Q_{\beta\beta} = 1730$ keV) is an attractive candidate due to large natural abundance (21.9%), allowing one to construct a sensitive apparatus with nonenriched Gd_2SiO_5:Ce crystal scintillators (GSO). A large-scale experiment with ^{160}Gd using a GSO multicrystal array with a total mass of 1–2 t ($\approx 200-400$ kg of ^{160}Gd) is suggested with the sensitivity to the Majorana neutrino mass ≈ 0.05 eV [34].

All proposals mentioned above require a significant amount of research and development to demonstrate their feasibility. Because of this, we are going to discuss the following safer proposals, which were designed on the basis of the best performed (Table 1) or running experiments.

CUORE. The running CUORICINO setup is designed as a pilot step for a future CUORE project, which would consist of one thousand TeO_2 bolometers (with total mass of 760 kg) operating at ≈ 10 mK. The excellent energy resolution of TeO_2 bolometers (≈ 5 keV at 2.5 MeV) is a powerful tool for discriminating the 0ν signal from the background. The CUORE sensitivity is quoted by the authors for different background rate at 2.5 MeV (0.1–0.01 counts/(yr kg keV)) and would be as high as $T_{1/2}^{0\nu} \geq (0.3-4) \times 10^{26}$ yr ($m_\nu \leq 0.1-0.04$ eV) [18].

EXO. A new approach to study 2β decay of ^{136}Xe ($Q_{\beta\beta} = 2468$ keV) makes use of the coincident detection of $^{136}Ba^{2+}$ ions (the final state of the ^{136}Xe decay on the atomic level) and the $0\nu2\beta$ signal with the energy of 2.5 MeV in a time projection chamber (TPC) filled with liquid or gaseous Xe [35, 36]. The EXO project intends to use the resonance ionization spectroscopy for the identification of $^{136}Ba^{2+}$ ions in a 40-m^3 TPC (the energy resolution at 2.5 MeV is FWHM $\approx 5\%$) operated at 5–10-atm pressure of enriched xenon (≈ 1 t of ^{136}Xe). The estimated sensitivity to neutrino mass is ≈ 0.05 eV [37]. The conventional pilot TPC (no Ba ion detection) with 200 kg of enriched ^{136}Xe is under construction now.

There are three large-scale projects for the 2β-decay quest of ^{76}Ge.

MAJORANA. The idea of this proposal is to use 210 HP Ge (enriched in ^{76}Ge to $\approx 86\%$) semiconductor detectors (≈ 2.4-kg mass of a single crystal), which are contained in "conventional" superlow background cryostats [38]. The detectors are shielded by HP lead or copper. Each crystal will be supplied with six azimuthal and two axial contacts, and hence spatial information will be available for the detected events. It is anticipated that a segmentation of the crystals and a pulse-shape analysis of the data would reduce the background rate of the detectors to the level of ≈ 0.01 counts/(yr kg keV) at the energy 2 MeV. On this basis, the projected half-life limit can be determined as $T_{1/2}^{0\nu} \geq 10^{27}$ yr, and depending on the NME calculations, one expects the following neutrino mass limits: $m_\nu \leq 0.05-0.15$ eV.

GENIUS. This project intends to operate 1 t of “naked” HP Ge (enriched in ^{76}Ge to $\approx 86\%$) detectors placed in extremely high purity liquid nitrogen (LN_2), which simultaneously serves as a cooling medium and as a shielding for the detectors [39]. In accordance with Monte Carlo simulations, the necessary dimensions of the liquid nitrogen shield which could fully suppress the radioactivity from the surroundings are about 12 m in diameter and 12 m in height, and the required radioactive purity of the liquid nitrogen should be at the level of $\approx 10^{-15}$ g/g for ^{40}K and ^{238}U, $\approx 5 \times 10^{-15}$ g/g for ^{232}Th, and 0.05 mBq/m^3 for ^{222}Rn. Due to this, the total GENIUS background rate in the energy region of the 2β decay of ^{76}Ge may be reduced down to ≈ 0.2 counts/(yr keV t) [39, 40]. The projected sensitivity is estimated for a 10-yr measuring time as $T_{1/2}^{0\nu} \geq 10^{28}$ yr, i.e., a neutrino mass constraint $m_\nu \leq 0.015-0.05$ eV.

GEM. Aiming to make realization of the high-sensitivity ^{76}Ge experiment simpler, the GEM design is based on the following ideas [41]: (a) Similarly to GENIUS ≈ 400 “naked” HP Ge detectors (enriched in ^{76}Ge to 86%, mass of ≈ 2.5 kg each) will operate in ultrahigh-purity liquid nitrogen. (b) Liquid nitrogen is contained in the vacuum cryostat (made of HP copper), whose dimensions are as small as possible consistent with necessity of eliminating contributions of the radioactive contaminants in the Cu cryostat to the background of the HP Ge detectors. (c) The shield is composed of two parts: an inner shielding—ultrahigh-purity liquid nitrogen ($\approx 10^{-15}$ g/g for ^{40}K and ^{238}U, $\sim 5 \times 10^{-15}$ g/g for ^{232}Th, and 0.05 mBq/m^3 for ^{222}Rn); an outer part—high-purity water, whose volume is large enough ($\oslash 11 \times 11$ m) to suppress external background. It was proved by Monte Carlo simulations that, for such a design, the necessary LN_2 volume will be reduced substantially (≈ 40 t instead of ≈ 1000 t in GENIUS), and the GEM sensitivity is similar to that of GENIUS: $T_{1/2}^{0\nu} \geq 10^{28}$ yr ($m_\nu \leq 0.015$ eV) [41].

CAMEO. This project [42] is a further development of the pilot 2β-decay studies of ^{116}Cd performed by the Kiev–Florence collaboration in the Solotvina Underground Laboratory since 1989 [43]. Let us briefly recall their main results. Cadmium tungstate ($^{116}CdWO_4$) crystal scintillators, enriched in ^{116}Cd to 83%, have been grown for the search. Their light output (peak emission at 480 nm with decay time of ≈ 13 μs) is $\approx 30-35\%$ as compared with that of NaI(Tl). Four $^{116}CdWO_4$ crystals with a total mass of 330 g are viewed by a low-background 5 in.-PMT through one light guide 10 cm in diameter and 55 cm long. The ^{116}CdWO$_4$ crystals are surrounded by an active shield made of 15 CdWO$_4$ crystals of large volume with a total mass of 20.6 kg. These are viewed by a low-background PMT through an active plastic light guide ($\oslash 17 \times 49$ cm). The whole CdWO$_4$ array is situated within an additional active shield made of plastic scintillator $40 \times 40 \times 95$ cm; thus, together with both active light guides, a complete 4π active shield of the main (^{116}CdWO$_4$) detector is provided. The outer passive shield consists of high-purity copper (3–6 cm), lead (22.5–30 cm), and polyethylene (16 cm). Two plastic scintillators installed above the passive shield serve as cosmic muon veto. The data acquisition records the amplitude, arrival time, and pulse shape (PS) of each ^{116}CdWO$_4$ event. The PS analysis is based on an optimal digital filter and ensures clear discrimination between γ rays and α particles [44], as well as selection of "illegal" events: double pulses, signals from active light guide, etc.

Due to active and passive shields and as a result of the time-amplitude and PS analysis of the data, the background rate of the ^{116}CdWO$_4$ detector in the energy region 2.5–3.2 MeV ($Q_{\beta\beta}$ of ^{116}Cd is 2.8 MeV) is reduced to 0.04 counts/(yr kg keV). It is the lowest background rate which has ever been reached with crystal scintillators. After 14 183 h of measurements the half-life limit on the neutrinoless 2β decay of ^{116}Cd has been set as $T^{0\nu}_{1/2} \geq 1.7(2.6) \times 10^{23}$ yr at 90% (68%) C.L. The latter corresponds to a restriction on the neutrino mass of $m_\nu \leq 1.7(1.4)$ eV at 90% (68%) C.L. [10].

Substantial advancement of this bound would be possible in the case of further enhancement of sensitivity, which is the main goal of the CAMEO project. It is proposed [42] to operate ≈ 100 kg of enriched ^{116}CdWO$_4$ crystals (total number of ^{116}Cd nuclei is $\approx 1.5 \times 10^{26}$) allocated in the liquid scintillator of the BOREXINO Counting Test Facility (CTF [45]). The CTF consists of an external ≈ 1000-t water tank ($\oslash 11 \times 10$ m), which serves as a passive shield for a 4.8-m^3 liquid scintillator contained in an inner vessel, 2.1 m in diameter. The radiopurity of water is $\approx 10^{-14}$ g/g for U/Th and $\approx 10^{-10}$ g/g for K. The high-purity ($\approx 5 \times 10^{-16}$ g/g for U/Th) liquid scintillator (1.5 g/l of PPO in pseudocumene) has an attenuation length ≥ 5 m and a principal scintillator decay time of ≈ 5 ns. The inner transparent vessel made of nylon film (0.5 mm thick) allows one to collect the scintillation light with the help of 100 PMTs (8 in.) fixed on the 7-m-diameter support structure.

In the preliminary CAMEO design, 40 enriched ^{116}CdWO$_4$ crystals (≈ 2.5 kg each) are allocated in the liquid scintillator of the CTF and homogeneously distributed on a sphere with diameter 0.8 m. It is supposed that 200 PMTs with light concentrators are fixed at a diameter of 5 m, providing an optical coverage of 80%. The GEANT Monte Carlo simulation of the CdWO$_4$ scintillation light[4)] propagation in the considered geometry gives ≈ 4000 photoelectrons for a 2.8-MeV energy deposit; thus, a $0\nu2\beta$-decay peak of ^{116}Cd would be measured with an energy resolution of FWHM = 4%. The feasibility of obtaining such an energy resolution with CdWO$_4$ crystal has been successfully demonstrated by the measurements with a CdWO$_4$ crystal ($\oslash 40 \times 30$ mm) placed in transparent paraffin oil [42]. An increase in the light collection up to $\approx 42\%$ has been obtained, which leads to improvement of the CdWO$_4$ energy resolution in the whole energy region. The FWHM values (7.4% at 662 keV, 5.4% at 1173 keV, and 4.3% at 2615 keV) are similar to those for NaI(Tl) crystals and have never been reached before with CdWO$_4$ scintillators.

The background simulation for CAMEO was performed with the help of the GEANT3.21 [46] and DECAY4 [47] codes. The simulated contributions from various background sources and the response functions for 2β decay of ^{116}Cd with $T^{2\nu}_{1/2} = 2.7 \times 10^{19}$ yr and $T^{0\nu}_{1/2} = 10^{25}$ yr are depicted in Fig. 4. On this basis, the sensitivity of the CAMEO experiment can be calculated as $T^{0\nu}_{1/2} \geq 10^{26}$ yr, which translates to a neutrino mass bound of $m_\nu \leq 0.06$ eV. On the other hand, it is evident from Fig. 4 that $0\nu2\beta$ decay of ^{116}Cd with a half-life of $\approx 10^{25}$ yr would be clearly registered [42].

Moreover, these results can be advanced further by exploiting 1 t of ^{116}CdWO$_4$ detectors ($\approx 1.5 \times 10^{27}$ nuclei of ^{116}Cd) placed in one of the existing or future large underground neutrino detectors such as BOREXINO, SNO, or KamLAND. The sensitivity is estimated as $T^{0\nu}_{1/2} \geq 10^{27}$ yr ($m_\nu \leq 0.02$ eV) [42]. The proposed CAMEO technique with ^{116}CdWO$_4$ crystals is extremely simple and reliable; thus, such experiments can run stably for decades.

Now let us analyze the discovery potential of the projects reviewed by using calculated dependences of that quantity versus the energy resolution of the detector (Fig. 2) and by taking into account the energy resolutions claimed in each particular proposal. Unfortunately, the results of such an analysis are not optimistic, and one conclusion is clear: only projects with high energy resolution (GEM,

---

[4)] We recall that the CdWO$_4$ scintillator yields $\approx 1.5 \times 10^4$ emitted photons per 1 MeV of energy deposited.

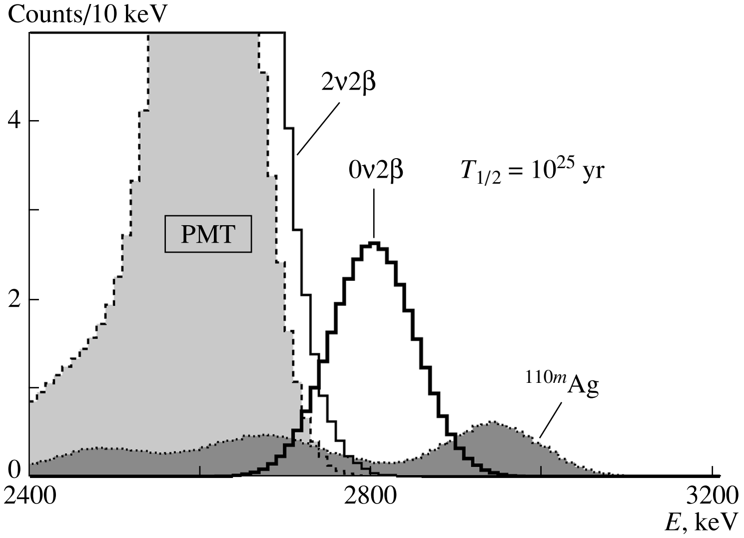

Fig. 4. The response functions of the CTF with 100 kg of ^{116}CdWO$_4$ crystals (5-yr measuring time) for $2\nu2\beta$ decay of ^{116}Cd ($T^{2\nu}_{1/2} = 2.7 \times 10^{19}$ yr) and $0\nu2\beta$ decay with $T^{0\nu}_{1/2} = 10^{25}$ yr (solid histograms). The simulated contribution from ^{208}Tl in the PMTs (dashed histogram) and from cosmogenic ^{110m}Ag in ^{116}CdWO$_4$ crystals (dotted curve).

GENIUS, MAJORANA with the HP ^{76}Ge detectors, and CUORE with ^{130}TeO$_2$ bolometers) have a chance of detecting $0\nu2\beta$ decay with the rate corresponding to neutrino mass $m_\nu \approx 0.01$ eV. As regards the CUORE, it should be noted, however, that the complexity of the cryogenic technique requires the use of a lot of different construction materials in the setup, which makes it quite difficult to reduce background to the same superlow level as that obtained in the best experiments with TPC [12], semiconductor [13, 14], and scintillation [10] detectors. Because of this, the CUORE sensitivity would be limited, and in fact, the expected results are quoted by the authors for different background rate at 2.5 MeV [18].

The discovery potential of other proposals is much more modest. For example, for the EXO (FWHM = 5% at the $Q_{\beta\beta}$ energy), it equals $T^{0\nu}_{1/2} \approx 10^{26}$ yr (i.e., $m_\nu \approx 0.15$ eV); for the MOON (FWHM = 7% at the $Q_{\beta\beta}$ energy), it is $T^{0\nu}_{1/2} \approx 2 \times 10^{23}$ yr ($m_\nu \approx 2$ eV); and for the CAMEO (FWHM = 4%), the corresponding value is $T^{0\nu}_{1/2} \approx 2 \times 10^{25}$ yr ($m_\nu \approx 0.15$ eV). Let us recall, however, that ^{116}CdWO$_4$ crystals, which will be used in the CAMEO experiment, can also work as cryogenic detectors with an energy resolution of about 10 keV [48]. Therefore, if the ^{116}CdWO$_4$ crystals produced for the CAMEO project were measured (at the next step of research) in the CUORE apparatus, the discovery potential of such an experiment would be greatly enhanced (see Fig. 2). At the same time, such a measurement would allow one to overcome the drawback of the CUORE setup associated with the background limitation. First, it is because the $Q_{\beta\beta}$ energy of ^{116}Cd (2.8 MeV) is higher than that for ^{130}Te (2.5 MeV). Secondly, as was successfully demonstrated with CaWO$_4$ crystals [49], simultaneous phonon and scintillation light detection—which is also possible with ^{116}CdWO$_4$ crystals—is a very powerful tool for additional background discrimination.

Hence, we can conclude that a challenging scientific goal to observe $0\nu2\beta$ decay with the rate corresponding to neutrino mass $m_\nu \approx 0.01$ eV could be feasible for several of the future 2β-decay experiments (namely, GEM, GENIUS, MAJORANA with HP ^{76}Ge detectors, and CUORE with ^{116}CdWO$_4$ crystals), while other projects (CAMEO, CUORE with ^{130}TeO$_2$ crystals, DCBA, EXO, ^{160}Gd, MOON, etc.) would be able to set the restrictions on the neutrino mass at the level of $m_\nu \leq 0.05$ eV.

REFERENCES

1. Y. Fukuda *et al.* (Super-Kamiokande Collab.), Phys. Rev. Lett. **86**, 5651 (2001).
2. Q. R. Ahmad *et al.* (SNO Collab.), Phys. Rev. Lett. **89**, 011301 (2002).
3. K. Eguchi *et al.* (KamLAND Collab.), Phys. Rev. Lett. **90**, 021802 (2003).
4. M. H. Ahn *et al.*, Phys. Rev. Lett. **90**, 041801 (2003).
5. J. D. Vergados, Phys. Rep. **361**, 1 (2002).
6. Yu. G. Zdesenko, Rev. Mod. Phys. **74**, 663 (2002).
7. S. R. Elliot and P. Vogel, Annu. Rev. Nucl. Part. Sci. **52**, 115 (2002).
8. J. Schechter and J. W. F. Valle, Phys. Rev. D **25**, 2951 (1982).

9. V. I. Tretyak and Yu. G. Zdesenko, At. Data Nucl. Data Tables **80**, 83 (2002).
10. F. A. Danevich *et al.*, Phys. Rev. C **62**, 045501 (2000); **68**, 035501 (2003).
11. C. Arnaboldi *et al.*, Phys. Lett. B **557**, 167 (2003).
12. R. Luescher *et al.*, Phys. Lett. B **434**, 407 (1998).
13. H. V. Klapdor-Kleingrothaus *et al.*, Eur. Phys. J. A **12**, 147 (2001).
14. C. E. Aalseth *et al.*, Phys. Rev. C **59**, 2108 (1999); Phys. Rev. D **65**, 092007 (2002).
15. A. Staudt *et al.*, Europhys. Lett. **13**, 31 (1990).
16. Yu. G. Zdesenko *et al.*, Phys. Lett. B **546**, 206 (2002).
17. L. Simard (NEMO Collab.), Nucl. Phys. B (Proc. Suppl.) **110**, 372 (2002); A.-I. Etienvre, hep-ex/0306027 (2003).
18. G. Gervasio (CUORE Collab.), Nucl. Phys. A **663&664**, 873 (2000); CUORE Collab., hep-ex/0302021 (2003).
19. A. Faessler and F. Simkovic, J. Phys. G **24**, 2139 (1998).
20. J. Suhonen and O. Civitarese, Phys. Rep. **300**, 123 (1998).
21. P. Vogel, in *Current Aspects of Neutrino Physics*, Ed. by D. O. Caldwell (Springer, Berlin, 2001), p. 177.
22. E. Fiorini *et al.*, Lett. Nuovo Cimento **3**, 149 (1970).
23. M. Doi, T. Kotani, and E. Takasugi, Prog. Theor. Phys. Suppl. **83**, 1 (1985).
24. G. Audi and A. H. Wapstra, Nucl. Phys. A **595**, 409 (1995).
25. K. J. R. Rosman and P. D. P. Taylor, Pure Appl. Chem. **70**, 217 (1998).
26. A. A. Artyukhov *et al.*, Yad. Fiz. **61**, 1336 (1998) [Phys. At. Nucl. **61**, 1236 (1998)].
27. V. I. Tretyak and Yu. G. Zdesenko, At. Data Nucl. Data Tables **61**, 43 (1995).
28. M. Doi *et al.*, Prog. Theor. Phys. **66**, 1739 (1981).
29. J. M. Blatt and V. F. Weisskopf, *Theoretical Nuclear Physics*, 7th ed. (Wiley, New York, 1963).
30. H. Ejiri *et al.*, Phys. Rev. Lett. **85**, 2917 (2000).
31. Y. Suzuki, in *Proceedings of the International Workshop on Low-Energy Solar Neutrinos, LowNu2, Tokyo, Japan, 2000*, Ed. by Y. Suzuki (World Sci., Singapore, 2001).
32. A. Sh. Georgadze *et al.*, in *Proceedings of the International Workshop on Technique and Application of Xenon Detectors, Tokyo, Japan, 2001* (World Sci., Singapore, 2002), p. 144.
33. N. Ishihara *et al.*, Nucl. Instrum. Methods Phys. Res. A **373**, 325 (1996); **443**, 101 (2000).
34. F. A. Danevich *et al.*, Nucl. Phys. A **694**, 375 (2001).
35. M. K. Moe, Phys. Rev. C **44**, 931 (1991).
36. M. Miyajima *et al.*, KEK Proc. **91** (5), 19 (1991).
37. M. Danilov *et al.*, Phys. Lett. B **480**, 12 (2000).
38. C. E. Aalseth *et al.*, hep-ex/0201021; C. E. Aalseth and H. S. Miley, Nucl. Phys. B (Proc. Suppl.) **110**, 392 (2002).
39. H. V. Klapdor-Kleingrothaus *et al.*, J. Phys. G **24**, 483 (1998).
40. O. A. Ponkratenko, V. I. Tretyak, and Yu. G. Zdesenko, in *Proceedings of the International Conference on Dark Matter in Astro- and Particle Physics, Heidelberg, Germany, 1998*, Ed. by H. V. Klapdor-Kleingrothaus and L. Baudis (IOP, Bristol, 1999), p. 738.
41. Yu. G. Zdesenko *et al.*, J. Phys. G **27**, 2129 (2001).
42. G. Bellini *et al.*, Phys. Lett. B **493**, 216 (2000).
43. F. A. Danevich *et al.*, Pis'ma Zh. Éksp. Teor. Fiz. **76**, 417 (1989) [JETP Lett. **49**, 476 (1989)].
44. T. Fazzini *et al.*, Nucl. Instrum. Methods Phys. Res. A **410**, 213 (1998).
45. G. Alimonti *et al.*, Nucl. Instrum. Methods Phys. Res. A **406**, 411 (1998).
46. R. Brun *et al.*, *CERN Program Library Long Write-up W5013* (CERN, 1994).
47. O. A. Ponkratenko *et al.*, Phys. At. Nucl. **63**, 1282 (2000).
48. A. Alessandrello *et al.*, Nucl. Phys. B (Proc. Suppl.) **35**, 394 (1994).
49. S. Cebrian *et al.*, Phys. Lett. B **563**, 48 (2003).

Physics of Atomic Nuclei, Vol. 67, No. 11, 2004, pp. 1984–1988. From Yadernaya Fizika, Vol. 67, No. 11, 2004, pp. 2008–2012.

The Extrapolation of NEMO Techniques to Future Generation 2β-Decay Experiments*

A. S. Barabash**
(and the NEMO Collaboration)
Institute of Theoretical and Experimental Physics, Moscow, Russia
Received December 4, 2003

Abstract—The possibilities of using NEMO techniques for future neutrinoless double-beta decay experiments are discussed. The main idea is to have a realistic program with planned sensitivity for half-life measurement on the level of $\sim(1.5-2)\times 10^{26}$ yr (sensitivity to neutrino mass $\sim$0.04–0.1 eV). It is argued that this can be achieved using the improved NEMO technique to study 100 kg of ^{82}Se. A possible scheme for a future SUPERNEMO detector and its main characteristics are presented. Such a detector can also be used to investigate $0\nu\beta\beta$ decay in ^{100}Mo, ^{130}Te, and ^{116}Cd with a sensitivity of up to $\sim(2-5)\times 10^{25}$ yr or with a sensitivity to neutrino mass of $\sim$0.04–0.26 eV. © *2004 MAIK "Nauka/Interperiodica"*.

1. INTRODUCTION

The main goal of the NEMO-3 experiment is to study the neutrinoless double-beta decay ($0\nu\beta\beta$) of ^{100}Mo with a sensitivity of $\sim 10^{25}$ yr, which corresponds the sensitivity for the effective neutrino mass $\langle m_\nu\rangle$ of the order of 0.1–0.3 eV. In 1988, the NEMO collaboration started an R&D program in order to develop a detector to study $0\nu\beta\beta$ decay with such a sensitivity. Two prototypes, NEMO-1 [1] and NEMO-2 [2] have proven the feasibility of this approach and have contributed to background studies for the NEMO-3 project [3]. The NEMO-2 detector made measurements of the half-lives of the allowed double-beta decay ($2\nu\beta\beta$) of ^{100}Mo [4], ^{116}Cd [5], ^{82}Se [6], and ^{96}Zr [7]. The NEMO-3 detector is now operating in the Frejus Underground Laboratory (4800 m w.e.), and the first results were presented at the NDM'03 Symposium by V. Vasiliev and H. Ohsumi. In this paper we investigate the possibilities for NEMO techniques in future, more sensitive neutrinoless double-beta decay experiments.

2. BRIEF DESCRIPTION OF NEMO-2 AND NEMO-3

We present a brief description of NEMO-2 and NEMO-3, because for the future NEMO-4 or SUPERNEMO detector we will use similar techniques. For definiteness, we shall use SUPERNEMO as the name of the detector. The concept of SUPERNEMO was first presented in [8].

2.1. NEMO-2

The NEMO-2 [2] consists of a 1-m^3 tracking volume filled with helium gas and 4% ethyl alcohol at atmosphere pressure (Fig. 1). Vertically bisecting the detector is a planar source foil (1×1 m). The tracking portion of the detector was made of open Geiger cells with octagonal cross sections constructed with 100-μm nickel wires. On each side of the source there are 10 planes of 32 cells which alternate between vertical and horizontal orientations. The cells provide three-dimensional track reconstruction of charged particles by recording the drift time and two plasma propagation times in each cell. A calorimeter made of scintillator blocks covers two opposing vertical sides of the tracking volume. Two configurations of the calorimeter were implemented. The first one consisted of two planes of 64 scintillators ($12\times 12\times 2.25$ cm) associated with "standard" photomultiplier tubes (PMTs). This configuration was used in the experiment with ^{100}Mo. The other configuration consisted of two planes of 25 scintillators ($19\times 19\times 10$ cm) with PMTs made with low-radioactive glass. The tracking volume and scintillators were surrounded by a lead (5 cm) and iron (20 cm) shield. The performance and operating parameters were as follows: the threshold for the scintillators was set at 50 keV, the energy resolution (FWHM) was 18% at 1 MeV, and the time resolution was 275 ps for a 1 MeV electron (550 ps at 0.2 MeV).

The NEMO-2 detector operated in the Frejus Underground Laboratory (4800 m w.e.) from 1991 to 1997. During this period $\beta\beta$-decay processes for ^{100}Mo, ^{116}Cd, ^{82}Se, ^{96}Zr, and ^{94}Zr were investigated.

---

*This article was submitted by the author in English.

**e-mail: `Alexander.Barabash@itep.ru`

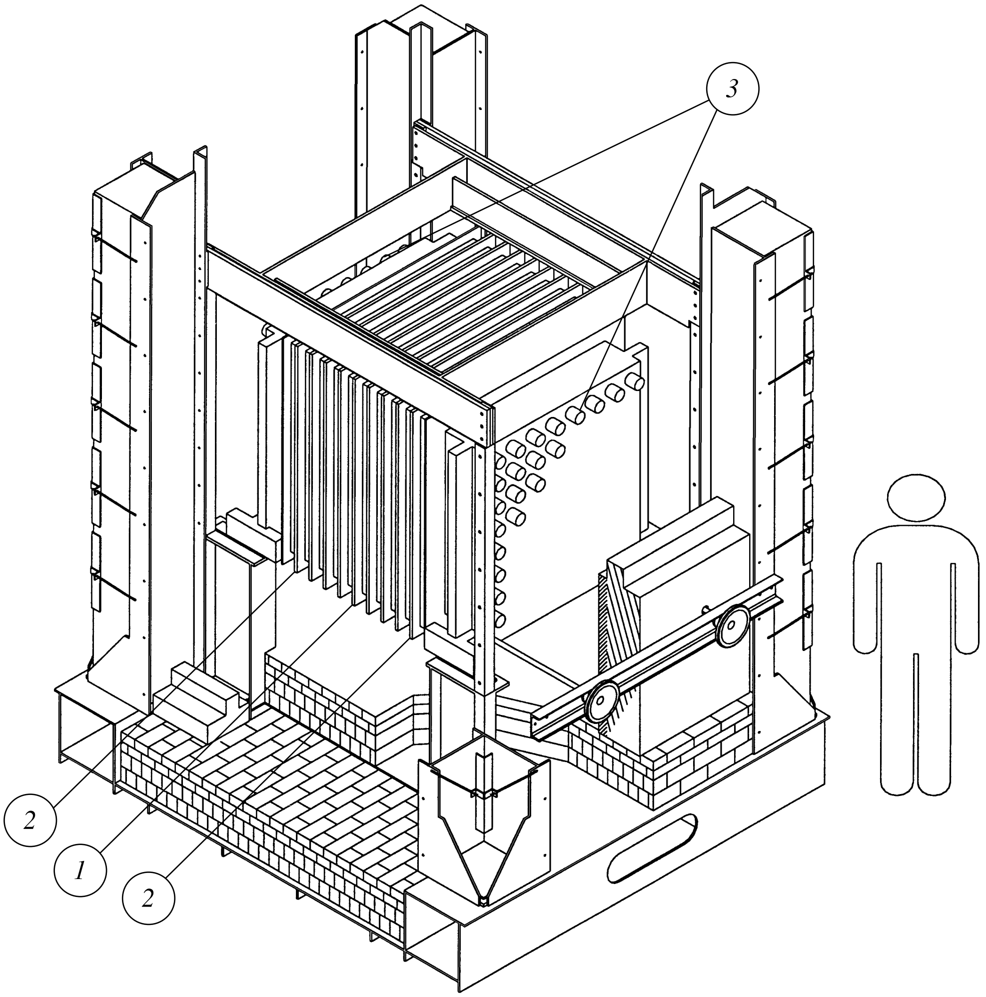

Fig. 1. The NEMO-2 detector. *1*—Central frame with the metallic foil; *2*—tracking device of 10 frames with 2 × 32 Geiger cells each; *3*—scintillator array. (The shielding is not shown.)

Half-life values for $2\nu\beta\beta$-decay and half-life limits on $0\nu\beta\beta$, $0\nu\beta\beta\chi^0$, and the $0\nu\beta\beta$ transition to the 2^+ and 0^+ excited states have also been extracted from the data [4–7, 9].

2.2. NEMO-3

The NEMO experiment [3] uses a tracking detector which is not only able to measure the full energy released but also other parameters of the process such as the single electron energy, the angle between the electrons, and the coordinates of the event vertex. The optimal operating parameters of the detector were determined with the prototype NEMO-2 [2, 4–7]. Currently, the NEMO-3 detector is operating and accommodates 10 kg of various double beta decay candidates (^{100}Mo, ^{116}Cd, ^{82}Se, ^{130}Te, ^{96}Zr, ^{150}Nd, and ^{48}Ca). The sensitivity of the detector after 5 yr of measurement will be at a level of 10^{25} yr for $0\nu\beta\beta$ decay ($\langle m_\nu \rangle \sim 0.1$–$0.3$ eV), $\sim 10^{23}$ yr for $0\nu\beta\beta\chi^0$ decay ($\langle g_{ee} \rangle \sim 10^{-5}$) and, finally, $\sim 10^{22}$ yr for $2\nu\beta\beta$ decay.

A view of the detector's cylindrically symmetric geometry is shown in Fig. 2. The detector consists of a tracking volume filled with helium gas and a thin (~ 50 μm) source foil that divides the tracking volume vertically into two concentric cylinders with a calorimeter at the inner and outer walls. The tracking system consists of 6180 2.7 m long Geiger cells which are parallel to the detector's vertical axis. The accuracy for the vertex reconstruction is on the level of 1 cm (1σ). Energy and time-of-flight measurements are performed by the plastic scintillators covering the two concentric surfaces discussed above and their associated end caps (top and bottom of the detector). The total number of low-radioactive photomultipliers is 1940. At 1 MeV, the energy resolution, which depends on the scintillator shape and the associated PMT, ranges from 13 to 17% (FWHM) and the time resolution is 250 ps (1σ). The detection threshold is

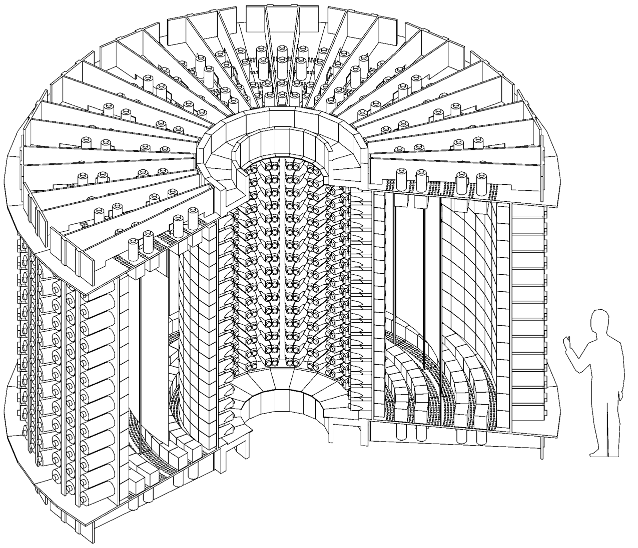

Fig. 2. Schematic view of the NEMO-3 detector.

30 keV. A magnetic field (~25 G) is used to reject backgrounds connected with pair creation and incoming electrons. External shielding, made of 20 cm thick low-radioactivity iron, covers the detector in order to reduce γ-ray and thermal-neutron external backgrounds coming from the LMS laboratory cave. Water tanks on the side walls and wood on the top and bottom of the detector thermalize fast neutrons and constitute the neutron shield. In June 2002, all 20 sectors of the NEMO-3 detector and its magnetic field coil and the iron shield were installed. The detector began to take its first data, which allowed a preliminary analysis of $0\nu\beta\beta$, $2\nu\beta\beta$ and starting a background study. In the beginning of 2003, the final tuning of the detector, the laser system, and the neutron shielding construction were finished, and from February 14, the detector started taking data with stable conditions.

Presently, the detector is operating with 6.9 kg of ^{100}Mo, 0.93 kg of ^{82}Se, 0.45 kg of ^{116}Cd, 0.45 kg of ^{130}Te, 37 g of ^{150}Nd, 9.4 g of ^{96}Zr, 7 g of ^{48}Ca and with some sectors filled with foils especially designed to check for backgrounds (0.6 kg of Cu and 0.6 kg of $^{\rm nat}$TeO$_2$). The first results obtained with NEMO-3 are presented in [10].

3. SUPERNEMO—THE NEXT GENERATION OF EXPERIMENT USING THE NEMO TECHNIQUES

3.1. Main Ideas

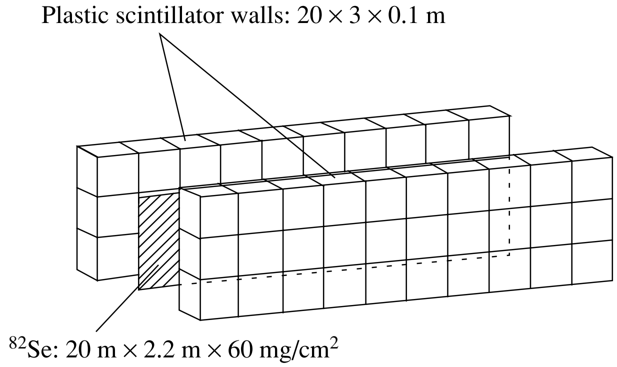

Fig. 3. The scheme of one SUPERNEMO module.

(a) The main goal is to propose a realistic project, which can be achieved within a reasonable time scale. This is the motivation for using (i) the very well-known NEMO technique and (ii) only a 100 kg source, which can be produced in a few years in Russia.

(b) The next idea is to select the isotope for which maximal sensitivity can be reached, and, to this end, we propose 100 kg of ^{82}Se, because of the high energy of the $0\nu\beta\beta$ transition ($E_{2\beta} = 3$ MeV) and the rather low probability of 2ν decay, which makes a small contribution to the 0ν region. In addition, ^{82}Se can be produced using the centrifuge method. This is why we hope to produce 100 kg quite easily and with a reasonable cost.

(c) Finally, we propose a modular scheme for the new detector. Four identical modules with 25 kg of enriched source in each. This would make it possible to start taking data quite soon (before finishing the entire construction).

A scheme for one module of the detector is shown in Fig. 3. The module consists of two plastic scintillator counter walls with the source between them. On each side of the source, there are a few layers of Geiger cells. As in NEMO-2 and NEMO-3, the electron energy will be measured by plastic scintillator counters and tracks will be reconstructed using information from the Geiger cells. The new installation might be located at the Frejus Underground Laboratory (4800 m w.e.) or at some other underground laboratory (such as Gran Sasso, for example).

3.2. The Main Parameters of the Installation

The main parameters of the installation are the following:

(i) 100-kg source of ^{82}Se;

(ii) planar geometry (four modules);

(iii) weight of plastic scintillator, 50 t;

(iv) ~ 5000 low-background PMTs (for 30 × 30 × 10 cm plastic scintillators);

(v) ~ 30 000 Geiger cells;

(vi) passive shielding of 20 cm Fe and 20 cm borated polyethylene.

The best present limits at 90% C.L. on $0\nu\beta\beta$ decay for ^{82}Se, ^{100}Mo, ^{116}Cd, ^{130}Te and the expected sensitivity of NEMO-3 and SUPERNEMO

^{82}Se	^{100}Mo	^{116}Cd	^{130}Te	$\langle m_\nu \rangle$, eV
The best present limits				
$>1.4 \times 10^{22}$ yr [12]	$>5.5 \times 10^{22}$ yr [13]	$>7 \times 10^{22}$ yr [14]	$> 2.1 \times 10^{23}$ yr [15]	<1.2–12
NEMO-3				
$\sim 2 \times 10^{25}$ yr	$\sim(5$–$8) \times 10^{24}$ yr	$\sim 4 \times 10^{24}$ yr	$\sim 1 \times 10^{24}$ yr	~ 0.1–1.2
SUPERNEMO				
$\sim(1.8$–$2) \times 10^{26}$ yr	$\sim 5 \times 10^{25}$ yr	$\sim 4.6 \times 10^{25}$ yr	$\sim 2 \times 10^{25}$ yr	~ 0.04–0.26

Note: The last column shows the best present limits on the effective neutrino mass $\langle m_\nu \rangle$ and the sensitivity to $\langle m_\nu \rangle$ of the NEMO-3 and SUPERNEMO experiments (nuclear matrix element values from [16–18] and [19] were used).

The planar geometry simplifies the construction and makes it possible to use standard blocks and components. Notice that the number of PMTs is only higher by a factor of 2.5 than for NEMO-3 and the number of Geiger cells is only higher by a factor of 5, which leads to the observation that one module of SUPERNEMO will be even simpler than the NEMO-3 detector.

3.3. Characteristics of the Detector

The main characteristics of the detector are the following:

(i) energy resolution of 10–12% (FWHM) at 1 MeV;

(ii) time resolution of 250 ps at 1 MeV;

(iii) vertex resolution of 1 cm (1σ);

(iv) efficiency (0ν decay) of $\sim$ 20%;

(v) purity of ^{82}Se is <0.05 mBq/kg for ^{214}Bi and <0.005 mBq/kg for ^{208}Tl.

One can see that the main characteristics of SUPERNEMO are approximately the same as for NEMO-3. However, with SUPERNEMO, we hope to obtain better energy resolution (10–12% instead of 13–17% in NEMO-3) and higher efficiency (20% instead of 12%) and we are confident that these requirements can be realized. The reasons for this is that during production of the plastic scintillator counters for NEMO-3 many counters already had an intrinsic resolution of $\sim$ 10–12%. Furthermore, an improved selection efficiency can be achieved as a result of some improvements (no magnetic field, better geometry, decreasing the number of wires in the tracking volume, decreasing the diameter of the wires, and improved selection of events).

3.4. Sensitivity of the Experiment

3.4.1. External background. The external background of the NEMO-3 detector was estimated in [11]. One can extrapolate these results to SUPERNEMO and demonstrate that the external background in the energy interval 2.8–3.2 MeV after 5 yr of measurement will be smaller than one event in the case of ^{100}Mo and ^{82}Se. For ^{116}Cd and ^{130}Te the background was estimated as $\sim$10 and $\sim$100 events, respectively.

3.4.2. Internal background. There are two contributions to the internal background. The first is the radioactive impurities inside the source, and the second is the tail of the $2\nu\beta\beta$ decay. On the basis of experience that we now have, we believe that it is possible to reach the SUPERNEMO requirements for the purity of the source and reach a level of zero event contribution to the background. Thus, the main internal background is associated with the tail of the $2\nu\beta\beta$ decay. This contribution was estimated using the expected parameters of SUPERNEMO for the four most prospective isotopes ^{82}Se, ^{100}Mo, ^{116}Cd, and ^{130}Te. The results are $\sim$1–2, $\sim$20, $\sim$5, and $\sim$0 background events, respectively.

3.4.3. Expected sensitivity. Using the background and efficiency estimates, one can expect a sensitivity of measurements for the identified isotopes (see table). The expected sensitivity is calculated for 100 kg of enriched sources and for 5 yr of measurement. All of the isotopes mentioned above can be produced in such quantities using the centrifuge method in Russia over a reasonable time. In the case of ^{130}Te, even natural Te ($\sim$ 34% of ^{130}Te) can be used. The estimated sensitivity of SUPERNEMO with a natural Te source is $\sim 7 \times 10^{24}$ yr (the sensitivity to neutrino mass is $\sim$0.2–0.5 eV). Of course, other prospective isotopes (for example, ^{150}Nd, ^{96}Zr, and ^{48}Ca) could also be investigated. The main problem is the difficulty in producing 100 kg of such isotopes at the present time.

4. CONCLUSION

The NEMO techniques can be extended to a larger SUPERNEMO detector with 100 kg of ^{82}Se. The expected sensitivity for 5 yr of measurement is estimated at $\sim(1.5-2) \times 10^{26}$ yr, which corresponds to a sensitivity in $\langle m_\nu \rangle$ at the level of $\sim$0.04–0.1 eV. The same detector can be used to investigate $0\nu\beta\beta$ decay for other prospective nuclei (^{100}Mo, ^{116}Cd, and ^{130}Te) with a sensitivity of $\sim(2-5) \times 10^{25}$ yr.

The data from the NEMO-3 experiment will give information about the external and internal backgrounds, the efficiency for 0ν and 2ν decays, and the effect of a magnetic field. We expect to start work on the proposal for SUPERNEMO very soon.

ACKNOWLEDGMENTS

Part of this work was carried out with the support of INTAS (grant no. 00-00362).

REFERENCES

1. D. Dassie *et al.*, Nucl. Instrum. Methods Phys. Res. A **309**, 465 (1991).
2. R. Arnold *et al.*, Nucl. Instrum. Methods Phys. Res. A **354**, 338 (1995).
3. NEMO Collab., Preprint No. 94-29, LAL (1994).
4. D. Dassie *et al.*, Phys. Rev. D **51**, 2090 (1995).
5. R. Arnold *et al.*, Z. Phys. C **72**, 239 (1996).
6. R. Arnold *et al.*, Nucl. Phys. A **636**, 209 (1998).
7. R. Arnold *et al.*, Nucl. Phys. A **658**, 299 (1999).
8. A. S. Barabash *et al.*, Czech. J. Phys. **52**, 575 (2002).
9. R. Arnold *et al.*, Nucl. Phys. A **678**, 341 (2000).
10. V. Vasilyev *et al.*, in *Proceedings of the Symposium on Neutrino and Dark Matter in Nuclear Physics, Nara, Japan, 2003.*
11. Ch. Marquet *et al.*, Nucl. Instrum. Methods Phys. Res. A **457**, 487 (2001).
12. S. R. Elliot *et al.*, Phys. Rev. C **46**, 1535 (1992).
13. H. Ejiri *et al.*, Phys. Rev. C **63**, 065501 (2001).
14. F. A. Danevich *et al.*, Phys. Rev. C **62**, 045501 (2000).
15. A. Alessandrello *et al.*, Phys. Lett. B **486**, 13 (2000).
16. J. Suhonen and O. Civitarese, Phys. Rev. C **49**, 3055 (1994).
17. M. Aunola and J. Suhonen, Nucl. Phys. A **643**, 207 (1998).
18. F. Simkovic *et al.*, Phys. Rev. C **60**, 055502 (1999).
19. S. Stoica and H. V. Klapdor-Kleingrothaus, Nucl. Phys. A **694**, 269 (2001).

Physics of Atomic Nuclei, Vol. 67, No. 11, 2004, pp. 1989–1994. From Yadernaya Fizika, Vol. 67, No. 11, 2004, pp. 2013–2017.
Original English Text Copyright © 2004 by Anisimovsky, Ivashkin, Kudenko.

DOUBLE-BETA DECAY AND RARE PROCESSES

New Search for T Violation in the Decays of the Charged Kaon[*]

V. V. Anisimovsky[**], **A. P. Ivashkin, and Yu. G. Kudenko**
(for the KEK–PS E246 Collaboration)
Institute for Nuclear Research, Russian Academy of Sciences, Moscow, Russia

Received December 4, 2003

Abstract—We report the results of the measurement of T-violating transverse muon polarization in the decays $K^+ \to \mu^+\nu_\mu\pi^0$ ($K_{\mu3}$) and $K^+ \to \mu^+\nu_\mu\gamma$ ($K_{\mu2\gamma}$) performed in experiment E246 at KEK. The preliminary results obtained for the entire data set taken in the period 1996–2000 are consistent with no T violation in both decays. © *2004 MAIK "Nauka/Interperiodica".*

1. INTRODUCTION

The purpose of the E246 experiment is to measure the transverse component of the muon polarization in the decay $K^+ \to \mu^+\nu_\mu\pi^0$ ($K_{\mu3}$). We were also able to extract $K^+ \to \mu^+\nu_\mu\gamma$ ($K_{\mu2\gamma}$) decay as a by-product. The transverse muon polarization is a T-odd observable defined as $P_T = \mathbf{s}_\mu \cdot (\mathbf{p}_{\pi(\gamma)} \times \mathbf{p}_\mu)/|\mathbf{p}_{\pi(\gamma)} \times \mathbf{p}_\mu|$, where $\mathbf{p}_\pi$ is used for $K_{\mu3}$ and $\mathbf{p}_\gamma$ for $K_{\mu2\gamma}$, respectively.

In the framework of the phenomenological consideration, the transverse muon polarization can be related to the $K_{\mu3}$ and $K_{\mu2\gamma}$ form factors. For $K_{\mu3}$ the T-violating polarization is proportional to the imaginary part of the ratio of $K_{\mu3}$ form factors: $P_T \propto m_\mu m_K \mathrm{Im}(\xi)$, where $\xi = f^-/f^+$ and f^+, f^- are defined through

$$M_{K_{\mu3}} \sim G_\mathrm{F} \sin\theta_\mathrm{C} \Big[f^+(q^2)(p_K^\lambda + p_\pi^\lambda) + f^-(q^2)(p_K^\lambda - p_\pi^\lambda) \Big] \left[\bar{u}_\mu \gamma_\lambda (1-\gamma_5) u_\nu \right].$$

The standard model (SM) predicts a vanishing value of less than 10^{-7} for P_T in $K_{\mu3}$ [1]. The calculations of P_T due to the electromagnetic final-state interactions result in a value of less than 10^{-5} [2]. There are several nonstandard models predicting a sizeable value for P_T: multi-Higgs models, SUSY with squarks mixing, SUSY with R-parity violation, leptoquark models [3, 4]. The values predicted in these models vary from 4×10^{-4} to 10^{-2}.

In the case of $K_{\mu2\gamma}$, the transverse polarization is related to the decay form factors in a more complicated way: $P_T(x,y) = \sigma_V(x,y)\mathrm{Im}(\Delta_V + \Delta_A) + [\sigma_V(x,y) - \sigma_A(x,y)]\mathrm{Im}(\Delta_P)$, where $\sigma_V(x,y)$ and $\sigma_V(x,y) - \sigma_A(x,y)$ are the functions of the $K_{\mu2\gamma}$ kinematic parameters (shown in Fig. 1) and $\Delta_{V,A,P}$ are the contributions of nonstandard interactions to the effective form factors [5]. Although the SM prediction for P_T in $K_{\mu2\gamma}$ is as small as for $K_{\mu3}$ [1], the contribution of the final-state interaction to this value is $\leq 10^{-3}$ [6], i.e., considerably larger than in the case of $K_{\mu3}$ decay. The predictions for nonzero P_T for $K_{\mu2\gamma}$ come from the same nonstandard models mentioned for $K_{\mu3}$ and also from left–right symmetric models [4, 5, 7]. The expected values vary from 3×10^{-3} to 10^{-2}.

A noteworthy peculiarity of these predictions obtained in different models is the correlations between the expected values of P_T for $K_{\mu3}$ and $K_{\mu2\gamma}$ [3, 4, 7]: in the three-Higgs doublet model the P_T expectations are related as $P_T(K_{\mu3}) \sim 2P_T(K_{\mu2\gamma})$; in SUSY with squarks mixing, the relation for P_T induced by Higgs exchange is $P_T(K_{\mu3}) \sim -2P_T(K_{\mu2\gamma})$, while for P_T arising from W-boson exchange $P_T(K_{\mu3}) \sim 0$, $P_T(K_{\mu2\gamma}) \neq 0$; in SUSY with R-parity violation, the relation is $P_T(K_{\mu3}) \sim P_T(K_{\mu2\gamma})$; in left–right symmetric models we have $P_T(K_{\mu3}) = 0$, $P_T(K_{\mu2\gamma}) \neq 0$.

The previous experimental results for $K_{\mu3}$ came from the BNL experiment, which used kaon decays in flight [8]: $P_T = (-3.1 \pm 5.3) \times 10^{-3}$, $\mathrm{Im}(\xi) = (-1.6 \pm 2.5) \times 10^{-2}$ as well as from E246 [9]: the result obtained for the data collected during the 1996–1997 period was $P_T = (-4.2 \pm 4.9(\mathrm{stat.}) \pm 0.9(\mathrm{syst.})) \times 10^{-3}$, $\mathrm{Im}(\xi) = (-1.3 \pm 1.6(\mathrm{stat.}) \pm 0.3(\mathrm{syst.})) \times 10^{-2}$. Both results indicated no T violation in $K_{\mu3}$. For $K_{\mu2\gamma}$, there has been no P_T measurement, so our result is the first one.

---

[*] This article was submitted by the authors in English.

[**] e-mail: `valera@al20.inr.troitsk.ru`

1063-7788/04/6711-1989$26.00 © 2004 MAIK "Nauka/Interperiodica"

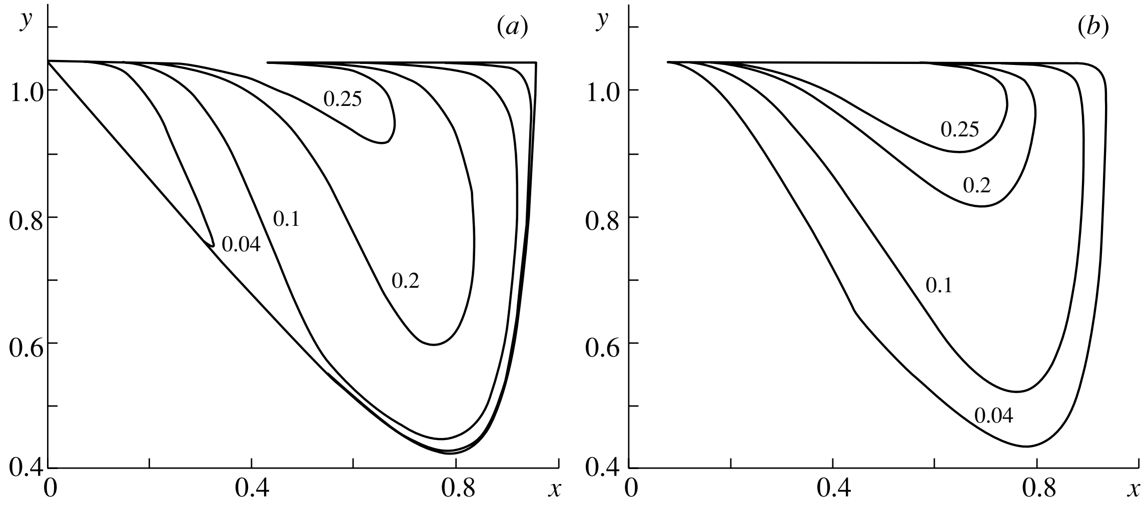

Fig. 1. The contour lines of $[\sigma_V(x,y)]$ (a) and $[\sigma_V(x,y)-\sigma_A(x,y)]$ (b) over the Dalitz plot. The standard $K_{\mu 2\gamma}$ kinematic variables are $x=2E_\gamma/m_K$ and $y=2E_\mu/m_K$.

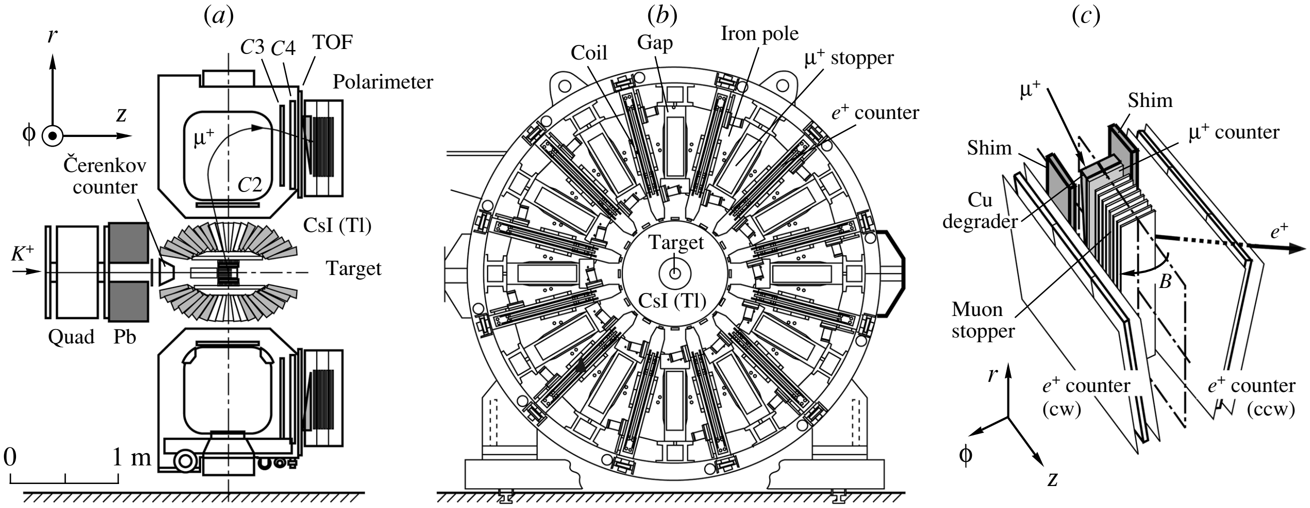

Fig. 2. The layout of the E246 detector: (a) side view, (b) end view, and (c) one sector of the polarimeter.

2. EXPERIMENT

The E246 apparatus is shown in Fig. 2 and described in detail elsewhere [10]. Kaons with $P_{K^+} = 660$ MeV/c are identified by a Čerenkov counter, slowed in an $\mathrm{Al}+\mathrm{BeO}$ degrader and then stopped in a target array of 256 scintillating fibers located at the center of a 12-sector superconducting toroidal spectrometer. Charged particles from kaon decays in the target were tracked by means of multi-wire proportional chambers at the entrance ($C2$) and exit ($C3$ and $C4$) of each magnet sector along with the target and a scintillation ring hodoscope around the target. The momentum resolution of $\sigma_p = 2.6$ MeV/c at $p = 205$ MeV/c was obtained using monoenergetic products from the two-body decay $K^+ \to \pi^+\pi^0$ ($K_{\pi 2}$). The energies and angles of the photons from π^0 decays were measured by a CsI(Tl) photon detector consisting of 768 modules. The photon detector covers a solid angle of 3π steradian, with openings for the beam entry and exit and 12 holes for charged particles to pass into the magnet gaps. To suppress accidental background from the beam, timing information from each crystal was used. A good time resolution of 3.5 ns (rms) at 100 MeV was achieved. Energy resolution of $\sigma_E/E = 2.7\%$ at 200 MeV, angular resolutions of $\sigma_\theta = 2.3°$, and an invariant mass resolution of $\sigma_{\gamma\gamma} = 9$ MeV/c^2 were obtained. Muons entering the polarimeter (Fig. 2c) were degraded by an $\mathrm{Al}+\mathrm{Cu}$ block and stopped in a stack of pure Al plates. Positrons from $\mu^+ \to e^+\nu\bar{\nu}$ decays of stopped muons were detected by positron counters, which were located azimuthally between the muon stoppers. The trigger included the signals from Čerenkov, target, TOF, and positron counters along with requiring at least one hit in the CsI(Tl) calorimeter.

The T-violating asymmetry was extracted using a double ratio:

$$A_T = \frac{1}{4}\left[\frac{(N_{\text{cw}}/N_{\text{ccw}})_{\text{fwd}}}{(N_{\text{cw}}/N_{\text{ccw}})_{\text{bwd}}} - 1\right].$$

Here, N_{cw} and N_{ccw} are the sums over all 12 sectors of the counts of clockwise (cw) and counterclockwise (ccw) emitted positrons and fwd and bwd denote events with the photon (or π^0) going forward or backward with respect to the beam direction. The sign of A_T for forward events is opposite to that for backward events, which allows us to employ a double ratio method, which reduces most systematic errors and enhances the effect. Moreover, considerable reduction of systematic effects was achieved due to the azimuthal symmetry of the 12-sector detector.

The value of P_T is related to A_T by

$$P_T = \frac{A_T}{\alpha f(1-\beta)},$$

where α is the analyzing power of the polarimeter, f is an angular attenuation factor, and β is the overall fraction of backgrounds.

3. ANALYSIS

The extraction and analysis of $K_{\mu 3}$ and $K_{\mu 2\gamma}$ events comprised several procedures common for both decays. The common stage included target analysis, charged particle tracking and TOF analysis, and the analysis of muon decay in the polarimeter. The active target analysis included target energy deposition and target timing cuts to get rid of kaon decays in-flight. The momentum of a charged particle reconstructed by a four-point tracking procedure was used to suppress $K_{\mu 2}$ and $K_{\pi 2}$ decays by selecting events with $p < 190$ MeV/c. The cut on χ^2 for the charged particle track was used to suppress $K_{\pi 2}$ decays with π^+ decay in flight. To separate muons and positrons (thereby suppressing K_{e3}) we used TOF technique to calculate the charged particle mass, and then, on the scatter plot of the TOF energy deposition versus the TOF-reconstructed mass square, we separated the muon cloud from the positron one. Finally, the common stage included the signal extraction from the positron time spectra in the polarimeter.

The second stage of event selection was specific for each decay mode. For $K_{\mu 3}$, we selected one-photon events with $E_\gamma > 70$ MeV and two-photon events that satisfy the constraints on the invariant mass of the two photons and on the missing mass (the reconstructed mass of the missing neutrino): $\sim 70 < M_{\gamma\gamma} <\sim 180$ MeV/c^2 and $-25\,000 < M^2_{\text{miss}} < 20\,000$ MeV$^2/c^4$. Additionally, we used the cuts on the opening angles between two photons and between muon and π^0 ($\Theta_{\gamma\gamma} > 60°$ and $\Theta_{\mu\pi} < 160°$) to suppress kaon decays in-flight and $K_{\pi 2}$.

The second stage for $K_{\mu 2\gamma}$ selected one-photon events with $E_\gamma > 50$ MeV and comprised three major cuts: a constraint on the neutrino missing mass $-0.7 \times 10^4 < M^2_{\text{miss}} < 1.5 \times 10^4$ MeV$^2/c^4$, a cut on the neutrino momentum $p_\nu > 200$ MeV/c, and a cut on the opening angle between muon and photon $\Theta_{\mu\gamma} < 90°$. These cuts suppressed the $K_{\mu 3}$ by a factor of 70, while sustaining a $K_{\mu 2\gamma}$ loss by a factor of 2. Figure 3 shows the spectra of M^2_{miss} and p_ν for both Monte Carlo (MC) ($K_{\mu 3}$ and $K_{\mu 2\gamma}$) and experimental data.

The background fractions for extracted $K_{\mu 3}$ and $K_{\mu 2\gamma}$ events were estimated using experimental spectra along with the MC simulation data. For $K_{\mu 3}$ the major background contributions come from CsI(Tl) accidental hits, K_{e3} and $K_{\pi 2}$. All these backgrounds do not induce spurious asymmetry and only dilute the sensitivity to P_T. The total background fraction for $K_{\mu 3}$ was estimated to be $\leq 16.0\%$.

In the case of $K_{\mu 2\gamma}$, the situation is much worse due to the predominant background of $K_{\mu 3}$ events with one photon escaping the CsI(Tl) detector. Such events almost completely mimic $K_{\mu 2\gamma}$ kinematics, so they cannot be suppressed without a considerable loss of useful $K_{\mu 2\gamma}$ events. The optimized $K_{\mu 2\gamma}$ cuts reduced the background fraction from $K_{\mu 3}$ to about 17%. The background $K_{\mu 3}$ events might have nonzero P_T, thereby inducing spurious transverse asymmetry. Fortunately, we measure P_T in $K_{\mu 3}$ with higher sensitivity in the same experiment and can reliably estimate this effect. Therefore, we can safely assume no spurious contribution to P_T from the $K_{\mu 3}$ background. The second major source of background is accidental photons in the CsI(Tl) detector. It was suppressed to a level of $\leq 8\%$ by requiring a photon energy threshold of 50 MeV and a coincidence between a signal from a charged particle and a photon signal in the CsI within a window of ± 15 ns. Other background modes are suppressed, by the $K_{\mu 2\gamma}$-specific cuts, to a negligible level. The total background fraction for the $K_{\mu 2\gamma}$ sample was estimated to be $\leq 25\%$.

The valuable part of the asymmetry analysis includes the extraction of the value of the normal asymmetry A_N, which is proportional to the T-even

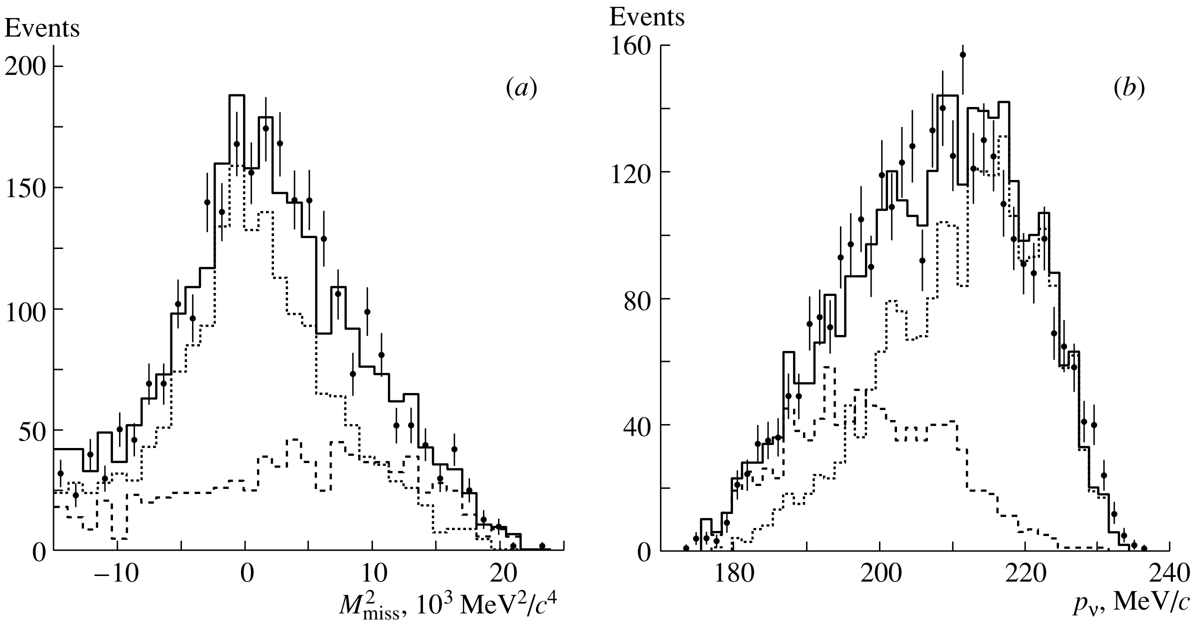

Fig. 3. The spectra of the neutrino missing mass (*a*) and momentum (*b*) for $K_{\mu2\gamma}$ selection. The black dots with error bars show the experimental data. MC simulation: dotted histogram—$K_{\mu2\gamma}$, dashed histogram—$K_{\mu3}$, solid histogram—$K_{\mu2\gamma} + K_{\mu3}$.

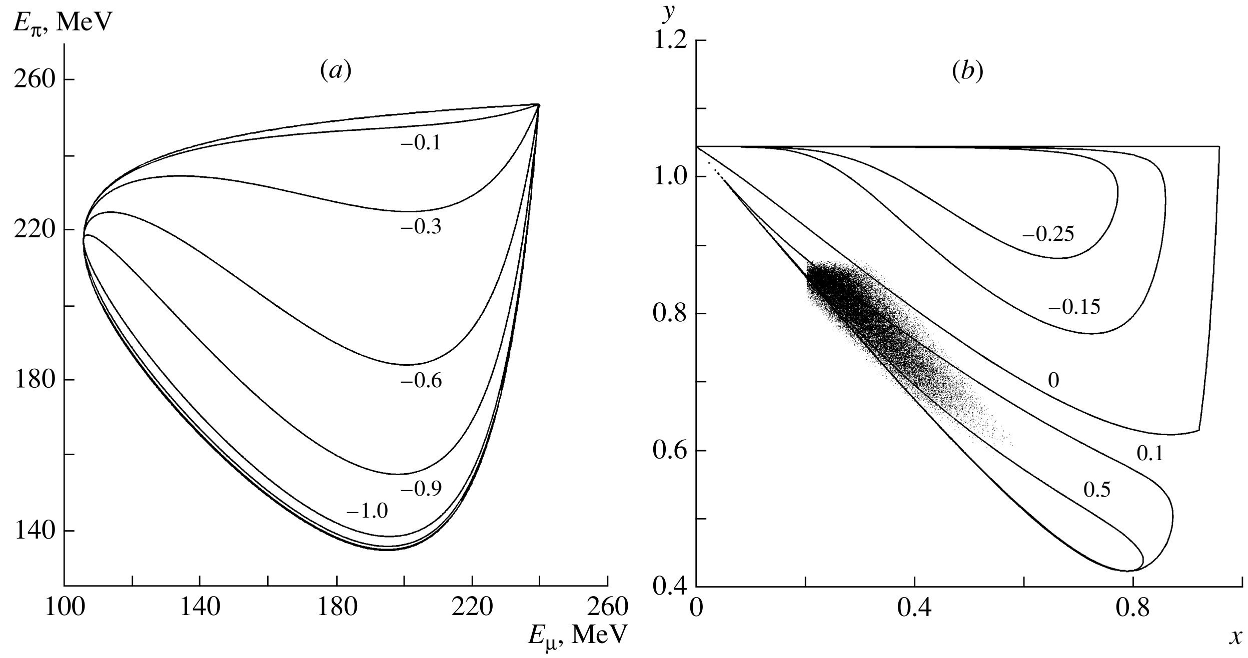

Fig. 4. Contour lines of the normal polarization over the Dalitz plot: $K_{\mu3}$ (*a*) and $K_{\mu2\gamma}$ (*b*). The dots represent the $K_{\mu2\gamma}$ experimental data.

muon polarization, i.e., the in-plane component of the muon polarization normal to the muon momentum. It can be measured by selecting events with π^0 (or photon for $K_{\mu2\gamma}$) moving into the left or right hemisphere with respect to the median plane of the given magnet sector. The theoretical calculations indicate that the normal polarizations for $K_{\mu3}$ [11] and $K_{\mu2\gamma}$ [5] have opposite signs for the kinematic region where selected events are located, as shown in Fig. 4. For one-photon $K_{\mu3}$ events, we obtained $A_N(K_{\mu3}(1\gamma)) = (-3.87 \pm 0.06) \times 10^{-2}$ while for $K_{\mu2\gamma}$ we have $A_N(K_{\mu2\gamma}) = (+3.67 \pm 0.44) \times 10^{-2}$.

This gives us robust evidence of the sufficiently pure $K_{\mu 3}$ and $K_{\mu 2\gamma}$ selection. The study of the dependence of the normal asymmetry on the energy of π^0 shows sound agreement with the theoretical calculation. By comparing the values of the normal asymmetry and normal polarization obtained using MC simulation using the relation $A_N = \alpha P_N$, we are able to extract the value of the polarimeter analyzing power $\alpha = 0.289 \pm 0.015$.

The main systematic uncertainties in P_T come from magnetic field rotation, misalignment of detector components, CsI(Tl) accidental background, beam profile asymmetry, and decay plane rotation. The important point is that the sources of systematics are mostly the same for both measured decays, so we can estimate the systematic contributions using a large sample of $K_{\mu 3}$ data and then use the same error value for $K_{\mu 2\gamma}$. Most of the systematic effects are canceled by the unique features of the setup (azimuthal symmetry, double ratio, etc.). We evaluated the contributions from all relevant sources using the MC simulation data and compared them with the experimental distributions [9]. The overall systematic error was estimated to be $\delta P_T = 0.92 \times 10^{-3}$, which is well below the level of the statistical error.

4. RESULTS

After the analysis of the entire data set collected in the period 1996–2000, we obtained the results for both $K_{\mu 3}$ and $K_{\mu 2\gamma}$. For $K_{\mu 3}$, we selected 6.3×10^6 one- and two-photon forward/backward events and, using the angular attenuation factor value extracted from the MC simulation ($f = 0.72$–0.77 for 2γ events and $f = 0.56$–0.66 for 1γ events), the preliminary result $P_T = (-1.12 \pm 2.17(\text{stat.}) \pm 0.92(\text{syst.})) \times 10^{-3}$ is obtained. Using the relation $P_T = \text{Im}(\xi)\Phi$ (where Φ is a kinematic factor, evaluated from MC simulation $\Phi \sim 0.2$–0.3), we get $\text{Im}(\xi) = (-0.28 \pm 0.69(\text{stat.}) \pm 0.30(\text{syst.})) \times 10^{-2}$ [12]. The dependences of the transverse asymmetry on the beam cycle, π^0 energy, and magnet sector number indicate no systematic irregularity and thus confirm the robustness of our systematics study. The results indicate no evidence of T violation in $K_{\mu 3}$ and can be interpreted as limits on the measured quantities: $|P_T| < 4.3 \times 10^{-3}$ at 90% C.L. and $|\text{Im}(\xi)| < 1.3 \times 10^{-2}$ at 90% C.L. We have performed the first measurement of P_T in the $K_{\mu 2\gamma}$ decay (it is also the first $K_{\mu 2\gamma}$ measurement below the $K_{\pi 2}$ peak). The result obtained for the 1996–1998 data was published in [13]. Here we present the result of the analysis of the whole data set of 1.88×10^5 forward and backward events. We obtained the value $P_T = (-0.14 \pm 1.44(\text{stat.}) \pm 0.10(\text{syst.})) \times 10^{-2}$ with an evaluated attenuation factor of $f = 0.80 \pm 0.03$. Similar to as in the case of $K_{\mu 3}$, we see no indication of T violation in this decay, and we can put the limit $|P_T| < 2.4 \times 10^{-2}$ (90% C.L.)

5. CONCLUSION

We have performed new measurement of T-violating muon polarization in two decays ($K_{\mu 3}$ and $K_{\mu 2\gamma}$) for which several nonstandard models predict nonzero P_T values. For $K_{\mu 2\gamma}$ decay, our result is the first one. At the current level of experimental sensitivity, we see no evidence for T violation and our results allowed us to impose constraints on several nonstandard models: the three-Higgs doublet model (the most stringent experimental constraint), SUSY with squark mixing, SUSY with R-parity violation, the leptoquark models, and left–right symmetric models (see, for example, [14]). Much higher statistical sensitivity to $P_T \leq 10^{-4}$ can be reached in a proposed experiment [15] with a high intensity low-energy separated kaon beam at J-PARC [16]. In addition, the P_N values in $K_{\mu 3}$ and $K_{\mu 2\gamma}$ can be measured with high accuracy in this experiment, which provides a new sensitive method for determination of the kaon form factor values in these decays [17].

REFERENCES

1. E. Golowich and G. Valencia, Phys. Rev. D **40**, 112 (1989); I. I. Bigi and A. I. Sanda, Cambridge Monogr. Part. Phys. Nucl. Phys. Cosmol. **9**, 1 (2000).
2. A. R. Zhitnitsky, Yad. Fiz. **31**, 1024 (1980) [Sov. J. Nucl. Phys. **31**, 529 (1980)]; V. P. Efrosinin *et al.*, Phys. Lett. B **493**, 293 (2000).
3. C. Q. Geng and S. K. Lee, Phys. Rev. D **51**, 99 (1995); G. H. Wu and J. N. Ng, Phys. Lett. B **392**, 93 (1997); M. Fabbrichesi and F. Vissani, Phys. Rev. D **55**, 5334 (1997); G. Belanger and C. Q. Geng, Phys. Rev. D **44**, 2789 (1991).
4. M. Kobayashi, T. T. Lin, and Y. Okada, Prog. Theor. Phys. **95**, 361 (1996).
5. C. H. Chen, C. Q. Geng, and C. C. Lih, Phys. Rev. D **56**, 6856 (1997).
6. V. V. Braguta *et al.*, Phys. Rev. D **66**, 034012 (2002).
7. G. H. Wu and J. N. Ng, Phys. Rev. D **55**, 2806 (1997).
8. S. R. Blatt *et al.*, Phys. Rev. D **27**, 1056 (1983).
9. M. Abe *et al.* (KEK-E246 Collab.), Phys. Rev. Lett. **83**, 4253 (1999); Nucl. Phys. A **663**, 919 (2000).
10. M. Abe *et al.* (E246 KEK PS Collab.), Nucl. Instrum. Methods Phys. Res. A **506**, 60 (2003).
11. N. Cabibbo and A. Maksymowicz, Phys. Lett. **9**, 352 (1964); **11**, 360(E) (1964); **14**, 72(E) (1965).
12. M. Abe *et al.* (KEK-E246 Collab.), Nucl. Phys. A **721**, 445 (2003).
13. V. V. Anisimovsky *et al.* (KEK-PS E246 Collab.), Phys. Lett. B **562**, 166 (2003).

14. F. L. Bezrukov, D. S. Gorbunov, and Y. G. Kudenko, hep-ph/0304146.
15. Y. G. Kudenko and A. N. Khotyantsev, Yad. Fiz. **63**, 890 (2000) [Phys. At. Nucl. **63**, 820 (2000)].
16. *Proceedings of the International Workshop on JHF Science, 1998*, Ed. by J. Chiba, M. Furusaka, H. Miyatake, and S. Sawada, Vols. I–III, KEK Proc. No. 98-5 (1998).
17. F. L. Bezrukov, D. S. Gorbunov, and Y. G. Kudenko, Phys. Rev. D **67**, 091503 (2003).

Physics of Atomic Nuclei, Vol. 67, No. 11, 2004, pp. 1995–2001. From Yadernaya Fizika, Vol. 67, No. 11, 2004, pp. 2018–2024.
Original English Text Copyright © 2004 by Kochetov.

First Results from the NEMO-3 Experiment*

O. I. Kochetov**
(on behalf of the NEMO Collaboration[1])
Joint Institute for Nuclear Research, Dubna, Moscow oblast, 141980 Russia

Received April 16, 2004

Abstract—The main goal of the NEMO-3 experiment is to search for neutrinoless double-beta decay and thus to investigate physics beyond the Standard Model. The expected sensitivity for the effective Majorana neutrino mass is on the order of 0.1 eV. The NEMO-3 detector has been completely installed in the Modane Underground Laboratory (LSM), France, and has been taking data since February 2003. In this paper, a brief description of the NEMO-3 detector and some performances of the initial runs are presented. The first preliminary results for both two-neutrino ($2\beta2\nu$) and neutrinoless double-beta decay ($2\beta0\nu$) of ^{100}Mo, ^{82}Se, ^{116}Cd, and ^{150}Nd are given. *© 2004 MAIK "Nauka/Interperiodica".*

1. INTRODUCTION

The recent results on solar neutrino flux measurements at SNO (Sudbury Neutrino Observatory, Canada), solar and atmospheric neutrinos at Super-Kamiokande (Japan), and reactor antineutrinos at KamLAND (Japan) [1–3] clearly indicate that neutrinos of various flavors (electron, muon, and tau) have nonzero rest masses and a flavor mixing property, which manifests itself in neutrino oscillation, i.e., transition of one neutrino type into another. However, despite this remarkable progress in proof of neutrino oscillation, the question of absolute values of neutrino mass eigenstates is still an open question. Only simultaneous analysis of new experiments on neutrinoless double-beta decay and on measurement of the beta spectrum of low-energy beta transitions may lead to experimental determination of these values and give an answer to the question whether neutrinos are Majorana or Dirac particles.

Observation of neutrinoless double-beta decay ($\beta\beta0\nu$) is the most promising test of the Majorana nature of the neutrino. Contrary to two-neutrino double-beta decay ($\beta\beta2\nu$), this process violates lepton number conservation by two units and also requires a helicity flip which can be produced only by the neutrino being massive or by the existence of right-handed lepton charged currents. It is proposed that there is an exchange of neutrinos between two neutrons in the same nucleus leading to the emission of two electrons. The Majorana mass term enables transitions through the $V-A$ interaction alone. Thus, $\beta\beta0\nu$ decay opens the gates of new physics beyond the Standard Model and is a very attractive topic in particle physics today for both theoretical and experimental physicists [4]. Investigation of $\beta\beta0\nu$ in transitions to a 2^+ excited state is also possible using a Majorana mass term if the $V+A$ interaction exists. Other mechanisms may contribute to the double-beta-decay process without neutrino emission, in particular, the emission of a Majoron, the boson associated with the spontaneous symmetry breaking of lepton number. Research on this process imposes additional constraints on the experiment, as it involves a three-body-decay spectrum in the final state with the Majoron not being detected. In addition to this, the systematic study of $\beta\beta2\nu$ decay of various isotopes will be an important contribution to nuclear physics and nuclear matrix element (NME) calculations. To fully understand the double-beta-decay process, all three different decay modes must be investigated. This is the objective of the NEMO-3 experiment.

Until now, the most sensitive experiments on the search for $\beta\beta0\nu$ decay have been "calorimetric" experiments with highly pure germanium detectors of enriched ^{76}Ge (Heidelberg–Moscow and IGEX) [5, 6]. The boundary for the $\beta\beta0\nu$ decay lifetime

---

*This article was submitted by the author in English.

[1] The NEMO Collaboration includes CENBG, IN2P3-CNRS et Université de Bordeaux I, Gradignan, France; LPC, IN2P3-CNRS et Université de Caen, France; JINR, Dubna, Russia; LSCE, CNRS, Gif-sur-Yvette, France; ITEP, Moscow, Russia; INR RAS, Moscow; INEEL, Idaho Falls, USA; Jyväskylä University, Finland; LAL, IN2P3-CNRS et Université de Paris-Sud, Orsay, France; MHC, South Hadley, Mass., USA; IReS IN2P3-CNRS et Université Louis Pasteur, Strasbourg, France; CTU, Prague, Czech Republic; Charles University, Prague, Czech Republic; Saga University, Japan; and UCL, London, UK.

**e-mail: `kochet@nusun.jinr.ru`

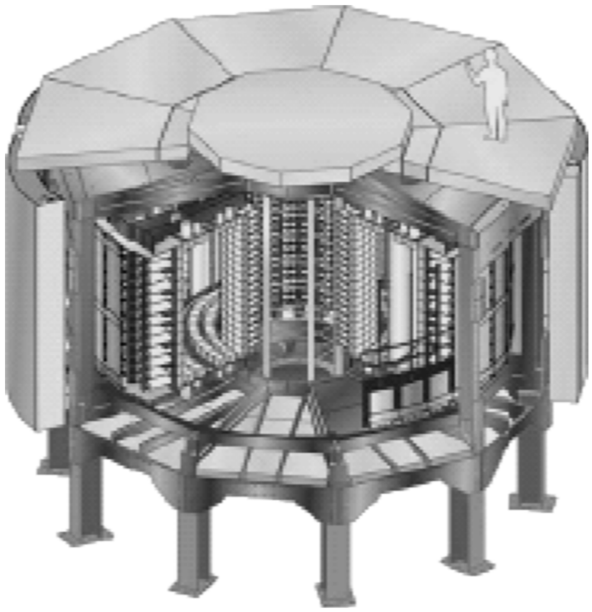

Fig. 1. Final layout of the NEMO-3 detector, surrounded with magnetic field coil, iron shield, and neutron shield.

of ^{76}Ge obtained in these experiments is over 2×10^{25} yr, which corresponds to the limit for the Majorana electron-neutrino mass below 0.3–1.0 eV depending on the uncertainty of the calculated NME. In both experiments, data taking went on for over 10 years and now their sensitivity limit has been attained.

The main goal of the NEMO-3 experiment [7] is to study $\beta\beta0\nu$ decay of various isotopes and to probe the half-life up to $\sim 10^{25}$ yr (^{100}Mo), which corresponds to the expected sensitivity of the effective Majorana neutrino mass $\langle m_\nu \rangle$ down to the 0.1-eV region. This sensitivity is the highest one among the present direct tracking experiments and is very similar to the present best inclusive measurements of ^{76}Ge.

In 1989, the NEMO Collaboration started a research and development program aimed at constructing a detector which would be able to achieve a sensitivity up to 0.1 eV of the effective electron-neutrino mass $\langle m_\nu \rangle$. Such a detector must be based on direct detection of two electron tracks by using a tracking device in combination with measurement of electron energies by using a plastic scintillator calorimeter. Two prototypes NEMO-1 and NEMO-2 have proved technical feasibility and have also permitted background studies to be performed. Since May 2002, the NEMO-3 detector has been operating in the Modane Underground Laboratory (LSM). At the beginning of 2003, final tuning of the detector and laser survey system and installation of the neutron shielding were finished. In February 2003, the NEMO-3 detector started data taking under stable conditions.

2. THE NEMO-3 DETECTOR

The NEMO-3 detector is a combined (track gas detectors + scintillation calorimeters + magnetic field) assembly (Fig. 1) capable of measuring not only the total energy of $\beta\beta$-decay electrons but also all other parameters of this process for all $\beta\beta$-interesting isotopes of total mass up to $\sim$20 kg. To shield NEMO-3 against cosmic-ray background, it is installed in the Modane Underground Laboratory, built in a branch near the middle of the 13-km Fréjus highway tunnel connecting France and Italy. The thickness of the rock above the laboratory is 1700 m (4800 mwe). Under these conditions the cosmic-ray background is as small as 4 muons/(m^2 d).

The NEMO-3 detector has the shape of a torus (Fig. 1). The detector diameter is 6 m in total and its height is 2.8 m. It is a knockdown modular structure of $\sim$20 segments. The NEMO-3 recording system comprises a track detector of 6180 Geiger gas counters and a calorimeter of 1940 plastic scintillators viewed by low-background PMTs (3- and 5-in. Hamamatsu phototubes). The $\beta\beta$ sources in the form of thin foils are placed in the middle of the sectors.

The tracking detector ($\sim$20-m^3 active volume) is filled with a mixture of He, 4% ethyl alcohol, and 1% argon from a special continuous-flow gas system. The typical length of an electron track is 1 m with radial longitudinal resolutions 0.4 and 0.8 cm, respectively. Scintillation detectors are used for energy and time-of-flight measurements as well as to produce a fast trigger signal. Scintillators are arranged into two concentric cylindrical walls making up the inner and outer surfaces of the detector. The upper and lower planes of the facility have additional rows of scintillator blocks between the rows of the Geiger counter cells to provide $\sim 4\pi$ geometry. The energy resolution $\Delta E/E$ of the scintillation calorimeter is in the range from 12 to 16%, depending on the sizes and configurations of scintillators, and the time resolution is 250 ps for 1-MeV electrons. The total mass of the scintillators is 6400 kg, and the working surface area of all scintillators is about 50 m^2.

Double-beta-decay sources of enriched isotopes are thin foils (30–60 mg/cm^2) placed directly into the gas volume of the track part. Thus, seven $\beta\beta$ isotopes (^{48}Ca, ^{82}Se, ^{96}Zr, ^{100}Mo, ^{116}Cd, ^{130}Te, ^{150}Nd) of total mass about 10 kg are simultaneously measured in the NEMO-3 detector now. The preparation of these sources is described in [8]. Table 1 summarizes the isotopes currently housed in NEMO-3 with their total mass and decay mode of interest. The very pure natural tellurium oxide and copper are included to study the background processes in the 3-MeV region induced by the external γ-ray flux.

A laser-based calibration system was installed for the daily control on the calorimeter stability of the energy-and-time calibration parameters. The energy resolution and the gain stability are checked during the test runs with the ^{90}Sr and ^{207}Bi calibration sources.

The magnet coil surrounds the detector and produces a vertical homogeneous magnetic field (25 G) in the tracking volume. This magnetic field is used for e^-/e^+ charge recognition by measuring the curvature of the track. An external shield of 20-cm low-radioactive iron protects the detector from external γ rays and thermal neutrons. Water tanks on the side wall and the wood shield on the top and bottom of the detector suppress the flux of fast neutrons. The blocks of plastic scintillators (10-cm thickness) work as an additional gamma and neutron shield too. All materials used in the detector have been selected for their high radiopurity by gamma spectroscopy with ultralow-background Ge detectors.

With the use of the magnetic field, the iron shield, and the additional neutron shield, the external background is reduced by two orders of magnitude. Thus, one can expect no events from external background in the region of interest for the ^{100}Mo $\beta\beta0\nu$ decay for 5-yr measurements.

3. PERFORMANCES OF THE NEMO-3

In order to measure a precise value of the absolute energy released in $\beta\beta$ decay, appropriate energy calibrations of the calorimeter are needed. Each sector of the NEMO-3 detector is equipped with vertical copper tubes along the edges of the $\beta\beta$-source foils. During calibration runs, the radioactive calibration sources are inserted into these tubes with precisely fixed positions.

The ^{207}Bi and ^{90}Sr calibration sources are used for energy calibrations. Decay of ^{207}Bi provides two conversion electrons of 482 and 976 keV (K lines) suited for a calibration in the energy region up to 1 MeV. To measure energies up to 3 MeV or more, one needs an additional calibration point which is obtained using the beta-decay spectrum with the endpoint energy at 2283 keV from ^{90}Y (^{90}Sr daughter). The relation between the electric charge signal and deposited energy has been examined to be almost linear up to 4 MeV.

A laser calibration system, in which laser light is distributed to all 1940 PMTs by optical fibers, is available for (i) the daily survey of the calorimeter stability, (ii) the calorimeter linearity check up to 12 MeV, and (iii) the determination of the time—energy relation for each PMT. The stability of the laser calibration system itself is ensured by six reference PMTs coupled to ^{207}Bi calibration sources. Variation of the laser standard peak position in the daily survey gives information about the PMT gain changes. Almost all scintillators are stable in time with a gain variation of less than 2%.

Table 1. Sources installed in the NEMO-3 detector and their radioactivity measured by Ge spectroscopy

Isotope	Study	Mass, g	^{214}Bi, mBq/kg	^{208}Tl, mBq/kg
^{100}Mo	$\beta\beta0\nu, \beta\beta2\nu$	6914	<0.39	<0.11
^{82}Se	$\beta\beta0\nu, \beta\beta2\nu$	932	1.2 ± 0.5	0.4 ± 0.1
^{116}Cd	$\beta\beta0\nu, \beta\beta2\nu$	405	<2	<0.8
^{130}Te	$\beta\beta0\nu, \beta\beta2\nu$	454	<0.7	<0.5
^{150}Nd	$\beta\beta2\nu$	36.6	<3.0	10 ± 2
^{96}Zr	$\beta\beta2\nu$	9.4	<16	<10
^{48}Ca	$\beta\beta2\nu$	7.0	<4	<2
Cu	Background	621	<0.12	<0.04
^{nat}TeO$_2$	Background	614	<0.17	<0.09

For time calibration, the relative timing offset for each channel is determined with ^{60}Co calibration sources which emit two coincident γ rays, as well as with ^{207}Bi calibration sources. Another method of the time calibration is based on the use of high-energy crossing electrons in the runs with the Am—Be neutron source. The advantage of this method is that correct time—energy dependence for electrons is taken into account. The average time resolution was found to be 250 ps (1σ) for 1-MeV electrons, which is enough to distinguish between a single-electron event crossing through the detector and two-electron $\beta\beta$ signal from the source foil.

For the tracking detector performance, it is important to demonstrate (i) relations between drift time and drift velocity inside drift Geiger cells, (ii) radial and longitudinal position resolutions of electron tracks, (iii) e^-/e^+ charge recognitions under the magnetic field, and (iv) position resolutions of vertex points.

The ^{207}Bi calibration sources, which are used for the calorimeter calibrations, are also very useful for the study of the spatial resolution of the vertex of electron tracks, since two conversion electrons are available and the positions of the calibration sources are well known. The transversal and longitudinal resolutions of drift cells in the one-electron channel at 1 MeV were found to be equal to 0.25 and 0.95 cm, respectively. In the two-electron channel, the spatial resolutions of the two-electron vertex are equal to 0.6 and 1.3 cm, respectively.

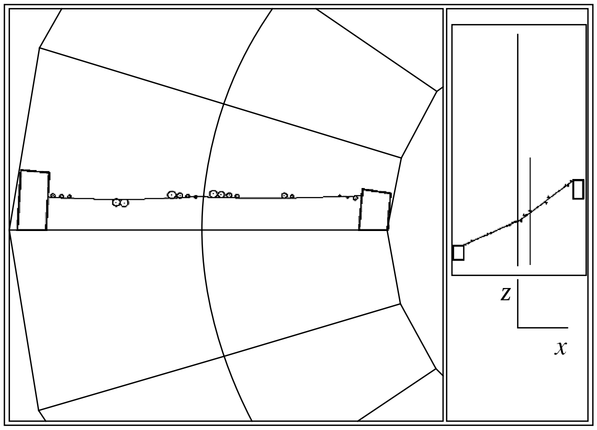

Fig. 2. The one-crossing electron event.

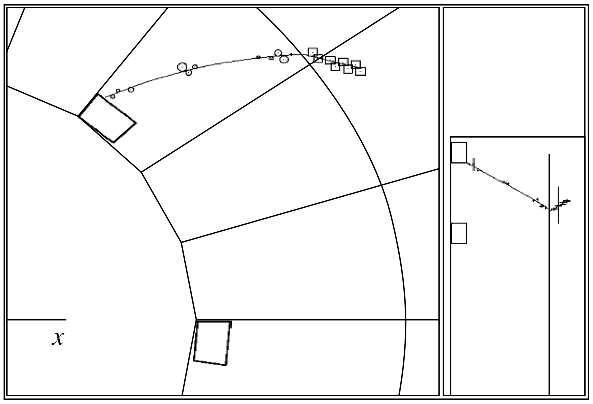

Fig. 4. The single-e^- and delayed-α event.

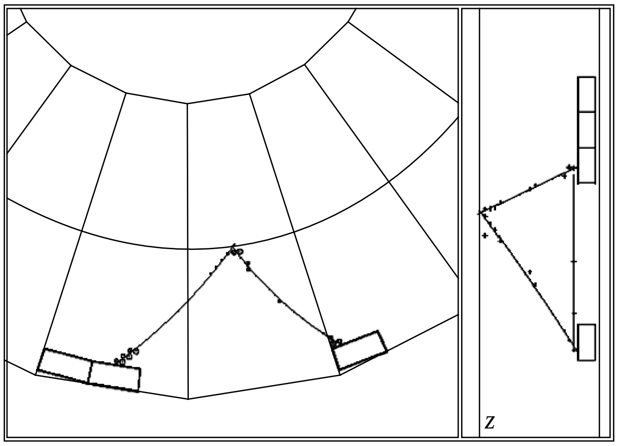

Fig. 3. The e^+e^- pair event.

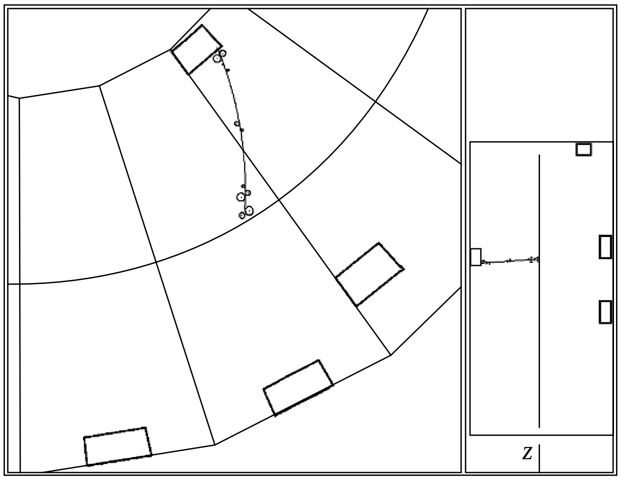

Fig. 5. The single-e^- and three-γ ray event.

High-energy one-crossing electron events have been used for this purpose to analyze multiple-scattering effects. Such electrons were found to be produced easily by putting a neutron source (Am–Be) on the side of the detector. Fast neutrons are thermalized in the plastic scintillators and then captured with gamma radiation inside the detector. As a result, high-energy electrons are created by the Compton scattering of the γ rays. Using the high-energy crossing electrons, one can determine the relation between drift time and drift distance too. The probability of misidentifying electrons and positrons under the magnetic field was also studied using similar events. This probability goes up gradually with the energy, but the absolute value is only 3% for a 1-MeV electron.

The combination of a tracking detector, calorimeter, and magnetic field allows NEMO-3 to identify electrons, positrons, γ rays, and delayed α particles. An electron (or positron) in the detector corresponds to a curved track associated with the "hit" scintillator recording the energy deposited, a γ-ray signal corresponds to a scintillator hit without an associated track, and an α particle is a straight short track, possibly delayed up to 700 μs. Thus, one can identify almost all the background channels, for example, $e\gamma$, $e\gamma\gamma$, ..., $e\alpha$, $e\gamma\alpha$, etc. In Figs. 2–5, one can see events corresponding to background as follows: one-crossing electron event created by a Compton scattering of a high-energy γ ray (Fig. 2), a e^-e^+ pair created by a γ ray in the source foil (Fig. 3), an event with an electron and delayed α track from the ^{214}Bi $\rightarrow$ ^{214}Po $\rightarrow$ ^{210}Pb chain (Fig. 4), and an event with one e^- and three γ rays (Fig. 5).

Analysis of the first accumulated data shows that ^{214}Bi from radon is the main background source for the $\beta\beta0\nu$ studies. The ^{214}Bi radiopurity in the source foils was previously checked by gamma spectroscopy. The NEMO-3 requirement (less than 0.3 mBq/kg) was achieved for the ^{100}Mo source foils. However, the source foils are surrounded by the tracking chamber,

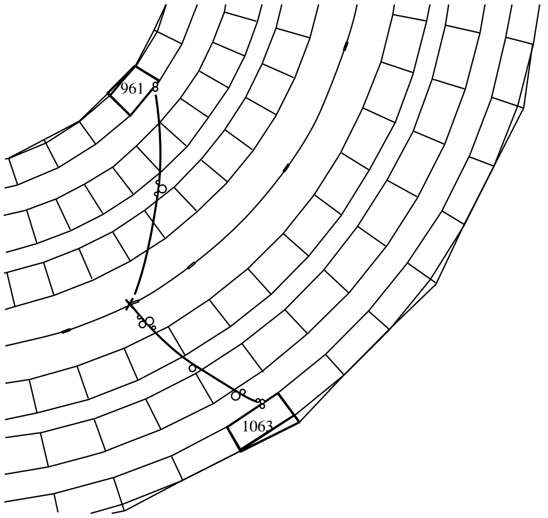

Fig. 6. The two-electron event.

where the working gas currently has a weak contamination of radon with ^{214}Bi as a daughter isotope. The radon has been monitored with use of a radon detector with a sensitivity of about 1 mBq/m^3. The inlet gas of the tracking chamber has been found to be free from radon at a level of less than 3 mBq/m^3, while the outlet gas is contaminated with 20–30 mBq/m^3 [9]. Delayed e–α channel measurements from ^{214}Bi $\rightarrow$ ^{214}Pb $\rightarrow$ ^{210}Pb in the NEMO-3 detector itself also lead to similar radon concentrations. The radon concentration in the air of the LSM experimental hall is about 10 Bq/m^3. The origin of the radon inside the detector is small leaks in the tracking chamber. The radon concentration in the working gas leads to a ^{214}Bi deposit on the foils. It corresponds to activity a few times greater than the NEMO-3 requirement. That is why an antiradon "tent" with radon-free air surrounding the detector is now under construction.

4. FIRST PRELIMINARY RESULTS

Although the main goal of the experiment is to search for $\beta\beta0\nu$ decay, the analysis procedure starts with $\beta\beta2\nu$ decay. It is necessary to study the detector properties and background conditions and to demonstrate detector operation. $\beta\beta2\nu$ decay is also an important contribution to nuclear physics. After this, one can proceed to searches for $\beta\beta0\nu$ decay. The signal from $\beta\beta0\nu$ decay may be revealed by an excess of events in the two-electron sum energy spectrum ($E_1 + E_2$) in the window of interest [2.8–3.2] MeV for ^{100}Mo $Q_{\beta\beta} = 3.03$ MeV.

A double-beta-decay event is tagged by two-electron tracks associated with PMT "hits" in time and originated from the same vertex point in a source foil. Events near the vertex with delayed Geiger hits (α particle) are rejected. Figure 6 shows a typical $\beta\beta$ event.

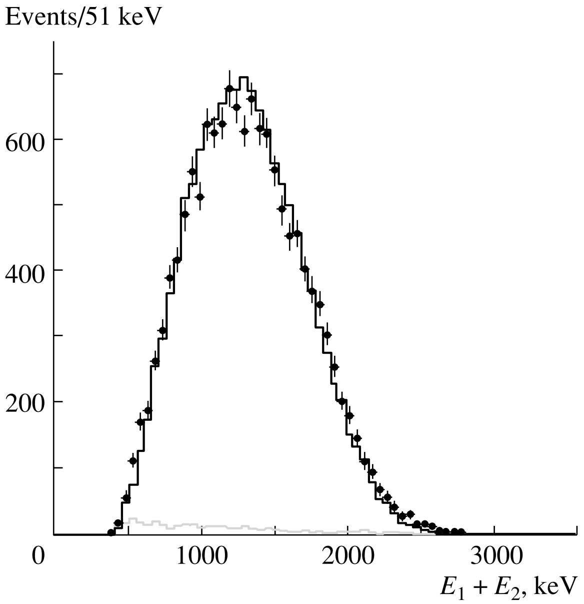

Fig. 7. The $\beta\beta$ two-electron sum energy spectrum for the ^{100}Mo source (points); estimated background (gray line) is subtracted. The solid line corresponds to a MC simulation of $\beta\beta2\nu$ decay of ^{100}Mo.

For the first 640-h run, 13 750 events were selected for the ^{100}Mo sources, with a signal-to-background ratio of 40. The corresponding experimental two-electron sum energy spectrum ($E_1 +$ E_2) (background is subtracted), as well as the MC simulated spectrum, is presented in Fig. 7. The ex-

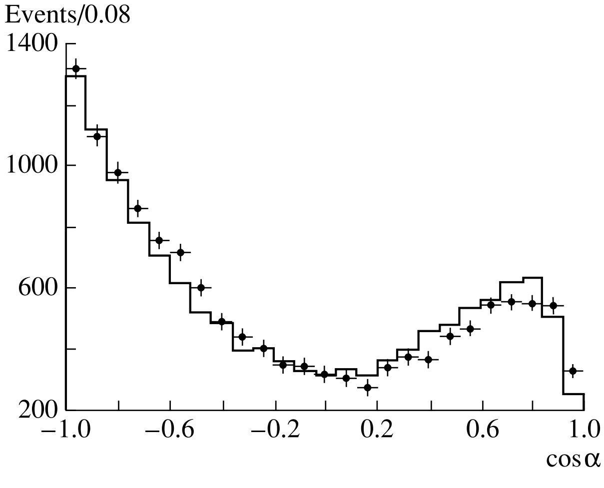

Fig. 8. The angular distribution between the electrons in $\beta\beta$ events from ^{100}Mo, background subtracted. The solid line corresponds to the MC prediction.

Table 2. Preliminary results from the NEMO-3 experiment for $\beta\beta$ decay of ^{100}Mo, ^{82}Se, ^{116}Cd, and ^{150}Nd

Isotope	Time, h	N_{ee}	$T_{1/2}^{2\nu}$, 10^{19} yr	$T_{1/2}^{0\nu}$, 10^{22} yr (90% C.L.)	$T_{1/2}^{0\nu\chi}$, 10^{21} yr (90% C.L.)
^{100}Mo	650	13 750	0.78 ± 0.009(stat.) ± 0.08(syst.)	>6.0	>1.8
^{82}Se	1850	400	9.1 ± 0.4(stat.) ± 0.9(syst.)	>4.7	>8
^{116}Cd	1850	336	3.1 ± 0.15(stat.) ± 0.3(syst.)	>1.6	>1.7
^{150}Nd	1850	147	0.77 ± 0.07(stat.) ± 0.08(syst.)	>0.14	>0.26

perimental and simulated angular distributions of the two-electron events are given in Fig. 8.

The preliminary value of the half-life of $\beta\beta2\nu$ decay measured for ^{100}Mo is obtained as

$$T_{1/2}^{2\nu} = [7.80 \pm 0.09(\mathrm{stat.}) \pm 0.80(\mathrm{syst.})] \times 10^{18}\ \mathrm{yr}.$$

A conservative estimate of the systematic error has been taken as 10%, due to all possible uncertainties in the detector efficiency.

There are no events observed in the $\beta\beta0\nu$ energy window 2.8–3.2 MeV (Fig. 7). However, there is one event very close to it, with the total energy of 2.78 MeV. Since the daily laser corrections for energy calibration have not yet been applied in this analysis, to be conservative, the window was enlarged slightly to 2.75–3.20 MeV. Then a conservative limit for the $\beta\beta0\nu$ process including this event becomes

$$T_{1/2}^{0\nu} > 6 \times 10^{22}\ \mathrm{yr}\ (90\%\ \mathrm{C.L.}),$$

which corresponds to the following limit on the effective neutrino mass:

$$\langle m_\nu \rangle < 1.2\text{–}2.7\ \mathrm{eV}\ (90\%\ \mathrm{C.L.}).$$

The region of interest for the $\beta\beta$ decay with Majoron emission ($\beta\beta0\nu\chi$) was analyzed in the [2.6–3.2] MeV energy window. There are nine candidate events observed, while five are expected from $\beta\beta2\nu$ decay and background, so the corresponding limit for the half-life and the coupling constant is

$$T_{1/2}^{0\nu\chi} > 1.8 \times 10^{21}\ \mathrm{yr},$$

$$g_{ee} < (0.56\text{–}1.70) \times 10^{-4}\ (90\%\ \mathrm{C.L.}).$$

Nuclear matrix elements used for these calculations were taken from [10, 11].

The same analysis as described for ^{100}Mo was applied to ^{82}Se, ^{116}Cd, and ^{150}Nd sources for 1850 h of analyzed data. As a result, 400, 336, and 147 useful events were selected in $\beta\beta2\nu$ regions of interest for ^{82}Se, for ^{116}Cd, and for ^{150}Nd, respectively. In Figs. 9–11, the resulting ($E_1 + E_2$) spectra are represented. The signal-to-background ratio was greater than 3 in all cases. The obtained values of the $\beta\beta2\nu$-decay half-lives of these isotopes are summarized in Table 2.

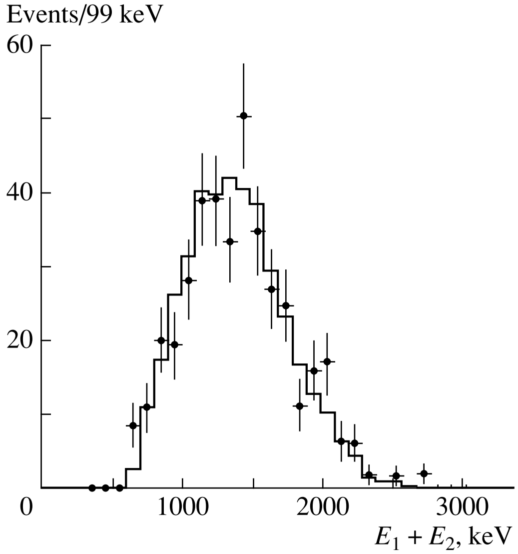

Fig. 9. The $\beta\beta$ two-electron sum energy spectrum for the ^{82}Se source. The solid line represents the MC prediction.

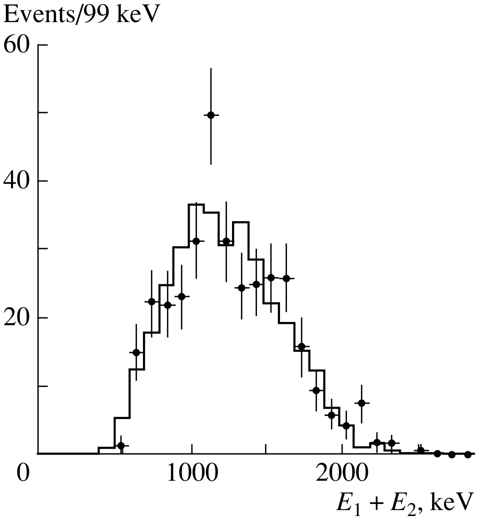

Fig. 10. The $\beta\beta$ two-electron sum energy spectrum for the ^{116}Cd source. The solid line represents the MC prediction.

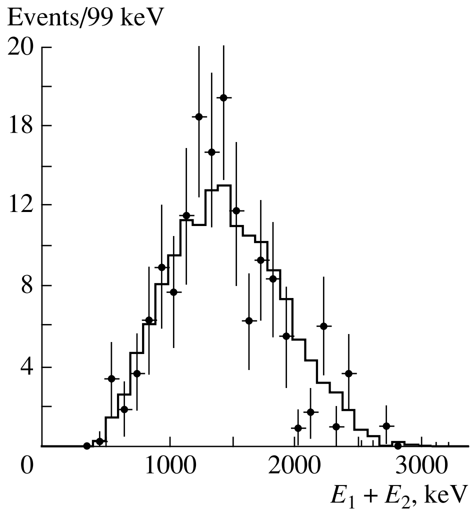

Fig. 11. The $\beta\beta$ two-electron sum energy spectrum for the ^{150}Nd source. The solid line represents the MC prediction.

5. CONCLUSION

The NEMO-3 detector is now fully operating and taking data under stable conditions. The tracking detector and calorimeter performance were checked and were found to be working perfectly. The background is low enough to start $\beta\beta0\nu$-decay search. However, further improvements are already planned to solve the radon problem. Our goal is to reduce considerably the radon concentration inside the NEMO-3 setup after improving the radon-free air factory and construction of a special cavity around the detector assembly. The first portion of data has been analyzed and the preliminary results for the $\beta\beta$ decays of ^{100}Mo, ^{82}Se, ^{116}Cd, and ^{150}Nd are presented in this report.

ACKNOWLEDGMENTS

We would like to thank the Modane Underground Laboratory staff for their technical assistance in building and running the experiment.

Part of this work was carried out with the support of INTAS, grant no. 00-00362.

REFERENCES

1. Y. Fukuda *et al.* (Super-Kamiokande Collab.), Phys. Rev. Lett. **81**, 1562 (1998).
2. Q. R. Ahmad *et al.* (SNO Collab.), Phys. Rev. Lett. **89**, 11301 (2002).
3. K. Eguchi *et al.* (KamLAND Collab.), Phys. Rev. Lett. **90**, 21802 (2003).
4. S. M. Bilenky *et al.*, Phys. Rep. **379**, 69 (2003).
5. H. V. Klapdor-Kleingrothaus *et al.*, Eur. Phys. J. A **12**, 147 (2001).
6. C. E. Aalseth *et al.*, Phys. Rev. D **65**, 092007 (2002).
7. NEMO Collab., Preprint LAL 94-29, LAL (Orsay, 1994).
8. R. Arnold *et al.* (NEMO Collab.), Nucl. Instrum. Methods Phys. Res. A **474**, 93 (2001).
9. Y. Takeuchi *et al.*, Nucl. Instrum. Methods Phys. Res. A **421**, 334 (1999).
10. F. Simkovic *et al.*, Phys. Rev. C **60**, 055502 (1999).
11. S. Stoica and H. V. Klapdor-Kleingrothaus, Nucl. Phys. A **694**, 269 (2001).

Physics of Atomic Nuclei, Vol. 67, No. 11, 2004, pp. 2002–2010. From Yadernaya Fizika, Vol. 67, No. 11, 2004, pp. 2025–2032.
Original English Text Copyright © 2004 by Aalseth, Anderson, Arthur, Avignone III, Baktash, Ball, Barabash, Brodzinski, Brudanin, Bugg, Champagne, Chan, Cianciolo, Collar, Creswick, Doe, Dunham, Easterday, Efremenko, Egorov, Ejiri, Elliott, Ely, Fallon, Farach, Gaitskell, Gehman, Grzywacz, Hazma, Hime, Hossbach, Jordan, Kazkaz, Kephart, King III, Kochetov, Konovalov, Kouzes, Lesko, Macchiavelli, Miley, Mills, Nomachi, Palms, Pitts, Poon, Radford, Reeves, Robertson, Rohm, Rykaczewski, Saborov, Sandukovsky, Shawley, Stekhanov, Tornow, van de Water, Vetter, Warner, Webb, Wilkerson, Wouters, Young, Yumatov.

The Majorana Neutrinoless Double-Beta Decay Experiment*

C. E. Aalseth¹⁾, D. Anderson¹⁾, R. Arthur¹⁾, F. T. Avignone III²⁾, C. Baktash³⁾, T. Ball⁴⁾, A. S. Barabash⁵⁾, R. L. Brodzinski¹⁾, V. B. Brudanin⁶⁾, W. Bugg⁷⁾, A. E. Champagne⁸⁾˒⁹⁾, Y.-D. Chan¹⁰⁾, T. V. Cianciolo³⁾, J. I. Collar¹¹⁾, R. W. Creswick²⁾, P. J. Doe¹²⁾, G. Dunham¹⁾, S. Easterday¹⁾, Yu. V. Efremenko³⁾˒⁷⁾, V. G. Egorov⁶⁾, H. Ejiri¹³⁾, S. R. Elliott⁴⁾, J. Ely¹⁾, P. Fallon¹⁰⁾, H. A. Farach²⁾, R. J. Gaitskell¹⁴⁾, V. Gehman¹²⁾, R. Grzywacz³⁾, R. Hazma¹³⁾, H. Hime⁴⁾, T. Hossbach¹⁾˒²⁾, D. Jordan¹⁾, K. Kazkaz¹²⁾, J. Kephart⁸⁾˒¹⁵⁾, G. S. King III²⁾, O. I. Kochetov⁶⁾, S. I. Konovalov⁵⁾, R. T. Kouzes¹⁾, K. T. Lesko¹⁰⁾, A. O. Macchiavelli¹⁰⁾, H. S. Miley¹⁾, G. B. Mills⁴⁾, M. Nomachi¹³⁾, J. M. Palms²⁾, W. K. Pitts¹⁾, A. W. P. Poon¹⁰⁾, D. C. Radford³⁾, J. H. Reeves¹⁾˒²⁾, R. G. H. Robertson¹²⁾, R. M. Rohm⁸⁾˒¹⁶⁾, K. Rykaczewski³⁾, K. Saborov⁸⁾˒¹⁵⁾, V. G. Sandukovsky⁶⁾, C. Shawley¹⁾, V. N. Stekhanov⁵⁾, W. Tornow⁸⁾˒¹⁶⁾, R. G. van de Water⁴⁾, K. Vetter¹⁷⁾, R. A. Warner¹⁾, J. Webb¹⁸⁾, J. F. Wilkerson¹²⁾, J. M. Wouters⁴⁾, A. R. Young⁸⁾˒¹⁵⁾, and V. I. Yumatov⁴⁾**
(The Majorana Collaboration)

Received April 16, 2004

Abstract—The proposed Majorana double-beta decay experiment is based on an array of segmented intrinsic Ge detectors with a total mass of 500 kg of Ge isotopically enriched to 86% in ^{76}Ge. A discussion is given of background reduction by material selection, detector segmentation, pulse shape analysis, and electroformation of copper parts and granularity. Predictions of the experimental sensitivity are given. For an experimental running time of 10 years over the construction and operation of the Majorana setup, a sensitivity of $T_{1/2}^{0\nu} \sim 4 \times 10^{27}$ yr is predicted. This corresponds to $\langle m_\nu \rangle \sim 0.003$–$0.004$ eV according to recent QRPA and RQRPA matrix element calculations. © *2004 MAIK "Nauka/Interperiodica"*.

1. INTRODUCTION

The range of interest of the effective mass of the electron neutrino favored by the results of neutrino oscillation experiments is now well within the grasp of a well-designed germanium (^{76}Ge) zero-neutrino double-beta decay ($0\nu\beta\beta$ decay) experiment. The observation of this decay mode would be the only known practical experiment to demonstrate that neutrinos

---

* This article was submitted by the authors in English.

1) The Pacific Northwest National Laboratory, Richland, WA, USA.

2) Department of Physics and Astronomy, University of South Carolina, Columbia, SC, USA.

3) Oak Ridge National Laboratory, Oak Ridge, TN, USA.

4) Los Alamos National Laboratory, P-Division, Los Alamos, NM, USA.

5) Institute of Theoretical and Experimental Physics, Bol'shaya Cheremushkinskaya ul. 25, Moscow, 117259 Russia.

6) Joint Institute for Nuclear Research, Dubna, Moscow oblast, 141980 Russia.

7) Department of Physics and Astronomy, University of Tennessee, Knoxville, TN, USA.

8) Triangle Universities Nuclear Laboratory, Durham, NC, USA.

9) Department of Physics and Astronomy, University of North Carolina, Chapel Hill, NC, USA.

10) Lawrence Berkeley National Laboratory, Berkeley, CA, USA.

11) Center for Cosmology, Enrico Fermi Institute, University of Chicago, Chicago, IL, USA.

12) Department of Physics, University of Washington, Seattle, WA, USA.

13) Research Center for Nuclear Physics, Osaka University, Japan.

14) Department of Physics, Brown University, Providence, RI, USA.

15) Department of Physics, North Carolina State University, Raleigh, NC, USA.

16) Department of Physics, Duke University, Durham, NC, USA.

17) Lawrence Livermore National Laboratory, Livermore, CA, USA.

18) New Mexico State University, Carlsbad, NM, USA.

** e-mail: `avignone@sc.edu`

are Majorana particles. In the case of Majorana neutrinos, $0\nu\beta\beta$ decay is by far the most sensitive way to determine the mass scale of neutrino mass eigenvalues.

Neutrino oscillation data clearly establish that there are three eigenstates that mix and that have mass. The flavor eigenstates, $|\nu_{e,\mu,\tau}\rangle$, are connected to the mass eigenstates, $|\nu_{1,2,3}\rangle$, via a linear transformation:

$$|\nu_l\rangle = \sum_{j=1}^{3} |u_{lj}^L| e^{i\delta_j} |\nu_j\rangle, \tag{1}$$

where $l = e, \mu, \tau$, and the factor $e^{i\delta_j}$ is a CP phase, ±1 for CP conservation.

The decay rate for the $0\nu\beta\beta$-decay mode driven by the exchange of a massive Majorana neutrino is expressed as follows:

$$\lambda_{\beta\beta}^{0\nu} = G^{0\nu}(E_0, Z)|\langle m_\nu\rangle|^2 |M_{\mathrm{F}}^{0\nu} - (g_A/g_V)^2 M_{\mathrm{GT}}^{0\nu}|^2, \tag{2}$$

where $G^{0\nu}$ is a factor including phase space and couplings; $|\langle m_\nu\rangle|$ is the Majorana neutrino mass parameter discussed below; $M_{\mathrm{F}}^{0\nu}$ and $M_{\mathrm{GT}}^{0\nu}$ are the Fermi and Gamow–Teller nuclear matrix elements, respectively; and g_A and g_V are the axial vector and vector coupling constants, respectively. The mass parameter, $|\langle m_\nu\rangle|$, is the "effective Majorana mass of the electron neutrino." After multiplication by a diagonal matrix of Majorana phases, it is expressed in terms of the first row of the 3×3 matrix of (1) as follows:

$$|\langle m_\nu\rangle| \equiv \Big| |u_{e1}^L|^2 m_1 + |u_{e2}^L|^2 m_2 e^{i\phi_2} + |u_{e3}^L|^2 m_3 e^{i(\phi_3+\delta)} \Big|, \tag{3}$$

where $e^{i\phi_{2,3}}$ are the Majorana CP phases (±1 for CP conservation in the lepton sector). These phases do not appear in neutrino oscillation expressions and, hence, have no effect on the observations of oscillation parameters. The phase angle δ does appear in oscillation experiments. The oscillation experiments have, however, constrained the mixing angles and thereby the u_{lj}^L coefficients in (3). Using the best-fit values from the SNO and Super-Kamiokande solar neutrino experiments and the CHOOZ and Palo Verde reactor neutrino experiments, we arrive at the following expression [1–4]:

$$|\langle m_\nu\rangle| \equiv \Big| (0.75^{+0.02}_{-0.04}) m_1 + (0.25^{+0.04}_{-0.02}) m_2 e^{i\phi_2} + (<0.026) m_3 e^{i(\phi_3+\delta)} \Big|, \tag{4}$$

where the errors were computed from the published confidence level values. The bound on $|u_{e3}^L|^2$ is at a 95% C.L. and the errors on the first two coefficients are 1σ.

The results of the solar neutrino and atmospheric neutrino experiments imply the mass square differences $\delta m_{ij}^2 = |m_i^2 - m_j^2|$ but cannot distinguish between two mass patterns (hierarchies): the so-called "normal" hierarchy, in which $\delta m_{\mathrm{solar}}^2 = m_2^2 - m_1^2$ and $m_1 \simeq m_2 \ll m_3$, and the "inverted" hierarchy, where $\delta m_{\mathrm{solar}}^2 = m_3^2 - m_2^2$ and $m_3 \simeq m_2 \gg m_1$. In both cases, $\delta m_{\mathrm{atm}}^2 \simeq m_3^2 - m_1^2$. Considering the values in (4), we make the simplifying approximation $|u_{e3}|^2 \ll |u_{e1,2}|^2$ and we set $|u_{e3}|^2 \approx 0$. After a few straightforward algebraic manipulations and using the central values of (4), we can write the following approximate expressions [4]

$$|\langle m_\nu\rangle| \cong m_1 \left| \frac{3}{4} + \frac{1}{4} e^{i\phi_2} \left(1 + \frac{\delta m_{\mathrm{solar}}^2}{2m_1^2}\right) \right| \tag{5}$$

for the case of "normal" hierarchy and

$$|\langle m_\nu\rangle| \cong \sqrt{m_1^2 + \delta m_{\mathrm{atm}}^2} \left| \frac{3}{4} e^{i\phi_2} + \frac{1}{4} e^{i\phi_3} \right| \tag{6}$$

in the "inverted" hierarchy case. There is of course no evidence favoring either hierarchy. In Table 1, we show the predicted central values of $\langle m_\nu\rangle$ as a function of the lightest neutrino mass eigenvalue, m_1. These values define the desired target sensitivities of next generation $0\nu\beta\beta$-decay experiments. The Majorana ^{76}Ge experiment is designed to reach deep into the mass range of interest.

2. GENERAL DESCRIPTION OF THE MAJORANA EXPERIMENT

The proposed Majorana detector is an array of Ge detectors with a total mass of 500 kg of Ge that is isotopically enriched to 86% in ^{76}Ge. The final configuration is not fixed; however, several have been evaluated with respect to cryogenic performance and background reduction and rejection. This discussion will concentrate on a conventional modular design using ultralow-background cryostat technology developed by the International Germanium Experiment (IGEX). It will also utilize new pulse-shape discrimination hardware and software techniques developed by the collaboration and detector segmentation to reduce background.

The most sensitive $0\nu\beta\beta$-decay experiments thus far have been the Heidelberg–Moscow [5] and IGEX [6] ^{76}Ge projects that set lower limits on $T_{1/2}^{0\nu}$ of 1.9×10^{25} and 1.6×10^{25} yr, respectively. They both utilized Ge enriched to 86% in ^{76}Ge and operated deep underground. The projection is that the Majorana background will be reduced by a factor of 50 over

Table 1. Central values of $\langle m_\nu \rangle$ (in meV) for the range of interest of m_1 ($m_1 < m_2 < m_3$), using the approximate Eqs. (5), (6)*

Normal hierarchy ($m_1 \simeq m_2 \ll m_3$)				Inverted hierarchy ($m_3 \simeq m_2 \gg m_1$)			
$e^{i\phi_2} = -1$		$e^{i\phi_2} = +1$		$e^{i\phi_2} = -e^{i\phi_3}$		$e^{i\phi_2} = +e^{i\phi_3}$	
m_1	$\|\langle m_\nu \rangle\|$	m_1	$\|\langle m_\nu \rangle\|$	m_1	$\|\langle m_\nu \rangle\|$	m_1	$\|\langle m_\nu \rangle\|$
0	2.09	0	2.09	0	22.4	0	44.7
20	10.0	20	20.0	20	24.5	20	49.0
40	20.0	40	40.0	30	26.9	30	53.9
60	30.0	60	60.0	75	43.7	75	87.3
80	40.0	80	80.0	100	54.8	100	109.5
100	50.0	100	100.0	200	102.5	200	204.9
200	100.0	200	200.0	400	201.2	400	402.5
400	200.0	400	400.0				

* The value for $m_1 = 0$ was calculated prior to the expansion.

the early IGEX data prior to pulse-shape analysis (from 0.2 to 0.011 counts/(keV kg yr)). This will occur mainly by the decay of the internal background due to cosmogenic neutron spallation reactions that produce ^{56}Co, ^{58}Co, ^{60}Co, ^{65}Zn, and ^{68}Ge in the germanium by limiting the time above ground after crystal growth, careful material selection, and electroforming copper cryostats. One component of the background reduction will arise from the granularity of the detector array. In Fig. 1, an option for a detector configuration is shown for one module. Each of these modules would have three levels of 19 detectors in a close-packed array. Each detector is 62 mm in diameter and 70 mm long with a mass of ~ 1.1 kg. In Fig. 2, an alternative cooling option is shown which clusters all the detectors in a copper vacuum chamber which can then be cooled by immersing the chamber in a vessel of liquid nitrogen or in a jacket of cooled gas.

3. RECENT PROGRESS IN Ge DETECTOR TECHNOLOGY

Majorana will not simply be a volume expansion of IGEX. It must have superior background rejection and better electronic stability. The summing of 200 to 250 individual energy spectra can result in serious loss of energy resolution for the overall experiment. In IGEX, instabilities lead to a degradation of 25% in the energy resolution of the 117 mol yr of data. The collaboration has overcome these problems and the technology is now available. First, detectors electronically segmented into 12 individual volumes in a

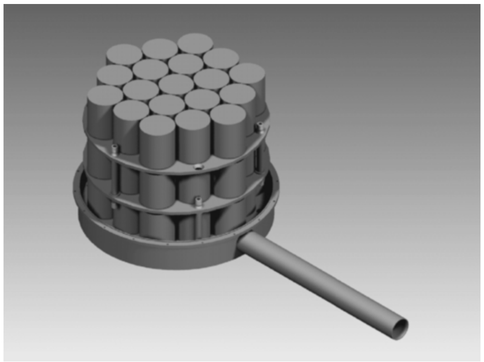

Fig. 1. Possible 57-crystal module. Each crystal is contained in its own copper can.

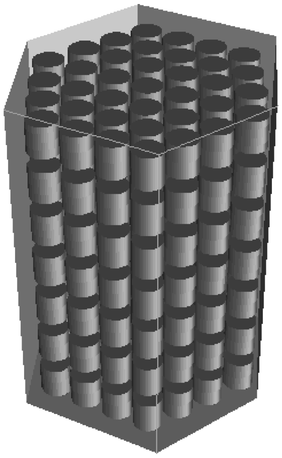

Fig. 2. Alternative cooling scheme. Crystals are grouped in a single copper cryostat.

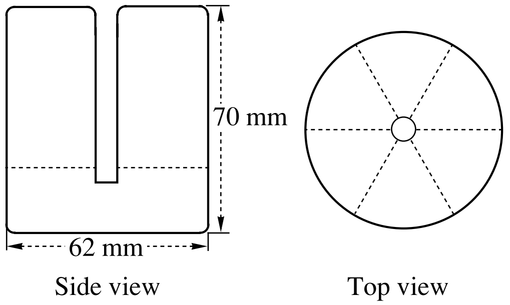

Fig. 3. A six-by-two twelve-segment detector.

single n-type intrinsic Ge detector are available from two companies: Advanced Measurement Technology (ORTEC) and Canberra Industries. Second, completely digital electronics from XIA (X-ray Instrumentation Associates) has been used by our group to demonstrate unprecedented stability, very low energy thresholds (<1 keV) for a 2-kg Ge detector, and a vast improvement in pulse-shape discrimination.

In the few years since the production of the 2-kg IGEX intrinsic Ge detectors, the new technology has evolved in the two industrial companies known to us. Large semicoaxial n-type detectors have been fitted with a series of azimuthal electrical contacts along their length, and one or more axial contacts in the central hole. A configuration with six-azimuthal-segment by two-axial-segment geometry is shown in Fig. 3. After Monte Carlo studies and discussions with detector manufacturers, several configurations are available that the Majorana Collaboration believes strike a good balance between cost, background reduction, and production efficiency. The six-by-two configuration in Fig. 3 was used in the Monte Carlo simulations that produced the data shown in Fig. 4 for a single detector. The internal ^{60}Co modeled in the figure is produced by cosmic-ray neutrons during the preparation of the detector. Formation begins after the crystal is pulled. Its elimination by segmentation and pulse-shape analysis is crucial.

The saga of pulse-shape discrimination (PSD) in the IGEX project has been slow and painful, finally culminating in success. Current techniques depend entirely on experimental calibration and do not utilize pulse-shape libraries. The ability of these techniques to be easily calibrated for individual detectors makes them practical for large detector arrays.

A major contributor to this success has been the availability of commercial digital spectroscopy hardware. Digitizing a detector preamplifier signal, all subsequent operations on the signal are performed digitally. Programmable digital filters are capable of producing improved energy resolution, long-term stability, and excellent dynamic range. The particular unit used in these studies was the four-channel Digital Gamma Finder (DGF-4C) unit developed and manufactured by XIA Inc. The DGF-4C has four independent, 14-bit 40-MHz ADCs. The ADCs are followed by first-in first-out (FIFO) buffers capable of storing 1024 ADC values for a single event. In parallel with each FIFO is a programmable digital filter and trigger logic. The digital filter and trigger logic for each channel is combined into a single field programmable gate array (FPGA). Analog input data are continuously digitized and processed at 40 MHz. The DGF-4C is then a smart filter of incoming pulses. If, for example, a signal has a pulse width incompatible with the usual collection time of 200–300 ns or is oscillatory (like microphonic noise), the filters can be programmed to reject it. This feature can also be used to allow the very low energy thresholds required in dark matter searches as well as eliminating the broad spectrum of artificial pulses from high-voltage leaks and electromagnetic interference that can even add noise pulses in the region of $0\nu\beta\beta$ decay.

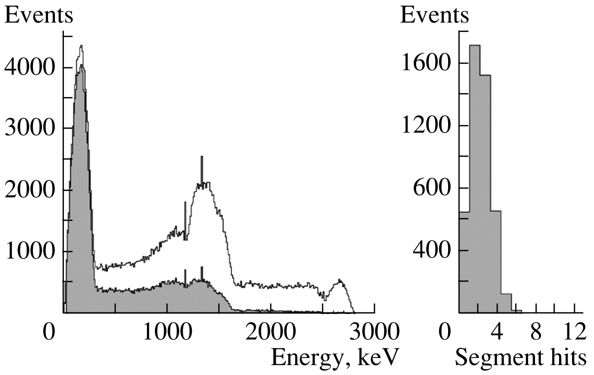

Fig. 4. Monte Carlo simulation of internal ^{60}Co background. Left shows a spectrum before (light) and after (gray) a one-segment-only cut is applied. Right shows a histogram of number of segments hit for events falling in 2.0–2.1 MeV ROI.

The 14-bit ADCs produce pulse forms that allow the discrimination between single-site interactions in the detector crystal, characteristic of $0\nu\beta\beta$ decay, and the multiple-site interactions characteristic of most gamma-ray background events near 2 MeV. Experimental example pulses are shown in Fig. 5. An example single-site event from the 1592-keV double-escape peak of the ^{208}Tl 2615-keV line is shown as the bottom signal. The top signal is an example multisite pulse from the full energy peak of the ^{212}Bi line at 1620 keV.

4. ULTIMATE SENSITIVITY OF THE MAJORANA EXPERIMENT

To estimate the sensitivity of the Majorana experiment we begin with the published spectrum from an

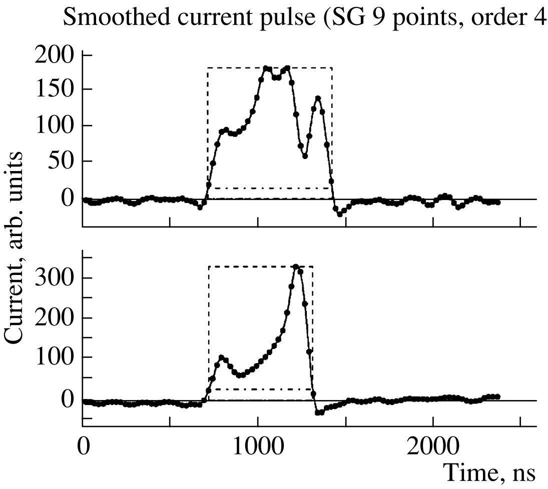

Fig. 5. The top pulse is due to a multiple-location ionization deposit; the bottom pulse is due to a localized deposit.

enriched IGEX germanium detector that had been operated under 4000-mwe shielding from cosmic rays [7]. The components of the background were computed based on the use of validated spallation mechanisms and rates [8]. The computed rate in the region of interest ($R_c = 0.29$ counts/(keV kg yr)) from the spallation isotopes actually exceeded the experimentally measured count rate ($R_e = 0.1$ counts/(keV kg yr)). Therefore, a conservative estimate of 0.2 counts/(keV kg yr) has been taken as an intermediate value. In practice, lower values would be possible by keeping high-energy neutrons away from the raw enriched material and by fabricating the detector underground.

It is instructive to scale the count rate of the previous experiment to that of the initial Majorana plan, a 500-kg detector operated for 10 years. We correct that rate to account for the decay of activities that will occur before and during the experiment. Finally, we correct the rate to account for the new technologies that we plan to employ.

The detector used for these sensitivity estimates had been zone refined, so that the ^{60}Co ($T_{1/2} = 5.2$ yr) inside the crystal, created by cosmic-ray-generated neutrons, was expected to be low. But the detector had been above ground long enough before zone refining to reach equilibrium with respect to ^{68}Ge ($T_{1/2} = 271$ d), another important internal contaminant. The first reduction in this background rate comes from decay during the underground array construction period. This has been calculated using a modest rate of production and assuming quarterly shipments of enriched material during the construction period. Decay during the construction period underground would decrease the ^{68}Ge by an average factor of 0.24 and an additional factor of 0.11 during the data acquisition of the experiment. Similarly, ^{60}Co would decay during construction to reduce the count rate to 0.73 of the original rate by the start of the experiment, and during the 10-yr data acquisition, the average rate during the experiment would be 0.55 times that at the beginning. Thus, accounting for decay, the average background rate during the experiment would be 0.01 counts/(keV kg yr). Thus, the effect of predeployment decay is effectively a reduction of 94%, or a factor of 17.8.

The number of ^{76}Ge atoms in 500 kg of enriched germanium (86% ^{76}Ge) is $N = 3.41 \times 10^{27}$. The optimum energy window of $\delta E = 3.568$ keV is expected to capture 83.8% of the events in a sharp peak at 2039 keV. If $B = b\delta EN\delta t$ and δt is 10 years, we would expect to observe 199 background counts.

The next step in estimating the sensitivity of the experiment is to apply two new but easily implemented techniques. The first is the pulse-shape-analysis technique discussed above. This method has been shown to accept $\varepsilon_{\mathrm{PSD}} = 80.2\%$ of single-site pulses (like double-beta decay) and to reject 73.5% of background. The second technique involves the electrical segmentation of the detector crystal to form several smaller segments as discussed earlier. A simplified Monte Carlo analysis, assuming the efficiency $\varepsilon_{\mathrm{PSD}}$ is independent of that of segmentation, $\varepsilon_{\mathrm{SEG}}$, was carried out only to count the segments with significant energy deposition and reject events with a multiplicity greater than one. This cut accepted $\varepsilon_{\mathrm{SEG}} = 90.7\%$ of double-beta decay pulses and rejected 86.2% of backgrounds like ^{60}Co and ^{68}Ge, which are highly multiple. Applying the background reduction factors to the simple calculation above, only 7.28 counts of the original 199 counts survive in our 3.568-keV analysis window, a reduction of 96.3%, or a factor of 27.3 (Table 2).

The estimated background is ~ 7.3 events; therefore, the sensitivity of the experiment is $\sim 3.8 \times 10^{27}$ yr at 90% C.L. because we predict that 3.7 events will be the maximum number attributable to $0\nu\beta\beta$ decay to a 90% C.L. The computation of the $0\nu\beta\beta$ half-life must then take into account this number of observable counts, the cut efficiencies, and the fraction of the $0\nu\beta\beta$-decay peak found in the analysis window. Thus,

$$T_{1/2} = \frac{\ln 2 \cdot N\Delta t\varepsilon_{\mathrm{PSD}}\varepsilon_{\mathrm{SEG}} \cdot 83.8\%}{3.72} = 3.8 \times 10^{27}\ \mathrm{yr}. \qquad (7)$$

Table 2. Estimation of sources of activity from early IGEX data and predicted Majorana background

Spallation isotope	$T_{1/2}$, d	Rate, counts/(keV kg yr)			Counts		
		from [7]	after construction	during experiment	total in ROI	after PSD rejection	after seg. rejection
^{68}Ge	270.82	0.1562	0.03702	3.93×10^{-3}	70.15	18.59	2.57
^{56}Co	77.27	0.0238	0.00212	6.43×10^{-5}	1.15	0.30	0.04
^{60}Co	1925.2	0.0177	0.01294	7.15×10^{-3}	127.55	33.80	4.66
^{58}Co	70.82	0.0024	0.000202	5.60×10^{-6}	0.10	0.03	0.00
Total		0.2	0.0523	0.0112	198.95	52.72	7.28

A standard relation between the half-life and the effective Majorana mass of the electron neutrino is

$$\langle m_\nu \rangle = \frac{m_e}{\sqrt{F_N T_{1/2}}}, \qquad (8)$$

where F_N is a nuclear factor computed by various authors. The variety of nuclear calculations gives a range of observable effective Majorana neutrino mass from 0.02 to 0.07 eV. Later, we present an update of the status of nuclear matrix elements.

Many other formulations of this sensitivity calculation are possible. For instance, it is possible to calculate the expected rate of background due to cosmogenic isotopes in the crystal assuming many different scenarios producing far less initial background. This is a reasonable approach and it would lead to a lower starting background. It is possible, however, to hypothesize away all backgrounds without regard to the effort involved. We chose to start with a known, reproducible starting point so that the result would be credible and attainable. The many details of the technologies involved ranging from lead bricks to multidimensional parametric pulse analysis are too lengthy to be described here.

The calculations in this section have covered in some detail the effects of backgrounds on a 5000-(kg yr) experiment in which the mass is 500 kg and the time is 10 yr. A completely different approach would be to consider ways of reducing the time needed to complete the experiment by allowing different total masses of enriched material. In this approach, one might optimize not for lowest cost but for shortest total time to completion, including construction. Many details are not considered in this estimate, such as increased labor costs and increased detector production costs. Figure 6 shows the results of a simple analysis with background rates similar to [7]. Rates of enrichment above 200 kg/yr are purely hypothetical, but might be reached by employing more than one Russian enrichment facility. This simple analysis shows that a significantly reduced schedule is possible with greater investment in enrichment.

5. EXTRACTION OF THE NEUTRINO-MASS PARAMETER FROM DOUBLE-BETA DECAY HALF-LIVES

The two key goals of $0\nu\beta\beta$-decay experiments are (i) to determine whether neutrinos are Majorana particles and (ii) to measure the neutrino mass eigenvalues. The latter requires nuclear matrix elements, which must be calculated with specific nuclear models. It is now widely accepted that nuclides that are $\beta\beta$-decay candidates, ^{76}Ge, ^{100}Mo, ^{130}Te, and ^{136}Xe, for example, are above the nuclear shells where current versions of the nuclear shell model are reliable; however, ^{76}Ge is probably the best candidate for future shell-model calculations of $0\nu\beta\beta$-decay matrix elements. Nevertheless, at present, we must rely on schematic models until the development of microscopic models is more advanced. In 1986, Vogel and Zirnbauer introduced the quasiparticle random phase approximation (QRPA) [9]. Since then, there have been many developments and variations, frequently with widely disparate results.

Frequently, bounds on $\langle m_\nu \rangle$ are extracted from experimental limits on $0\nu\beta\beta$-decay half-lives using nuclear matrix elements from all or many available nuclear models. The results can vary by factors of three or more. This is not satisfactory because it does not account for theoretical progress. An example of the variation in extracted values is clearly seen in Table 3.

Until now, conventional wisdom has held that knowledge of $2\nu\beta\beta$-decay rates would not be useful in determining $0\nu\beta\beta$-decay matrix elements, because the intermediate nuclear states are very different. Recently, however, Rodin, Faessler, Simkovic, and Vogel showed that, in the context of QRPA and renormalized QRPA (RQRPA), this is not the case [28]. They make a well-documented case that: “When

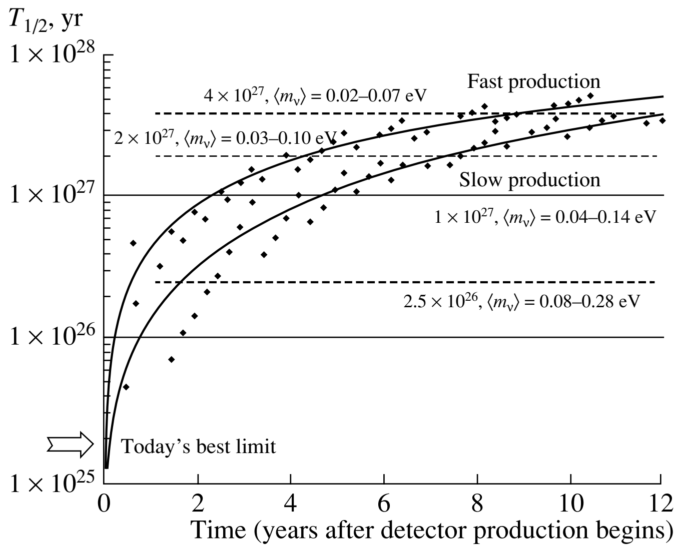

Fig. 6. Sensitivity vs. time of the Majorana reference plan using conservative background assumptions. The upper curve assumes a production of germanium of 200 kg/yr for a total of 500 kg. Milestones in half-life are shown at 0.25, 1.0, 2.0, and 4.0 × 10^{27} yr. Scatter about the trend lines is due to the integer nature of the Poisson distribution.

the strength of the particle—particle interaction is adjusted so that the $2\nu\beta\beta$-decay rate is correctly reproduced, the resulting $M^{0\nu}$ values become essentially independent of the size of the basis and of the form of different realistic nucleon—nucleon potentials. Thus, one of the main reasons for variability of the calculated $M^{0\nu}$ within these methods is eliminated."

Accordingly, one would conclude that accurate measurements of $2\nu\beta\beta$-decay half-lives will have a very meaningful impact on the predictions of $0\nu\beta\beta$-decay matrix elements in the same nuclei. Contrary to previous conventional wisdom, accurate $2\nu\beta\beta$-decay measurements may now be very important in the realm of neutrino physics. Rodin *et al.* investigated the effect of the choice of the single-particle (s.p.) space on $M^{0\nu}$ and also used three different realistic nucleon—nucleon interactions utilizing the Bonn-CD [29], the Argonne [30], and the Nijmegen [31] potentials. The result is that $M^{0\nu}$ varies very little over the nine different combinations of s.p. space and interaction.

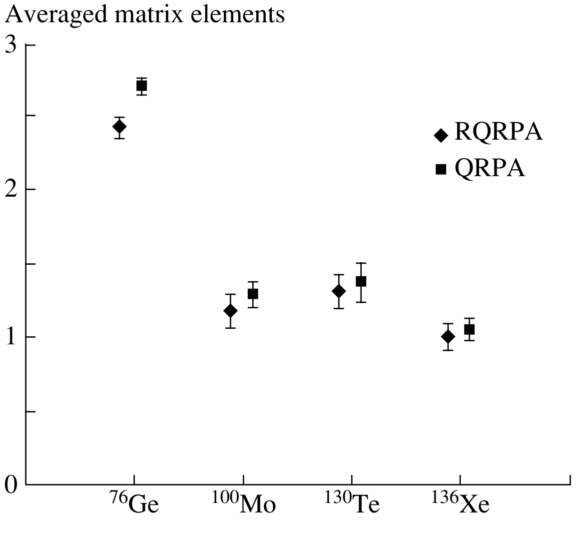

Fig. 7. Results of the nuclear matrix calculations of Rodin *et al.* [28].

The effects of neglecting s.p. states further from the Fermi level were investigated for ^{76}Ge, ^{100}Mo, ^{130}Te, and ^{136}Xe. In the case of interest here, ^{76}Ge, the three s.p. spaces used were (i) the 9 levels of the oscillator shells $N = 3$ and 4; (ii) the addition of the $N = 2$ shell; and, finally, (iii) the 21 levels from all states in the shells with $N = 1$, 2, 3, 4, and 5. For each change in s.p. space, the residual interaction must be adjusted by adding a pairing interaction and a particle—hole interaction renormalized by an overall strength parameter, g_{ph}. The value $g_{ph} \sim 1$ was found to reproduce the giant Gamow—Teller resonance in all cases. Finally, QRPA equations include the effects of particle—particle interaction, renormalized by an overall strength parameter g_{pp} that, in each case, was adjusted to reproduce the known $2\nu\beta\beta$-decay rate correctly. Figure 7 clearly shows the unprecedented stability against variations in the model space and in the realistic nucleon—nucleon interaction used.

Finally, we use these results to compute the predicted sensitivity of the Majorana experiment to the effective Majorana mass of the electron neutrino. In the notation of [28], $\langle m_\nu \rangle = [|M^{0\nu}|(G^{0\nu}T^{0\nu}_{1/2})^{1/2}]^{-1}$.

Table 3. Values of the nuclear structure parameter $F_N G^{0\nu} |M_{\rm F}^{0\nu} - (g_A/g_V)^2 M_{\rm GT}^{0\nu}|^2$ calculated with different nuclear models (the effective Majorana mass of the electron neutrino, $\langle m_\nu \rangle$, is given for $T_{1/2}^{0\nu}(^{76}\mathrm{Ge}) = 4 \times 10^{27}$ yr)

F_N, yr^{-1}	$\langle m_\nu \rangle$, eV	Reference
1.58×10^{-13}	0.020	[10]
2.88×10^{-13}	0.015	[11]
1.12×10^{-13}	0.024	[12]
1.12×10^{-13}	0.024	[13]
1.18×10^{-13}	0.024	[14]
6.97×10^{-14}	0.031	[15]
7.51×10^{-14}	0.029	[15]
1.90×10^{-14}	0.059	[16]
1.42×10^{-14}	0.068	[17]
7.33×10^{-14}	0.030	[17]
2.75×10^{-14}	0.049	[18]
1.33×10^{-13}	0.022	[19]
8.29×10^{-14}	0.028	[20]
8.27×10^{-14}	0.028	[21]
6.19×10^{-14}	0.032	[22]
2.11×10^{-13}	0.018	[22]
1.16×10^{-13}	0.024	[23]
5.22×10^{-14}	0.035	[24]
$(2.70\text{–}3.2) \times 10^{-15}$	0.155–0.143	[25]
$(1.80\text{–}2.2) \times 10^{-14}$	0.060–0.054	[25]
$(5.50\text{–}6.3) \times 10^{-14}$	0.034–0.032	[25]
1.21×10^{-14}	0.073	[26]
1.85×10^{-14}	0.059	[26]
3.63×10^{-14}	0.042	[26]
6.50×10^{-14}	0.032	[26]
7.57×10^{-14}	0.029	[27]

They give $|M^{0\nu}| = 2.40 \pm 0.07$ (RQRPA) and $|M^{0\nu}| = 2.68 \pm 0.06$ (QRPA) with $G^{0\nu} = 0.30 \times 10^{-25}$ yr^{-1} eV^{-2}. If we choose the round number $T_{1/2}^{0\nu} = 4 \times 10^{27}$ yr for the predicted sensitivity of the Majorana experiment, then the values of the mass parameter corresponding to this half-life are $\langle m_\nu \rangle = 0.038 \pm 0.007$ eV using RQRPA and $\langle m_\nu \rangle = 0.034 \pm 0.006$ eV with QRPA. A very similar value, $\langle m_\nu \rangle = 0.028 \pm 0.005$ eV, results from using the matrix elements from the recent paper by Civitarese and Suhonen [32]. These values are well within the range of interest tabulated in Table 1, which implies that the Majorana experiment is predicted to reach well into the interesting range of neutrino mass. Should nature have placed the mass below this range, the Majorana array can be expanded and possibly upgraded with newer technology that may emerge, as intrinsic Ge detectors can be redeployed many times in different configurations.

REFERENCES

1. S. Pascoli and S. T. Petcov, Phys. Lett. B **544**, 239 (2002).
2. K. Cheung *et al.,* Phys. Lett. B **562**, 97 (2003).
3. J. N. Bahcall, M. C. Gonzales-Garcia, and C. Pena-Garay, J. High Energy Phys. **07**, 054 (2002); Phys. Rev. C **66**, 035802 (2002).
4. F. T. Avignone III and G. S. King III, in *Proceedings of the 4th International Workshop on Identification of Dark Matter, York, UK, 2002*, Ed. by N. J. Spooner and V. Kudryavtsev (World Sci., Singapore, 2003), p. 553.
5. L. Baudis *et al.*, Phys. Rev. Lett. **83,** 41 (1999); A small subgroup has published a claim of discovery. See: H. V. Klapdor-Kleingrothaus *et al.*, Mod. Phys. Lett. **110** (1), 57 (2002).
6. C. E. Aalseth *et al.*, Phys. Rev. D **65**, 092007 (2002).
7. R. L. Brodzinski *et al.*, J. Radioanal. Nucl. Chem. **193**, 61 (1995).
8. F. T. Avignone III *et al.*, Nucl. Phys. B (Proc. Suppl.) **28**, 280 (1992).
9. P. Vogel and M. R. Zirnbauer, Phys. Rev. Lett. **57**, 3148 (1986).
10. W. C. Haxton and G. F. Stephenson, Jr., Prog. Part. Nucl. Phys. **12,** 409 (1984).
11. T. Tomoda, A. Faessler, K. W. Schmid, and F. Grümmer, Nucl. Phys. A **452**, 591 (1986).
12. K. Muto, E. Bender, and H. V. Klapdor-Kleingrothaus, Z. Phys. A **334**, 187 (1989).
13. A. Staudt, K. Muto, and H. V. Klapdor-Kleingrothaus, Europhys. Lett. **13**, 31 (1990).
14. T. Tomoda, Rep. Prog. Phys. **54**, 53 (1991).
15. J. Suhonen, O. Civitarese, and A. Faessler, Nucl. Phys. A **543**, 645 (1992).
16. E. Caurier, F. Nowacki, A. Poves, and J. Retamosa, Phys. Rev. Lett. **77**, 1954 (1996).
17. G. Pantis, F. Simkovic, J. D. Vergados, and A. Faessler, Phys. Rev. C **53**, 695 (1996).
18. F. Simkovic, J. Schwinger, M. Veselsky, *et al.,* Phys. Lett. B **393**, 267 (1997).
19. M. Aunola and J. Suhonen, Nucl. Phys. A **643**, 207 (1998).
20. A. Faessler and F. Simkovic, J. Phys. G **24**, 2139 (1998).
21. C. Barbero, F. Krmpotic, A. Mariano, and D. Tadic, Nucl. Phys. A **650**, 485 (1999).
22. F. Simkovic, G. Pantis, J. D. Vergados, and A. Faessler, Phys. Rev. C **60**, 055502 (1999).
23. S. Stoica and H. V. Klapdor-Kleingrothaus, Eur. Phys. J. A **9**, 345 (2000).
24. J. Suhonen, Phys. Lett. B **477**, 99 (2000).

25. A. Bobyk, W. A. Kaminski, and F. Šimkovic, Phys. Rev. C **63**, 051301(R) (2001).
26. S. Stoica and H. V. Klapdor-Kleingrothaus, Nucl. Phys. A **694**, 269 (2001).
27. S. Stoica and H. V. Klapdor-Kleingrothaus, Phys. Rev. C **63**, 064304 (2001).
28. V. A. Rodin, A. Faessler, F. Šimkovic, and P. Vogel, Phys. Rev. C **68**, 044302 (2003).
29. R. Machleidt, Adv. Nucl. Phys. **19**, 189 (1989).
30. R. B. Wiringa, V. G. J. Stoks, and R. Schiavilla, Phys. Rev. C **51**, 38 (1995).
31. V. G. J. Stoks, R. A. M. Klomp, C. P. F. Terheggen, and J. J. de Stewart, Phys. Rev. C **49**, 2950 (1994).
32. O. Civitarese and J. Suhonen, nucl-th/0208005.

Physics of Atomic Nuclei, Vol. 67, No. 11, 2004, pp. 2011–2016. From Yadernaya Fizika, Vol. 67, No. 11, 2004, pp. 2033–2038.

DOUBLE-BETA DECAY AND RARE PROCESSES

First Results of a Search for the Two-Neutrino Double-Beta Decay of ^{136}Xe with High-Pressure Copper Proportional Counters*

Yu. M. Gavriljuk, A. M. Gangapshev, V. V. Kuzminov, N. Ya. Osetrova, S. I. Panasenko**[1]**, and S. S. Ratkevich**[1]*****

Baksan Neutrino Observatory, Institute for Nuclear Research, Russian Academy of Sciences, Russia

Received January 20, 2004

Abstract—A description of a low-background installation for a new stage of the experimental search for the $2\beta(2\nu)$ decay of ^{136}Xe with high-pressure copper proportional counters is presented. The first estimate of the decay half-life limit based on the data measured over 4140 h yields $T_{1/2} \geq 2.4 \times 10^{21}$ yr (90% C.L.).

There is a number of theoretically calculated half-lives for the two-neutrino double-beta decay of ^{136}Xe: 8.2×10^{20} [1], 1.1×10^{21} [2], and 1.5×10^{19}–2.1×10^{22} yr [3]. However, this process in ^{136}Xe has not yet been found. In 1999, a limit of $T_{1/2} \geq 8.3 \times 10^{20}$ yr (90% C.L.) was obtained by using three large wall-less high-pressure proportional counters (MWPC) [4]. Another limit of $T_{1/2} \geq 1.0 \times 10^{22}$ yr was obtained in 2002 in the experiment DAMA/LXe with a scintillation detector filled with liquid xenon enriched up to 68% in ^{136}Xe [5]. The first limit was found by analyzing the spectrum obtained by subtraction of the MWPC background spectrum (when the MWPC was filled with natural xenon, 9.2% ^{136}Xe) from the MWPC enriched sample spectrum (when the MWPC was filled with xenon enriched in ^{136}Xe to 93%). The expected effect of this comparison is a positive excess of events in the energy region of interest. The absence of such an excess within bounds of statistical errors allowed us to set the limit, provided that this error was considered as a maximum possible effect.

Only one spectrum was obtained in the second case. To calculate their limit, it was assumed that, at any effect-to-background ratio in the energy range under investigation, the effect did not exceed the actually measured background increased by a systematic error given in σ units (σ is a standard deviation). Actually, this method does not allow one to find the effect and could be used only to find a limit. To discover such an effect, it is necessary either to measure directly the background of the installation under the same conditions or to simulate the background. To perform the simulations, one should know the composition and activity of the background sources exactly, as well as the function of the detector response. It should be mentioned that, in the DAMA/LXe experiment, such work has not yet been done.

The sensitivity of the experimental installation with three MWPCs to the two-neutrino double decay is restricted by the proper background of the detectors made from a titanium alloy. Since the use of the MWPCs has already demonstrated high efficiency, it was decided to carry out a new stage of the experiment with copper proportional counters instead of titanium ones.

In [6], we presented our first results of a background measurement in the new copper proportional counters (CPC). Three CPCs were made according to the conventional scheme with one central anode and without the inner ring multiwire guard counter. Measurements were carried out in the old low-background shielding consisting of 15 cm of Pb, 8 cm of borated polyethylene (BP), and 12 cm of Cu. The installation is located in the underground laboratory of the Baksan Neutrino Observatory at a depth of 4900 m w.e.

The sensitivity (S) of the installation with new CPCs was increased by a factor of 3.8 in comparison with the sensitivity of the installation with MWPC. The background measured in the CPC located near the shield wall was found to be higher than the background of the central CPC. It was suggested that the reason is insufficient thickness of the copper shield

---

*This article was submitted by the authors in English.

[1] Kharkov National University, Kharkov, Ukraine.

**e-mail: `bno_vvk@mail.ru`

***e-mail: `ratkevich@univer.kharkov.ua`

Table

Counter and series	Gas	^{136}Xe, 10^{24} atoms	Δt, h	ΔN, events (0.8–1.8 MeV)	Rn, events	ΔN − Rn, events
X1	^{136}Xe	3.56	2070	1433	197	1236
X2	$^{\mathrm{nat}}$Xe	0.35	2070	1579	328	1251
Y1	$^{\mathrm{nat}}$Xe	0.35	2070	1087	247	840
Y2	^{136}Xe	3.56	2070	1200	440	760

layer (the central CPC is separated from near-shield wall counters by a copper layer of 8 cm on all sides).

Synchronous change of the counting rates in the two CPCs under investigation was found. Such behavior can be explained by change in the ^{222}Rn content in the air cavities near the detectors. To minimize the detector counting rate caused by ^{222}Rn in the air, the low-background shielding was reconstructed. One CPC was taken out and the resulting free space was used to increase the copper layer thickness from 12 to 20 cm. A layer of polyethylene film was inserted between the lead and BP and glued at the end walls of the copper shield to the organic glass walls. A system to blow the inner hermetic volume of the CPC shield with liquid nitrogen vapor was made. Two LA-n10M6 double-channel digital oscilloscopes with a dynamical amplitude range of $2^8 \times (1-256)$ were introduced into the recording system.

A high voltage (3.8 kV) is applied to the anode of the CPC. The signals are taken out with charge-sensitive preamplifiers (CSP) from the both ends of the anode wire of each CPC (signals PC1 and PC2) through high-voltage separating capacitors. They further go to the inputs of the amplifiers containing three parallel output channels: the shaping amplifier (SA), the fast amplifier without shaping (FA), and the differential discriminator (DD). Signals from the SA outputs are applied to the inputs of the amplitude digital converter (ADC), and signals from the FA outputs are applied to inputs of the LA-n10M6 and simultaneously (via the summer and additional SA) to the separate ADC. Standard pulses from the DD outputs related to one CPC are applied to the inputs of the coincidence circuit (CC). The latter generates a starting signal in the corresponding digital oscilloscope (DO). Such switching-on allows us to significantly diminish (by a factor of 10) the volume of information recorded in the experiment for it eliminates a false pulse from single (PC1 or PC2 only) noise or induced pulses.

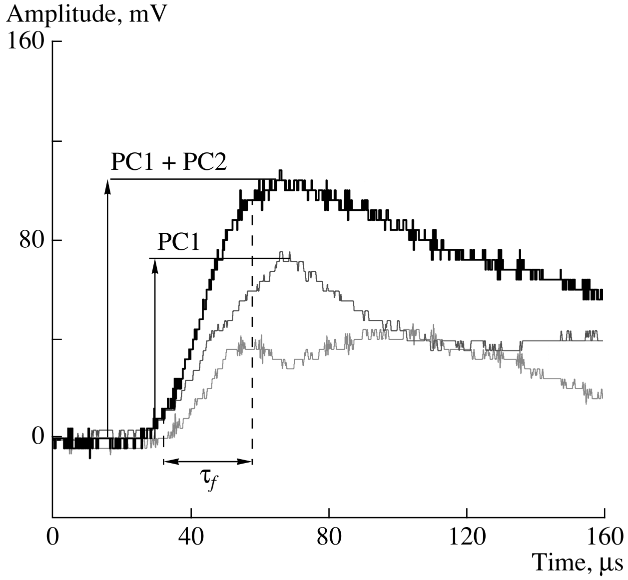

Fig. 1. Shapes of coinciding pulses from both CSPs of the CPC (PC1 and PC2).

Such pulses have opposite polarity at the CPS outputs because of the CPS inputs connected to a closed circuit through the anode resistance. A current passing through this resistance has opposite directions at the CPS inputs. Simultaneously, due to the same reason, pulses caused by microdischarges in the high-voltage separating capacitors forming a series chain in relation to the CPS inputs are excluded. High-voltage bringing circuits have an equivalent capacitor parallel to the CSP inputs. Microdischarges in this capacitor give pulses of the same polarity in both CSPs. Separating them from ionization pulses and then rejecting them is possible in two independent ways. First, they differ from working pulses in their shape. Second, pulses of microdischarges have a coordinate along the anode wire which is located outside the working length of the anode. The coordinate is determined as the ratio PC1/(PC1 + PC2). Values of the PC1 and PC2 signals at the same summed amplitude are determined as the ratio of resistance of the shoulders of the anode wire from the place of the avalanche formation to the ends of the anode. Information coming from all ADCs is recorded in the personal computer memory and used mainly to control the installation work stability. Four ADCs record the amplitude of pulses which pass through SA with integration (τ_i) and differentiation (τ_d) times equal to

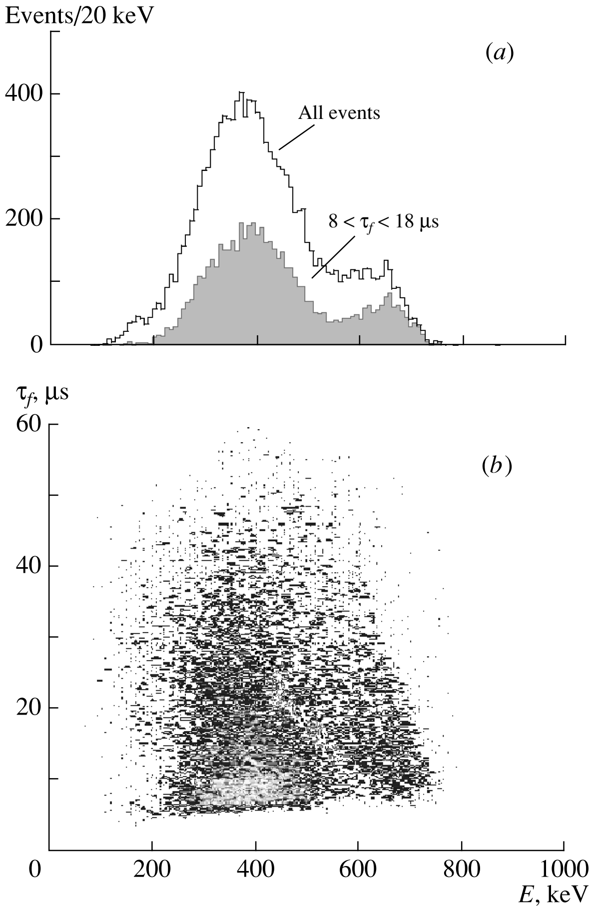

Fig. 2. (*a*) Amplitude spectra of the pulses from the ^{137}Cs source (662 keV) and (*b*) distribution of event intensity vs. energy E and τ_f.

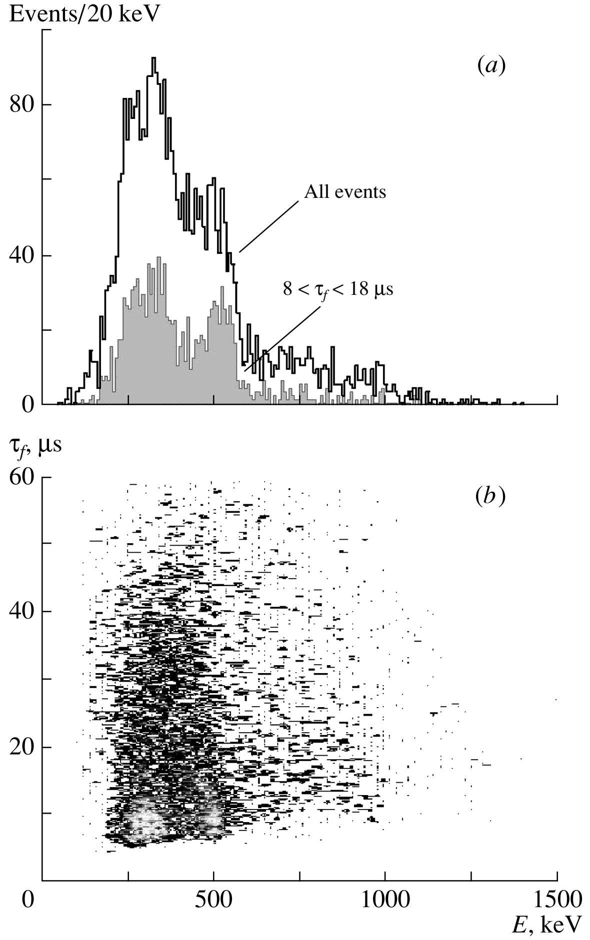

Fig. 3. (*a*) Amplitude spectra of the pulses from the ^{22}Na source (511, 1275 keV) and (*b*) distribution of event intensity vs. energy E and τ_f.

24 μs. Such values of shaping time were chosen in order to decrease the influence of the CPC pulse front duration on the energy resolution. The fifth ADC is used to calibrate amplitudes of the signals registered by the DO as well as to obtain information about pulse fronts. The calibration is carried out with the 511-keV line of the ^{22}Na source. During the calibration, τ_i and τ_d in the SA of the fifth channel are set to 12 μs. The line of 511 keV is set into the 511 ± 4 channel by gain justification in the FA channels of the input amplifiers. The necessity of such calibration of the DO is caused by a poor accuracy of their direct calibration due to a small number of DO digital channels (256). The shaping times $\tau_i = 0$ and $\tau_d = 0.75$ μs were used in the main measurements. The amplitudes of the pulses (P12) formed in such a way depend on the rise time of the input pulses. While analyzing all ADC data, the P12/(PC1 + PC2) ratio is used to select pulses according to their form. Additional information about the characteristics of the recording devices can be found in [7].

Shapes of coinciding pulses from both CSPs of the same CPC are presented in Fig. 1 as an example. Those shapes are recorded by the two-channel DO. Points of determination of the parameters PC1, PC2, and τ_f (front duration within 10 to 90% of maximum amplitude) are marked.

The length of the recording interval is 1024 channels. The frequency of polling was chosen to be 6.25 MHz (160 ns/channel). The amplitude (PC1 + PC2) corresponds to the energy of 511 keV. Comparing shapes of pulses PC1 and PC2, one can see an antiphase harmonic component, whose origin is associated with mutual influence of the preamplifiers. The phase and amplitude of this harmonic process depend on the high-voltage filters and preamplifier input circuit parameters. This component is totally compensated in the sum signal (PC1 + PC2). Amplitude spectra of the pulses from a ^{137}Cs source (662 keV) are presented in Fig. 2*a*. The upper spectrum includes all the events, the low spectrum includes the events with $8 \le \tau_f \le 18 \mu$s. The distri-

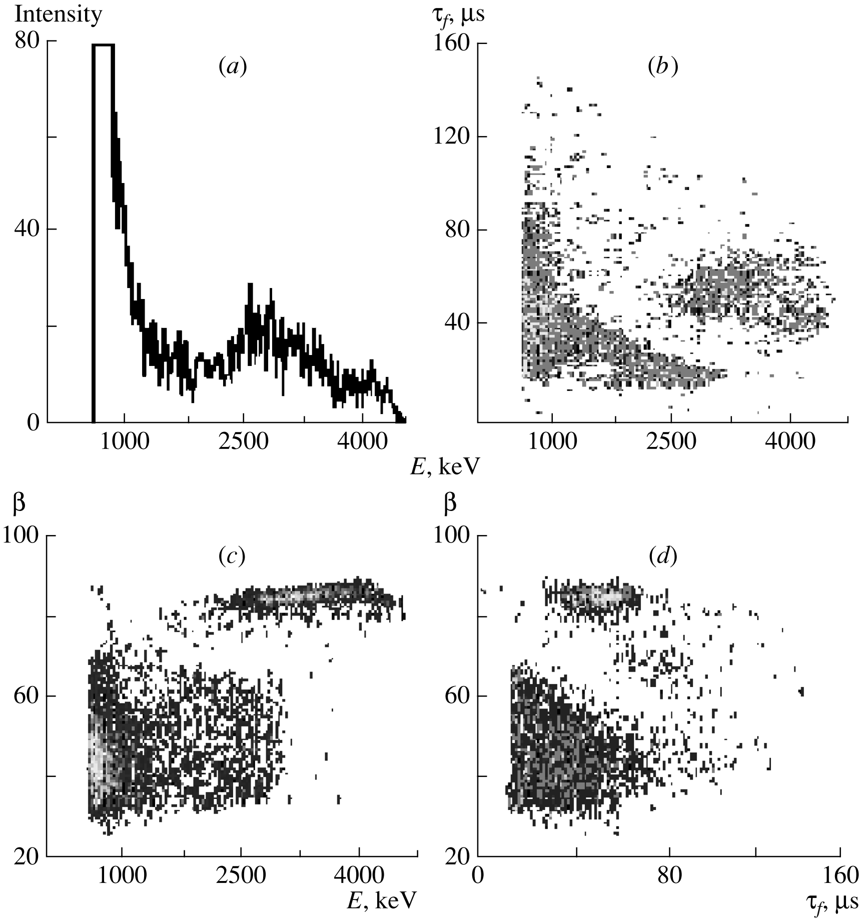

Fig. 4. Background event distributions in counter X for the first series X1 collected over 2070 h: (*a*) an amplitude spectrum; (*b*) distribution of activity in coordinates (τ_f, E); (*c*) distribution in coordinates ($\beta = 100 \cdot \mathrm{PC1}/(\mathrm{PC1} + \mathrm{PC2})$, E); (*d*) distribution in coordinates (β, τ_f).

bution of event intensity (I) vs. energy (E) and τ_f is shown in Fig. 2*b* (one single point corresponds to one single event). It can be seen from Fig. 2*a* that resolution of the 662-keV line of the low spectrum (12.5%) is noticeably better than that of the upper one. The reason for this distinction becomes clear if we look at Fig. 2*b*, where the amplitude of the pulses (with energy of 662 keV) decreases while the front duration increases. In general, this decrease could be explained by discharge of the feedback capacitor $C_{\mathrm{o.c.}}$ in the CSP during the time of collection of ionization electrons from the track of a primary particle. The size of the track in its projection onto the radius which determines the collection time depends on the orientation and the form of the track. The mean distance of the track to the anode determines the increase in the size of the ionization electron cloud due to diffusion while the cloud is drifting to the anode. The larger the size of the track in its projection onto the radius and the greater its distance from the anode, the longer the front of the pulses and the more noticeable the contribution of the $C_{\mathrm{o.c.}}$ discharge. This influence could simply be corrected through the data processing.

Other possible causes of the amplitude dependence on the front duration are in the process of clarification. Similar distributions for the ^{22}Na source (511, 1275 keV) are presented in Fig. 3. In the main measurement, both CPCs were filled with xenon samples up to 14.8 atm. In the first series, counter 1 (or X) was filled with the enriched xenon sample (93% ^{136}Xe) and counter 2 (or Y) was filled with xenon depleted of light isotopes (9.2% ^{136}Xe). During the process of light isotope depletion, radioactive ^{85}Kr was removed as well. The measurement time in the first series was 2070 h. After 45 days had passed since filling the counters, the main measurements were started. During this starting phase of the experiment, different methodical measurements were carried out. At the same time, this period served as a pause before the main measurements, as it was during this phase that the nonequilibrium ^{222}Rn born in the purification

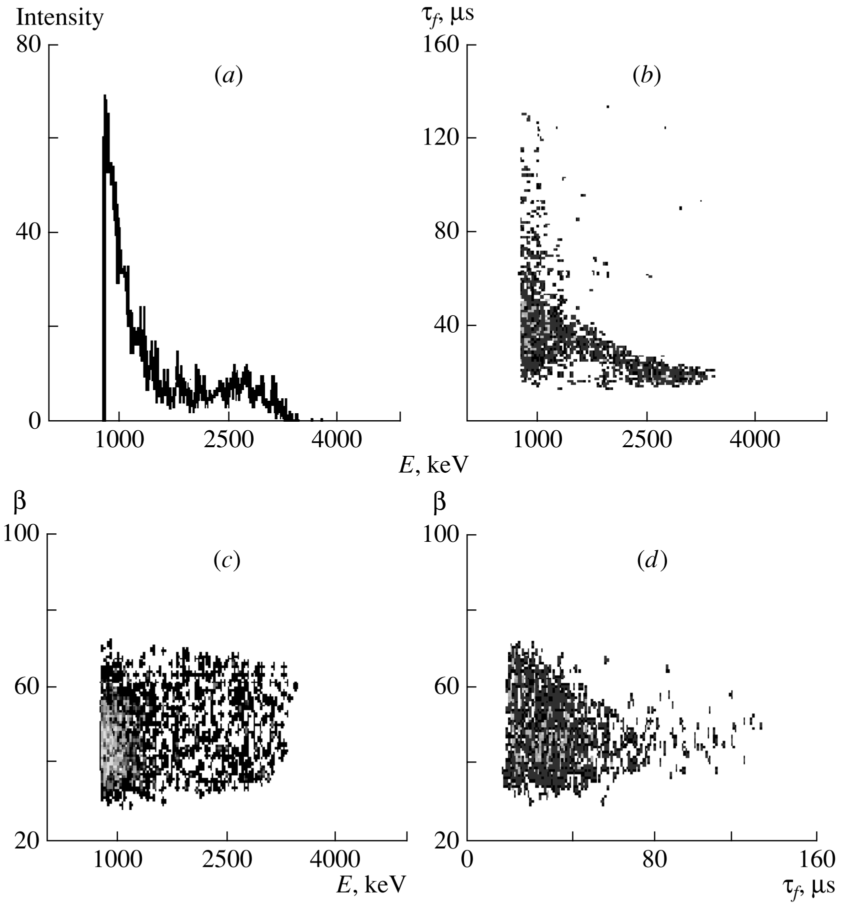

Fig. 5. Event selection carried out in the interval $30 \leq \beta \leq 70$ in counter X for the first series X1 collected over 2070 h.

system and carried into the counters together with the purified xenon was decaying.

Background event distributions in the counter X for the first series X1 collected over 2070 hours are shown in Fig. 4. There are distributions of (a) an amplitude spectrum; (b) intensity in coordinates (τ_f, E); (c) intensity in coordinates ($\beta = 100 \cdot \mathrm{PC1}/(\mathrm{PC1} + \mathrm{PC2})$, E); and (d) intensity in coordinates (β, τ_f) in Fig. 4. Events with the parameter $\beta \leq 23$ were preliminarily excluded from consideration (the length of the anode working part is $30 \leq \beta \leq 70$). They are associated with microdischarges at the output PC2 of the counter. Their number greatly exceeded the number of other events, thus complicating the understanding of the whole picture. Events with $\beta > 70$ caused microdischarges at the output PC1 of the counter. Event selection in the interval $30 \leq \beta \leq 70$ allows us to eliminate this background component completely. The results of this selection are shown in Fig. 5. In the amplitude spectrum (Fig. 5a) at the energy ~2.7 MeV, one can see a peak corresponding to alpha particles generated in the decay process of equilibrium ^{222}Rn, its daughter ^{218}Po and ^{214}Po. An oblique stripe in the (τ_f, E) distribution (Fig. 5b) is due to alpha particles. This source of the background is considered in more detail in a separate work [8]. The contribution of these alpha particles can be subtracted from the total background of the counter.

Measurements for the second series were started immediately after refilling of the counters. During the first ~400 h, a damping contribution of nonequilibrium ^{222}Rn decay to the event intensity time distribution was observed.

Out of the total sampling of measurements in the second series (2815 h), the data collected during the interval 745–2815 h (2070 h) were taken out in order to compare with the data of the first series. The spectra of the background and its event distribution vs. β and τ_f for the X and Y counters in both series are presented in Fig. 6: (a) background of the counter X in the first (X1) and second (X2) series; (b) event distribution in the spectrum (a) vs. front duration (τ_f); (c) event distribution in spectrum (a) vs. the parameter β. Spectra (d)–(f) depict the same for the counter Y. In both cases, the event selection was carried out by using the pulse shape. This is a reason

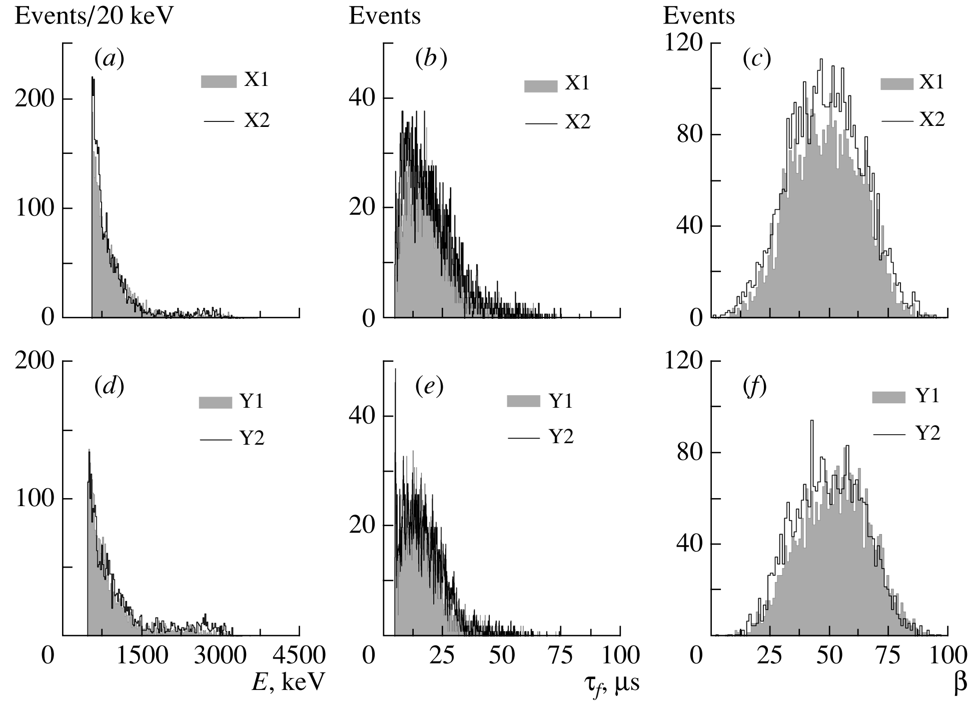

Fig. 6. Obtained spectra of the background and its event distribution vs. β and τ_f for X and Y counters in both series: (*a*) background of the counter X in the first (X1) and second (X2) series; (*b*) event distribution in the spectrum (*a*) vs. front duration (τ_f); (*c*) event distribution in the spectrum (*a*) vs. the parameter β. (*d*)–(*f*) Spectra depict the same for the counter Y.

why a part of low-energy events (due to noise) has the parameter β outside the working range.

The table presents the counter background, as well as the ^{222}Rn contribution, for the first and second series in the energy range 0.8–1.8 MeV.

The result of background subtraction for the counter X $(\Delta N\ \mathrm{X1} - \mathrm{Rn\ X1}) - (\Delta N\ \mathrm{X2} - \mathrm{Rn\ X2})$ is equal to $-15 \pm 56(\mathrm{stat.})^{+22}_{-19}(\mathrm{syst.})$. The analogous result for the counter Y is equal to $-80 \pm 54(\mathrm{stat.})^{+68}_{-59}(\mathrm{syst.})$. The systematic errors are caused by possible shift in calibration of each spectrum within ±0.5 channel. The increased systematic error for the counter Y is explained by recording of pulses in the first and second series with different DOs.

The combined result for the time measurement of 4140 h is -95^{+108}_{-102}. The mean-square error adjusted to one year of measurement is 229.

Considering the efficiency of the event detection $\varepsilon = 0.417$ in the interval 0.8–1.8 MeV, the half-life limit is yielded by the expression

$$T_{1/2} \geq (0.693 \cdot 3.21 \times 10^{24} \cdot 0.417)/1.645\bar{\sigma}$$
$$= 2.4 \times 10^{21}\ \mathrm{yr}\,(90\%\ \mathrm{C.L.}).$$

ACKNOWLEDGMENTS

The work is in process and is supported by the Russian Foundation for Basic Research (project no. 01-02-16069).

REFERENCES

1. J. Engel, P. Vogel, and M. Zirnbauer, Phys. Rev. C **37**, 731 (1988).
2. O. Rumjantsev and M. Urin, Phys. Lett. B **443**, 51 (1998).
3. Z. Staudt, K. Muto, and H. V. Klapdor-Kleingrothaus, Europhys. Lett. **13**, 31 (1990).
4. Yu. M. Gavriljuk, V. V. Kuzminov, N. Ya. Osetrova, and S. S. Ratkevich, Phys. Rev. C **61**, 035501 (2000).
5. R. Bernabei *et al.*, Phys. Lett. B **546**, 23 (2002).
6. A. Kh. Apshev *et al.*, in *Proceedings of the XI International School on Particles and Cosmology, Baksan Valley, Kabardino-Balkaria, Russia, 2001*; Preprint No. 96-105, INR RAS (Moscow, 2003).
7. G. V. Volchenko *et al.*, Instrum. Exp. Tech. **42**, 34 (1999).
8. Yu. M. Gavriljuk, A. M. Gangapshev, V. V. Kuzminov, *et al.*, this Conference.

Physics of Atomic Nuclei, Vol. 67, No. 11, 2004, pp. 2017–2020. From Yadernaya Fizika, Vol. 67, No. 11, 2004, pp. 2039–2042.

DOUBLE-BETA DECAY AND RARE PROCESSES

Analysis of α-Particle Background Events in a High-Pressure Proportional Counter*

Yu. M. Gavriljuk, A. M. Gangapshev, V. V. Kuzminov,**
N. Ya. Osetrova, S. I. Panasenko[1], and S. S. Ratkevich[1]
Baksan Neutrino Observatory, Institute for Nuclear Research, Russian Academy of Sciences, Russia
Received January 20, 2004

Abstract—The results of amplitude spectrum measurement and data processing of ^{222}Rn and its daughter nucleus decays in a high-pressure copper proportional counter filled with xenon at a pressure of 14.8 atm are given. The preliminary estimates of the α/e ratio for different E/P values are also presented. *© 2004 MAIK "Nauka/Interperiodica".*

1. INTRODUCTION

A new search for $2\beta(2\nu)$ decay of ^{136}Xe is performed at the Baksan Neutrino Observatory. Two large proportional counters made of copper (CPC) are used as detectors [1]. The background in this experiment is substantially reduced in comparison with the previous experiment with titanium proportional counters [2]. The first measurements showed that the CPC intrinsic background is mostly due to the ^{222}Rn and ^{222}Rn daughter nucleus decays in the working gas. The ^{222}Rn is generated by ^{226}Ra impurities in the CPC inner construction materials. To define the amplitude spectrum shape of ^{222}Rn and its daughter nucleus decays, as well as to determine the contribution of α-particle events to the background of the CPC, a special measurement was carried out.

2. EXPERIMENTAL SETUP

The measurement was carried out with a CPC filled with xenon at a pressure of 14.8 atm. The ^{222}Rn was added to the xenon during the filling procedure. The CPC is usual cylindrical proportional counter with an inner diameter of 140 mm and diameter of the anode wire of 10 μm. The operating length of the counter is equal to 595 mm. The CPC is inside the low-background shielding of Pb (15 cm), borated polyethylene (8 cm), and Cu (12 cm) layers. It is located in an underground laboratory at a depth of 4900 m w.e. The applied voltage is 3800 V. The gas amplification factor is about 55. Signals PC1 and PC2 are read out from both ends of the anode wire through the preamplifiers and applied to the LA-n10M6 digital oscilloscope through the amplifiers. This readout system allowed us to determine a relative coordinate along the anode wire by the equation $\beta = \mathrm{PC1}/(\mathrm{PC1}+\mathrm{PC2})$. The parameter β is used to reject events of microdischarges both in the outward high-voltage circuits and on the anode insulator surfaces. The amplitude spectrum was constructed as the sum $A = \mathrm{PC1}+\mathrm{PC2}$. The pulse rise time ($\tau_f$) was also used for the data analysis (Fig. 1).

In Fig. 2, the decay chain of ^{222}Rn up to ^{210}Pb is shown. The calculated track lengths of the α particles with the energy 5.49, 6.00, and 7.69 MeV are equal to 1.7, 2.0, and 2.7 mm, respectively. The time delay between the first and the last electrons from the

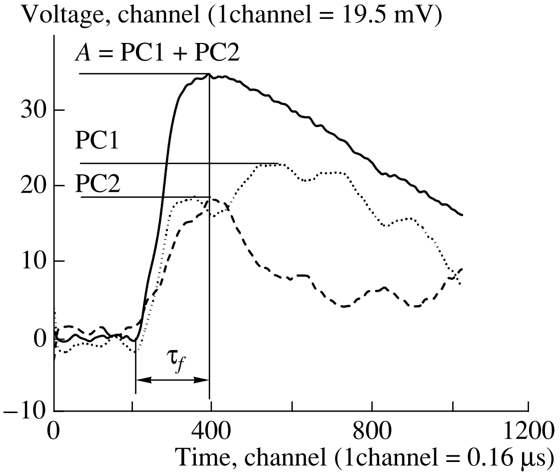

Fig. 1. Sample of pulses. The pulse-rise-time parameter τ_f (from $0.03A$ to A) is marked.

---

*This article was submitted by the authors in English.

[1] Kharkov National University, Kharkov, Ukraine.

**e-mail: `gangapsh@list.ru`

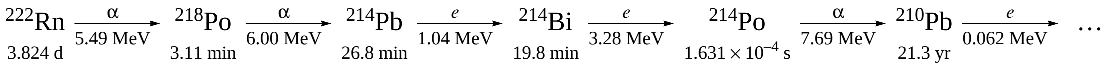

$$\underset{3.824\text{ d}}{^{222}\text{Rn}} \xrightarrow[5.49\text{ MeV}]{\alpha} \underset{3.11\text{ min}}{^{218}\text{Po}} \xrightarrow[6.00\text{ MeV}]{\alpha} \underset{26.8\text{ min}}{^{214}\text{Pb}} \xrightarrow[1.04\text{ MeV}]{e} \underset{19.8\text{ min}}{^{214}\text{Bi}} \xrightarrow[3.28\text{ MeV}]{e} \underset{1.631\times10^{-4}\text{ s}}{^{214}\text{Po}} \xrightarrow[7.69\text{ MeV}]{\alpha} \underset{21.3\text{ yr}}{^{210}\text{Pb}} \xrightarrow[0.062\text{ MeV}]{e} \ldots$$

Fig. 2. The decay chain of ^{222}Rn up to ^{210}Pb.

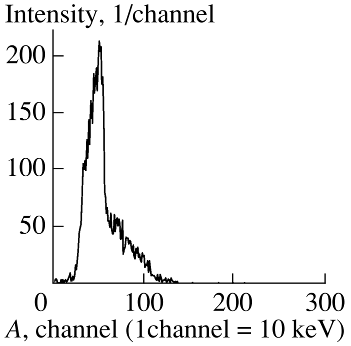

Fig. 3. The amplitude spectrum of ^{22}Na source.

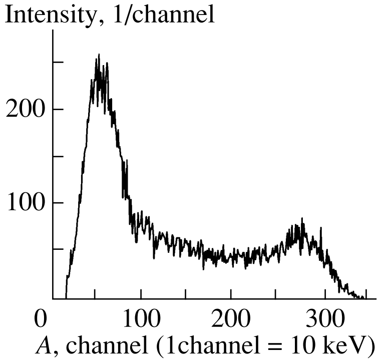

Fig. 5. The amplitude spectrum of ^{222}Rn and its daughter nucleus decays.

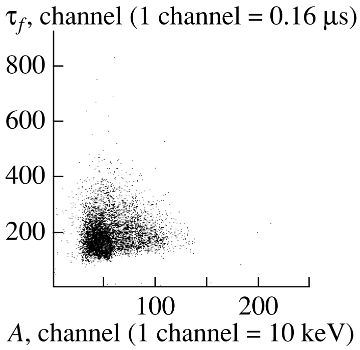

Fig. 4. The A–τ_f distribution of ^{22}Na events.

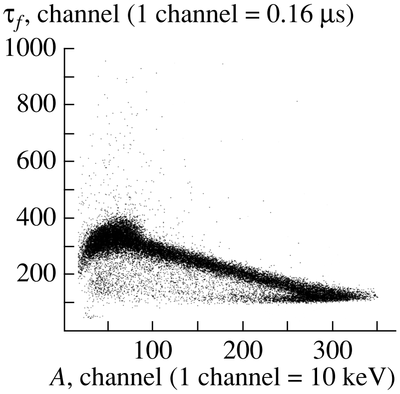

Fig. 6. The A–τ_f distribution of events from ^{222}Rn and its daughter nucleus decay.

α-particle track depends on the track length, distance between the track center and the anode wire (radius), and the track orientation.

3. RESULTS

The calibration of the CPC was performed with a ^{22}Na source (511 keV, 1275 keV). The measured amplitude spectrum and the A–τ_f distribution of the ^{22}Na events are shown in Figs. 3 and 4, respectively. The detection threshold is about 300 keV. In Fig. 5, the amplitude spectrum of ^{222}Rn is shown. The wide peak around channel 270 (2.7 MeV) is due to the α particles from ^{222}Rn and its daughter nucleus decays. Moreover, most of the spectrum at smaller energies is due to the α particles. The mechanism of spectrum formation and structure of the spectrum can be clarified from the analysis of the A–τ_f distribution (Fig. 6). The contribution of the CPC intrinsic background to the measured spectrum is negligible; therefore, the measurements were carried out for only 108 h.

The shape of the A–τ_f distribution of events in Fig. 6 can be described in the following way. The charged ^{218}Po ions appear after the ^{222}Rn decays and drift to the electrodes according to their charges. Therefore, there are three areas where the α-active nuclei decay. First is the gas between the anode wire and the cathode, where most of the events are due to ^{222}Rn decays. Second is the anode wire surface, where negatively charged ^{218}Po and other ions are deposited. Third is the cathode surface, where positively charged ^{218}Po and other ions are deposited.

We assume that daughter atoms of the ^{218}Po decay do not change their charge and stay on the same electrode. It is necessary to note that, in our case, the charge distribution of the ^{218}Po ions, after decay of

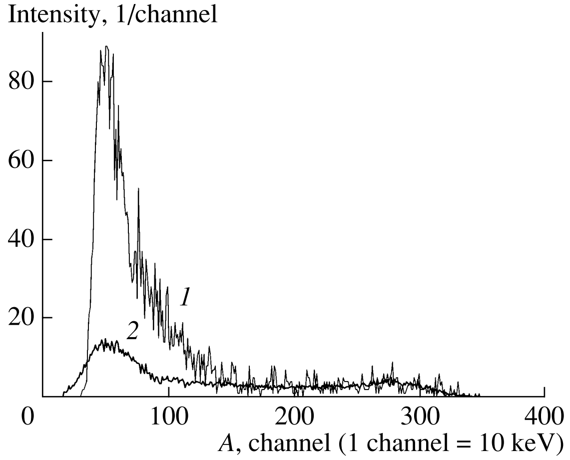

Fig. 7. The background spectrum (*1*) of CPC measured for 1600 h in comparison with ^{222}Rn spectrum (*2*).

^{222}Rn in xenon, is unknown. The number of ^{218}Po ions deposited at the anode could be less because of a loss of electrons by the ions in an extremely strong electric field near the anode. Both the recombination factors in a track of the α particle and the collection time of the electrons from this track depend on the radius in accordance with the dependence of the electric field strength on the radius.

Therefore, the events from the first region give pulses with different τ_f and A and compose a "road" in Fig. 6 which connects two high-event density areas (small τ_f—large A and large τ_f—small A).

The events from the second region give pulses with small τ_f and large A. Since the recombination effect is minimal because of the strong electric field in this area, there are also ^{222}Rn events at a radius of less than 10 mm. In this area, the value of the collected charge from the tracks of the α particles is connected with recombination of electrons with mother and neighboring ions. The energy scale in Fig. 5 is calibrated by pulses from the electrons. The maximum of the α peak corresponds to the energy of 2.7 MeV. If this peak is due to the α particles from the ^{222}Rn decay (5.49 MeV), then half of the primary ionization electrons are captured by mother ions. The recombination of the electrons with the avalanche ions is also possible. The values of these effects depend on the electron cloud density, while the density of the cloud depends on both the value of the recombination effect in the primary track and the cloud size (the cloud expands during drift to the anode due to diffusion of electrons). Some of the α particles lose their energy when going through the anode.

The events from the third region give pulses with large τ_f and small A. Events of the copper surface alpha activity are also in that region. Some events

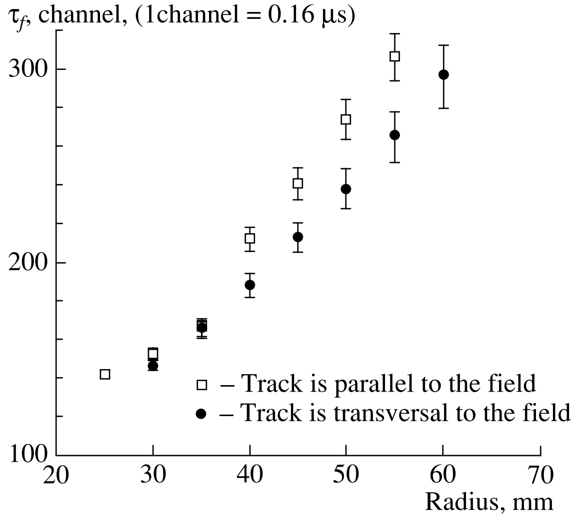

Fig. 8. The dependence of τ_f on radius for 5.49-MeV α particles.

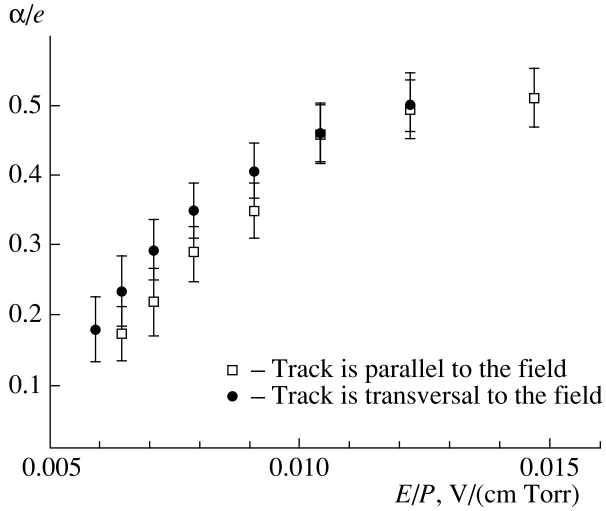

Fig. 9. The dependence of α/e ratio on E/P for 5.49-MeV α particles.

with an amplitude higher than 0.75 MeV are connected with the electrons from β decays of ^{214}Pb ($\approx$1%) and ^{214}Bi ($\approx$30%) [3, 4]. If β decay takes place at the anode, all the electrons give a contribution to the spectrum, while the β decay at the cathode allows half of the electrons to go into the cathode material. In Fig. 6, the events from the electrons give the rare-point area background. For the energy region of 0.75–1.80 MeV, $\approx$12% of events in the spectrum are due to the electrons (Fig. 5).

In Fig. 7, the background spectrum (*1*) in one of the CPCs measured for 1600 h is presented in comparison with the ^{222}Rn spectrum (*2*). Spectrum *2* is normalized to spectrum *1* by using the sum of events with amplitudes higher than 2.00 MeV. The ratio of the event number of spectrum *2* to that of spectrum *1* is equal to ≈ 0.34 in the energy region of 0.75–1.80 MeV, where the possible effect from $2\beta(2\nu)$ decay of ^{136}Xe is expected.

The precise knowledge of the ^{222}Rn spectrum is very important when the equilibrium radon content changes in time. The possible reason for the change could be some fluctuation of the temperature of the surrounding environment and counters, as well as some fluctuation of the amount of dust microparticles from the gas cleaning system after refilling of the counters. Therefore, it is necessary to subtract the intrinsic ^{222}Rn contribution from the background spectra before comparing different CPC spectra.

The A–τ_f distribution of events in Fig. 6 was used to determine the α/e ratio for different electric field strength and different angles between track axes and the electric field strength line. The dependence of τ_f on radius and track orientation was calculated (Fig. 8). Afterwards, the α/e ratio was determined. To exclude α events from the cathode and the anode, only events with $\tau_f > 135$ channel and $A > 90$ channel were used in the analysis. The results are presented in Fig. 9.

ACKNOWLEDGMENTS

The work is supported by the Russian Foundation for Basic Research (project nos. 01-02-16069 and 02-02-16136mas).

REFERENCES

1. Yu. M. Gavriljuk, V. V. Kuzminov, N. Ya. Osetrova, and S. S. Ratkevich, Phys. Rev. C **61**, 035501 (2000).
2. A. Kh. Apshev *et al.*, in *Proceedings of the XI International School on Particles and Cosmology, Baksan Valley, Kabardino-Balkaria, Russia, 2001* (INR RAS, Moscow, 2003), p. 96.
3. A. Peisert and F. Sauli, CERN 84-08, *Experimental Physics Division 13* (1984).
4. *Beta-Radiation of Fission Products. A Handbook* (Atomizdat, Moscow, 1978), pp. 383, 384 [in Russian].

Physics of Atomic Nuclei, Vol. 67, No. 11, 2004, pp. 2021–2026. From Yadernaya Fizika, Vol. 67, No. 11, 2004, pp. 2043–2047.
Original English Text Copyright © 2004 by Raina, Shukla, Rath, Dixit, Chaturverdi, Chandra, Dhiman, Singh.

DOUBLE-BETA DECAY AND RARE PROCESSES

The *np* Interaction Effects on the Double-Beta Decay Nuclear Matrix Elements for Medium-Mass Nuclei*

P. K. Raina[1)]**, **A. Shukla**[1)], **P. K. Rath**[2)], **B. M. Dixit**[2)], **K. Chaturverdi**[2)], **R. Chandra**[2)], **S. K. Dhiman**[3)], and **A. J. Singh**[3)]

Received January 20, 2004; in final form, April 22, 2004

Abstract—The quality of Hartree–Fock–Bogolyubov wave functions is tested by comparing the theoretically calculated results with the available experimental data for a number of spectroscopic properties like yrast spectra, reduced $B(E2)$ transition probabilities, quadrupole moments, and g factors for the nuclei involved in $2\nu\beta\beta$ decay. It is observed that the np interactions vis-à-vis the deformations of the intrinsic ground states of medium-mass nuclei play a crucial role in the fine tuning of the nuclear matrix elements $M_{2\nu}$. *© 2004 MAIK "Nauka/Interperiodica".*

It is well established by now that the implications of nuclear $\beta\beta$ decays are far reaching in nature in general. Neutrinoless $\beta\beta$ decay in particular is one of the very rare promising processes to test the physics beyond the Standard Model (SM) of fundamental particles. These aspects of nuclear $\beta\beta$ decay have been excellently elaborated in a number of review articles over the past years [1–8].

$2\nu\beta\beta$ decay, a second-order process of weak interaction that conserves the lepton number exactly, is allowed in the SM. The half-life of $2\nu\beta\beta$ decay is a product of an accurately known phase space factor and appropriate nuclear transition matrix element $M_{2\nu}$. The half-lives of $2\nu\beta\beta$ decay have already been measured for about ten nuclei and the values of $M_{2\nu}$ can be extracted directly. Consequently, the validity of different models employed for nuclear structure calculations can be tested by calculating the $M_{2\nu}$.

It is observed that, in all cases, the $2\nu\beta\beta$-decay matrix elements are sufficiently quenched. The main motive of all the theoretical calculations is to understand the physical mechanism responsible for the suppression of the $M_{2\nu}$. The $M_{2\nu}$ is calculated mainly in three types of models. One is the shell model and its variants. The second is the quasiparticle random phase approximation (QRPA) and extensions thereof. The third type is classified as the alternative models. The details about these models—their advantages as well as shortcomings—have been excellently discussed by Suhonen and Civitarese [5] and Faessler and Simkovic [6].

All the nuclei undergoing $\beta\beta$ decay are of even–even type. Hence, the pairing degrees of freedom play an important role. Moreover, it has been conjectured that the deformation can play a crucial role in $\beta\beta$-decay rates. Hence, it is desirable to have a model that incorporates the pairing and deformation degrees of freedom on equal footing in its formalism. For this purpose, the projected Hartree–Fock–Bogolyubov (PHFB) model is one of the most natural choices. Coincidentally, most of the $\beta\beta$-decaying nuclei fall in the medium-mass region. The success of the PHFB model in explaining the observed experimental trends in this mass region has motivated us to apply the PHFB wave functions to the study of nuclear $\beta\beta$ decay as well.

The mass region $A \approx 100$ provides us with a nice example of shape transitions [9], where, at one end, nuclei can be described in terms of shell model wave functions involving a small number of configurations and, at the other end of this region, we find good evidence of rotational collectivity. These nuclei lie between doubly magic ^{132}Sn and strongly deformed ^{100}Zr, near which the structural changes are rather rapid with the addition of protons and neutrons. In the past, there have been many attempts [10–15] to explore the factors responsible for the structural changes in this mass region.

Federman and Pittel [14] computed the deformation energy in the framework of Hartree–Fock–Bogolyubov (HFB) theory in conjunction with the surface delta interaction (SDI), suggesting that the neutron–proton (np) interaction in the spin–orbit

---

*This article was submitted by the authors in English.

[1)] Department of Physics and Meteorology, IIT, Kharagpur, India.

[2)] Department of Physics, University of Lucknow, Lucknow, India.

[3)] Department of Physics, H. P. University, Shimla, India.

[**] e-mail: `pkraina@phy.iitkgp.ernet.in`

partner (SOP) orbits $1g_{9/2}$ and $1g_{7/2}$ in this case may be instrumental vis-à-vis the onset of deformation in Mo isotopes with $A > 100$. A systematic study of the behavior of the low-lying collective states of neutron-rich even Cd, Pd, Ru, and Mo isotopes has led to the conclusion that these structural changes are related to the exceptionally strong np interaction in this region. It has also been observed that the np interactions among the SOP orbits have a deformation-producing tendency and the systematics of low-lying states are intricately linked with the nature of np interaction.

The sensitivity of the yrast spectra and the transition charge densities (TCD) to the np interaction strength has led to the fixing of these strengths very accurately and has been demonstrated [15] through the examples of ^{110}Cd and ^{114}Cd. We have adopted this method for fixing the np strength of QQ interaction by looking at the spectra of the 2^+ state of the nuclei involved in $\beta\beta$ decay.

A large number of theoretical as well as experimental studies of $2\nu\beta\beta$ decay have already been done for $\beta^-\beta^-$ of ^{96}Zr, ^{100}Mo, ^{110}Pd, and ^{128,130}Te nuclei and e^+ $\beta\beta$ ($\beta^+\beta^+$, β^+EC, and ECEC) in the case of ^{96}Ru, ^{106}Cd, ^{124}Xe, and ^{130}Ba nuclei over the past few years with more emphasis on the ^{100}Mo and ^{106}Cd cases. $\beta\beta$ decay is not an isolated nuclear process. The availability of data permits a rigorous and detailed critique of the ingredients of the microscopic models used to provide a description of these nuclei.

We have studied $2\nu\beta\beta$ decay not isolatedly but together with other observed nuclear phenomena. This is in accordance with the basic philosophy of nuclear many-body theory, which is to explain all the observed properties of nuclei in a coherent manner. Hence, as a test of the reliability of the wave functions, we have calculated the yrast spectra, reduced $B(E2)$ transition probabilities, static quadrupole moments, and g factors and compared them with the available experimental data.

The theoretical formalism to calculate the half-life of the $2\nu\beta\beta$-decay mode has been given by Haxton and Stephenson [1], Doi *et al.* [2, 3], and Tomoda [4]. Very brief outlines of the calculation of nuclear transition matrix elements of the $\beta\beta$ decay in the PHFB model are presented here. Details of expressions used in calculation of spectroscopic properties can be found in Dixit *et al.* [16].

The half-life of $2\nu\beta\beta$ decay for the $0^+ \to 0^+$ transition is given by

$$\left[T_{1/2}^{2\nu}(0^+ \longrightarrow 0^+)\right]^{-1} = G_{2\nu}\left|M_{2\nu}\right|^2, \qquad (1)$$

where

$$M_{2\nu} = \sum_N \frac{\langle 0^+||\sigma\tau^+||1_N^+\rangle\langle 1_N^+||\sigma\tau^+||0^+\rangle}{E_N - (M_I + M_F)/2}, \qquad (2)$$

and the integrated kinematical factor $G_{2\nu}$ can be calculated with good accuracy [8]. If E_N is replaced by an average $\langle E_N\rangle$, the summation over intermediate states can be completed using the closure approximation and one obtains

$$\begin{aligned} M_{2\nu} &= -\frac{2M_{\rm GT}^{2\nu}}{\langle E_N\rangle - (M_I + M_F)/2} \qquad (3) \\ &= -\frac{2M_{\rm GT}^{2\nu}}{E_d}, \end{aligned}$$

where the double Gamow–Teller matrix element (DGT) $M_{\rm GT}^{2\nu}$ is defined as follows:

$$M_{\rm GT}^{2\nu} = \frac{1}{2}\left\langle 0^+ \left| \sum_{n,m} \sigma_n \cdot \sigma_m \tau_n^+ \tau_m^+ \right| 0^+ \right\rangle. \qquad (4)$$

Employing the HFB wave functions, one obtains the following expression for the $\beta\beta$ decay nuclear transition matrix element:

$$\begin{aligned} \langle M_{\rm GT}^{2\nu}\rangle &= [n_{Z-2,N+2}^{J_f=0} n_{Z,N}^{J_i=0}]^{-1/2} \qquad (5) \\ &\times \int_0^\pi n_{(Z,N),(Z-2,N+2)}(\theta) \\ &\times \frac{1}{4}\sum_{\alpha\beta\gamma\delta} \langle \alpha\beta\left|\sigma_1 \cdot \sigma_2 \tau^+\tau^+\right|\gamma\delta\rangle \\ &\times \sum_{\varepsilon\eta}\left[\left(1 + F_{Z,N}^{(\nu)}(\theta) f_{Z-2,N+2}^{(\nu)}\right)\right]_{\varepsilon\alpha}^{-1} (f_{Z-2,N+2}^{(\nu)})_{\varepsilon\beta} \\ &\times \left[\left(1 + F_{Z,N}^{(\pi)}(\theta) f_{Z-2,N+2}^{(\pi)}\right)\right]_{\gamma\eta}^{-1} (F_{Z,N}^{(\pi)})_{\eta\delta} \sin\theta d\theta, \end{aligned}$$

where

$$\begin{aligned} n^J &= \int_0^\pi \{\det[1 + F^{(\pi)}(\theta) f^{(\pi)\dagger}]\}^{1/2} \qquad (6) \\ &\times \{\det[1 + F^{(\nu)}(\theta) f^{(\nu)\dagger}]\}^{1/2} d_{00}^J(\theta)\sin(\theta)d\theta \end{aligned}$$

and

$$\begin{aligned} &n_{(Z,N),(Z-2,N+2)}(\theta) \qquad (7) \\ &= \{\det[1 + F_{Z,N}^{(\pi)}(\theta) f_{Z-2,N+2}^{(\pi)\dagger}]\}^{1/2} \\ &\times \{\det[1 + F_{Z,N}^{(\nu)}(\theta) f_{Z-2,N+2}^{(\nu)\dagger}]\}^{1/2}. \end{aligned}$$

The symbol π (ν) represents the proton (neutron). PHFB calculations are summarized by the coefficients (U_{im}, V_{im}) and $C_{ij,m}$ and their matrices $(F_{N,Z}(\theta))_{\alpha\beta}$ and $(f_{N,Z})$. The details can be found in [16].

In the present calculations, we treat the doubly even nucleus ^{76}Sr ($Z = N = 38$) as an inert core and the valence space is spanned by the orbits $1p_{1/2}$, $2s_{1/2}$, $1d_{3/2}$, $1d_{5/2}$, $0g_{7/2}$, $0g_{9/2}$, and $0h_{11/2}$ for protons and neutrons. The set of single particle energies (SPEs) but for $\varepsilon(0h_{11/2})$, which is slightly lowered, employed here is the same as that used in a number of successful shell model as well as variational model [10–16] calculations for nuclear properties in the mass region $A = 100$. The effective two-body interaction is the *PPQQ* type [17].

The strength of the pairing interaction is fixed through the relation $G_p = -30/A$ MeV and $G_n = -20/A$ MeV. These values of G_p and G_n have been used by Heestand *et al.* [18] to successfully explain the experimental $g(2^+)$ data of some even–even Ge, Se, Mo, Ru, Pd, Cd, and Te isotopes in Greiner's collective model [19]. The strengths of the like particle components of the QQ interaction are taken as $\chi_{pp} = \chi_{nn} = -0.0105$ MeV b^{-4}. These values for the strength of the interaction are comparable to those suggested by Arima [20] on the basis of an empirical analysis of the effective two-body interactions.

As an illustrative case, we look into the details of calculations for double-beta decay of the ^{100}Mo nucleus. χ_{pn} is varied so as to obtain the spectra of ^{100}Mo and ^{100}Ru in optimum agreement with the experimental results. In Table 1, we have presented the theoretically calculated yrast energies for levels of ^{100}Mo and ^{100}Ru for different values of χ_{pn}. It is clearly observed that, as χ_{pn} is varied by 0.0016 MeV b^{-4}, E_2 decreases by 0.2942 MeV in the case of ^{100}Mo and 0.2152 MeV in the case of ^{100}Ru, respectively. This is understandable as there is an enhancement in the collectivity of the intrinsic state with the increase in $|\chi_{pn}|$; hence, E_2 decreases. The optimum values of χ_{pn} corresponding to ^{100}Mo and ^{100}Ru are 0.01906 and -0.01838 MeV b^{-4}, respectively. Thus, for a given model space, SPEs, G_p, G_n, and χ_{pp}, we have fixed χ_{pn} through the experimentally available energy spectra.

From the overall agreement [16] between the calculated and observed electromagnetic properties, it is clear that the PHFB wave functions of ^{100}Mo and ^{100}Ru generated by fixing χ_{pn} to reproduce the yrast spectra are quite reliable.

The double-beta decay of ^{100}Mo → ^{100}Ru for the $0^+ \to 0^+$ transition has been investigated by many experimental groups [22, 23] as well as theoreticians by employing different theoretical frameworks [24–26]. In Table 2, we have compiled some of the latest available experimental and theoretical results along with our calculated $M_{2\nu}$ and the corresponding half-life $T_{1/2}^{2\nu}$. We have used a phase space factor $G_{2\nu} = 9.434 \times 10^{-18}$ yr^{-1} given by Doi *et al.* [2] and an energy denominator $E_d = 11.2$ MeV given by Haxton *et al.* [1]. In the fourth column of Table 2, we have presented the $M_{2\nu}$ extracted from the experimentally observed $T_{1/2}^{2\nu}$ using the phase space factor given above. The phase space integral has been evaluated for $g_A = 1.25$ by Doi *et al.* [2]. However, in heavy nuclei, it is more justified to use a nuclear matter value of g_A around 1.0. Hence, the experimental $M_{2\nu}$ and the theoretical $T_{1/2}^{2\nu}$ are calculated for $g_A = 1.0$ and 1.25. The present calculation and that of Hirsch *et al.* [25] using $SU(3)$(SPH) give a nearly identical value. They are close to the experimental result given by De Silva *et al.* [22] for $g_A = 1.25$, while, for $g_A = 1.0$, the above two $M_{2\nu}$ are in agreement with the results of NEMO. The calculated values given by Stoica [24] using SRPA(WS) are too low and those from Suhonen *et al.* [26] are slightly on the higher side. Further, the value $M_{2\nu}$ given by Hirsch *et al.* [25] using $SU(3)$(DEF) favors the results of NEMO [23] for $g_A = 1.25$.

Table 1. Variation in excitation energies (in MeV) of $J^\pi = 2^+$, 4^+, and 6^+ yrast states for ^{100}Mo and ^{100}Ru nuclei with change in χ_{pn} keeping fixed $G_p = -0.30$ MeV, $G_n = -0.20$ MeV, and $\varepsilon(0h_{11/2}) = 8.6$ MeV

Nucleus	χ_{pn}, MeV b^{-4}	E_{2^+}	E_{4^+}	E_{6^+}
^{100}Mo	0.01826	0.6865	1.7028	2.9355
	0.01866	0.5851	1.5333	2.7213
	0.01906	0.5356	1.4719	2.6738
	0.01946	0.4493	1.3070	2.4560
	0.01986	0.3923	1.1861	2.2854
		0.5355*	1.1356*	
^{100}Ru	0.01758	0.6597	1.8175	3.2746
	0.01798	0.5923	1.6733	3.0615
	0.01838	0.5395	1.5591	2.8940
	0.01878	0.4930	1.4531	2.7329
	0.01918	0.4445	1.3372	2.5519
		0.5396*	1.2265*	2.0777*

* Experiment [21].

Another example we take for the $0^+ \to 0^+$ $e^+\beta\beta$ ($\beta^+\beta^+$, β^+EC, and ECEC) decay of ^{106}Cd → ^{106}Pd. This transition has also been investigated by many experimental groups and in different theoretical frameworks. In Table 3, we have compiled some of the

Table 2. Experimental half-lives, $T_{1/2}^{2\nu}$, and corresponding nuclear matrix elements, $M_{2\nu}$, along with the theoretical values in different models for $0^+ \to 0^+$ $2\nu\beta^-\beta^-$ decay of ^{100}Mo

Experiment				Theory				
Ref.	Project	$T_{1/2}^{2\nu}$, 10^{18} yr	$\lvert M_{2\nu}\rvert$	Ref.	Model	$\lvert M_{2\nu}\rvert$	$T_{1/2}^{2\nu}$, 10^{18} yr	
							(a)	(b)
[22]	UC-Irvin	$6.82^{+0.38}_{-0.53} \pm 0.68$	(a) $0.125^{+0.012}_{-0.009}$	[16]	PHFB	0.152	4.57	11.15
			(b) $0.195^{+0.014}_{-0.020}$	[24]	SRPA(WS)	0.059	30.4	74.3
[23]	NEMO	$9.5 \pm 0.4 \pm 0.9$	(a) $0.106^{+0.008}_{-0.007}$	[25]	$SU(3)$(SPH)	0.152	4.59	11.2
			(b) $0.165^{+0.013}_{-0.010}$	[25]	$SU(3)$(DEF)	0.108	9.09	22.2
[8]	Average	8.0 ± 0.7		[26]	QRPA(EMP)	0.197	2.73	6.67

Note: The numbers corresponding to (a) and (b) are calculated for $g_A = 1.25$ and 1.0, respectively.

Table 3. Experimental limit on half-lives $T_{1/2}^{2\nu}$ and corresponding extracted matrix elements $M_{2\nu}$ along with their theoretically calculated values for 2ν ($\beta^+\beta^+$, β^+EC, ECEC) decay of ^{106}Cd for the $0^+ \to 0^+$ transition

Decay mode	Experiment		Theory				
	Ref.	$T_{1/2}^{2\nu}$, yr	Ref.	Model	$\lvert M_{2\nu}\rvert$	$T_{1/2}^{2\nu}$, yr	
						(a)	(b)
$\beta^+\beta^+$	[27]	$>2.4 \times 10^{20**}$	[31]	PHFB	0.238	35.42×10^{25}	89.56×10^{25}
	[28]	$>1.0 \times 10^{19*}$	[32]	QRPA	0.166	$72.79 \times 10^{25***}$	$180 \times 10^{25***}$
	[29]	$>9.2 \times 10^{17}$	[28]	QRPA	1.226	1.33×10^{25}	3.3×10^{25}
β^+EC	[27]	$>4.1 \times 10^{20}$	[31]	PHFB	0.238	8.97×10^{21}	22.69×10^{21}
	[28]	$>0.66 \times 10^{19*}$	[32]	QRPA	0.169	$17.79 \times 10^{21***}$	$44.0 \times 10^{21***}$
	[29]	$>2.6 \times 10^{17}$	[33]	$SU(4)$	0.198	13.00×10^{21}	32.15×10^{21}
ECEC	[30]	$>5.8 \times 10^{17}$	[31]	PHFB	0.238	11.24×10^{20}	28.42×10^{20}
			[32]	QRPA	0.169	$22.24 \times 10^{20***}$	$55.0 \times 10^{20***}$
			[33]	$SU(4)$	0.193	17.00×10^{20}	42.04×10^{20}

Note: The numbers corresponding to (a) and (b) are calculated for $g_A = 1.25$ and 1.0, respectively; * denotes the half-life limit for $0\nu + 2\nu$ mode, ** denotes the half-life limit for $0\nu + 2\nu + 0\nu M$ mode, and *** shows the half-life with WS potential.

latest available experimental [27–30] and theoretical results [31–33] along with our calculated $M_{2\nu}$ and corresponding half-lives $T_{1/2}^{2\nu}$. We have used phase space factors given by Doi and Kotani [3] and the average energy from Haxton and Stephenson [1]. Our calculated values are nearly half of the recently given QRPA results of Suhonen and Civitarese [32] for all the three modes. The theoretical values of PHFB and $SU(4)$ [33] are in better agreement (a factor of roughly two-thirds) for the β^+EC and ECEC modes.

From the above discussions, it is clear that the validity of nuclear models presently employed to calculate the $M_{2\nu}$ cannot be uniquely established due to error bars in experimental results as well as uncertainty in g_A. Further work is necessary on both the experimental and the theoretical front to judge the relative applicability, success, and failure of various

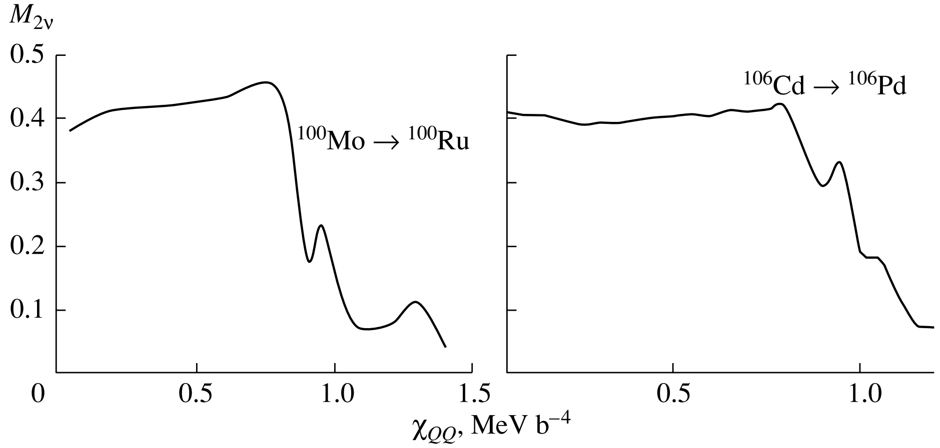

The dependence of $M_{2\nu}$ on the strength of quadrupole—quadrupole interaction χ_{QQ}.

models used so far for the study of double-beta decay processes.

As an example to see quantitatively the effect of deformation on $M_{2\nu}$ vis-à-vis the variation of the strength of the pn part of the QQ interaction, the results are displayed in the figure for the ^{100}Mo and ^{106}Cd cases. It is observed that the deformations of the HFB intrinsic states play an important role in the calculations of $M_{2\nu}$ and, hence, on the half-life.

To summarize, we have first tested the quality of HFB wave functions by comparing the theoretically calculated results for a number of spectroscopic properties of nuclei involved in double-beta decay. To be more specific we have computed the yrast spectra, reduced $B(E2)$ transition probabilities, quadrupole moments, and g factors. Some of the results have been presented for two very widely studied cases of $\beta^-\beta^-$ decaying ^{100}Mo and $e^+\beta\beta$ ($\beta^+\beta^+$, β^+EC, and ECEC) decaying ^{106}Cd nuclei. Reliability of the intrinsic wave functions for calculation of $2\nu\beta\beta$ nuclear matrix elements $M_{2\nu}$ has been discussed. Further, we have shown that the np interactions vis-à-vis the deformations of the intrinsic ground states of ^{100}Mo, ^{100}Ru, ^{106}Cd, and ^{106}Pd play important role in arriving at the appropriate nuclear matrix elements. A reasonable agreement between the calculated and observed spectroscopic properties as well as the $2\nu\beta\beta$-decay rate of most of the nuclei in the medium-mass region makes us confident in employing the same PHFB wave functions for the study of $0\nu\beta\beta$ decay.

REFERENCES

1. W. C. Haxton and G. J. Stephenson, Jr., Prog. Part. Nucl. Phys. **12**, 409 (1984).
2. M. Doi, T. Kotani, and E. Takasugi, Prog. Theor. Phys. Suppl. **83**, 1 (1985).
3. M. Doi and T. Kotani, Prog. Theor. Phys. Suppl. **87**, 5 (1992).
4. T. Tomoda, Rep. Prog. Phys. **54**, 53 (1991); J. D. Vergados, Phys. Rep. **361**, 1 (2002); A. S. Barabash, nucl-ex/0203001; J. D. Vergados, Phys. Rep. **133**, 1 (1986); A. Faessler, Prog. Part. Nucl. Phys. **21**, 183 (1988).
5. J. Suhonen and O. Civitarese, Phys. Rep. **300**, 123 (1998).
6. A. Faessler and F. Simkovic, hep-ph/9901215; J. Phys. G **24**, 2139 (1998).
7. H. V. Klapdor-Kleingrothaus, hep-ex/9907040; hep-ex/9901021; hep-ex/9802007; Int. J. Mod. Phys. A **13**, 3953 (1998).
8. E. R. Elliott and P. Vogel, Annu. Rev. Nucl. Part. Sci. **52**, 115 (2002).
9. E. Cheifetz *et al.*, Phys. Rev. Lett. **25**, 38 (1970).
10. A. Pandoh, R. Devi, and S. K. Khosa, Phys. Rev. C **60**, 047302 (1999).
11. Arun Bharti and S. K. Khosa, Nucl. Phys. A **572**, 317 (1994).
12. S. K. Khosa, P. N. Tripathi, and S. K. Sharma, Phys. Lett. B **119B**, 257 (1982).
13. S. K. Sharma, G. Mukherjee, and P. K. Rath, Phys. Rev. C **41**, 1315 (1990).
14. P. Federman and S. Pittel, Phys. Lett. B **77B**, 29 (1978); P. Federman, S. Pittel, and R. Campos, Phys. Lett. B **82B**, 9 (1979).
15. A. J. Singh and P. K. Raina, Phys. Rev. C **52**, R2342 (1995).
16. B. M. Dixit, P. K. Rath, and P. K. Raina, Phys. Rev. C **65**, 034311 (2002); **67**, 059901 (2003); K. Chaturvedi, B. M. Dixit, P. K. Rath, and P. K. Raina, Phys. Rev. C **67**, 064317 (2003).
17. M. Baranger and K. Kumar, Nucl. Phys. A **110**, 490 (1968).
18. G. M. Heestand, R. R. Borchers, B. Herskind, *et al.*, Nucl. Phys. A **133**, 310 (1969).
19. W. Greiner, Nucl. Phys. **80**, 417 (1966).
20. A. Arima, Nucl. Phys. A **354**, 19 (1981).
21. M. Sakai, At. Data Nucl. Data Tables **31**, 400 (1984).
22. A. De Silva, M. K. Moe, M. A. Nelson, and M. A. Vient, Phys. Rev. C **56**, 2451 (1997).

23. D. Dassie *et al.* (NEMO Collab.), Phys. Rev. D **51**, 2090 (1995).
24. S. Stoica, Phys. Lett. B **350**, 152 (1995).
25. J. G. Hirsch, O. Castanos, P. O. Hess, and O. Civitarese, Phys. Rev. C **51**, 2252 (1995).
26. J. Suhonen and O. Civitarese, Phys. Rev. C **49**, 3055 (1994).
27. P. Belli *et al.*, Astropart. Phys. **10**, 115 (1999).
28. A. S. Barabash *et al.*, Nucl. Phys. A **604**, 115 (1996).
29. F. A. Danevich *et al.*, Z. Phys. A **355**, 433 (1996).
30. A. Sh. Georgadze *et al.*, Yad. Fiz. **58**, 1170 (1995) [Phys. At. Nucl. **58**, 1093 (1995)].
31. A. Shukla, P. K. Raina, R. Chandra, and P. K. Rath (in press).
32. J. Suhonen and O. Civitarese, Phys. Lett. B **497**, 221 (2001).
33. O. A. Rumyantsev and M. G. Urin, Phys. Lett. B **443**, 51 (1998).

Physics of Atomic Nuclei, Vol. 67, No. 11, 2004, pp. 2027–2031. From Yadernaya Fizika, Vol. 67, No. 11, 2004, pp. 2048–2052.

DOUBLE-BETA DECAY AND RARE PROCESSES

Looking for SUSY with EDELWEISS-I and -II*

G. Gerbier, A. Benoît¹⁾, L. Bergé²⁾, A. Broniatowski²⁾, L. Chabert³⁾, B. Chambon³⁾, B. Chardin, M. Chapellier⁴⁾, P. Charvin⁵⁾, M. De Jésus³⁾, H. Deschamps, P. Di Stefano³⁾, D. Drain³⁾, L. Dumoulin²⁾, S. Fiorucci, J. Gascon³⁾, E. Gerlic³⁾, C. Goldbach⁵⁾, M. Goyot³⁾, M. Gros, J. P. Hadjout³⁾, S. Hervé, A. Juillard²⁾, A. de Lesquen, J. Mallet, S. Marnieros²⁾, O. Martineau³⁾, L. Mosca⁵⁾, X.-F. Navick, G. Nollez⁶⁾, P. Pari⁴⁾, C. Riccio⁵⁾, V. Sanglard³⁾, L. Schoeffel, M. Stern³⁾, and L. Vagneron³⁾**

(The EDELWEISS Collaboration)

CEA, Centre d'Études Nucléaires de Saclay, DSM/DAPNIA, Gif-sur-Yvette, France

Received April 16, 2004

Abstract—The latest results obtained by the EDELWEISS WIMP (weakly interacting massive particles) direct detection experiment using three heat-and-ionization 320-g germanium bolometers are given. Presently the most sensitive WIMP direct detection experiment for WIMP mass >30 GeV, EDELWEISS-I is testing a first region of SUSY models compatible with accelerator constraints. The status and main characteristics of EDELWEISS-II, involving in a first stage 28 germanium bolometers and able to accommodate up to 120 detectors, are briefly presented, together with neutron background estimates. *© 2004 MAIK "Nauka/Interperiodica".*

1. INTRODUCTION

The case for the WIMP hypothesis has become compelling over the last few years. After the recent satellite WMAP precision measurements of the cosmological microwave background (CMB) [1], the precision on the density of the Universe is now a few percent and $\Omega \sim 1.02 \pm 0.02$. On the other hand, the recent evidence for a nonzero cosmological constant or some other quintessential component leads to a new model of our Universe: a strange mixture of 2/3 of some cosmological repulsive component, 1/3 of exotic matter, with only a few percent of ordinary matter: 95% of the content of the Universe is unknown. The baryonic density, Ω_{baryon}, is impressively constrained by primordial nucleosynthesis [2] and cosmological constraints to $\sim (4.4 \pm 0.2)\%$, implying that matter is composed of nearly 85% of a mostly unobserved and noninteracting component.

Although we have now good evidence that neutrinos are indeed massive, the sensitivity reached by present searches excludes that neutrinos can fill the gap: experimental constraints impose that they contribute at most to 10% of the missing mass. Generically predicted by supersymmetric (SUSY) theories, weakly interacting massive particles (WIMPs) then provide a well-motivated candidate to solve the missing matter enigma, while, for the first time, direct and indirect detection experiments are beginning to test regions of supersymmetric model parameter space compatible with cosmological and accelerator constraints.

In the following, we will summarize the strategy and main results obtained by the EDELWEISS-I experiment in the direct detection of dark matter, using heat-and-ionization cryogenic Ge detectors. The experiment, which has been described elsewhere [3], is set in the low-background environment of the Modane Underground Laboratory (LSM), which reduces the muon cosmic background by a factor $\sim 2 \times 10^6$ compared to the flux at sea level. The neutron flux originating from the rock has been measured to be $\sim 1.6 \times 10^{-6}$ cm^{-2} s^{-1}. In the present

---

[*] This article was submitted by the authors in English.

[1)] Centre de Recherche sur les Très Basses Températures, SPM-CNRS, Grenoble, France.

[2)] Centre de Spectroscopie Nucléaire et de Spectroscopie de Masse, IN2P3-CNRS, Université Paris XI, Orsay, France.

[3)] Institut de Physique Nucléaire de Lyon-UCBL, IN2P3-CNRS, France.

[4)] CEA, Centre d'Études Nucléaires de Saclay, DSM/DRECAM, Gif-sur-Yvette, France.

[5)] Laboratoire Souterrain de Modane, CEA-CNRS, Modane, France.

[6)] Institut d'Astrophysique de Paris, INSU-CNRS, Paris, France.

[**] e-mail: `gilles.gerbier@lsm.in2p3.fr`

EDELWEISS-I setup, this neutron flux, in the MeV range, is strongly attenuated and degraded in energy by a paraffin shielding of thickness ∼30 cm. During the last four years, a series of data takings using several 320-g Ge detectors have allowed EDELWEISS to achieve the best sensitivity to WIMP interactions for all WIMP masses >30 GeV.

2. EXPERIMENTAL RESULTS

The Ge detectors presently used in the EDELWEISS experiment are described in [4, 5]. These detectors have a cylindrical geometry (70 mm in diameter and 20 mm thick) and their edges are beveled at an angle of 45° to improve charge collection near free lateral detector surfaces. Two distinct Al electrodes, a central and a guard ring electrode, are used for charge collection. The thermal sensor is a neutron transmutation doped germanium crystal (Ge-NTD) of few mm^3 glued onto the guard ring. Out of a total of seven 320-g bolometers, four were equipped with an additional 60-nm-thick Ge or Si amorphous layer providing improved charge collection efficiency for near-surface events [6]. Since January 2002, three 320-g detectors have been simultaneously operated in the EDELWEISS-I cryostat, all the signals being numerically filtered and triggered online. The quality of the LSM experimental site combined with copper, lead, and paraffin shielding of the cryostat [7], as well as material selection in the close vicinity of the detectors, reduces the γ-ray background down to ∼1.5 events/(keV kg d) in the low-energy interval relevant to WIMP interactions, and before background rejection. The residual neutron background after these shieldings is estimated to be 0.03 events/(kg d) above 20 keV [8].

3. DETECTOR CALIBRATION

The heat and ionization responses to γ-ray particles were calibrated using ^{57}Co, ^{60}Co, and ^{137}Cs sources. Ionization baseline resolutions are better than 1.5 keV FWHM for all channels, and the heat baseline FWHM resolution ranges from 0.4 to 1 keV depending on the detector. The recoil energy threshold using ionization triggering was 20 keV for the GSA3 detector and 30 keV for the GGA3 and GSA1 detectors (>99% efficiency). A summary of the bolometers' baselines, resolutions, and thresholds can be found in [5]. Owing to the simultaneous measurement of heat and ionization, the major part of the background signal in these detectors can be rejected. Indeed, nuclear recoils induced by neutrons and WIMPs are less ionizing than electron recoils induced by γ rays. The separation efficiency between electron and nuclear recoils is a very important feature for this type of detector. It is regularly controlled by measuring the factor Q (ratio of the ionization to recoil energy) during γ-ray calibrations. In particular, surface electron recoil events are expected to induce incomplete charge collection and give a lower Q factor, which could confuse them with nuclear recoil events. We observe that charge collection efficiency for surface events is much better for detectors equipped with amorphous Si or Ge layers and have measured that <0.03% of events are found in the recoil band during γ-ray calibrations.

4. RESULTS AND DISCUSSION

Three periods of low-background data have been realized using different bolometers. During the 2000 and 2002 runs, a total of 11.6 kg d of data were accumulated using the GeAl6 and GGA1 detectors [9, 10]. We will focus here on a new 2003 data-taking period, which accumulated an additional set of 18.9 kg d, based on three new detectors, GGA3, GSA1, and GSA3. The corresponding Q versus recoil energy diagrams are plotted in Fig. 1. The three detectors show very similar behavior with only two events lying in the neutron recoil band. These two events, together with three events at very low quenching factors, were all recorded within a few days. Conservatively, these two events are considered as real nuclear recoil events. Under this hypothesis, the spin-independent exclusion limit for the WIMP–nucleon cross section derived from these data, with cumulated statistics of 30.5 kg d, is almost identical to and confirms the sensitivity reached in the 2000–2002 data takings. Figure 2 shows the present EDELWEISS sensitivity, together with the constraints of the presently most sensitive experiments. In particular, the WIMP cross section associated with the best fit to the DAMA annual modulation candidate [12, 13], assuming standard halo parameters [14], is excluded at >99.99% C.L.

The DAMA group has contested this contradiction, invoking the uncertainty in the WIMP halo parameters. But Copi and Krauss [15] have recently shown that the contradiction remains model-independent when the relative sensitivity of both experiments is considered, unless unconventional couplings are used. A mixture of spin-dependent and spin-independent couplings has also been proposed to reconcile the conflicting experimental results between EDELWEISS and CDMS, on the one hand, and DAMA, on the other. But Kurylov and Kamionkowski [16] have shown that, except in a very small region in phase space in the WIMP–proton/WIMP–neutron plane, it seems impossible to reconcile the DAMA result with the EDELWEISS and CDMS [17, 18] negative results for all WIMP mass >18 GeV.

5. NEUTRON BACKGROUND STUDIES

Neutrons induce nuclear recoils as WIMPs do. They constitute the major physical source of background to eliminate.

In deep underground laboratories, most of the neutrons originate from fission and spallation processes in the surrounding rock, at the typical level of 10^{-6} cm^{-2} s^{-1} for the best sites. This first source can be efficiently reduced by an adequate shield (30 cm of paraffin for EDELWEISS-I and 50 cm of polyethylene for EDELWEISS-II setup). A second neutron component is associated with the neutron production by muons crossing the lead and copper shield, materials acting as neutron multipliers. While this source is about two orders of magnitude lower than the first one (without paraffin shield), we have found that it becomes dominant in the detector volume of EDELWEIIS-II due to the large 40-t surrounding lead shield. Fortunately, this background will be effectively reduced to a negligible level in EDELWEISS-II by identifying and vetoing, with an efficiency >95%, the muons crossing the protective setup around the detectors.

Fast neutrons originating from muon deep inelastic interactions in the rock thickness are known with considerably larger uncertainties, particularly with respect to the neutron multiplicity. For far away muons, not tagged by the muon veto, there is no efficient way to reject fast neutrons crossing the PE shield and interacting in the lead shield. This component has, however, been estimated to be at the level of the first source in the Ge detector volume.

Last, uranium present in the lead shield can also give rise to neutrons by fission reactions. From the upper limit on uranium contamination in our lead, we deduced an upper limit on this flux which can be as large as 3 times the first source. In Fig. 3, the various spectra at the detector level are compared after propagation from their initial production location (rock or lead shields) through the various shields. It turns out that all these spectra have rather similar shapes in the 0.5–5-MeV energy range, the most dangerous energy region for WIMP search. More details on these studies, conducted also within the ETNoμSiQ working group, can be found in [8].

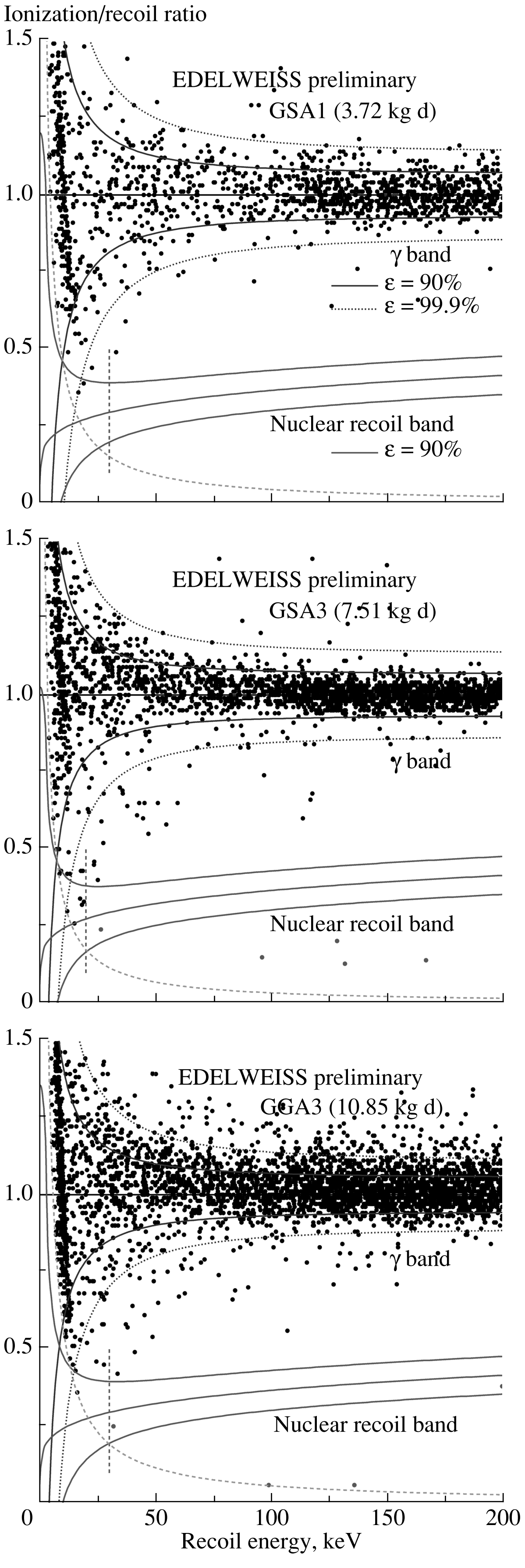

Fig. 1. Distribution of the ionization/heat ratio versus recoil energy for the 2003 low-background data for two out of the three 320-g Ge bolometers. Events observed both in the nuclear recoil band and below this band arrived within a period of a few days, compared to a total data-taking period of ∼3 months. Conservatively, the events observed in the nuclear recoil band are considered as real nuclear recoil events. The two lines which can be observed at ∼9.0 and ∼10.4 keV are due to the cosmogenic activation of germanium. The nuclear recoil band is determined by the condition of 90% acceptance.

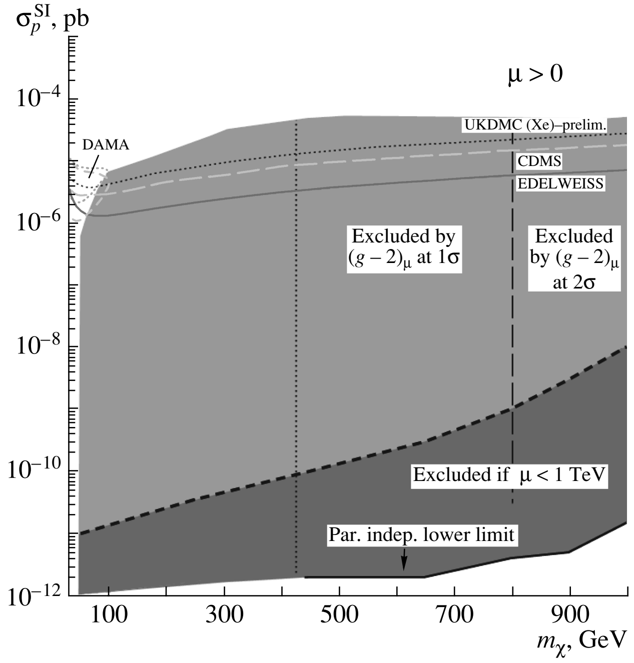

Fig. 2. Experimental sensitivities of the present most sensitive WIMP direct detection experiments (from [11]). The EDELWEISS result, without background subtraction, excludes the full 3σ zone of the DAMA signal (upper left corner) compatible with accelerator constraints, independently of the WIMP halo model parameters. The two shaded regions represent the phase space of SUSY models with present accelerator and $(g-2)_\mu$ constraints. The parameter-independent lower limit on the WIMP–proton cross section can be seen to be $\sim 10^{-12}$ pb.

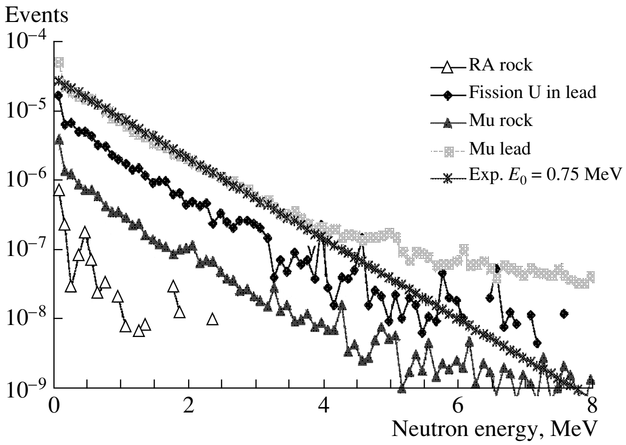

Fig. 3. Neutron energy spectra from the various sources at the location of the EDELWEISS detectors.

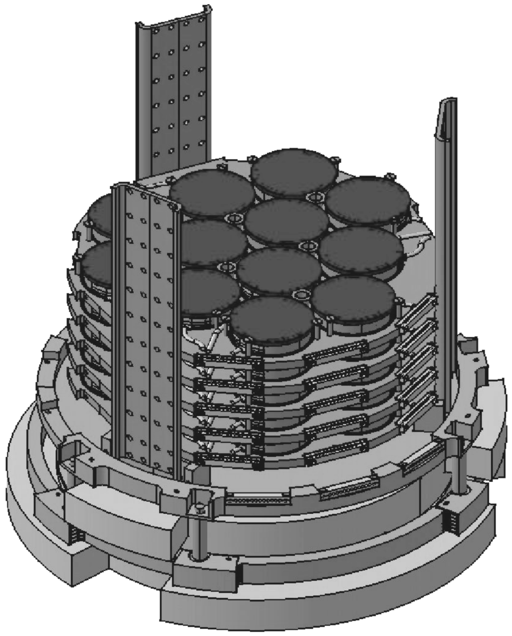

Fig. 4. Drawing of the EDELWEISS-II detector setup. Up to 120 Ge detectors of mass 320 g can be accommodated in a compact hexagonal arrangement at 10 mK. The lower plate, made of ultrapure archaeological lead, shields the detectors from the radioactivity of the dilution cryostat (not shown).

6. TOWARDS EDELWEISS-II AND FURTHER DETECTOR DEVELOPMENTS

An improved acquisition system with a very low energy threshold has been realized in the EDELWEISS-I experiment and data have been accumulated with close to 100% detection efficiency at $E_{\rm recoil} = 10$ keV. By the end of 2004, the EDELWEISS-I experiment will be dismantled and installation of the EDELWEISS-II experiment will take place. The goal is an increased sensitivity by a factor of 100 in terms of the WIMP cross-section exclusion limit. A new very low radioactivity cryostat able to cool 120 detectors down to 10 mK is presently being tested in the CRTBT laboratory in Grenoble (Fig. 4). In addition to 21 NTD-Ge-equipped 320-g bolometers, the first stage of EDELWEISS-II will include seven 400-g detectors, based on NbSi thin film thermistors capable of identifying near-surface events [19, 20]. Furthermore, implementation of charge pulse shape analysis on both types of detectors will allow event localization and greatly improve control of space-charge creation [21, 22]. As described above, the improved polyethylene 50-cm-thick shielding combined with the muon veto will hopefully bring down the neutron background recoil rate in the bolometers to about 0.003 event/(kg d). EDELWEISS-II should then be able to probe much more deeply the region of more favored SUSY models [23] and, hopefully, to detect WIMP candidates.

ACKNOWLEDGMENTS

We gratefully acknowledge the help of the technical staff of LSM and of the participating laboratories.

This work is supported in part by the EEC-Network program under contract HPRN-CT-2002-00322.

REFERENCES

1. D. N. Spergel *et al.*, astro-ph/0302209.
2. S. Burles *et al.*, Phys. Rev. D **63**, 063512 (2001).
3. Ph. Di Stefano *et al.*, Astropart. Phys. **14**, 329 (2001).
4. X. F. Navick *et al.*, Nucl. Instrum. Methods Phys. Res. A **444**, 361 (2000).
5. O. Martineau *et al.*, Nucl. Instrum. Methods Phys. Res. (in press).
6. P. N. Luke, C. S. Rossington, and M. F. Wesela, IEEE Trans. Nucl. Sci. **41**, 1074 (1994); LBNL-33980; T. Shutt *et al.*, Nucl. Instrum. Methods Phys. Res. A **444**, 340 (2000).
7. A. de Bellefon *et al.*, Astropart. Phys. **6**, 35 (1996).
8. G. Chardin and G. Gerbier (EDELWEISS Collab.), in *Proceedings of the 4th International Workshop on Identification of Dark Matter (IDM2002)*, Ed. by N. J. Spooner and V. Kudryavtsev (World Sci., Singapore, 2003), p. 470.
9. A. Benoit *et al.*, Phys. Lett. B **513**, 15 (2001).
10. A. Benoit *et al.*, Phys. Lett. B **545**, 43 (2002).
11. Y. G. Kim, T. Nihei, L. Roszkowski, and R. R. de Austri, J. High Energy Phys. **0212**, 034 (2002).
12. R. Bernabei *et al.*, Phys. Lett. B **480**, 23 (2000).
13. R. Bernabei *et al.*, Riv. Nuovo Cimento **26**, 1 (2003).
14. J. D. Lewin and P. F. Smith, Astropart. Phys. **6**, 87 (1996).
15. C. J. Copi and L. M. Krauss, Phys. Rev. D **67**, 103507 (2003).
16. A. Kurylov and M. Kamionkowski, hep-ph/0307185.
17. R. Abusaidi *et al.*, Phys. Rev. Lett. **84**, 5699 (2000).
18. D. Abrams *et al.* (CDMS Collab.), Phys. Rev. D **66**, 122003 (2002).
19. N. Mirabolfathi *et al.*, AIP Conf. Proc. **605**, 517 (2002).
20. S. Marnieros *et al.*, in *Proceedings of the 10th International Workshop on Low Temperature Detectors, Genoa, Italy, 2003*, Nucl. Instrum. Methods Phys. Res. A (in press).
21. A. Broniatowski *et al.*, in *Low Temperature Detectors*, Ed. by F. S. Porter *et al.*, AIP Conf. Proc. **605**, 521 (2002).
22. A. Broniatowski *et al.*, in *Proceedings of the 10th International Workshop on Low Temperature Detectors, Genoa, 2003,* Nucl. Instrum. Methods Phys. Res. A (in press).
23. J. Ellis, A. Ferstl, and K. A. Olive, Phys. Lett. B **481**, 304 (2000).

Physics of Atomic Nuclei, Vol. 67, No. 11, 2004, pp. 2032–2040. From Yadernaya Fizika, Vol. 67, No. 11, 2004, pp. 2053–2061.
Original English Text Copyright © 2004 by Howard.

Dark Matter Searches by the Boulby Collaboration and Liquid Xenon Prototype Development*

A. S. Howard**
(on behalf of the Boulby Dark Matter Collaboration[1])
High Energy Physics, Blackett Laboratory, Imperial College, London, United Kingdom

Received April 16, 2004

Abstract—The current status of direct dark matter searches by the Boulby Dark Matter Collaboration is presented with the latest result from the ZePLiN I liquid xenon detector. An upper limit in the interaction cross section per nucleon of $\sim 1 \times 10^{-6}$ pb for a WIMP mass of 100 GeV is found. Details of ZePLiN's II and III—two future liquid xenon dark matter are presented. Extensive two-phase liquid–gas xenon prototype work has been undertaken and results of characterization studies are presented. The detector response to internal alpha and external gamma and neutron sources is shown. The potential discrimination power of the two-phase technique is displayed. Finally, prospects for the future dark matter search program are discussed. © *2004 MAIK "Nauka/Interperiodica"*.

1. INTRODUCTION

The evidence for dark matter has recently been given a boost from the results of the WMAP Cosmic Microwave Background Survey [1]. The results of the fitted power spectrum indicate that ~23% of the Universe is made up of nonbaryonic "dark" matter, whereas the luminous baryonic matter constitutes only ~4%. The most theoretically favored candidate for nonbaryonic dark matter is the lightest supersymmetric party (LSP), which should only interact weakly. The current most probable mass for the LSP is 100 GeV due to SUSY model constraints from existing parameter measurements. In this paper, the current status of direct weakly interacting massive particle (WIMP) dark matter searches is presented together with prospects for future experiments and results from prototype detectors.

The Boulby Dark Matter Collaboration (formerly UKDMC) has been searching for nonbaryonic matter since the early 1990s. The collaboration comprises nine institutes from five countries. Recently, a new large (150 × 4 m) experimental facility has been constructed in the Boulby mine in North Yorkshire, England. The mine is a 1.1-km-deep working salt mine that offers an excellent environment for searching for dark matter. The depth and lack of local radiation is a particular benefit and reduces significantly background contributions from neutrons, muons, and other cosmic or radioactive sources.

The Boulby Dark Matter Collaboration is using liquid xenon as a target material for current (ZePLiN I) and future (ZePLiN's II, III) dark matter detectors. Xenon offers a close match between the expected 100-GeV most probable LSP and the xenon nucleus (121 GeV). Liquid xenon is an attractive choice of target material for a number of reasons, including the following:

(1) The nuclear mass is very close to the favored LSP mass (~100 GeV).

(2) It can be produced in large quantities relatively cheaply due to its cryogenic nature.

(3) It can be purified to very high levels (measured electron lifetimes >1 ms).

(4) It is very low background (^{85}Kr is the only major radioactive contaminant).

(5) Pulse-shape discrimination via scintillation.

(6) Two-phase discrimination via ionization and scintillation channels.

(7) The decay time of the scintillation has two major components: *recombination* and *deexcitation*.

(8) Ionization is also produced.

The primary signal source in xenon is scintillation in the vacuum ultraviolet at 175 nm. Initially, an electromagnetic interaction produces either excitation or ionization. The excited state can then form a dimer and deexcite via either a longer lived triplet or shorter singlet state. A schematic for the scintillation mechanism is shown in Fig. 1.

---

*This article was submitted by the author in English.

[1] Boulby Dark Matter Collaboration: Imperial, RAL, Sheffield; UCLA, Texas A&M; Pisa; ITEP; Coimbra; Edinburgh.

**e-mail: `a.s.howard@imperial.ac.uk`

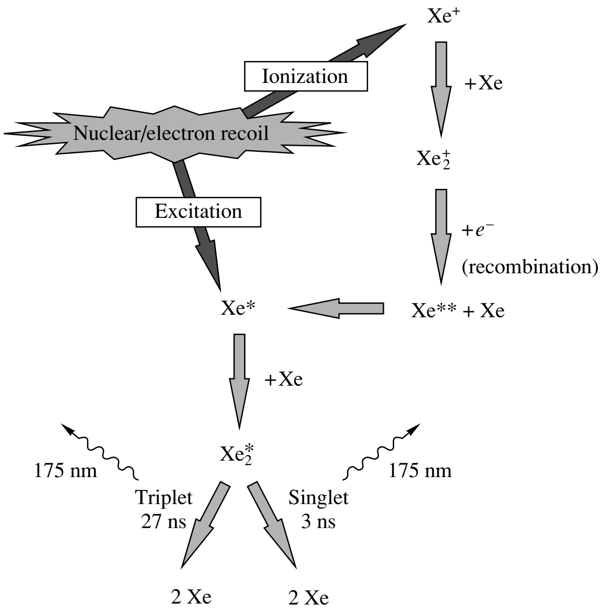

Fig. 1. The scintillation mechanism in liquid xenon.

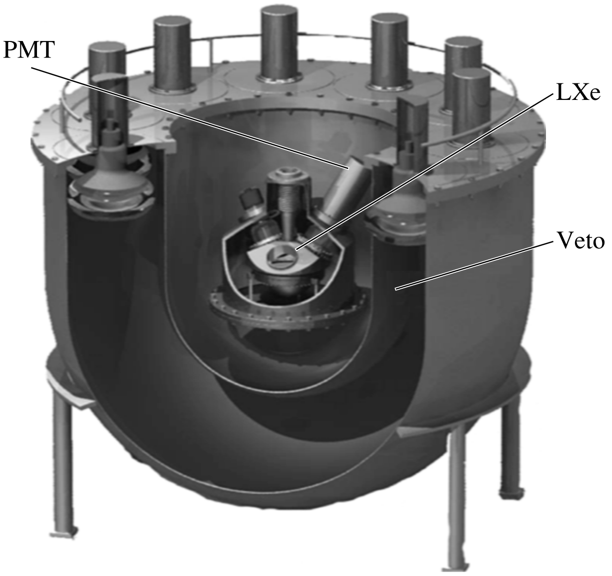

Fig. 2. A cut-away schematic of the ZePLiN I detector.

1.1. Two-Phase Xenon

In addition to the primary scintillation, interactions in xenon can also produce free ionization. Without an applied electric field this leads to characteristic recombination which allows the distinction between nuclear and electron recoils. Upon application of an electric field, the ionization can drift through the liquid phase and up towards the gas. With a sufficiently high electric field, the electrons can cross the liquid—gas interface and then drift through the gas at high velocity [2]. These electrons can then produce further photons via electroluminescence [3]. The multitude of subsequent photons produced leads to an "amplification" of the ionization signal and the possibility of single electron detection. Due to the different energy-loss densities, the probability for recombination between densely ionizing massive nuclear recoils and higher velocity electron recoils is vastly different. This then gives the possibility of excellent discrimination by merely measuring the scintillation and ionization signals. A WIMP interaction should generate a greater proportion of primary scintillation compared to ionization, whilst a background gamma interaction should produce approximately equal quantities of scintillation and ionization. Xenon can thus be used as a two-phase dark matter detector (so called due to the utilization of both the liquid and gas phases for the detection of scintillation and ionization).

2. THE ZePLiN I DARK MATTER DETECTOR

The ZePLiN I (ZonEd Proportional scintillation LIquid Noble gas) liquid xenon detector has been underground since January 2001. The detector comprises 3.1 kg of liquid xenon and utilizes three photomultipliers to detect the scintillation emission. The use of multiple PMTs allows the definition of an internal fiducial volume and also removes PMT glass radioactivity via the implementation of stand-off "spigots." A cut-away schematic is shown in Fig. 2. The target vessel is constructed out of oxygen-free copper to reduce radioactivity and impurity levels. Surrounding the vessel is a PXE-based organic liquid scintillator veto to remove high-energy gammas giving low-energy Compton scatters in the target. Liquid xenon scintillation has previously been shown to give good discrimination between background gammas and signal-like neutron-induced nuclear recoils [3—6]. With the ZePLiN I detector, a neutron calibration was carried with an Am—Be source at the surface prior to underground installation. The resultant time constant distribution (fitted to the exponential-like scintillation decay time) is shown in Fig. 3 for Compton gamma interactions (top graph) and for the Am—Be source (lower graph). A clear population of faster time constant nuclear recoils can be seen on the left of the graph. So far, 220 kg d of data have been acquired with the ZePLiN I detector and the resulting preliminary WIMP cross-section limit is shown in Fig. 4, the minimum of which is 10^{-6} pb for an optimum WIMP mass of $\sim$100 GeV.

This result is preliminary and requires further understanding in terms of threshold, energy resolution homogeneity, fiducial definition, and discrimination power, particularly at low energy.

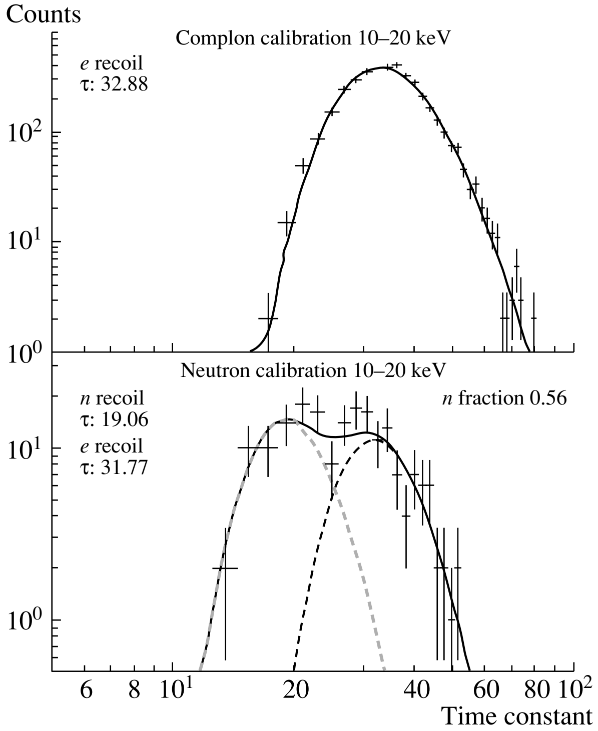

Fig. 3. The time constant measured in the ZePLiN I detector for Compton gamma interactions (top) and Am–Be elastic and inelastic nuclear recoils (bottom).

2.1. ZePLiN II

A two-phase xenon detector, ZePLiN II, is currently under construction and due for deployment at the end of 2004. The detector comprises 30 kg of liquid xenon operating in a low-electric-field "two-phase" liquid–gas mode. The choice of field provides enhanced positive gamma detection whilst still allowing limited pulse-shape discrimination between WIMP-induced nuclear recoils and background gamma events. A design schematic of the detector is shown in Fig. 5. The vessel is cast in brass to ease construction and reduce radioactivity. Internally, the use of PTFE and field shaping grids provides close to a 100% active volume. The electric field is insufficient (∼100 V/cm) to allow nuclear recoil ionization to separate; thus, a WIMP recoil signal does not contain secondary scintillation. Therefore, any insensitive regions will result in reduced performance.

Examples of PMT signals from a 1-kg ZePLiN II prototype are shown in Fig. 6. In the case of the alpha event (left-hand trace), clear suppression of the ionization and hence secondary scintillation can be seen, especially compared to a gamma interaction (right-hand trace). A two-phase plot of secondary-vs.-primary scintillation can be seen in Fig. 7 for signals induced by an Am–Be neutron source. A clear population with zero secondary ionization can be seen close to the x axis. In addition, the reduced electric field should allow second-order pulse-shape discrimination between gammas and nuclear recoils.

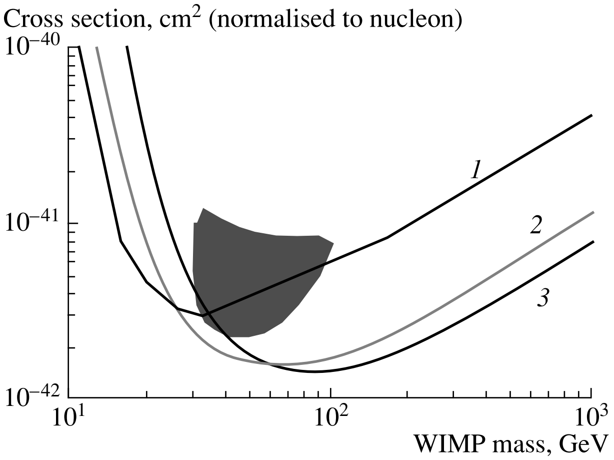

Fig. 4. The preliminary WIMP cross section/baryonic nucleon after 220 kg d of data from the ZePLiN I detector (*2*), in comparison with CDMS [7] (*1*), EDELWEISS [8] (*3*), and DAMA [9] (closed region).

2.2. ZePLiN III

In parallel to the development of ZePLiN II, a high-electric-field two-phase liquid xenon detector, ZePLiN III, is also being constructed and is due for installation underground by the end of 2004. The detector comprises 50 kg of xenon giving an active volume of ∼7 kg, fiducially defined as a high electric field (10 kV/cm), high extraction (∼99%) electroluminescent region. The electric field will, in particular, give extreme sensitivity to the ionization produced (single electron), whilst the internal PMT array provides position sensitivity, and the large xenon volume removes background (passive shielding through periphery volumes). A design drawing of the detector is shown in Fig. 8. Thirty-one 2-in. PMTs are submerged inside the liquid xenon to maximize light collection. Internal grids apply a high extraction electric field as well as a reverse field above the PMTs to reduce signals from internal radioactivity. The fields are configured to remove photoelectric feedback from the metal surfaces by only allowing electron drift paths under the liquid surface for regions close to the electrodes. The large magnitude of the electroluminescence signals allow position reconstruction of single electrons through the gas phase.

2.3. Prototype Two-Phase Work

Due to the planned novel use of two-phase liquid–gaseous xenon in the ZePLiN II and ZePLiN III

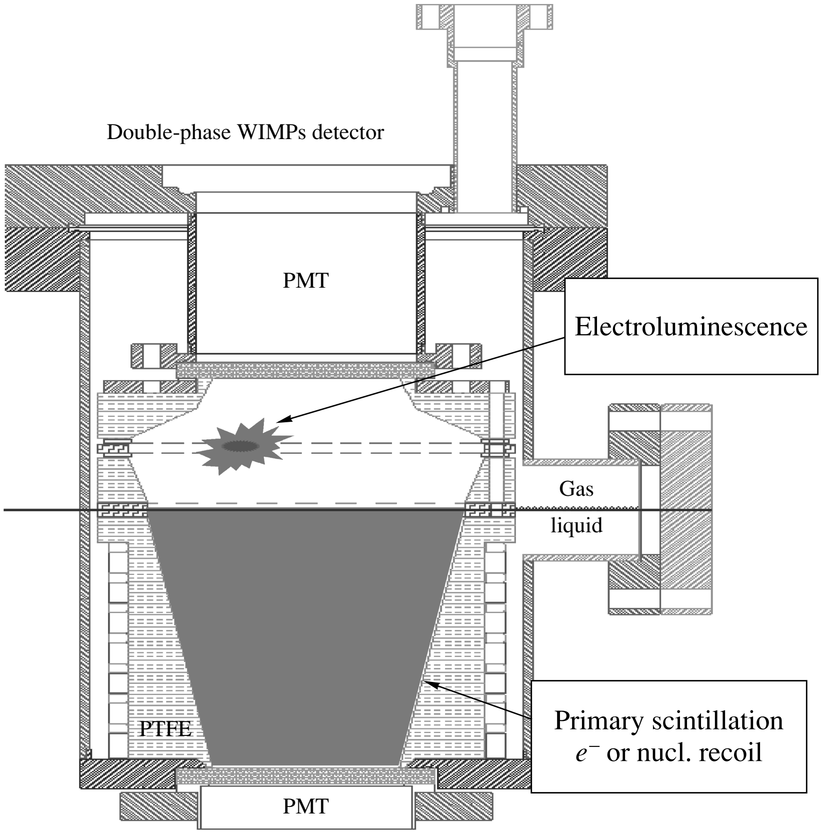

Fig. 5. A schematic design drawing of the ZePLiN II two-phase dark matter detector.

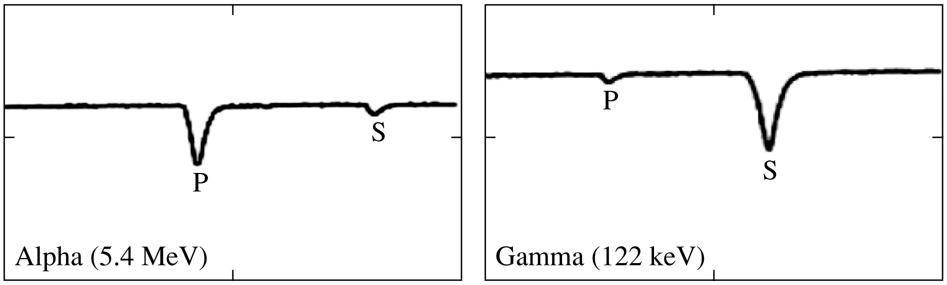

Fig. 6. Sample signals from alpha (left) and gamma (right) interactions in a ZePLiN II prototype.

detectors, extensive laboratory characterization has been carried out with smaller scale prototypes. Two systems have been fabricated: a 7-mini PMT array at the ITEP in Moscow (Fig. 9, left) and a slightly larger (4 kg) single PMT system at Imperial College in London (right) [11]. Both detectors have the PMTs immersed inside the liquid xenon to improve performance and light collection. Field shaping electrodes with high voltage and PMT grids are also placed inside the xenon volume. The upper HV grid contains an ^{241}Am alpha source to allow precise calibration with a well-defined interaction point. The source is mounted inside a lead "boat," causing the primary light to be shielded by about a factor of 10. A manually polished aluminum mirror is located in the gas phase to increase the light collection from the electroluminescence.

During normal operation, interactions occur in the region above the HV grid producing indirect (reflected) primary scintillation and free electrons. The electrons then drift through the liquid to the surface, where they are extracted into the gas. Whilst the ionization drifts through the gas, further (secondary) scintillation is observed due to electroluminescence. The electrons are finally added to the external circuit once they reach the mirror electrode.

The two-phase response has been measured for

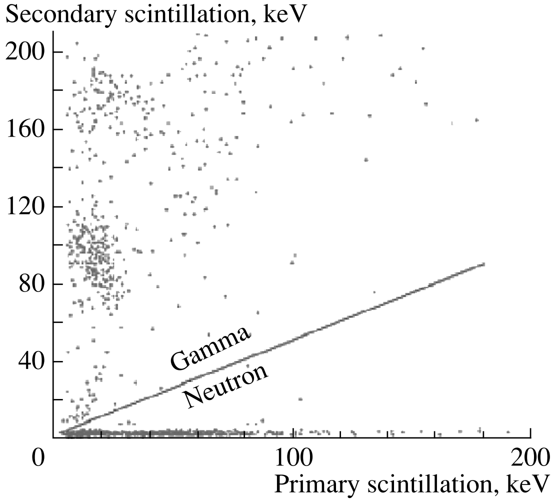

Fig. 7. Secondary-vs.-primary scintillation in response to an external Am–Be source for the ZePLiN II prototype [10].

a variety of interacting species and electric fields. A typical voltage–time trace from the PMT in the Imperial prototype is shown in Fig. 10. The trace was recorded using a Lecroy 7200 digital sampling oscilloscope. The initial primary scintillation signal can be seen on the left of the trace and is expanded in the bottom left-hand corner. After a delay equivalent to the drift time of electrons between the interaction site and the gaseous phase, the secondary electroluminescent signal can clearly be seen. The electroluminescent mechanism allows the detection of both scintillation and ionization photometrically. In addition, the increased magnitude of the signal for the ionization will greatly enhance the sensitivity and, more importantly, reduce the threshold of a dark matter detector. By increasing the electric field up to 5 kV/cm in the liquid and 10 kV/cm in the gas, it is possible to detect and trigger on single electrons drifting through the gas phase. The interaction shown in Fig. 10 is for an alpha particle, which due to plasma charge effects actually has a reduced ionization yield of approximately 4%. Despite this suppression, the magnitude of the signal is still significantly larger than the primary scintillation. For an electron recoil via a gamma interaction, the ionization should be close to 100%. Therefore, by measuring merely the size of the primary (S1) and secondary (S2) signals, a distinction can be made between alpha and gamma particles. This discrimination ability is displayed in Fig. 10 with the alpha signal indicated by the faint red marks and interactions from photons from an external ^{60}Co source shown by the darker blue marks. A cut was made on the drift time to allow unbiased separation between alphas and gammas, since the alpha particles have a precise localization and hence drift time, whereas the gammas should interact uniformly in z.

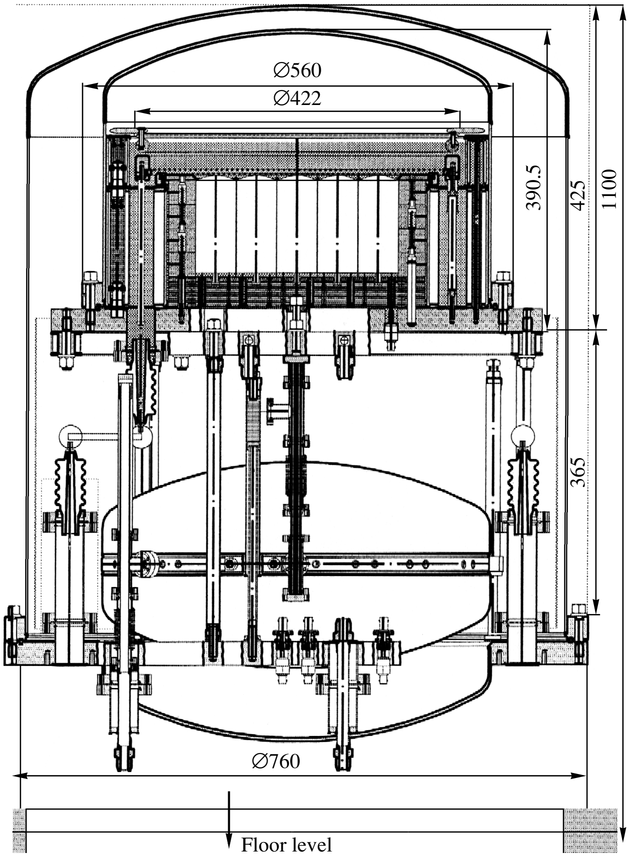

Fig. 8. The ZePLiN III dark matter detector.

2.4. ITEP Prototype Neutron Study

Since expected WIMP interactions should lead to low-energy elastic nuclear recoils, it is important to be able to distinguish between neutron-induced nuclear recoils and photon–electron recoils. An investigation using a 14.4-MeV D–T neutron beam has been carried out with the ITEP prototype detector. Results of the primary to secondary correlation are shown in Fig. 11.

Two distinct regions can be seen, due to gammas (on the right) and neutrons (on the left very close to the y axis). The regions were produced with a calibration ^{22}Na source for the gammas and by pulsing the D–T neutron source for the neutron population. Although the distinction is clear, the magnitude of the difference is difficult to quantify due to the quality of the light collection. Therefore, to clarify the signals, a second larger scale prototype is in the process of being constructed at ITEP. A design impression can be seen in Fig. 12.

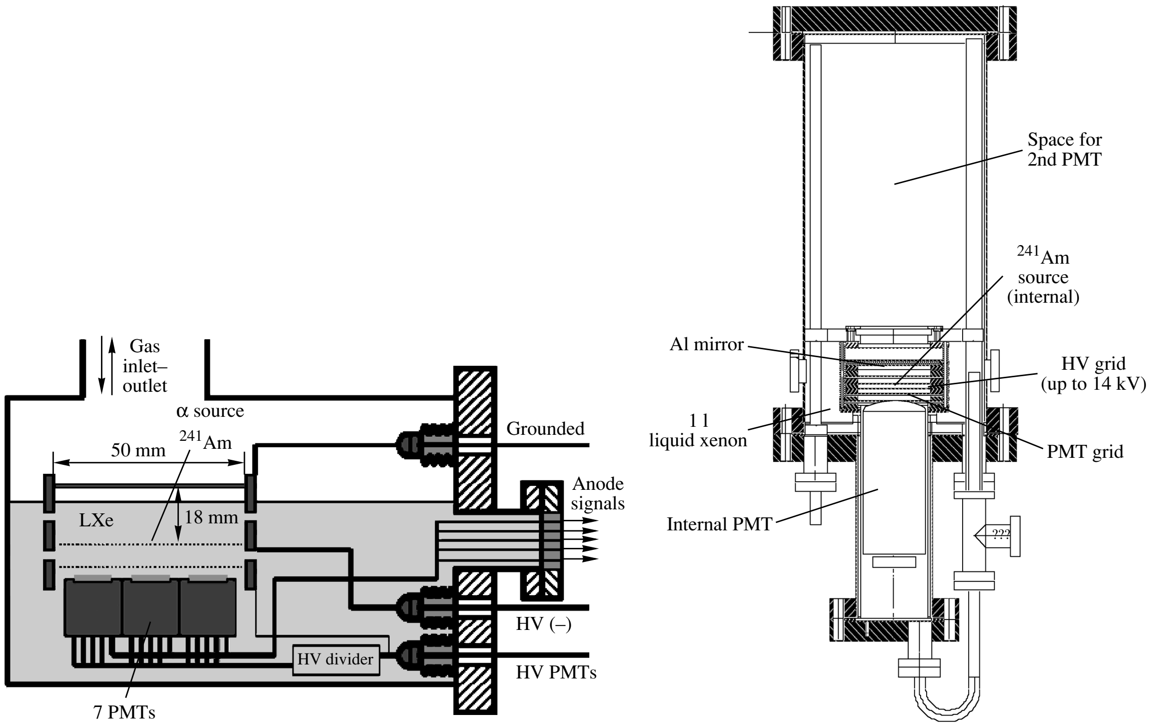

Fig. 9. The ITEP (left) and Imperial College (right) prototype two-phase xenon detectors.

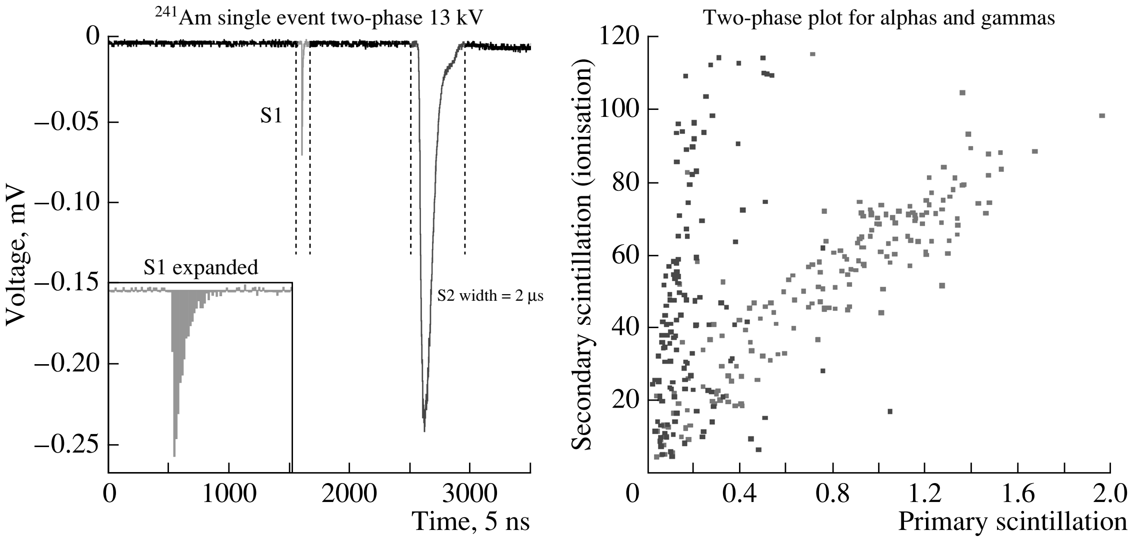

Fig. 10. A typical voltage–time trace for an internal alpha interaction in the Imperial College liquid xenon two-phase detector (left) and the resulting two-phase plot of scintillation (S1) vs. ionization (S2) (right). Clear discrimination can be shown between alpha (light dots) and gammas (dark).

2.5. Imperial College Prototype Neutron Study

In addition to the ITEP study, a separate investigation has been carried out at Imperial College using a gamma-tagged Am–Be neutron source. The Am–Be source produces 4.43-MeV gammas time-coincident with the neutron, the requirement of which allows a large suppression of background. The experimental arrangement is shown in Fig. 13. A large 10-kg CsI crystal is employed to detect the 4.43-MeV gamma. Using this technique together with a multivariate trigger requirement on the xenon pulse shape leads to primary and secondary scintillation signals with very small amplitudes from what are believed to be neutron-induced elastic recoils.

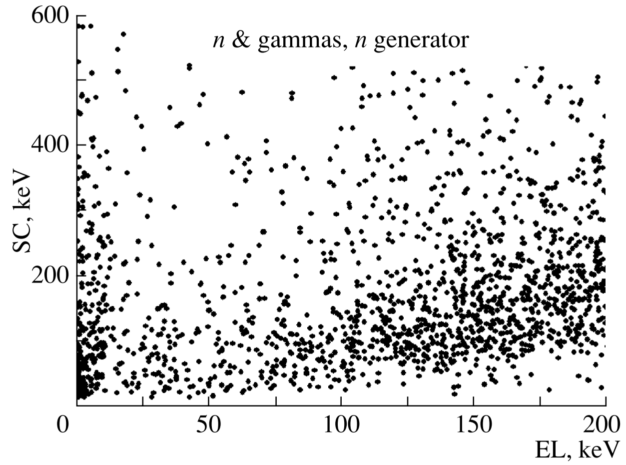

Fig. 11. S1 vs. S2 neutron spectrum for the ITEP prototype (note that S1 is the abscissa).

A distribution can be produced which is distinct from both gammas and alphas, as can be seen in Fig. 14. The magnitude of the S1 pulse is suppressed in the alpha case due to the inverted nature of the source holder and subsequent shadowing of the primary scintillation, resulting in a larger S2/S1 ratio. Scaling this according to the known inefficiency results in a much closer match of the ratios for alphas and suspected nuclear recoils (Fig. 15). Although not conclusive, this is the first positive indication as to the size of nuclear recoil ionization and magnitude of discrimination power for this two-phase technique.

3. GEANT 4 SIMULATION

It is clear that the two-phase technique leads to complicated signal shapes and some subtleties in order to understand fully the detector output. For this purpose, an extensive Geant 4 [12] simulation has been developed. This included all physics processes down to an energy of 250 eV and also ray tracing of the optical photons back to the PMT. In addition, a ZePLiN III simulation code has been extended to include ionization drifting and subsequent electroluminescence production in the gas phase.

The full laboratory geometry was included in order to accurately simulate the neutron source within our arrangement (extensive long-time interval scattering together with capture and activation can occur with neutrons). The inclusion of low-Z materials, such as wooden cupboards and benches, is important for this study.

Initially, comparison of the simulation with the observed spectrum from the internal ^{241}Am source at zero field was made. This benefited understanding of the locality of interactions in the vicinity of the source and also allowed tuning of the optical material properties (at 175 nm, these are hard to determine experimentally). For the more demanding neutron simulations, large quantities of processing power are required to produce significant numbers of events and facilitate optimization of experimental setups. This is very much work that is ongoing together with the development of parallelization tools and large-scale computing farms [13, 14].

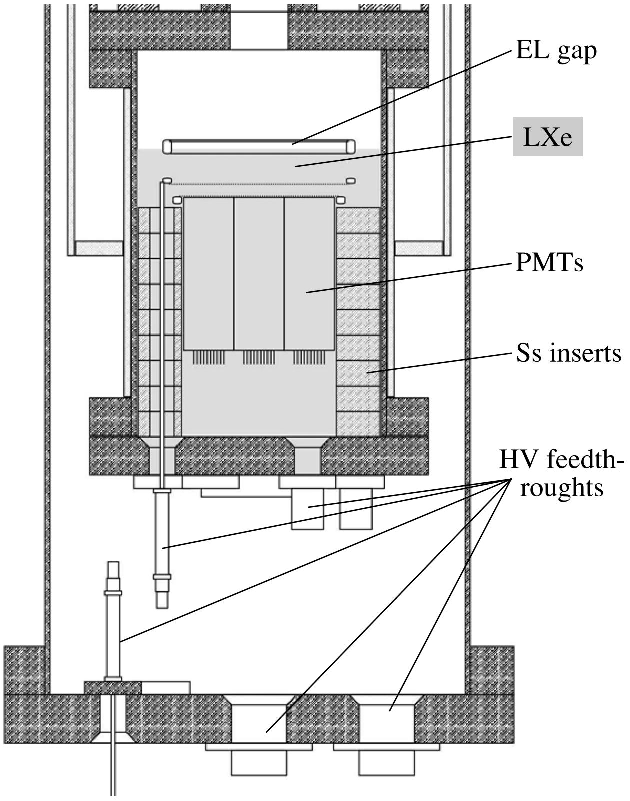

Fig. 12. A design impression of a new dark matter detector proposed for ITEP.

4. FUTURE PROSPECTS

The potential discrimination power of the two-phase technique is large; therefore, the opportunity exists for rapidly reducing the SUSY WIMP interaction cross section with the advent of the ZePLiN II and III detectors. In addition, the prospects for actual discovery are becoming real, and already plans are underway to build a very large scale 1-t dark matter detector, which will have the goal of attaining a measurement capability down to 0.0001 events/(kg d). It is proposed to extend the technology of the ZePLiN's with various concepts for modularity and functionality.

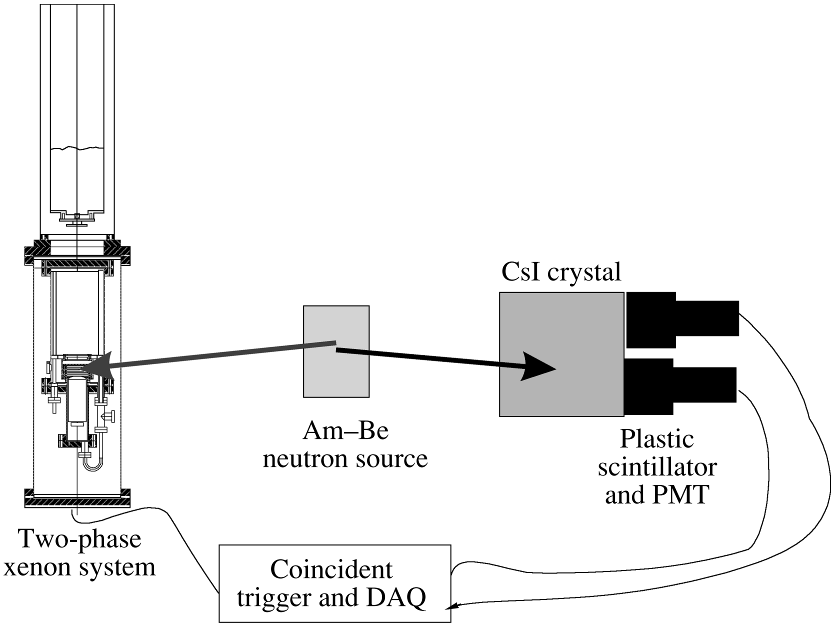

Fig. 13. The experimental configuration for Am–Be gamma tagging.

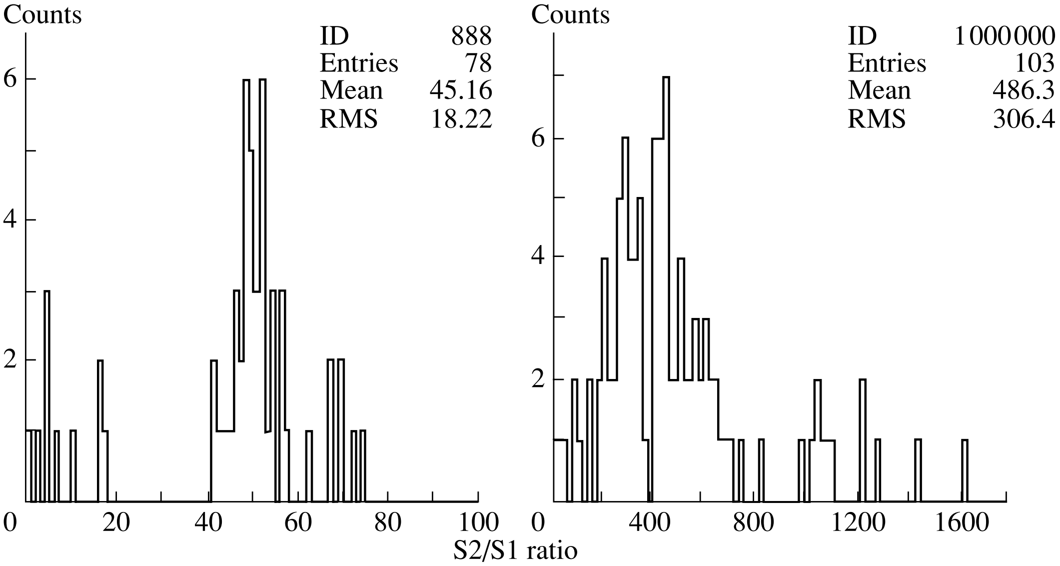

Fig. 14. The S2/S1 ratio for alpha (left) and gamma (right) signals from the Imperial two-phase prototype.

5. CONCLUSIONS

Two-phase xenon offers the possibility for excellent discrimination between signal-like nuclear recoils and background electron recoils. This offers good prospects for the direct search for WIMP dark matter particles in the future. Provisional analysis of neutron calibration of a two-phase system indicates that nuclear recoil ionization is slightly smaller than that produced by an alpha particle. Systematic study and analysis with respect to background and trigger bias is required to fully understand this result. The ZePLiN I dark matter detector has been taking data underground since January 2001. The preliminary result from 220 kg d of data gives an upper limit in the interaction cross section per nucleon of $\sim 1 \times 10^{-6}$ pb for a WIMP mass of 100 GeV. The construction of future dark matter detectors, ZePLiN's II and III is well under way and they should be deployed underground towards the end of 2004. Initial design studies into a one-ton system, ZePLiN MaX, have been initiated.

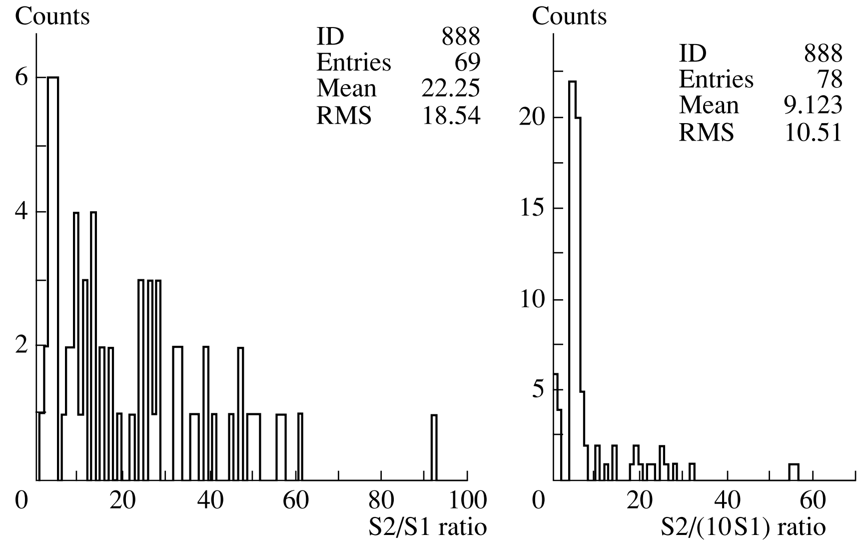

Fig. 15. Comparison of the S2/S1 ratio between nuclear recoils (left) and alphas (right).

ACKNOWLEDGMENTS

The financial support of INTAS and PPARC is gratefully acknowledged.

REFERENCES

1. C. L. Bennett *et al.*, Astrophys. J. **148**, 1 (2003).
2. E. M. Gushchin, A. A. Kruglov, V. V. Litskevich, *et al.*, Zh. Éksp. Teor. Fiz. **76**, 1685 (1979) [Sov. Phys. JETP **49**, 856 (1979)].
3. ICARUS Collab., Nucl. Instrum. Methods Phys. Res. A **329**, 567 (1993).
4. ICARUS Collab., Nucl. Instrum. Methods Phys. Res. A **449**, 147 (2000).
5. R. Bernabei *et al.*, Phys. Lett. B **436**, 379 (1998).
6. D. Akimov *et al.*, Phys. Lett. B **524**, 245 (2002).
7. D. Abrams *et al.*, Phys. Rev. D **66**, 122003 (2002).
8. A. Benoit *et al.*, Phys. Lett. B **545**, 43 (2002).
9. R. Bernabei *et al.*, Phys. Lett. B **480**, 23 (2000).
10. H. Wang, Phys. Rep. **307**, 263 (1998).
11. A. S. Howard *et al.*, in *Proceedings of the 3rd International Workshop on Identification of Dark Matter* (World Sci., Singapore, 2001), p. 457.
12. S. Agostinelli *et al.*, Nucl. Instrum. Methods Phys. Res. A **506**, 250 (2003).
13. A. S. Howard *et al.*, Nucl. Phys. B (Proc. Suppl.) **125**, 320 (2003).
14. J. Moscicki *et al.*, Nucl. Phys. B (Proc. Suppl.) **125**, 327 (2003).

Physics of Atomic Nuclei, Vol. 67, No. 11, 2004, pp. 2041–2043. From Yadernaya Fizika, Vol. 67, No. 11, 2004, pp. 2062–2064.
Original English Text Copyright © 2004 by Tikhomirov, Yuralevich.

Neutrino Emission and Oscillations in White Dwarf Matter Accreting onto a Primordial Black Hole*

V. V. Tikhomirov** and **S. E. Yuralevich**

Institute for Nuclear Problems, Belarussian State University, Minsk, 220050 Belarus

Received January 20, 2004

Abstract—Properties of the neutrinos emitted during an accretion of white dwarf matter by a primordial black hole are considered. The possibility of detecting these neutrinos and their oscillations is discussed. *© 2004 MAIK "Nauka/Interperiodica".*

Primordial black holes (PHBs) [1, 2] could form from primordial inhomogeneities, topological defects, and phase transitions in the early Universe. Both PBH detection and proof of their nonexistence could give invaluable information about the earliest stages of cosmological expansion.

The search for Hawking radiation has not allowed one to detect even the most actively radiating PHBs which had initial masses close to the Hawking mass, $M_* \simeq 5 \times 10^{14}$ g, and are completing their evaporation at present. The abundance of heavier PBHs could not be constrained by Hawking radiation at all.

An alternative direction of searches for PBHs can be founded on their influence on star evolution. As far back as in his paper [2], Hawking mentioned that a nuclear-size PBH could absorb a neutron star (NS) for a million years. An NS absorption, however, will be difficult to use for PBH detection [3]. If the most widespread stars at the stage of nuclear burning are considered, their absorption by a PBH still has not been understood in detail. However, taking into consideration their much lower density, one can suppose that their absorption time will exceed the lifetime of PBHs with most pressing masses $M \sim M_*$.

In our opinion, the most real possibility of PBH search is provided by white dwarfs (WD). Both the simplicity of their equation of state and metric variation unimportance drastically simplify the WD absorption picture. Their high density makes absorption time comparable with the Hubble time. It is even more important that the WD matter accretion is accompanied by intense neutrino emission, opening up a real possibility to observe the WD absorption.

Thus, cold WD matter is described by the degenerate electron Fermi gas equation of state, characterized by a dimensionless parameter

$$x = x(n) = \frac{p_{\mathrm{F}}(n)}{m_e c} \simeq 0.80\sqrt[3]{\rho_6}, \qquad (1)$$

which is equal to the Fermi momentum $p_{\mathrm{F}}(n) = (3\pi^2 n)^{1/3}\hbar$ of electrons in $m_e c$ units, where n is the electron number density, and m_e, c, and $\hbar$ are the electron mass, the speed of light, and the Planck constant, respectively. As an example, we will consider the carbon WD case for which $m' \simeq 2 \times 1.66 \times 10^{-24}$ g (m' is the nuclear rest mass which falls at one electron). The last value leads to the estimate (1), where ρ_6 is the WD matter density expressed in units of 10^6 g/cm^3. The equality $x = 1$ is fulfilled for $\rho_6 \simeq 2$. Recall that the conditions $x \ll 1$ and $x \gg 1$ hold for ultrarelativistic and nonrelativistic electrons, respectively.

Excluding the last tens of seconds, over a billion years of WD absorption, its density in the essential accretion region remains constant and nearly equals the central WD density ρ_c in the absence of a PBH [3]. The accretion flow can be considered in this case as that in a uniform medium with the density ρ_c at infinity. Such a flow is characterized by the "sound point" r_s being a special point of the accretion equations [4, 5]. The degree of WD matter compression at this point is determined by the relation [3]

$$x_s = x_s(x_0) = \sqrt{2x_0(x_0 + \sqrt{1 + x_0^2})}, \qquad (2)$$

connecting the parameter value (1) at the sound point $x_s = x(r_s)$ with its value $x_0 = x(n_c)$ at infinity. Equation (2) simplifies to

$$x_s \simeq 2x_0 + \frac{1}{4x_0} \qquad (3)$$

---

[*] This article was submitted by the authors in English.

[**] e-mail: `tikh@inp.minsk.by`

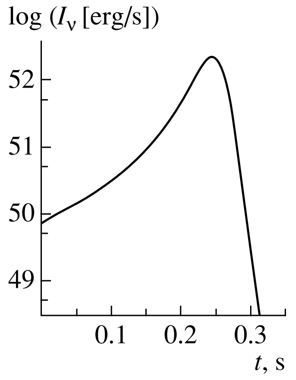

Time dependence of neutrino emission intensity, measured from the moment of absorption as a percent of initial WD mass. The WD central density without PBH equals $\rho_c = 10^9$ g/cm^3.

in the case of ultrarelativistic WDs demonstrating that the degree of compression $\rho(r_s)/\rho_c$ exceeds eight.

The value of parameter x_s, in particular, characterizes the influence of WD central density on the time of its absorption by a PBH. The well-known equations of stationary spherical accretion [4, 5] allow one to find the expression [3]

$$T_{\text{abs}} = \frac{\pi\hbar^3}{\sqrt{3}G^2 m'^{5/2} m_e^{3/2} M}\frac{1}{(1+x_s^2)^{3/4}} \qquad (4)$$

$$= \frac{27}{(M/10^{15}\text{ g})}\frac{1}{(1+x_s^2)^{3/4}} \times 10^9\ [\text{yr}]$$

for the WD absorption time, where G is the gravitational constant. It demonstrates that a WD of any density is absorbed by a PBH of mass $M \gg M_*$ in less than the Hubble time and that the densest WDs have enough time to be absorbed also by PBHs with $M \simeq M_*$.

Further accretion motion from r_s to the gravitational radius r_g proceeds according to the simple relation

$$x(r) \simeq x_{\text{max}}\sqrt{r_g/r}, \qquad (5)$$

leading to the maximum value

$$x_{\text{max}} = x(r_g) \simeq 42(1+x_s^2)^{1/4} \qquad (6)$$

of the parameter (1) reached at $r = r_g$. The corresponding Fermi energy $\varepsilon_{\text{F}}(r_g) \simeq m_e c x(r_g)$ reaches 20–100 MeV, not only exceeding the threshold energies $\Delta = 13.88$ MeV (for carbon) and $\Delta = 12.17$ MeV (for boron) of neutronization reactions

$$^{12}_{6}\text{C} + e^- \to {}^{12}_{5}\text{B} + \nu, \quad {}^{12}_{5}\text{B} + e^- \to {}^{12}_{4}\text{Be} + \nu \qquad (7)$$

of carbon WD matter, but also being sufficient to supply the energy $E \leq \varepsilon_{\text{F}} - \Delta$ of several tens of MeV to neutrinos produced in these reactions. This way, the neutrino emission provides a significant energy release on which the suggested approach of PBH search could be based.

The main part of this energy is released at the final stage of WD absorption described by the relativistic collapse equations [6] supplemented with equations

$$\dot{n} = -nu' - \frac{2nu}{r} - n_{\text{C}}\Gamma_{\text{C}} - n_{\text{B}}\Gamma_{\text{B}}, \qquad (8)$$

$$\dot{n}_{\text{C}} = -n_{\text{C}}u' - \frac{2n_{\text{C}}u}{r} - n_{\text{C}}\Gamma_{\text{C}},$$

$$\dot{n}_{\text{B}} = -n_{\text{B}}u' - \frac{2n_{\text{B}}u}{r} + n_{\text{C}}\Gamma_{\text{C}} - n_{\text{B}}\Gamma_{\text{B}}$$

of evolution of the radial component u of WD matter 4-velocity and of the number densities $n_{\text{C,B}}$ of carbon (C) and boron (B) nuclei participating in reactions (7), characterized by probabilities $\Gamma_{\text{C,B}}$. Dots and primes denote time and radius derivatives, respectively. A time dependence of the neutrino emission intensity is given in the figure for the case of WD central density $\rho_c = 10^9$ g/cm^3. It demonstrates that neutrino emission intensity reaches $(1–2) \times 10^{52}$ erg/s for about 0.1 s, taking away more than 10^{51} erg. The average neutrino energy is 16 MeV in this case.

Such a neutrino burst will initiate $\simeq$300 (kpc/R)^2 neutrino events in the Super-Kamiokande telescope, thus allowing one to detect it at a distance R of up to 10 kpc. A Hyper-Kamiokande type telescope containing about 10^6 t of water will be able to detect such bursts within the entire Galaxy.

Opening up a new way of PBH search, the neutrino bursts described can also give valuable information on neutrino properties. Like a supernova case, a neutrino burst accompanying WD absorption by a PBH may give information on the neutrino mixing angles and the type of neutrino mass spectrum hierarchy. The main properties of neutrino oscillations in the WD matter can be found following the approach [7] based on the condition of maximum violation of adiabaticity.

We will neglect the changes in upper WD layer structure at the moment of most intense neutrino emission. The nonrelativistic Fermi gas region in which resonance neutrino transitions occur in WDs is described by the equation

$$xx' = -\frac{m'GM(r)}{m_e c^2 r^2}. \qquad (9)$$

The most plausible candidates for observation are powerful neutrino bursts accompanying the absorption of WDs with the central density $\rho_c \sim 10^9$ g/cm^3. Since the mass fraction of nonrelativistic Fermi gas layers is small in such WDs, one can assume $M(r) = M_{\rm WD} = \text{const}$ and find the solution of Eq. (9):

$$x(r) = \left[\frac{2m'GM_{\rm WD}}{m_e c^2}\left(\frac{1}{r} - \frac{1}{r_{\rm WD}}\right)\right]^{1/2}, \tag{10}$$

where $r_{\rm WD}$ is the WD radius not greatly exceeding 2000 km at $\rho_c \sim 10^9$ g/cm^3. The condition $2\sqrt{2}G_{\rm F}nE = \Delta$ of maximum violation of adiabaticity is fulfilled at $x \simeq x_p$, where

$$x_p \simeq 1.89\left[\frac{\Delta[\text{eV}^2]}{E[\text{MeV}]}\right]^{1/3}, \tag{11}$$

$G_{\rm F}$ is the Fermi constant, E is the neutrino energy, and Δ is the difference of masses of neutrino states experiencing resonance interaction. For neutrino energy $E = 10$ MeV, one has $x_p = x_L = 0.036$ for "light" $\Delta = \Delta_L = 7.3 \times 10^{-5}$ eV^2 and $x_p = x_H = 0.12$ for "heavy" $\Delta = \Delta_H = 2.5 \times 10^{-3}$ eV^2. One can see that the WD Fermi gas is indeed nonrelativistic in the resonance region. Following the recipe [7], one can evaluate the crossing probabilities

$$P_L = \frac{\exp(\pi r_L \Delta_L c_{12}^2/E) - 1}{\exp(\pi r_L \Delta_L/E) - 1} \simeq c_{12}^2, \tag{12}$$

$$P_H = \frac{\exp(\pi r_H \Delta_H c_{13}^2/E) - 1}{\exp(\pi r_H \Delta_H/E) - 1} \simeq \exp\left(-\frac{\pi r_H \Delta_H s_{13}^2}{E}\right), \tag{13}$$

where $c_{12} = \cos\theta_{12}$, $c_{13} = \cos\theta_{13}$, $s_{13} = \sin\theta_{13}$ (θ_{12} and θ_{13} are vacuum neutrino mixing angles), and $r_L = -n(r_L)/n'(r_L)$ and $r_H = -n(r_H)/n'(r_H)$ are the density scale factors. Approximate right-hand parts of Eqs. (12) and (13) are written out in accordance with the values $\pi r_L \Delta_L/E = 0.026$ and $\pi r_H \Delta_H c_{13}^2/E = 10$ in a dense WD with $r_{\rm WD} \simeq 2000$ km and $M_{\rm WD} \simeq 1.4\,M_\odot$.

Equations (12) and (13) allow one to evaluate the electron-neutrino survival probabilities greatly simplified due to the conditions $\cos(2\theta_{12}^m) = \cos(2\theta_{13}^m) = -1$ (θ_{12}^m and θ_{13}^m are neutrino mixing angles in WD matter) fulfilled in the dense region of WD matter neutronization from which neutrinos are emitted. The survival probability equals

$$P_{ee}^{\rm dir} = U_{e1}^2 P_L P_H + U_{e2}^2[1 - P_L]P_H + U_{e3}^2[1 - P_H] \tag{14}$$

in the case of direct hierarchy ($\Delta_H > 0$). Substituting the numerical value of the angle θ_{12} in equalities $U_{e1}, U_{e2}, U_{e3} = c_{13}c_{12}, c_{13}s_{12}, s_{13}$, one can represent Eq. (14) in the form

$$P_{ee}^{\rm dir} = P_H(c_{12}^4 c_{13}^2 + s_{12}^4 c_{13}^2 - s_{13}^2) + s_{13}^2 \simeq \exp(-10 s_{13}^2)(0.625 - 1.625 s_{13}^2) + s_{13}^2. \tag{15}$$

Similarly, one obtains

$$P_{ee}^{\rm inv} = U_{e2}^2[1 - P_L] + U_{e1}^2 P_L \simeq (c_{12}^4 + s_{12}^4)c_{13}^2 \simeq 0.625(1 - s_{13}^2) \tag{16}$$

in the case of inverse hierarchy ($\Delta_H < 0$). Both (15) and (16) equal 0.625 in the limit of $\theta_{13} \to 0$. However, at $\sin^2\theta_{13} = 0.05$ and $\sin^2\theta_{13} = 0.036$ (see [8]), the probability (15) decreases to $P_{ee}^{\rm dir} = 0.38$ and 0.43, respectively. Thus, one can conclude that, measuring the ν_e and $\nu_{\mu/\tau}$ number ratio in the neutrino burst accompanying a WD absorption by a PBH, one can measure the $\sin^2\theta_{13}$ angle and determine the type of neutrino mass spectrum hierarchy if this angle is not very close to zero. In addition, the small value of the considered neutrino burst duration opens up good possibilities to directly limit the values of $\Delta_{L,H}$.

REFERENCES

1. J. B. Zel'dovich and I. D. Novikov, Astron. Zh. **43**, 758 (1966) [Sov. Astron. **10**, 602 (1966)].
2. S. W. Hawking, Mon. Not. R. Astron. Soc. **152**, 75 (1972).
3. S. E. Juralevich and V. V. Tikhomirov, astro-ph/0202445.
4. S. Shapiro and S. Teukolsky, *Black Holes, White Dwarfs, and Neutron Stars* (Wiley, New York, 1983).
5. F. Michel, Astrophys. Space Sci. **15**, 153 (1972).
6. C. W. Misner and D. H. Sharp, Phys. Rev. **136**, B571 (1964).
7. G. L. Fogli *et al.*, Phys. Rev. D **65**, 073008 (2002).
8. J. N. Bahcall and C. Peña-Garay, hep-ph/0305159.

Physics of Atomic Nuclei, Vol. 67, No. 11, 2004, pp. 2044–2049. From Yadernaya Fizika, Vol. 67, No. 11, 2004, pp. 2065–2070.
Original English Text Copyright © 2004 by Malinin.

Astroparticle Physics with AMS-02*

A. G. Malinin**
(on behalf of the AMS Collaboration)
Institute for Physical Science and Technology, University of Maryland, USA

Received January 20, 2004

Abstract—The main physics goals of the AMS-02 experiment in the astroparticle domain are searches for antimatter and dark matter. The discovery potential of primordial antimatter by AMS-02 is presented, emphasizing the completeness of the AMS-02 detector for these searches. Meanwhile, antiproton detection suffers from a large secondary interaction background; the anti-^{4}He or anti-^{3}He signal would allow one to probe the Universe for existence of antimatter. The expected signal in AMS-02 is presented and compared to results from present experiments. The e^+ and antiproton channels will contribute to the dark matter detection studies. A SUSY neutralino candidate is considered. The expected flux sensitivities in a three-year exposure for the e^+/e^- ratio and antiproton yields as a function of energy are presented and compared to other direct and indirect searches. © *2004 MAIK "Nauka/Interperiodica"*.

INTRODUCTION

The Alpha Magnetic Spectrometer (AMS) is a particle physics experiment in space. Its initial space mission on board the Space Shuttle *Discovery* (STS-91) in June 1998 confirmed the basic concept of the experiment [1–3]. During this short flight, the AMS measured the GeV cosmic-ray fluxes over most of the Earth's surface for the first time [4–7] and provided the impetus to upgrade the instrument for the ISS mission to be launched in space in 2006 for a three-year mission (hereafter called AMS-02). These upgrades include among others a stronger superconducting magnet, as well as the addition of a transition radiation detector (TRD), a ring imaging Cherenkov (RICH) detector, and an electromagnetic calorimeter (ECAL). The upgraded instrument will provide data on cosmic radiation in a large range of energy from a fraction of a GeV to 3 TeV with very high accuracy and free from the atmospheric corrections needed for balloon-borne measurements. Its main physics goals in the astroparticle domain are searches for antimatter and dark matter as well as a necessary but interesting study of the Nature beam: the cosmic ray hadron and lepton components, which will allow new insights into the origin, acceleration mechanisms, and propagation history of cosmic rays.

The possible presence of cosmological antimatter and the nature of dark matter in the Universe are fundamental questions of modern astrophysics and cosmology. The existence (or absence) of antimatter nuclei in space is closely connected with the foundation of the theories of elementary particle physics, CP violation, baryon nonconservation, Grand Unified Theory (GUT), etc. Balloon-based cosmic-ray searches for antinuclei at altitudes up to about 40 km have been carried out for more than 20 yr. Antiprotons, which are produced as secondary products of hadronic interactions in the interstellar medium, have been observed by several experiments, but all searches for heavier antinuclei have been negative [8–14]. The absence of annihilation γ-ray peaks excludes the presence of large quantities of antimatter within a distance of about 10 Mpc from the Earth. The proposed baryogenesis models are not yet supported by particle physics experimental data; i.e., baryon nonconservation and large levels of CP violation have not been observed.

The evidence for the existence of dark matter (DM) comes from the observation of rotation velocities across the spiral galaxies, derived from the variation in the red shift. The rotation velocities rise rapidly from the galactic center and remain almost constant to the outermost regions of a galaxy. These observations are consistent with the gravitation motion only if the matter in the Universe is mostly nonluminous "dark matter." The mystery of the DM remains unsolved. Many candidates such as massive neutrino and supersymmetry theory (SUSY) lightest neutralinos were proposed. If the DM, or a fraction of it, is nonbaryonic and consists of almost noninteracting particles like neutralinos, it can be detected in cosmic rays through its annihilation into positrons or antiprotons, resulting in deviations (in the case of

---

*This article was submitted by the author in English.

**e-mail: `A.Malinine@cern.ch`

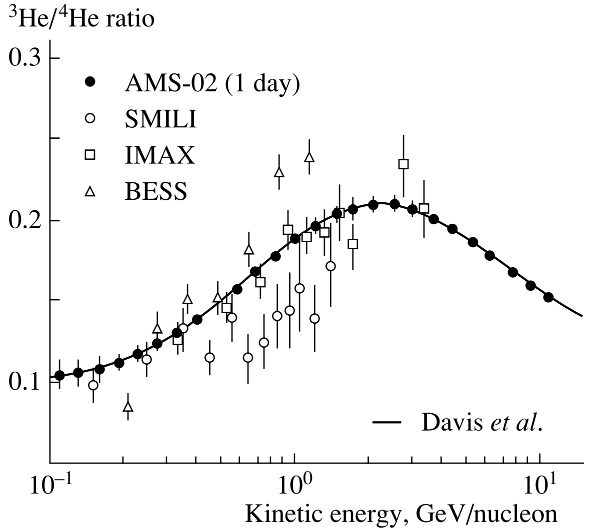

Fig. 1. Example of expected AMS-02 single-day ^{3}He/^{4}He ratio measurement.

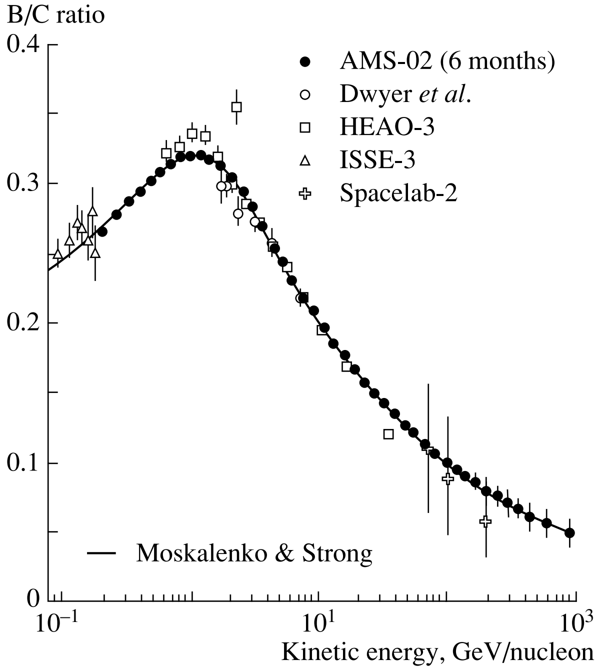

Fig. 2. Example of expected AMS-02 B/C ratio 6-month measurements.

antiprotons) or structures (in case of positrons) to be seen in the otherwise predictable cosmic-ray spectra. Considering the hypothesis of a possible clumpy DM, the expected fluxes of such primary positrons or antiprotons may be enhanced since the annihilation rate is proportional to the squared DM density [15], contrary to direct DM searches, which will suffer from a decreased probability for the Earth to be contained in an eventual DM clump.

Studying the primary and secondary cosmic-ray fluxes and energy distributions is not only a necessary step to understand the backgrounds on top of which a signal of “new physics” is expected, but also allows one to extract information on their transport history and on the nature and distribution of their sources [16]. A better understanding of the spectra of protons and He, which dominate the cosmic-ray abundance, is also important for atmospheric-neutrino flux calculations [17]. ^{3}He/^{4}He, B/C, and sub-Fe/Fe ratios allow one to measure the mean ISM density in the Galaxy crossed by a cosmic ray (the current measurement gives 9 g cm^{-2}). The ^{10}Be isotope with a half-life of 1.6×10^6 yr is the most important radioactive clock for measuring the age of cosmic rays. The ratio of radioactive ^{10}Be to stable ^{9}Be is sensitive to the propagation lifetime of cosmic rays and not to the total amount of matter traversed.

AMS-02 EXPERIMENT CAPABILITIES

A Monte Carlo physics performance study using the general AMS-02 computer model, based on the GEANT3 [18] and GEANT4 [19] simulation packages, was carried out. The calculated cosmic ray (CR) and background fluxes take into account the predicted geomagnetic conditions during the AMS-02 mission on the ISS. The simulated performance of AMS subdetectors was checked against the AMS flight and prototype test beam data and found to be in good agreement with them. Finally, more than 10^9 events containing $p^{\pm}$, He, $e^{\pm}$, and other CR particles at different energies have been fully simulated passing through the detector and then reconstructed. For every particular physics channel, the selection criteria were defined in order to separate the signal from background particles, and the expected number of signal events for the AMS-02 mission was obtained. Thanks to its large geometrical acceptance of about 1 m^2 sr, a high magnetic spectrometer resolving power of $BL^2 = 0.9$ T m^2, and three-year-long exposure time, AMS-02 will identify and measure over 10^9 protons with energies above 100 MeV, and 10^8 He, $10^5(10^4)$ carbon (boron) with energies above 100 MeV/nucleon. Light isotope separation based on velocity (RICH detector) and momentum measurement will be possible up to 10 GeV/nucleon.

In Figs. 1–3, the resulting expected AMS-02 measurements of the ^{3}He/^{4}He, B/C, and ^{10}Be/^{9}Be ratios are shown together with the present data and theoretical CR propagation from the leaky box (LBM) and diffusive halo (DHM) model predictions.

The MC results clearly show that AMS-02 will have a high potential to study beryllium as well as

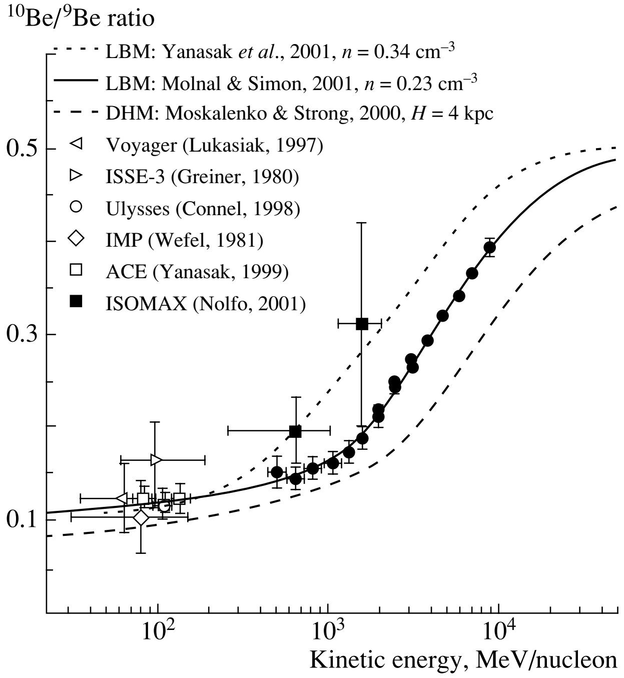

Fig. 3. AMS-02 ^{10}Be/^{9}Be ratio 6-month measurement potential. Closed circles are AMS-02 expectations.

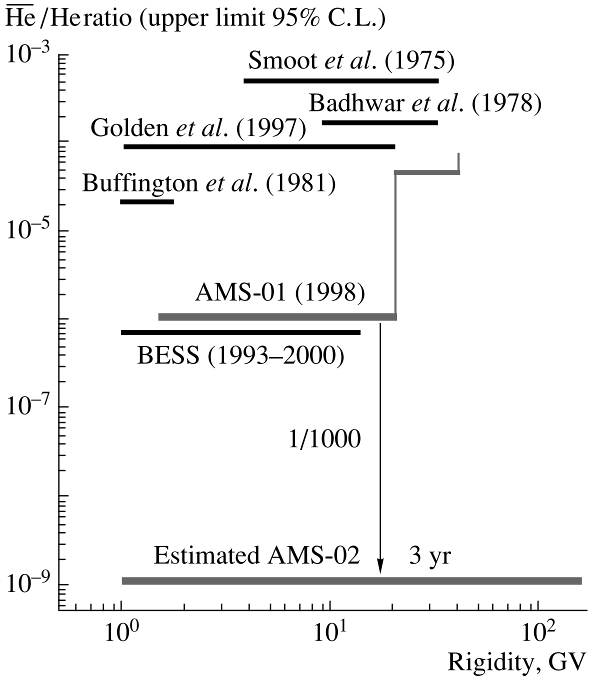

Fig. 5. The expected AMS-02 antihelium/helium flux ratio upper limit at 95% C.L.

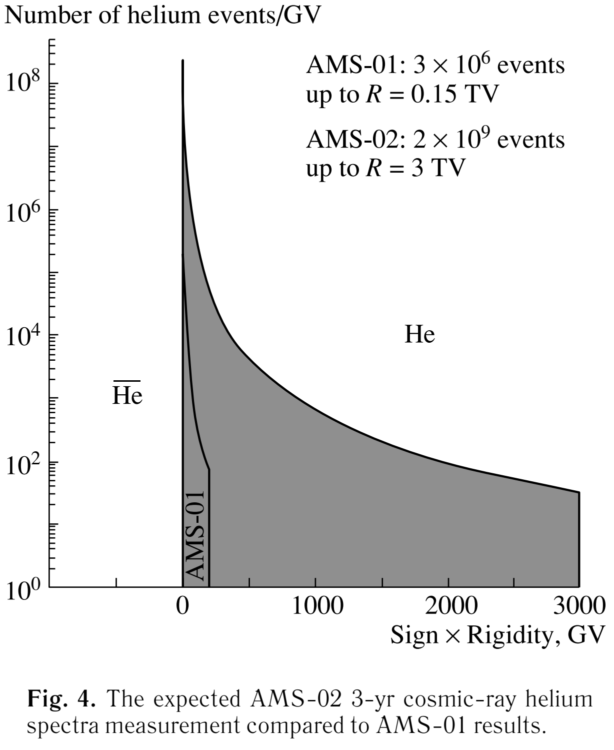

Fig. 4. The expected AMS-02 3-yr cosmic-ray helium spectra measurement compared to AMS-01 results.

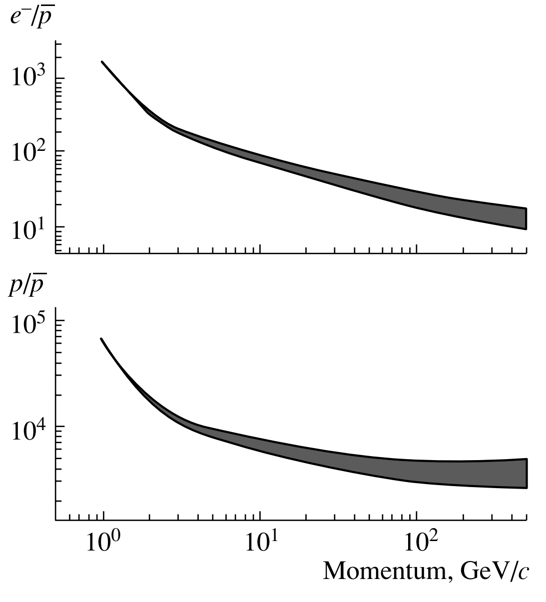

Fig. 6. Electron and proton backgrounds to antiproton signal ratios.

other isotopes in CR up to iron with unmatched precision measurements of the element abundances and the isotopic ratios. The CR propagation models will benefit from accurate AMS-02 data, which in turn will decrease the theoretical uncertainties for "new physics" signals.

The search for antimatter (anti-helium and heavier antinuclei) requires the capability to identify a charged particle and to measure its absolute rigidity value and the sign of its electric charge with the

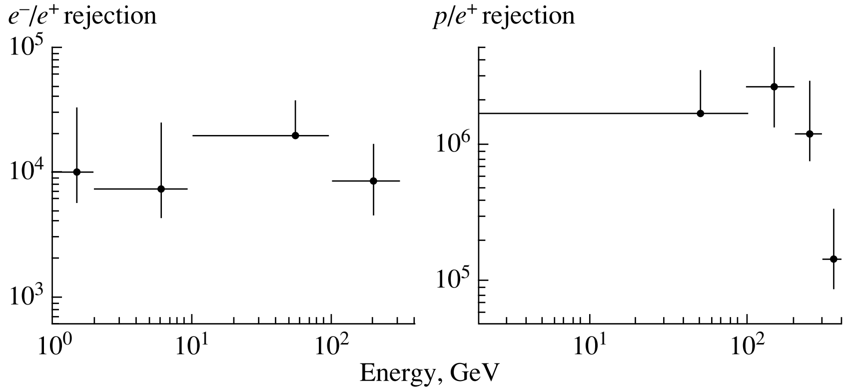

Fig. 7. The obtained e^+ rejection as a function of particle momentum against electrons (left panel) and protons (right panel).

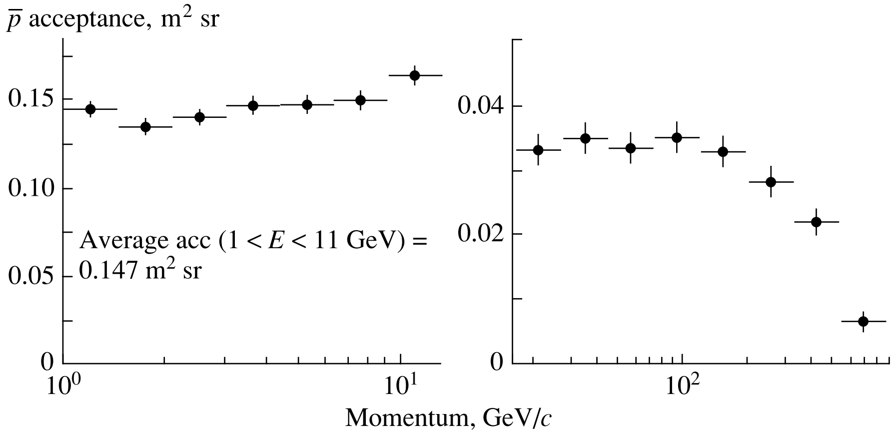

Fig. 8. The estimated average low-energy (left panel) and full range (right panel) AMS-02 antiproton acceptance after all cuts have been applied.

highest possible degree of confidence. A combined analysis based on AMS-02 redundant particle identification and a precise Silicon Tracker rigidity measurement allowed one to achieve over 10^9 background rejection power for the anti-helium signal. The corresponding measured spectra and anti-helium flux upper limit are shown in Figs. 4 and 5 together with the AMS-01 data and present limits.

The searches for DM signals in the antiproton and positron channels suffer from huge proton and electron backgrounds. To get the identification purity of the antiproton and positron samples equal to a few percent, an $O(10^4)$ to $O(10^6)$ background rejection level should be obtained (Fig. 6). To partly remove the proton background from positron signal, the TRD was used. The obtained TRD electron/hadron rejection ranged from 10^3 for 10-GeV and 10^2 for 300-GeV protons. Vetoing events with additional "hits" in the AMS-02 subdetectors in the vicinity of the reconstructed particle trajectory effectively removed the bulk of the interacted background. To discriminate positrons from protons and antiprotons from electrons at low energy, the AMS-02 RICH velocity measurement was used for particles with momentum less than 12.5 GeV/c. At higher energy, to further reduce the proton background, a 3D analysis of the ECAL energy distribution was done. Finally, the residual electron and/or proton background was removed by matching the energy deposition in the ECAL and the rigidity measured by Tracker. Figures 7 and 8 show the obtained background rejection against electrons and protons for a positron signal and AMS-02 antiproton acceptance after all cuts have been applied [20].

Figure 9 shows the simulation of the AMS-02 three-year high-statistics measurement of the cosmic antiproton spectrum up to 400 GeV and the residual background. In Fig. 10, an example of the AMS-02 antiproton flux measurement is shown together with the present experimental data compared to the various models of the secondary antiproton spectrum. The energy region around 10 GeV has less model

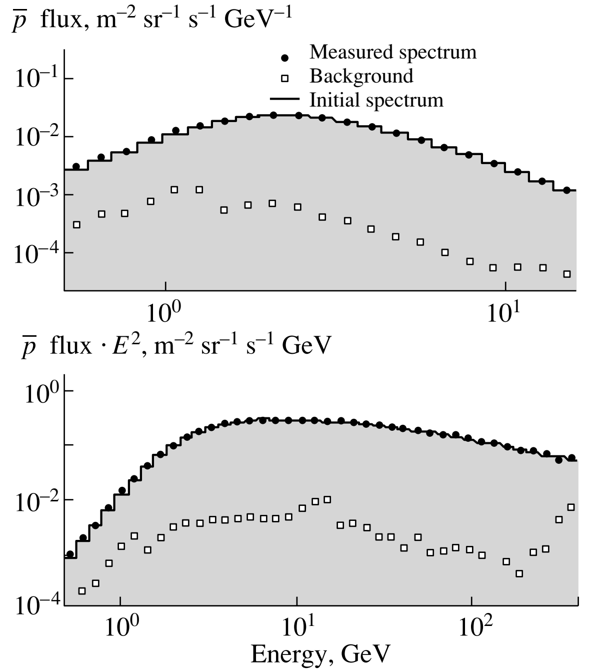

Fig. 9. Example of the AMS 3-yr combined measurement of the cosmic antiproton spectrum and residual background.

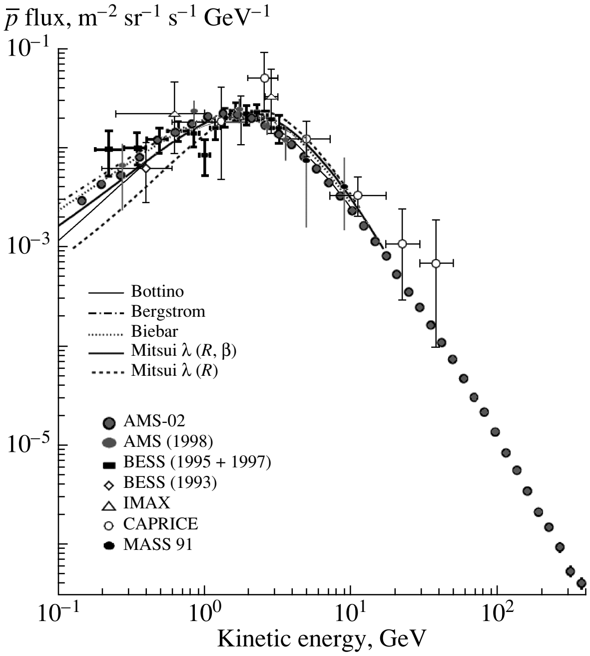

Fig. 10. Present cosmic-ray antiproton flux measurements together with an example of AMS-02 3-yr measurement.

dependence and looks more promising for possible DM related deviation searches.

The positron energy estimation was done by using

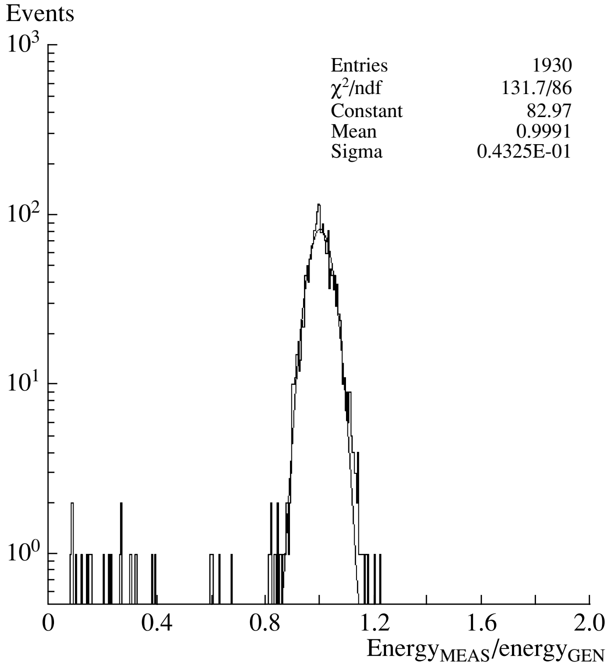

Fig. 11. MC prediction for the AMS-02 positron energy resolution function.

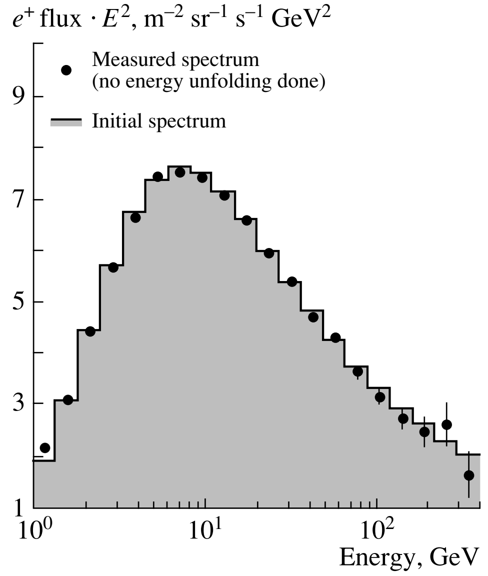

Fig. 12. Example of the AMS-02 3-yr combined measurement of the cosmic e^+ spectrum.

combined ECAL energy and Tracker rigidity quantities. Figure 11 shows the reconstructed energy resolution for 16-GeV positrons. An example of the positron expected spectrum is shown in Fig. 12 up to 400 GeV and without energy unfolding. The resulting spectrum was used to estimate the accuracy of the projected AMS-02 cosmic positron fraction measurement (less model-dependent value compared

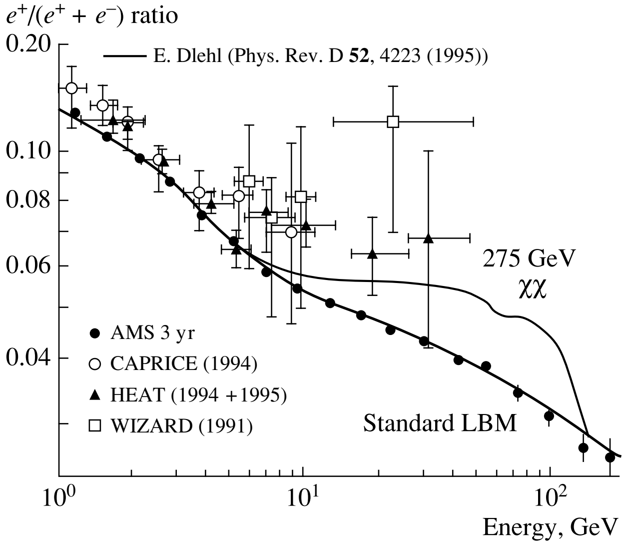

Fig. 13. Present cosmic positron fraction measurements and estimated 3-yr AMS-02 measurement. Solid lines are one of the most favorable SUSY scenarios and the standard LBM prediction.

to the positron flux). The result is shown in Fig. 13 together with the LBM prediction and one of the most favorable theoretical scenarios with a bump structure formed by the primary positrons originated from the annihilations of the SUSY neutralino DM candidate. The present cosmic-positron fraction-ratio measurements are generally compatible with a secondary origin; however, large uncertainties associated with the measurements do not allow one to exclude a primary positron component.

CONCLUSION

During the three-year mission in space, AMS-02 will perform precise, high-statistics cosmic-ray measurements in the fraction of GeV to few-TeV energy range. It will advance our knowledge of astroparticle physics phenomena and will have a high discovery potential of cosmic nuclear antimatter and dark matter.

REFERENCES

1. G. M. Viertel and M. Capell, Nucl. Instrum. Methods Phys. Res. A **419**, 295 (1998).
2. J. Alcaraz *et al.*, Nuovo Cimento A **112**, 1325 (1999).
3. D. Alvisi *et al.*, Nucl. Instrum. Methods Phys. Res. A **437**, 212 (1999).
4. J. Alcaraz *et al.*, Phys. Lett. B **461**, 387 (2000).
5. J. Alcaraz *et al.*, Phys. Lett. B **472**, 215 (2000).
6. J. Alcaraz *et al.*, Phys. Lett. B **484**, 10 (2000).
7. J. Alcaraz *et al.*, Phys. Lett. B **490**, 27 (2000).
8. G. F. Smoot *et al.*, Phys. Rev. Lett. **35**, 258 (1975).
9. G. Steigman *et al.*, Annu. Rev. Astron. Astrophys. **14**, 339 (1976).
10. G. Badhwar *et al.*, Nature **274**, 137 (1978).
11. A. Buffington *et al.*, Astrophys. J. **248**, 1179 (1981).
12. R. L. Golden *et al.*, Astrophys. J. **479**, 992 (1999).
13. J. F. Ormes *et al.*, Astrophys. J. Lett. **482**, L187 (1997).
14. T. Saeki *et al.*, Phys. Lett. B **422**, 319 (1998).
15. E. A. Baltz *et al.*, Phys. Rev. D **65**, 063511 (2002).
16. I. V. Moskalenko and A. W. Strong, Adv. Space Res. **27**, 717 (2001).
17. T. K. Gaiser, T. Stanev, *et al.*, Phys. Rev. D **54**, 5578 (1996).
18. R. Brun *et al.*, GEANT3, CERN-DD/EE/84-1 (Revised 1987).
19. S. Agistinelli *et al.* (GEANT4 Collab.), Nucl. Instrum. Methods Phys. Res. A **506**, 250 (2003).
20. V. Choutko, G. Lamanna, A. Malinin, and E. S. Seo, Int. J. Mod. Phys. A **17**, 1817 (2002).

Physics of Atomic Nuclei, Vol. 67, No. 11, 2004, pp. 2050–2053. From Yadernaya Fizika, Vol. 67, No. 11, 2004, pp. 2071–2074.

Salt Neutrino Detector for Ultrahigh-Energy Neutrinos*

M. Chiba[**], **T. Kamijo**[1)], **O. Yasuda**, **Y. Chikashige**[2)], **T. Kon**[2)], **Y. Takeoka**[2)], **and R. Yoshida**[2)]

Tokyo Metropolitan University, Department of Physics, Tokyo, Japan

Received January 20, 2004

Abstract—Rock salt and limestone are studied to determine their suitability for use as a radio-wave transmission medium in an ultrahigh energy (UHE) cosmic neutrino detector. A sensible radio wave would be emitted by the coherent Cherenkov radiation from negative excess charges inside an electromagnetic shower upon interaction of a UHE neutrino in a high-density medium (Askar'yan effect). If the attenuation length for the radio wave in the material is large, a relatively small number of radio-wave sensors could detect the interaction occurring in the massive material. We measured the complex permittivity of the rock salt and limestone by the perturbed cavity resonator method at 9.4 and 1 GHz to good precision. We obtained new results of measurements at the frequency at 1.0 GHz. The measured value of the radio-wave attenuation length of synthetic rock salt samples is 1080 m. The samples from the Hockley salt mine in the United States show attenuation length of 180 m at 1 GHz, and then we estimate it by extrapolation to be as long as 900 m at 200 MHz. The results show that there is a possibility of utilizing natural massive deposits of rock salt for a UHE neutrino detector. A salt neutrino detector with a size of 2 × 2 × 2 km would detect 10 UHE neutrino/yr generated through the GZK process. *© 2004 MAIK "Nauka/Interperiodica".*

Several cosmologically distant astrophysical systems, e.g., active galactic nuclei, are expected to generate ultrahigh-energy (UHE) cosmic neutrinos [1] with energies over 10^{15} eV (PeV). UHE neutrinos could travel long distances over 13 billion light years (ly), from the far or early Universe, regardless of 2.7 K cosmic-microwave background (CMB) and 1.9 K neutrino background (CNB) filling the Universe. Therefore, one could determine the UHE states of the early Universe by directly detecting UHE neutrinos. On the contrary, UHE protons and photons could travel only 163 M ly (50 Mpc) due to the Greisen, Zatsepin, and Kuz'min (GZK) cutoff process [2]. The UHE neutrinos could also give us new information about the space-filled substances. They could interact with CMB, CNB, etc., and therefore they would be scattered or regenerated at a small rate through their voyage.

The energy of the UHE neutrinos is far beyond the energy provided by an artificial accelerator. We could compare the interaction cross section with those predicted by the Standard Model of elementary particle physics in the unexplored energy region. At this energy, the Earth is no longer transparent to them [3], and the cross section would be measured by counting UHE neutrinos with respect to the zenith angle, which corresponds to the path length through the Earth.

There are UHE protons whose energy exceeds the threshold of 3–3 resonance production upon the collision with CMB in the GZK process. The resonance decays to a charged pion, which produces the UHE neutrinos (GZK neutrinos). The existence of the GZK neutrinos is certain and it is natural to try to detect them [4]. Their energies span over 10^{15}–10^{20} eV, and their fluxes are as low as 1 $\mathrm{km}^2\ \mathrm{d}^{-1}$ (Fig. 1). In order to detect the GZK neutrinos, a huge detector sensitive to the energy region is needed which also could supply one with information on the neutrino energy, its arrival direction, and time as well as on the flavor of the neutrino. With regard to the energy measurement, a calorimetric detection is better than a muon track detection.

Radio-wave detection is a suitable way to realize such a huge detector. Askar'yan [5] has proposed to detect the radio emissions with coherent amplification produced by excess negative charges in an electron–photon shower in dense materials, which is generated by the interaction of UHE neutrinos. For a low-density medium, the same effect was calculated in an atmospheric shower independently by Fujii and Nishimura [6]. Recently, the Askar'yan effect has been confirmed with a bunched electron beam at SLAC [7].

---

[*] This article was submitted by the authors in English.

[1)] Tokyo Metropolitan University, Department of Engineering, Tokyo, Japan.

[2)] Seikei University, Department of Engineering, Tokyo, Japan.

[**] e-mail: `chiba-masami@c.metro-u.ac.jp`

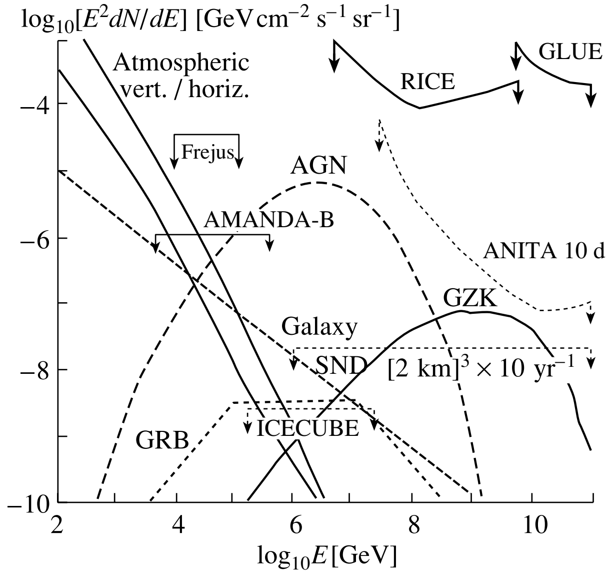

Fig. 1. Flux of cosmic UHE neutrinos with respect to the energies expected on the Earth.

From a practical point of view in construction of such a huge detector, one could not purify the detection medium. One can use a natural medium. We have been taking notice of a rock salt dome [8] as a high-density material, since it does not allow water penetration; moreover, it is of high purity. We are therefore interested in the possibility of using a natural rock salt mine as a UHE neutrino detector, namely, salt neutrino detector (SND). Furthermore, the attenuation length of the electromagnetic wave propagation in the microwave or longer wavelengths is expected to be long in the rock salt. If so, a moderate number of radio-wave sensors could detect neutrino interactions in a massive rock salt deposit. Rock salt deposits are distributed worldwide and there are many candidates for suitable sites [9]. Figure 2 shows a scheme for an SND (2 × 2 × 2 km) using a large volume of salt dome.

We measured the complex permittivity in rock salt, limestone, and granite samples by a perturbation method [10] using cavity resonators of 9.4 GHz (TE_{107}, $22 \times 10 \times 161.6$ mm, width × height × length) and 1.0 GHz (TM_{010}, $\varnothing 225$ mm × 30 mm, diameter × height), which had a Q value of 4000 and 10 000, respectively. Both resonators were made of copper with sample insertion holes at the center of the cavity. A sample piece having the same height of the cavity was inserted in between end surfaces of two copper rods. The sample was placed in the cavity with the surfaces making contact with those of the copper rods. The copper rods closed two sample insertion holes of the cavity at the center when the sample was inserted to form a complete cavity. The sample diameter was changed whether the sample volume fulfills the perturbation condition to measure the complex permittivities. We obtained the real part (the square of the refractive index) and the imaginary part (the attenuation in a medium) of the permittivity by measuring the decrease in the resonance frequency and the widening of the resonance width after insertion of the samples, respectively. The method is proper to measure the imaginary part of the permittivity for ultralow-loss material like rock salt. The attenuation length L_α is calculated using the following equations:

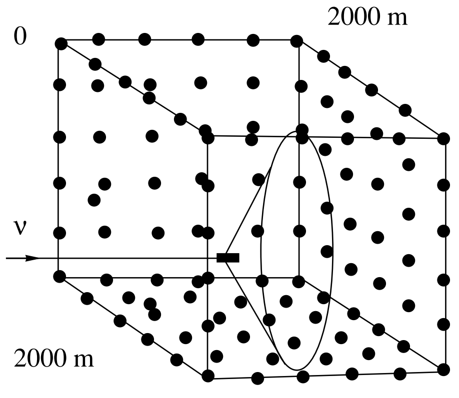

Fig. 2. Conceptual design of an underground salt neutrino detector is described. A moderate number of radio-wave sensors could detect the neutrino interaction in the massive rock salt. If the attenuation length $L_\alpha = 1$ km, 216 antennas set at 400 m intervals in 36 boreholes work as an imaging calorimetric detector.

$$\varepsilon = \varepsilon' - i\varepsilon'', \tag{1}$$

$$\tan\delta = \varepsilon''/\varepsilon', \tag{2}$$

$$L_\alpha = \frac{\lambda}{\pi\sqrt{\varepsilon'}\tan\delta}, \tag{3}$$

where ε', ε'', $\tan\delta$, and λ are the real and imaginary permittivity, loss tangent, and wavelength of the radio wave. At a distance of L_α, the electric field strength is diminished to $1/e$.

Two data sets given by Hippel [11] are shown in Fig. 3 at 10 MHz and 25 GHz, which are the lower limits of the attenuation length for the rock salt. Three data sets at 150, 300, and 750 MHz are given by Gorham *et al.* at United Salt's Hockley mine located in a salt dome near Houston, Texas [12]. The attenuation lengths were larger than 250 m, which were measured in situ. The other data have been measured by us and plotted in Fig. 3. The frequencies were widened using a few different modes of the cavities around 9.4 and 1.0 GHz. Accuracy of the measurement including the equipment and the sample treatment was mostly under 40 and 20% around 9.4 and 1.0 GHz, respectively. The uncertainty comes mainly from the

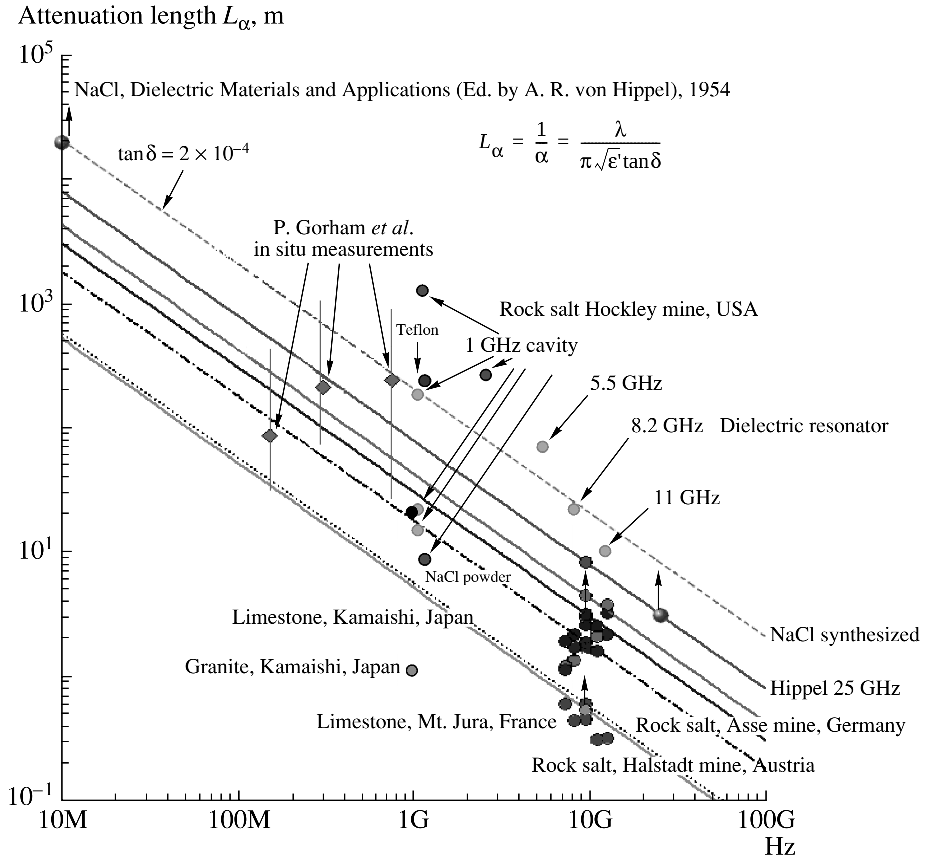

Fig. 3. Measured attenuation length for rock salt, limestone, and granite with respect to radio-wave frequency (in Hz). If $\tan\delta$ is constant with frequency, the attenuation lengths of the same material should be put on inclined lines with the same inclination.

surface condition of the samples like the smoothness, the stain, and the moisture. At 1 GHz, a synthetic rock salt sample showed $\varepsilon' = 5.9$, $\tan\delta = 4.3 \times 10^{-5}$, followed with $L_\alpha = 1080$ m. The samples from the Hockley salt mine show an attenuation length of 180 m at 1 GHz, and under the assumption of constant $\tan\delta$ with respect to frequency, we estimate by extrapolation that L_α will be as long as 900 m at 200 MHz. This value for the attenuation length is sufficient to construct the SND. However, it should be confirmed by direct measurement in the lower frequency region with good precision. Limestone and granite are popular species of rock in the world. We measured samples at the Kamaishi mine of Nittetsu Mining Co. Ltd., Japan. The attenuation lengths of limestone and granite are 1/10 and 1/100 compared with that of Hockley rock salt at 1 GHz, respectively. They could not be a good medium candidate for a radio-wave neutrino detector.

In conclusion, there is a possibility of utilizing natural massive deposits of rock salt for a UHE neutrino detector. An SND with a size of $2 \times 2 \times 2$ km would detect about 10 UHE neutrinos per year generated through GZK processes.

REFERENCES

1. F. W. Stecker, C. Done, M. H. Salamon, and P. Sommers, Phys. Rev. Lett. **66**, 2697 (1991).
2. K. Greisen, Phys. Rev. Lett. **16**, 748 (1966); G. T. Zatsepin and V. A. Kuz'min, Pis'ma Zh. Éksp. Teor. Fiz. **4**, 114 (1966) [JETP Lett. **4**, 78 (1966)].
3. R. Gandhi, C. Quigg, M. H. Reno, and I. Sarcevic, Astropart. Phys. **5**, 81 (1996); Phys. Rev. D **58**, 093009 (1998); G. Sigl, Phys. Rev. D **57**, 3786 (1998); J. Kwiecinski, A. D. Martin, and A. M. Stasto, Phys. Rev. D **59**, 093002 (1999); R. Horvat, Phys. Lett. B **480**, 135 (2000).
4. D. Saltzberg, D. Besson, P. Gorham, *et al.*, Proc. SPIE **4858**, 191 (2003).
5. G. A. Askar'yan, Zh. Éksp. Teor. Fiz. **41**, 616 (1961) [Sov. Phys. JETP **14**, 441 (1962)]; **48**, 988 (1965) [**21**, 658 (1965)].
6. M. Fujii and J. Nishimura, in *Proceedings of the 11th ICRC, Budapest, 1969*, p. 709.
7. P. Gorham, D. Saltzberg, P. Schoessow, *et al.*, Phys. Rev. E **62**, 8590 (2000); D. Saltzberg, P. Gorham, D. Walz, *et al.*, Phys. Rev. Lett. **86**, 2802 (2001).

8. M. Chiba, T. Kamijo, M. Kawaki, *et al.*, in *Proceedings of the 1st International Workshop for Radio Detection of High Energy Particles (RADHEP-2000)*, AIP Conf. Proc. **579**, 204 (2001); T. Kamijo and M. Chiba, *Memoirs of Faculty of Technology,* Tokyo Metropolitan Univ., No. 51 2001, 139 (2002); M. Chiba *et al.*, in *Proceedings of the First NCTS Workshop on Astroparticle Physics, Kenting, Taiwan, 2001* (World Sci., Singapore, 2002), p. 99; T. Kamijo and M. Chiba, Proc. SPIE **4858**, 151 (2003).
9. *Topography Dictionary,* Ed. by T. Machida *et al.* (Ninomiya Book, Tokyo, 1981), p. 110 [in Japanese]; J. L. Stanley, *Handbook of World Salt Resources* (Plenum, New York, 1969); T. H. Michel, *Salt Domes* (Gulf, Houston, 1979).
10. H. A. Bethe and J. Schwinger, NDRC Report D1-117 (1943); R. L. Sproull and E. G. Linder, Proc. IRE **34**, 305 (1946); J. C. Slater, Rev. Mod. Phys. **18**, 441 (1946); G. Birnbaum and J. Franeau, J. Appl. Phys. **20**, 817 (1949); N. Ogasawara, J. Inst. Elect. Eng. (Japan) **74**, 1486 (1954).
11. *Dielectric Materials and Applications*, Ed. by A. R. von Hippel (Wiley, 1954), pp. 302, 361; Landolt–Börnstein, *Zahlenwerte und Functionen aus Physik, Chemie, Astronomie, Geophysik und Technik, Eigenschaften der Materie in Ihre Aggregatzustaenden, 6. Teil, Elektrische Eigenschaften I*, Ed. by Herausgegeben von K. H. Hellwege und A. M. Hellwege (Springer, 1959), pp. 456, 505; R. G. Breckenbridge, J. Chem. Phys. **16**, 959 (1948).
12. P. Gorham, D. Saltzberg, A. Odian, *et al.*, Nucl. Instrum. Methods Phys. Res. A **490**, 476 (2002).

Physics of Atomic Nuclei, Vol. 67, No. 11, 2004, pp. 2054–2057. From Yadernaya Fizika, Vol. 67, No. 11, 2004, pp. 2075–2078.

RARE PROCESSES AND ASTROPHYSICS

NESTOR Experiment in 2003*

V. A. Zhukov[1)], A. Aloupis[2)], E. G. Anassontzis[2)], N. Arvanitis[3)], A. Babalis[3)], A. Ball[4)], L. B. Bezrukov[1)], G. Bourlis[5)], A. V. Butkevich[1)], W. Chinowsky[6)], P. E. Christopoulos[7)], A. Darsaklis[3)], L. G. Dedenko[1)], D. Elstrup[8)], E. Fahrun[8)], J. Gialas[9)], Ch. Goudis[7)], G. Grammatikakis[9)], C. Green[8)], P. K. F. Grieder[10)], S. K. Karaevsky[1)], P. Katrivanos[11)], U. Keussen[8)], J. Kiskiras[3)], Th. Knutz[8)], D. Korostylev[12)], K. Komlev[13)], J. Kontakxis[2)], P. Koske[8)], J. G. Learned[14)], V. V. Ledenev[13)], A. Leisos[5)], G. Limberopoulos[3)], J. Ludvig[6)], J. Makris[12)], A. Manousakis-Katsikakis[2)], E. Markopoulos[3)], S. Matsuno[14)], J. Mielke[8)], Th. Mihos[3)], P. Minkowski[10)], A. A. Mironovich[1)], R. Mitiguy[14)], S. Nounos[2)], D. R. Nygren[6)], K. Papageorgiou[3)], M. Passera[10)], C. Politis[7)], P. Preve[2)], G. T. Prybylsky[6)], J. Rathley[8)], L. K. Resvanis[2),3)], M. Rosen[14)], N. Schmidt[8)], Th. Schmidt[8)], I. Siotis[15)], A. E. Shnyrev[1)], J. Sopher[6)], T. Staveris[3)], G. Stavrakakis[16)], R. Stokstad[6)], N. M. Surin[1)], V. Tsagli[3)], A. Tsirigotis[3)], J. Tsirmpas[3)], S. Tzamarias[5)], O. Vasiliev[12)], O. Vaskin[13)], W. Voigt[8)], A. Vougioukas[3)], G. Voulgaris[2)], L. M. Zakharov[1)], and N. Ziabko[12)]

(The NESTOR Collaboration)

Received January 20, 2004

Abstract—NESTOR is a submarine high-energy muon and neutrino telescope, now under construction for deployment in the Mediterranean close to Greek shores. The first floor of NESTOR with 12 optical modules was deployed successfully in March 2003 together with the electronics system. All systems and the associated environmental monitoring units are operating properly and data are being recorded. The status of the NESTOR project is presented. We outline briefly the construction of the deepwater neutrino telescope, properties of the NESTOR site, infrastructure of the project, the deployment of the first floor, and its current operation. The first data are presented and plans for the next steps are summarized. © *2004 MAIK "Nauka/Interperiodica".*

1. THE NESTOR TOWER

NESTOR (Neutrino Extended Submarine Telescope with Oceanographic Research) will consist of a tower (Fig. 1) with 12 rigid hexagonal floors 32 m in diameter and spaced 30 m apart vertically [1–4]. Six arms attached to the central frame are built from titanium tubes to form a light-weight and rigid lattice girder structure. Three girders each 5 m long are connected one to another and to the central frame with hinges. This made the construction collapsible and very convenient for transportation and deployment. In water, folded arms open automatically or with the help

---

[*] This article was submitted by the authors in English.

[1)] Institute for Nuclear Research, Russian Academy of Sciences, pr. Shestidesyatiletiya Oktyabrya 7a, Moscow, 117312 Russia.

[2)] Physics Department, University of Athens, Greece.

[3)] NESTOR Institute for Deep Sea Research, Technology, and Neutrino Astroparticle Physics, Pylos, Greece.

[4)] CERN, Geneva, Switzerland.

[5)] School of Science and Technology, Hellenic Open University, Greece.

[6)] Lawrence Berkeley National Laboratory, Berkeley, CA, USA.

[7)] Physics and Astronomy Department, University of Patras, Greece.

[8)] Center for Applied Marine Science Research and Technology Westcoast (FTZ), Buesum, University of Kiel, Germany.

[9)] Physics Department, University of Crete, Greece.

[10)] Institute of Physics, University of Bern, Switzerland.

[11)] Institute of Informatics and Telecommunications NCSR DEMOKRITOS, Greece.

[12)] Institute for Geophysics, University of Hamburg, Germany.

[13)] Experimental Design Bureau of Oceanological Engineering, Russian Academy of Sciences, Moscow, Russia.

[14)] Department of Physics and Astronomy, University of Hawaii at Manoa, Honolulu, HI, USA.

[15)] National Science Foundation, Greece.

[16)] Institute for Geodynamics, Athens Observatory, Greece.

[**] e-mail: `vlzhukov@mail.ru`

of divers. All ends of the arms are coupled around the floor by ropes for stability.

The 1-m-diameter titanium sphere that houses the floor electronics is mounted at the central support frame. Two optical modules (OM) are installed at the end of each of the six arms, one facing upwards and the other downwards. The OMs are also installed above and below the central titanium sphere, making a total of 14 per floor. A full NESTOR tower will consist of 168 OMs.

A NESTOR optical module consists of a 15-in. HAMAMATSU photomultiplier (PMT) R2018-03 surrounded by a μ-metal cage inside a 17-in. glass pressure housing (the BENTHOS sphere) [4]. The PMT is fixed inside the glass sphere by a silicon gel gasket. Glycerin is used for optical coupling. Inside the glass spheres, a 24/2500-V dc converter and pressure gauge are mounted. The OM is connected to the central titanium sphere by a hybrid electrical cable with seven-pin deepwater connectors at both ends. Cables have coaxial and twisted pairs for PMT signal and power (24 V dc) transmission and HV control and monitoring.

Small LED modules will be installed between floors for OM calibration. The gain and the timing characteristics of the OMs will be monitored continuously by LEDs placed halfway between floors.

The tower is connected to the sea bottom unit, which contains the anchor and its release mechanism, the junction box for the electro-optical cable coming from shore, and a number of environmental monitoring units.

Connections of the shore cable to the junction box and internal cables from the junction box to each titanium sphere, from titanium sphere to the OMs, are all made at the surface during deployment. This avoids the use of deep submersible vehicles and wet-mating connections.

Eventually a number of such towers could be deployed to form a very large neutrino telescope.

2. THE NESTOR SITE

The NESTOR tower will be deployed in the deepest part of the Mediterranean, very close to the southwestern coast of Peloponnese. The deployment site is an underwater plateau 65 km^2 in area at an average depth of 3800 m, which is constant to within ±50 m over its entire area. The center of the plateau, with coordinates 36°37.5′ N, 21°34.6′ E, is approximately 20 km offshore. Therefore, the detector deployed at this site can be connected to shore by a modest length of cable.

Far from the effluents of major rivers, the NESTOR site benefits from extremely clear water with a transmittivity of 55 ± 10 m at 460-nm wavelength, weak water current consistently below 10 cm/s, and water temperature of 14°C [2]. The mean density of seafloor sediments is near 1.5 g/cm^3, which indicates a slow accumulation rate of 7–18 cm over 10 000 yr.

Data collected with fourfold coincidence trigger (in Hz)

	Thresholds at 30 mV	Thresholds at 120 mV
Measured total trigger rates ($\geq$ 4-fold)	2.61 ± 0.02	0.12 ± 0.01
MC prediction (atmospheric muons only)	0.141 ± 0.005	$0.12 + 0.01$

The optical background due to ^{40}K and bioluminescence was measured to be 75 kHz per OM at the 0.25 p.e. level. The bioluminescence bursts indicate a duration not longer than 15 s (3–5 s typically) and frequency of about 20 per hour.

3. THE NESTOR INFRASTRUCTURE

The NESTOR neutrino telescope is a part of the scientific program of the NESTOR Institute, in the town of Pylos on Navarino Bay. It has a very convenient location: 280 km from Athens, 40 km from Kalamata International Airport, 45 km from the industrial and port city of Kalamata. The NESTOR site is 15 nautical miles from Pylos.

The NESTOR infrastructure is well developed now. The institute's building (1000 m^2) houses a fully equipped electronics laboratory (analog and digital), offices, a conference room, library, and small workshop. There is a cluster of 36 dual Pentium-III-based computers, 500 MHz, with 36 GFLOPS, 4 GB RAM, 416 GB HD. A second building consists of a machine shop, equipped with turning, milling, drilling, cutting, welding, and other machines. An optical laboratory, equipped with all necessary stands for PMTs, OMs, and electronics system tests; a storage room; and large and small hyperbaric chambers are installed in the second building.

A 30-km-long deep-sea cable with 18 mono mode optical fibers has been laid from the shore to the deep-sea site. One copper conductor can deliver up to 6 kW of dc power. Power return is done electrolytically via the sea. The scientific payloads are attached at the end of the cable. The sea end of cable is liftable in order to change the deepwater equipment. The cable landing is terminated in the terminal cable station in the village of Methoni (11 km from Pylos).

NESTOR has a test facility built at a depth of 50 m in Navarino Bay, near Sfakteria Island. It can be

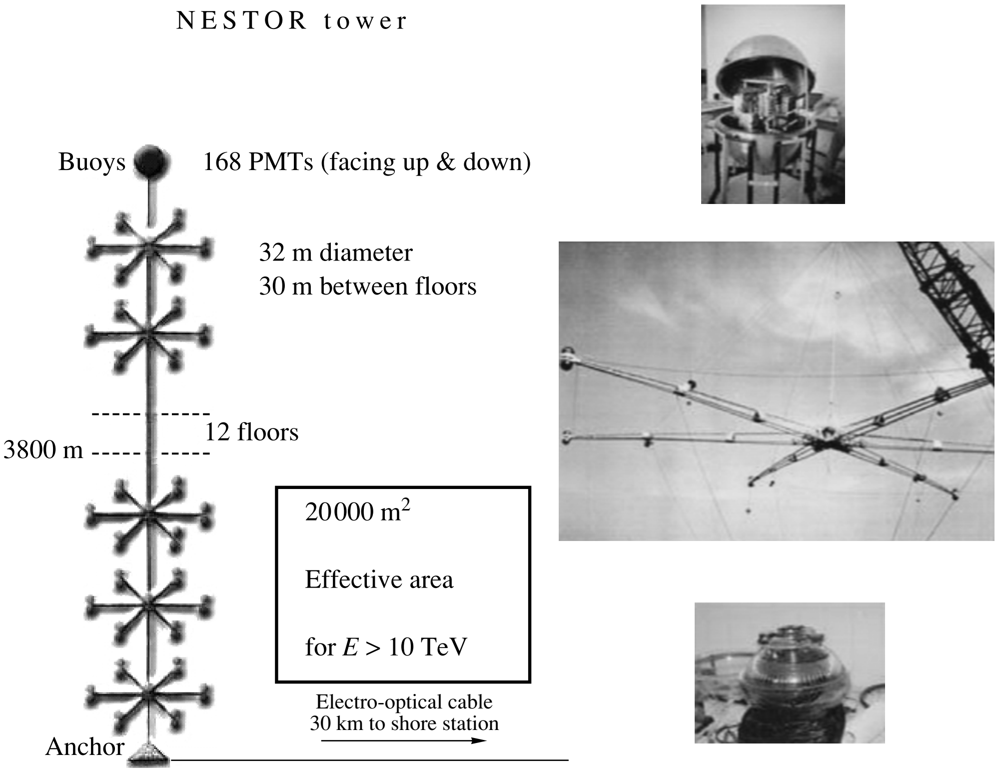

Fig. 1. The NESTOR tower.

used almost all year around. The 4.5-km-long deep-sea cable with 12 mono-mode fibers and one copper conductor joins the institute building with a junction box located on the sea end. The goal is that the deep-sea instruments should be tested for a long time in the bay before they are deployed in the depth.

The NESTOR owns a small fleet: a score of boats under 5 m plus a 12.5-m open-sea fast cruiser and a 6.2-m open-sea fast rigid hull inflatable boat. The cable laying vessel THALES of the Hellenic Telecommunication Organization is available to NESTOR, free of charge, for various tests. Moreover, the Pylos harbor has a host of medium size vessels with cranes and one large tugboat as well.

4. DEPLOYMENT OF THE FIRST DETECTOR FLOOR

The electro-optical cable from the shore station to the NESTOR site was laid in 2000. In January 2002, the end of the cable was brought to the surface by recovery rope and connected to the junction box on the telescope bottom unit or "pyramid." The pyramid also houses the power return electrode, the anchor with its release mechanism, and environmental monitors. Bad weather made it dangerous to attach a floor detector on that occasion. However, useful data were transmitted to the shore from the pyramid and long-term variations in environmental parameters were obtained. Since then, NESTOR has been awaiting the availability of a suitable vessel and good weather.

Only in 2003 was the pyramid brought back to the surface and the floor deployed. The present detector floor structure measures only 12 m in diameter but consists of the usual six arms and is equipped with 12 OMs. The detector floor was mounted 150 m above the anchor. There are LED calibration pulse modules installed 20 m above and 20 m below the center of the floor plane.

The titanium sphere contains a "housekeeping board" for control and monitoring of all systems and a "floor board" that performs the PMT pulse sensing, majority logic event triggering, coincidence rate scaling, and waveform capture and digitization, as well as data formatting and transmission. Parameters and functions can be downloaded over the optical link. The heart of the electronics system is the analog transient waveform digitizer (ATWD), developed at Lawrence Berkeley Laboratory. Each ATWD has four channels with 128 common-ramp, 10-bit Wilkinson ADCs and a present sampling rate of 282 MHz. A trigger is generated when the coincidence requirement for the floor is met and provides a time stamp for combining information from several floors.

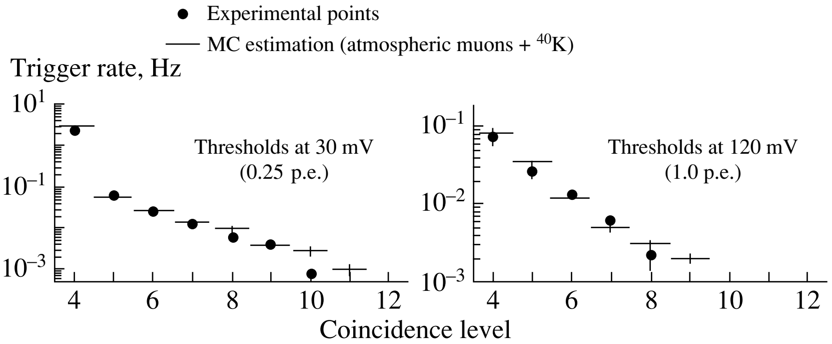

Fig. 2. Data from a depth of 4000 m. Preliminary trigger studies.

All deployment operations were made from a service vessel and consisted of the following four steps: (1) locate the cable terminal on the seafloor; (2) lift the anchor pyramid with the junction box on the deck of the service vessel; (3) connect the cable from the titanium sphere of the detector floor to the junction box, and (4) redeploy the anchor pyramid with the detector floor. Thus, all cable connections were made outside the water, on board the vessel. This procedure does not require any robot or special submarine, and it is cheap, quick, and efficient.

The purpose of this deployment is not only an engineering run but also carrying out an overall system performance test under real conditions at full depth with the unavoidable ^{40}K decays and bioluminescence backgrounds; studying the characteristics of the modules; testing the control and data acquisition system and the software, including the event reconstruction capability; and obtaining experience with the overall system operation.

Timing and coincidence studies were carried out and muon trajectories were reconstructed, focusing chiefly on very inclined, nearly horizontal muons. Overall system timing distributions were measured with the LED calibration flashers, comparing the relative timing between any two optical modules on neighboring arms facing either both up or both down. In all cases, the full width at half maximum was less than 8 ns. The coincidence window was set to 62 ns. In Fig. 2 and the table, the Monte Carlo—estimated and actually measured trigger rates for $\geq$ 4-fold coincidences at the 0.25 p.e. level is shown. The total trigger rates for $\geq$ 4-fold coincidences and thresholds of 0.25 and 1.0 p.e. are presented in the table.

5. CONCLUSION

The NESTOR project is well under way and the deployment of several fully equipped 32-m-diameter floor units is planned for the near future. To avoid delays dependent on a suitable ship, The Delta Verenike, a large, self-powered floating platform with GPS dynamic positioning, has been designed for the deployment of NESTOR. Construction is well advanced and delivery is expected soon.

REFERENCES

1. L. K. Resvanis, in *Proceedings of the 3rd NESTOR International Workshop, Pylos, Greece, 1993* (Univ. Press, Athens, 1993), p. 1.
2. E. G. Anassontzis *et al.,* Nucl. Instrum. Methods Phys. Res. A **349**, 242 (1994).
3. NESTOR—A Neutrino Astroparticle Physics Laboratory for the Mediterranean (1995), Vol. 2.
4. E. G. Anassontzis *et al.*, Nucl. Instrum. Methods Phys. Res. A **479**, 439 (2002).

Physics of Atomic Nuclei, Vol. 67, No. 11, 2004, pp. 2058–2061. From Yadernaya Fizika, Vol. 67, No. 11, 2004, pp. 2079–2082.

KLYPVE/TUS Space Experiments for Study of Ultrahigh-Energy Cosmic Rays*

B. A. Khrenov**, **V. V. Alexandrov**, **D. I. Bugrov**, **G. K. Garipov**, **N. N. Kalmykov**, **M. I. Panasyuk**, **S. A. Sharakin**, **A. A. Silaev**, **I. V. Yashin**, **V. M. Grebenyuk**1), **D. V. Naumov**1), **A. G. Olshevsky**1), **B. M. Sabirov**1), **R. N. Semenov**1), **M. Slunechka**1), **I. I. Skryl**1), **L. G. Tkatchev**1), **O. A. Saprykin**2), **V. S. Syromyatnikov**2), **V. E. Bitkin**3), **S. A. Eremin**3), **A. I. Matyushkin**3), **F. F. Urmantsev**3), **V. Abrashin**4), **V. Koval**4), **Y. Arakcheev**4), **A. Cordero**5), **O. Martinez**5), **E. Morena**5), **C. Robledo**5), **H. Salazar**5), **L. Villasenor**6), **A. Zepeda**7), **I. Park**8), **M. Shonsky**9), and **J. Zicha**10)

Skobeltsyn Institute of Nuclear Physics, Moscow State University, Vorob'evy gory, Moscow, 119992 Russia

Received January 20, 2004

Abstract—The KLYPVE space experiment has been proposed to study the energy spectrum, composition, and arrival direction of ultrahigh-energy cosmic rays (UHECR) by detecting from satellites the atmosphere fluorescence and scattered Cherenkov light produced by EAS, initiated by UHECR particles. The TUS setup is a prototype KLYPVE instrument. The aim of the TUS experiment is to detect dozens of UHECR events in the energy region of the GZK cutoff, to measure the light background, to test the atmosphere control methods, and to study stability of the optical materials, PMTs, and other instrumental parts in space environment. © *2004 MAIK "Nauka/Interperiodica"*.

1. INTRODUCTION

Among many important astrophysical problems, the nature, energy spectrum, and sources of ultrahigh-energy cosmic rays (UHECR) are of paramount importance. It is likely that the Galactic Center can be a source of cosmic rays with energies (1–2) × 10^{18} eV [1]. The change in the UHECR energy spectrum at (3–5) × 10^{18} eV may be explained by the change in the origin of the cosmic rays (from the galactic to the extragalactic one). For extragalactic protons with energies above 5 × 10^{19} eV, the Greisen–Zatsepin–Kuzmin (GZK) cutoff is expected due to interaction with relic photons. The flux of UHECR with energies above 10^{20} eV, measured by the AGASA array [2], is against the GZK cutoff and this result is stimulating various theoretical speculations [3]. However, in the last few years, the data from the HiRes detector are in favor of the cutoff [4], and certainly new more precise and conclusive data are needed for clarifying the UHECR phenomena. At present, a few new projects to study UHECR have been proposed, including experiments in space, among them the KLYPVE project [5, 6]. The TUS setup accommodated on the Russian RESURS satellite was proposed [7, 8] for study of all aspects of the KLYPVE operation in space. In this paper, the 2003 status of the KLYPVE/TUS projects is presented.

2. DETECTION METHOD AND THE MAIN PARTS OF THE INSTRUMENT

The KLYPVE/TUS detector on board a satellite has to record the fluorescent and scattered Cherenkov light generated by ultrahigh-energy EAS in the atmosphere. The height of the satellite orbit and the field

---

*This article was submitted by the authors in English.

1)Joint Institute for Nuclear Research, Dubna, Moscow oblast, 141980 Russia.

2)Rocket Space Corporation Energy, Consortium Space Regatta, Korolev, Russia.

3)Special Construction Bureau Luch, Syzran, Russia.

4)State Research and Production Space Center, Samara, Russia.

5)Benemerita Universidad Autonomia de Puebla, Puebla, México.

6)Universidad Michoacana, Morelia, México.

7)Depto de Fisica, Cinvestav-IPN, México City, México.

8)Department of Physics, UWHA Woman University, Seoul, Korea.

9)NIO KOMPAS, Turnov, Czech Republic.

10)Technical University, Prague, Czech Republic.

**e-mail: `khrenov@eas.sinp.msu.ru`

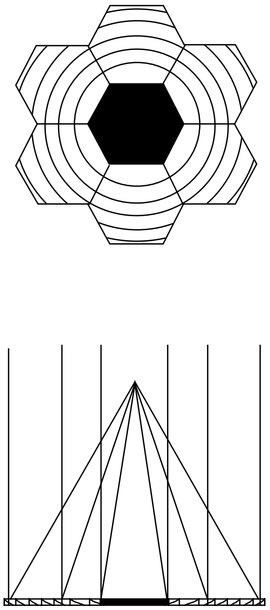

Fig. 1. TUS segmented mirror-concentrator. The central part is used only as a mechanical base of the mirror.

of view (FOV) of the detector determine the area of the atmosphere available for UHECR event detection. The rate of UHECR events depends on the detector energy threshold for detecting UHECR events in this area and on the range of zenith angles in which the primary UHECR particle parameters (energy, arrival direction) are determined from the recorded data. The available zenith angle range is determined by the pixel resolution of the photoreceiver. It was shown in the first KLYPVE and TUS papers [5–8] that simple optics of the mirror-concentrator and the PMT pixel grid in its focal plane may give a high rate of detected extremely high energy events (energies more than 5×10^{19} eV) when operating at orbit heights of 400–500 km: for the TUS setup, the expected (if the AGASA data are valid) rate is about 50 events per year (10 times higher than in the AGASA experiment), and for the KLYPVE detector, it will be higher and accuracy in measurement of primary particle parameters will be higher. The KLYPVE detector will start measurements with the energy threshold of 10^{19} eV, but the TUS (with smaller mirror-concentrator) will start to operate near an energy of 5×10^{19} eV. The program of the KLYPVE experiment in comparison with other UHECR projects is presented in [9].

The space KLYPVE (or TUS) detector has two main parts: a segmented Fresnel mirror-concentrator and a grid of pixels (PMTs) with the corresponding electronics in its focal plane. The main parameters of the KLYPVE and TUS detectors are presented in the table.

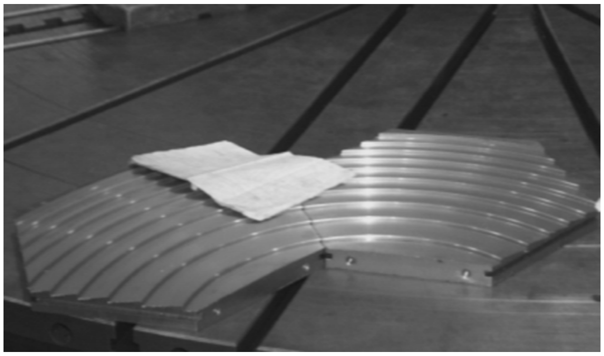

Fig. 2. Steel mold for production of mirror segments.

At present, the TUS detector is under construction with a mirror of six hexagonal segments (Fig. 1) that has an operating area of 1.4 m^2 and a focal distance 150 cm. Production of the samples of the mirror segment is organized as pressing the carbon plastic replicas off the steel mold (Fig. 2). The plastic mirror segments are placed on the frames—parts of the mechanical construction for the mirror development in space. The mirror and photoreceiver will be transported to space in a packed mode [5]. In the operating mode, the mirror segments on the corresponding frames will be fixed to one plane with an angular accuracy of 1 mrad.

The TUS photoreceiver is designed as an orthogonal network of $16 \times 16 = 256$ pixels. The pixel is a circular PMT with a square 1.5×1.5-cm window light guide. All pixels are covered by a UV filter, transparent in the fluorescence wavelength band 310–420 nm. The choice of the PMT is a compromise between a good time resolution, high sensitivity in the fluorescence wavelength range, stable performance in the presence of high light noise, fast recovery after exposure to the scattered day atmosphere light, and slow aging. The Hamamatsu PMT type R1463P with a multialcali cathode and a linear dynode system was selected. It was shown that the highest energy events

Table

Parameter	KLYPVE	TUS
Orbit height [km]	400	350–600
Mirror area [m^2]	10	1.4
Focal distance [m]	3	1.5
Pixel angular size [mrad]	5	10
FOV [rad]	0.24	0.16
Number of pixels	2304	256
Time sample of FADC [μs]	0.4	0.8

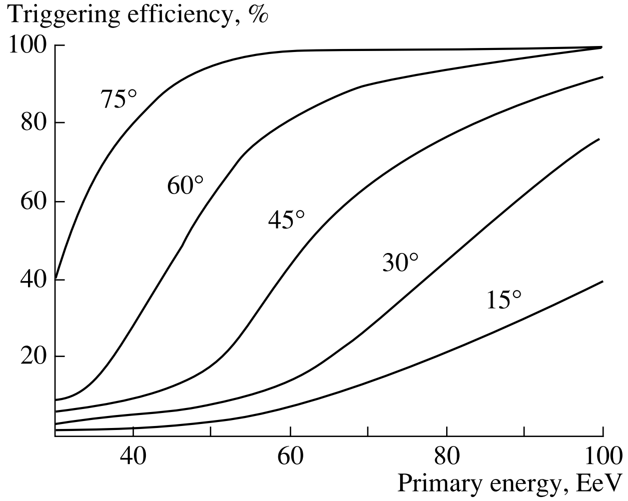

Fig. 3. The TUS triggering efficiency as a function of primary energy and zenith angles (values on the curves).

(energies more than 10^{20} eV) could be detected even in the background light of the Moon if the gain of the PMTs is adjusted to the background [6]. For this aim, the PMT voltage is made variable and a special circuit was suggested for keeping the gain of all tubes uniform in a range of gain varying by 10 times [10].

Pixels are organized in clusters: 16 pixels in line is a cluster having a common HV supply, a FADC channel, and a FIFO memory. Data are sampled in time bins t_s from every pixel in the cluster with the help of a multiplexer. Triggering and DAS are common for the whole retina of pixels. The FPGA technique is used for the digital part of the electronics.

The UHECR finding algorithm operates in two trigger levels: at the first level, the pixels with a signal above the first threshold q in integration time t_i are selected. At the second level, the group of triggered pixels making an EAS track are selected. At the onboard TUS computer, an additional separation of real UHECR events is made, and the data are compressed and prepared for sending to the mission center.

The prototype TUS "telescope" is planned for testing at the Cerra La Negra Mountains in Mexico [11]. The mountain TUS telescope will allow recording of EAS tracks at distances of 25–100 km from the detector. In the telescope field of view, atmosphere-transparency monitoring will be provided by a special control device using xenon lamp flashes.

3. THE UHECR EVENT SIMULATION

The UHECR events were simulated with the aim of testing the efficiency of the selection system and estimating the measurement accuracy. Development of EAS initiated by primary UHECR particles was considered within the framework of the CORSIKA/QGSJET model. A special UHECR event simulation program package SLAST was elaborated [12]. With the calculated EAS signals, the performance of the electronics designed for the KLYPVE/TUS detectors was simulated. It includes two lines of pixel signal analysis—performance of the digital oscilloscope with time sampling t_s and performance of the triggering system.

In the TUS detector digital oscilloscope, the signal is recorded as a PM tube anode potential in time samples $t_s = 0.8$ μs. Integration of the signal in time $t = 12$ μs, needed for the selection of useful EAS events, is done in a digital form. Time constant of the RC charge integration circuit at the anode is chosen equal to t_s. It was shown in the simulation of the digital oscilloscope performance that fluctuations of the signal sampled in time intervals $t_s = RC$ are close to fluctuations in the number of photoelectrons at the tube cathode for EAS of energies $E > 30$ EeV. It confirms that the digital oscilloscope operating with the selected time sample gives adequate data on the event.

Operation of the triggering system was simulated for various EAS energies and zenith angles. For a given signal threshold q in one pixel and number n of triggered neighbor pixels, the rate of background events and the efficiency of selecting the EAS of energy E and zenith angle θ were calculated. The DAS of the TUS electronics operates successfully with an average rate of background events of not more than 0.01 Hz. For the TUS detector, the noise triggering rate is expected at the level of 0.01 Hz for $q \simeq 5\sigma$ (σ is the noise in one pixel) and $n = 2$. For these q and n, the selection efficiency for various zenith angles as a function of the EAS primary energy E_0 is presented in Fig. 3. One can see that the triggering efficiency of the TUS telescope is more than 50% at zenith angles more than 60° at energies $E_0 = 45$ EeV. The rate of EAS events expected in TUS with the above energy threshold in operation with a duty cycle of 20% (moon nights included) in the observed area of the atmosphere of 4000 km^2 (orbit height 400 km) is about 100 per year. The reconstruction of the EAS cascade curve and measurements of primary particle energy and direction will be satisfactorily accurate at zenith angles $\theta > 75°$ and energies $E > 100$ EeV. Following the AGASA data the TUS expected rate of these extremely high energy events is about 20 per year.

For the KLYPVE detector, the energy threshold will be lower ($E_{\text{tr}} \simeq 10$ EeV) and the accuracy in the EAS parameters will be higher. The errors in primary energy, direction angles, and position of the EAS maximum for the KLYPVE telescope for energy $E \geq 30$ EeV and zenith angles $\theta > 60°$ are $\sigma_E/E < 20\%$; $\sigma_\theta, \sigma_\varphi < 5°$.

4. CONCLUSION

In 2004–2005, the TUS construction and its testing in the mountains should be finished. The TUS space mission is planned for 2006–2008. The aim of the TUS experiment is to detect dozens of UHECR events in the energy region of the GZK cutoff, to measure the light background, to test the atmosphere control methods, and to study stability of the optical materials, PMTs, and other instrumental parts in space environment. The KLYPVE project will be the next mission. The accommodation of KLYPVE on a space platform is under discussion.

REFERENCES

1. M. Teshima *et al.*, in *Proceedings of the 27th ICRC, Hamburg, 2001*, Vol. 1, p. 337.
2. M. Takeda *et al.*, Astropart. Phys. **19**, 447 (2003).
3. M. Nagano and A. A. Watson, Rev. Mod. Phys. **72**, 689 (2000); A. V. Olinto, Phys. Rep. **333–334**, 329 (2000).
4. D. R. Bergman *et al.* (HiRes Collab.), in *Proceedings of the 28th ICRC, Tsukuba, 2003*, Vol. 1, p. 397.
5. V. V. Alexandrov *et al.*, Byull. Mosk. Gos. Univ., Ser. 3: Fiz., Astron., No. 12, 33 (2000).
6. B. A. Khrenov and M. I. Panasyuk (KOSMOTEPETL Collab.), in *Proceedings of the International Workshop on Observing of Ultrahigh Energy Cosmic Rays from Space and Earth*, AIP Conf. Proc. **566**, 57 (2001).
7. V. V. Alexandrov *et al.*, in *Proceedings of the 27th ICRC, Hamburg, 2001*, Vol. 2, p. 831.
8. B. A. Khrenov *et al.*, Nucl. Phys. B (Proc. Suppl.) **113**, 115 (2002).
9. B. A. Khrenov, J. Phys. G **29**, 303 (2003).
10. G. K. Garipov *et al.* (KOSMOTEPETL Collab.), in *Proceedings of the International Workshop on Observing of Ultrahigh Energy Cosmic Rays from Space and Earth,* AIP Conf. Proc. **566**, 76 (2001).
11. H. Salazar *et al.*, in *Proceedings of the 28th ICRC, Tsukuba, 2003*, Vol. 2, p. 1009.
12. D. Naumov *et al.*, in *Proceedings of the 28th ICRC, Tsukuba, 2003*, Vol. 2, p. 1105.

Physics of Atomic Nuclei, Vol. 67, No. 11, 2004, pp. 2062–2065. From Yadernaya Fizika, Vol. 67, No. 11, 2004, pp. 2083–2086.
Original English Text Copyright © 2004 by Volkova.

RARE PROCESSES AND ASTROPHYSICS

Cosmic-Ray Muon and Atmospheric Neutrino Fluxes at Very High Energies*

L. V. Volkova**

Institute for Nuclear Research, Russian Academy of Sciences,
pr. Shestidesyatiletiya Oktyabrya 7a, Moscow, 117312 Russia

Received January 20, 2004

Abstract—Estimates of cosmic-ray muon and atmospheric neutrino fluxes at TeV energies are obtained taking into account a "prompt" production of muons and neutrinos through charmed-particle decays and a "direct" lepton-pair production through the Drell—Yan mechanism and resonances. It is found that the contribution of charmed particles to the muon flux is equal to that from the conventional sources (pion and kaon decays) at 60 TeV, and the same equality can take place at 10 and 1 TeV for muon and electron neutrinos, respectively (for particles coming to sea level in the vertical direction). This "direct" production contribution to muon and neutrino fluxes is estimated very arbitrarily, but it cannot be excluded that this contribution is equal to that from the conventional source at energies of 0.5 and 0.05 PeV for muons and muon neutrinos, respectively. Currently, the estimates of the "prompt" and the "direct" contributions to cosmic-ray muons and atmospheric neutrinos are only qualitative. This is true especially for the "direct" contribution. Nevertheless, it seems reasonable to attract attention to these potentially important sources of atmospheric muons and neutrinos. *© 2004 MAIK "Nauka/Interperiodica".*

1. INTRODUCTION

A new generation of large-scale installations, as, for example, AMANDA, will allow searches for primary cosmic rays up to ZeV energies and atmospheric or cosmic neutrino fluxes at a level of about 10^{-21} neutrino/(GeV cm^2 s sr). High-energy neutrino astronomy is becoming not only a theoretical science but also an experimental one (see, for example, [1]).

A number of modern EAS installations (AGASA, HiRes, Yakutsk) study primary cosmic radiation up to energies of 100 EeV. Looking for the nature of primary particles, one needs to know in a proper way fluxes of secondary particles which are produced in the atmosphere (such as muons and neutrinos) because these particles penetrating deep into the atmosphere could give an EAS imitating a primary radiation of high energies.

The current measurements the "prompt" atmospheric neutrino flux via down-going muons with neutrino telescopes are discussed in [2]. Additional data are needed to draw more concrete information on the considered problem.

With the ICECUBE setup, one will be able to look for cosmic neutrinos with energies in the PeV region. But to understand the data, one needs to know the atmospheric neutrino fluxes at the same energies, because atmospheric neutrinos are the main background for cosmic neutrinos.

In this work, we give estimates of fluxes of "prompt" muons and neutrinos which could be produced in the atmosphere through decays of charmed particles and "direct" fluxes of muons and neutrinos produced through resonances and the Drell—Yan process for energies up to 10 EeV.

2. MUONS AND NEUTRINOS FROM CHARM

In Figs. 1 and 2, the differential energy fluxes of cosmic-ray muons and atmospheric muon neutrinos are given. The "conventional" fluxes (recalculated with index $\gamma = 1.7$ for the primary nucleon spectrum) are taken from [3, 4] and "prompt" fluxes are taken from [5]. The latter were calculated in an empirical model [5]. The main features of this model are the following.

(1) The charm production cross sections are normalized to values measured at accelerators and are increased with the nucleon energy E_N increase as $\log E_N$.

(2) The differential spectra of produced charmed particles measured at accelerators are not changed significantly with an increase in nucleon energy in the

---

*This article was submitted by the author in English.

**e-mail: `volkova@inr.npd.ac.ru`

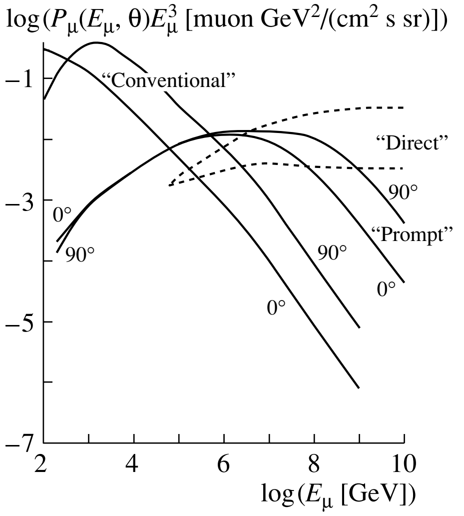

Fig. 1. The differential energy fluxes (multiplied by energy cube) of cosmic-ray muons. The solid curves are muons from pion and kaon decays ("conventional") and muons from charmed-particle decays ("prompt") for particles coming to sea level in the vertical ($\theta = 0°$) and horizontal ($\theta = 90°$) directions; the dashed curves are for muons from resonances and the Drell–Yan process ("direct"); the explanation for the upper and lower curves is given in the text, Section 5.

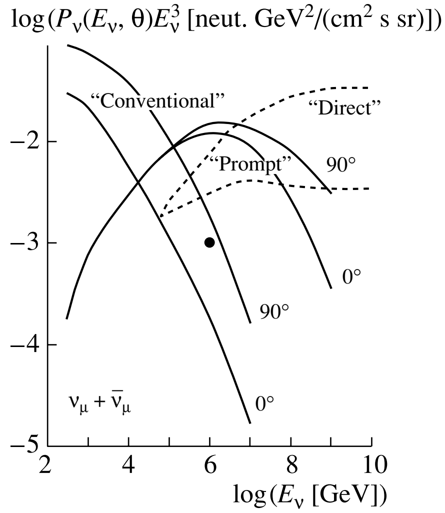

Fig. 2. The same as in Fig. 1, but for atmospheric muon neutrino fluxes. P^{ν} is the differential energy spectrum of muon neutrinos.

range of $x = E_{\eta}/E_N$, which gives the main contribution to the muon or neutrino fluxes. Here, E_{η} is the charmed-particle energy. Due to the very quick decrease of the cosmic-ray primary nucleon spectrum, one has $0.05 < x < 0.15$.

In the model, the calculations of charm production cross sections agree with calculations within the QGS model and the model's differential spectra of produced charmed particles agree with ones calculated in the QCD NLO. Furthermore, the fluxes of cosmic-ray muons calculated in the discussed model are supported by the data on cosmic-ray muon fluxes measured in [6] with the roentgen-emulsion camera of MSU—the measured contribution of "prompt" muons to the total muon flux at 60 TeV is equal to the contribution of the "conventional" mechanism with an accuracy of ±25% (for muons coming vertically to sea level).

3. MUONS AND NEUTRINOS FROM RESONANCES

Resonances are produced in interactions of primary nucleons with air nuclei in the atmosphere. The lifetime of these particles is extremely small (about 10^{-23}–10^{-24} s). They decay producing, in particular, muons:

$$N + A^{\text{air}} \to \text{resonance} \to \mu^+\mu^-. \tag{3.1}$$

With an increase in nucleon energy, the number of channels for production of different resonances increases and the cross section for production of a concrete resonance decreases. Nevertheless, it could be quite possible that the contribution to muon production of the processes with resonances is not significantly varied with energy.

The kinematical equation for propagation of the muons produced in (3.1) through the atmosphere at very high energies (neglecting these muon decays) can be written as

$$\frac{\partial P^{\mu}(E_{\mu}, x)}{\partial x} \tag{3.2}$$

$$= \frac{\partial}{\partial E_{\mu}}(\beta(E_{\mu})P^{\mu}(E_{\mu}, x)) + G^{\mu}_{\text{res}}(E_{\mu}, x),$$

where $P^{\mu}(E_{\mu}, x)$ is the differential energy spectrum of muons produced through resonance decays (the number of muons with energy E_{μ} in the interval $E_{\mu} \div (E_{\mu} + dE_{\mu})$ at depth x [g/cm^2] in the atmosphere); $\beta(E_{\mu})$ is the energy loss of a muon at 1 g/cm^2, $\beta(E_{\mu}) = \beta_1(E_{\mu}) + \beta_2(E_{\mu})E_{\mu}$, $\beta_1(E_{\mu})$ and $\beta_2(E_{\mu})$ being very weak functions of energy; and $G^{\mu}_{\text{res}}(E_{\mu}, x)$ is the function of muon production through resonances (the number of muons with energy E_{μ} in the interval $E_{\mu} \div (E_{\mu} + dE_{\mu})$ produced in resonance decays at depth x [g/cm^2] in the atmosphere):

$$G^{\mu}_{\text{res}}(E_{\mu}, x) = \sum_n W^{\mu\pm}_{\text{res}} \frac{\sigma^{\text{res}}}{\sigma^{NA^{\text{air}}}_{\text{in}}} \tag{3.3}$$

$$\times \int\limits_{E_{\mu}}^{\infty} P^N(E_N, x)\frac{dW(E_N, E_{\mu})}{dE_{\mu}}dE_N,$$

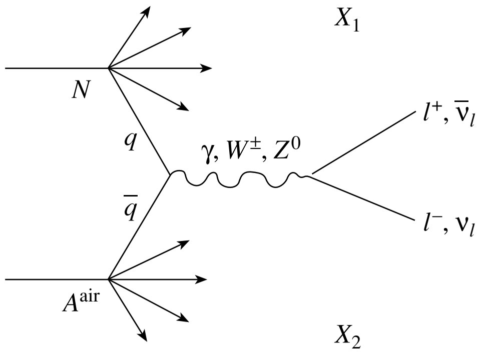

Fig. 3. Process of lepton–antilepton pair production through quark–antiquark ($q\bar{q}$) annihilation into a virtual photon γ or $W^{\pm}$, Z^0 bosons with the following decay to lepton pairs (X_1, X_2 are all other particles produced in the interaction).

where the sum $\sum_n$ runs over all possible resonances which produce muon pairs; $W^{\mu^{\pm}}_{\rm res}$ is the probability to produce a muon pair in decay of a resonance; $\sigma^{\rm res}/\sigma^{NA^{\rm air}}_{\rm in}$ is the ratio of the resonance production cross section to that of inelastic interaction of a nucleon with an air nucleus; P^N is the differential energy spectrum of nucleons; and $dW(E_N, E_\mu)/dE_\mu$ is the probability that, in an interaction of a nucleon with energy E_N with an air nucleus, a muon with energy E_μ in the interval $E_\mu \div (E_\mu + dE_\mu)$ is produced.

The solution of Eq. (3.2) has the form

$$P^{\mu}(E_\mu, x) = \int\limits_0^x G^{\mu}_{\rm res}(\varepsilon(E_\mu, x-t), t) \times \exp(\beta_2(x-t))dt, \quad (3.4)$$

where

$$\varepsilon(E_\mu, x-t) = E_\mu \exp(\beta_2(x-t)) + \frac{\beta_1}{\beta_2}(\exp(\beta_2(x-t)) - 1). \quad (3.5)$$

An estimate of the ratio Y of the function of muon production through resonance to that for muon production from pions is

$$Y = \frac{G^{\mu}_{\rm res}}{G^{\mu}_{\pi}} \sim \frac{\sigma_{\rm res}}{\sigma_\pi} W^{\mu^{\pm}}_{\rm res}\left(1 + \frac{E_\mu}{E^{\rm cr}_{\pi}(\theta)}\right), \quad (3.6)$$

where σ_π is the pion production cross section and $E^{\rm cr}_{\pi}(\theta)$ is so-called pion critical energy (the energy at which the probability of pion decay at one nuclear interaction length is equal to the probability for nuclear interaction; it is 121 GeV for pions in the atmosphere going in the vertical direction and 1030 GeV for particles going in the horizontal direction).

For $E_\mu \gg E^{\rm cr}_{\pi}$,

$$Y = \frac{G^{\mu}_{\rm res}}{G^{\mu}_{\pi}} \sim \frac{\sigma_{\rm res}}{\sigma_\pi} W^{\mu^{\pm}}_{\rm res}\frac{E_\mu}{E^{\rm cr}_{\pi}(\theta)} = Y_0 E_\mu. \quad (3.7)$$

This ratio increases with increasing energy.

4. LEPTON PAIRS FROM DRELL–YAN PROCESS

A lepton–antilepton pair ($l^{\pm} = e^{\pm}, \mu^{\pm}, \tau^{\pm}$) can be produced in an interaction of a nucleon with an air nucleus in the atmosphere:

$$N + A^{\rm air} \to l^+ + l^- + X. \quad (4.1)$$

The scheme of the interaction in the framework of the quark–parton mechanism is shown in Fig. 3. This way to produce lepton pairs is called the Drell–Yan mechanism.

Muons and neutrinos produced through process (4.1) in the atmosphere are to be taken into account when fluxes of these particles are calculated. The equations for the propagation of these muons and neutrinos through the atmosphere and their solutions are quite similar to those given in Section 3.

5. ESTIMATES BASED ON COSMIC-RAY MUON DATA

Let us assume that the contribution of resonances and the Drell–Yan process to cosmic-ray muon fluxes is equal to the uncertainties in the measured contribution from charmed particles. This value is about 25% [6] of the value of the cosmic-ray muon flux from the conventional process (from pions and kaons) for muons coming to sea level in the vertical direction at a muon energy of 60 TeV:

$$P^{\mu}_{\rm direct}/P^{\mu}_{\rm conv} \sim 0.25. \quad (5.1)$$

The estimated fluxes of muons and neutrinos produced through the “direct” mechanism are shown in Figs. 1 and 2 with dashed curves (the lower curves are for the assumption that the ratio of the “direct” particle production cross section to that of pions does not change with increasing energy).

It is possible to consider a fantastic but not a completely false case when the fraction of nuclear interactions going through resonances is increased with an increase in nucleon energy. For example, if the cross section for direct production is increased and becomes at 10^{10} GeV

$$\sigma_{\rm res} \sim 10\%\, \sigma^{pA^{\rm air}}_{\rm in}, \quad (5.2)$$

then one obtains the “direct” muon and neutrino fluxes given in Figs. 1 and 2 with the upper dashed curves.

The contribution of the “direct” mechanism is practically isotropic for all considered energies.

6. CONCLUSION

From Figs. 1 and 2, it is seen that, at an energy larger than 10^5–10^6 GeV, the contribution of the "direct" muons to the total cosmic-ray muon flux can start to overcome the contribution from the conventional sources (from decays of pions and kaons). In such a case, the EAS measured at sea level could be produced not high in the atmosphere by primary particles coming to the Earth, but by the "direct" muons, which could penetrate deep into the atmosphere. This "direct" muon component could be noticed in installations deep underground.

Soon, modern neutrino telescopes (like ICECUBE) will be able to measure neutrino fluxes at a level of 10^{-21} particles/(GeV cm^2 s sr). The closed circle in Fig. 2 shows the sensitivity of such an installation to the "prompt" and "direct" contribution. It is seen from the figure that, for correct interpretation of the data, it is necessary to know the atmospheric neutrino fluxes.

Of course, estimates of the fluxes of "direct" (produced through resonances or the Drell–Yan process) muon and neutrino fluxes can be made presently only with high uncertainty. But it seems to be reasonable to keep in mind that these channels for muon and neutrino production exist and that they should be taken into account when one deals with very high energy particles.

ACKNOWLEDGMENTS

I am grateful to the Russian Foundation for Basic Research (project no. 03-02-16436-a) and the (grant 1782.2003.2) of the leading Scientific Schools.

REFERENCES

1. F. Halzen, astro-ph/0301143.
2. G. Gelmini, P. Gondolo, and G. Varieschi, Phys. Rev. D **67**, 017301 (2003).
3. L. V. Volkova, G. T. Zatsepin, and L. A. Kuz'michev, Sov. J. Nucl. Phys. **29**, 645 (1979).
4. L. V. Volkova, Yad. Fiz. **31**, 1510 (1980) [Sov. J. Nucl. Phys. **31**, 784 (1980)].
5. L. V. Volkova and G. T. Zatsepin, Yad. Fiz. **64**, 313 (2001) [Phys. At. Nucl. **64**, 266 (2001)].
6. G. T. Zatsepin, N. P. Il'ina, N. N. Kalmykov, *et al.*, Izv. Ross. Akad. Nauk, Ser. Fiz. **61**, 559 (1997).

Physics of Atomic Nuclei, Vol. 67, No. 11, 2004, pp. 2066–2072. From Yadernaya Fizika, Vol. 67, No. 11, 2004, pp. 2087–2093.
Original English Text Copyright © 2004 by Derbin, Smirnov, Zaimidoroga.

RARE PROCESSES AND ASTROPHYSICS

On the Possibility of Detecting Solar *pp* Neutrino with the Large-Volume Liquid Organic Scintillator Detector*

A. V. Derbin[1], **O. Yu. Smirnov**[2]**, and **O. A. Zaimidoroga**[2]

Received January 20, 2004

Abstract—It is shown that a large-volume liquid organic scintillator detector with an energy resolution of 10 keV at 200 keV (1σ) will be sensitive to solar *pp* neutrinos, if operated at the target radiopurity levels for the Borexino detector or the solar neutrino project of KamLAND. © *2004 MAIK "Nauka/Interperiodica".*

1. INTRODUCTION

Present information on the solar neutrino spectrum is based on the very tail of the total neutrino flux (about 0.2%). The low-energy part of the spectrum, and, in particular, the *pp*-neutrino flux, has not been measured directly yet. After the observation of reactor neutrino oscillations by the KamLAND Collaboration [1], the spectrometry of the low-energy solar neutrinos is important for the confirmation of the LMA MSW scenario and for the restriction of the allowed LMA parameter region [2], as well as for the search for neutrino nonstandard properties.

The *pp*-neutrino measurement is a critical test of stellar evolution theory and of neutrino oscillation solutions. The *pp*-neutrino flux is predicted by the standard solar model (SSM) with a precision of the order of 1%, in contrast to the 20% precision predictions of the high-energy neutrino flux from the ^{8}B. A discussion of the physics potential of the *pp*-solar neutrino flux can be found in [3, 4] and [5]. A number of projects aiming to build *pp*-neutrino spectrometers are in different stages of research and development. The principal characteristics of the existing proposals [6–14] are shown in Table 1. The operating gallium radiochemical experiments sensitive to solar *pp* neutrinos (SAGE [15] and GALLEX [16]) are not cited in the table, because they do not provide spectrographic information.

The main problem in neutrino detection is the very small cross sections of the neutrino interactions with matter; this demands large detectors with a very low intrinsic background. Below, we summarize briefly the achievements in the purification of liquid organic scintillators, and on the basis of the developed techniques, we propose a high-resolution detector, filled with a liquid organic scintillator, with an energy threshold as low as 170–180 keV, capable of registering solar *pp* neutrinos. A preliminary description has been reported in [17].

2. PURITIES ACHIEVED WITH LIQUID SCINTILLATOR DETECTORS

For the present moment, the record on liquid organic scintillator purity with a large scale sample has been achieved with the Borexino [18, 19], Counting Test Facility (CTF), and KamLAND detector [1]. The available data are summarized in Table 2. While the CTF is a prototype detector operating with 4 t of liquid scintillator [21, 22], the KamLAND detector is loaded with 1000 t of liquid scintillator. Both detectors demonstrate very good purification of the scintillator for U–Th and ^{222}Rn. The values cited in Table 2 for the ^{238}U and ^{232}Th content are obtained by counting the number of the decay sequences from ^{214}Bi and ^{212}Bi under the assumption of secular equilibrium. A precise measurement of the abundance of ^{40}K was not possible with the CTF because of the sensitivity level, but is expected to be much better because of the high efficiency of water extraction for the removal of K ions [19]. The investigation performed in the framework of the Borexino program shows that the content of the ^{85}Kr and ^{39}Ar can be significantly decreased by the proper choice of the N_2 for the stripping. The goals for the purity in both the Borexino and the KamLAND project for the observation of the solar neutrinos are similar.

The importance of the purification of the liquid scintillator from ^{39}Ar and ^{85}Kr was understood during the operation of the CTF.

---

*This article was submitted by the authors in English.

[1] Petersburg Nuclear Physics Institute, Russian Academy of Sciences, Gatchina, 188350 Russia.

[2] Joint Institute for Nuclear Research, Dubna, Moscow oblast, 141980 Russia.

**e-mail: `osmirnov@jinr.ru`

3. THE DESIGN OF THE DETECTOR

Even in the event that the desired purity can be achieved in the future Borexino and KamLAND experiments, direct measurements in the *pp*-neutrino energy region are impossible with these big detectors. In fact, the presence of the beta-decaying ^{14}C isotope in the liquid organic scintillator sets a lower threshold on the detector sensitivity. The measured content of the ^{14}C in the liquid scintillator used in the CTF detector was at the level of 2×10^{-18} g/g with respect to the ^{12}C content [24], and this is the only measurement available at such a low concentration. Though the end point of the ^{14}C β decay is only 156 keV, the energy resolutions of the CTF, as well as Borexino and KamLAND, are not good enough at this energy in order to set a threshold lower than 250 keV.

Thus, the efforts should be concentrated on the construction of a compact detector with the highest possible energy and spatial resolution. We suggest using PMTs supplied with hexagonal light concentrators in order to provide 4π coverage, in comparison to 21% for CTF and 30% for Borexino and KamLAND. Additional energy-resolution improvement (about 15%) in the low-energy region can be achieved by using an energy reconstruction technique discussed in [25]. Good spatial resolution is needed in order to provide an active shielding from the external background, mainly gammas with energy 1.45 MeV coming from the ^{40}K decay in the PMT material. An additional passive shielding with 200 cm of ultrapure water is considered in the present design.

The possible geometry of the detector is presented in Fig. 1 in comparison with Borexino and CTF sketches. The inner vessel is a transparent spherical nylon bag with a radius of 240 cm, containing 60 t of ultrapure pseudocumene (1,2,4-trimethylbenzene C_9H_{12}) with 1.5 g/g of PPO (2,5-diphenyloxazole). The active shielding is provided by 100 cm of the outer layer of scintillator. The 800 PMTs are mounted on an open structure at a distance of 440 cm from the detector's center (distance is counted from the PMT photocathode). We considered also the use of the 8-in. ETL9351 series photomultiplier [26]. The comparison of the geometrical parameters of Borexino, CTF, and the proposed detector is presented in Table 3.

The detector should be supplied with an external muon veto system. The muon veto system consisting of about 50 additional PMTs can be mounted on the top and on the bottom of the cylindrical external tank. The muon recognition efficiency should be at the level of 99.99% in order to guarantee a missed-muon count of <0.1 per day. The muon flux at the LNGS underground laboratory is about 7 times less than that at the Kamioka site.

4. SIMULATION OF THE BACKGROUND

The sensitivity of the detector to the solar *pp* neutrinos depends on the background level in the 170–250 keV energy window. As in Borexino, CTF [18, 21], and the KamLAND solar neutrino project [23], the main sources of background are:

internal background, including ^{14}C beta-decay counts in the neutrino window;

background from the radon dissolved in the buffer;

external gamma background;

cosmic-ray background.

We considered the contamination of the liquid scintillator with the radionuclides on the levels given in Table 2 for Borexino.

The Monte Carlo (MC) method has been used in our calculations in order to simulate the detector response to the background events. The code is split into two parts: the electron–gamma shower simulation (EG code) and the simulation of the recorded charge and position (REG code). The EG code generates a random position event with a random initial direction (for gammas) and follows the gamma–electron shower using the EGS-4 code [27]. The electrons and alphas are not propagated in the program and are considered to be pointlike, with the position at the initial coordinates. The mean registered charge corresponding to the electron's energy E_e is calculated as

$$Q_e = AE_e f(k_B, E_e) f_R(r), \qquad (1)$$

where $f_R(r)$ is a factor taking into account the dependence of the recorded charge on the distance from the detector's center and $f(k_B, E_e)$ is the quenching factor for electrons.

The factor $f_R(r)$ was estimated with the MC method, simulating the light collection from the source, placed at different distances from the detector's center. The quenching factor $k_B = 0.0167$ was independently measured for the scintillator on the basis of pseudocumene (PC) [28]. This value is in agreement with a high-statistics fit of the ^{14}C β spectrum of the CTF data.

The mean registered charge corresponding to an alpha of energy E is calculated as

$$Q_\alpha = AE_\alpha f_\alpha(E) f_R(r), \qquad (2)$$

where $f_\alpha(E)$ is the quenching factor for alphas. The following approximation of the quenching factor $f_\alpha(E)$ was used for the simulations with PC [29]:

$$f_\alpha(E) = \frac{1}{20.3 - 1.3E},$$

where alpha energy E is measured in MeV.

The gammas were propagated using the EGS-4 code. As soon as an electron of energy E_e appears

Table 1. Key characteristics of the solar neutrino projects sensitive to the *pp* neutrino

Project [reference]	Method	Thres-hold, keV	Resolution	Mass, t	Reaction	SSM *pp* events, d^{-1}
LENS (Yb) [6]	^{176}Yb, LS	$301(\nu)$	7% (1 MeV)	20 (8% in nat. Yb)	$^{176}\mathrm{Yb} + \nu_e \to$ $^{176}\mathrm{Lu} + e^-$	0.5
LENS (In) [7]	^{115}In, LS	$118(\nu)$	18% (100 keV)	20	$^{115}\mathrm{In} + \nu_e \to$ $^{115}\mathrm{Sn}^*(613) + e^-$	1.4 $\epsilon(pp) = 0.25$
GENIUS [8]	^{76}Ge, scattering	$11(e^-)$ $59(\nu)$	0.3% (300 keV)	1 10	$\nu + e^- \to \nu + e^-$	1.8 18
HERON [9]	Superfluid ^{4}He, rotons/phonons + UV	$50(e^-)$ $141(\nu)$	10% (50 keV)	20 (28)	$\nu + e^- \to \nu + e^-$	5.5 (LMA)
XMASS [10]	Liquid Xe, scintillator	$50(e^-)$ $141(\nu)$	11% (300 keV)	10	$\nu + e^- \to \nu + e^-$	10
HELLAZ [11]	He (5 atm), TPC	$100(e^-)$ $217(\nu)$	6% (800 keV)	2000 m^3	$\nu + e^- \to \nu + e^-$	7
MOON [12]	Drift chambers	$168(\nu)$	12.4% FWHH (1 MeV)	3.3	$\nu_e +^{100}\mathrm{Mo} \to$ $^{100}\mathrm{Tc} + e^-$	1.1
MUNU [13]	TPC, CF_4, direction	$100(e^-)$ $217(\nu)$	16% FWHH (1 MeV)	0.74 (200 m^3)	$\nu + e^- \to \nu + e^-$	0.5
NEON [14]	He, Ne, scintillator	$20(e^-)$ $82(\nu)$	16% FWHH (100 keV)	10	$\nu + e^- \to \nu + e^-$	18
Present work	LS	$170(e^-)$ $310(\nu)$	10.5 keV (200 keV)	10	$\nu + e^- \to \nu + e^-$	1.8 1.1 (LMA)

Table 2. Achieved and targeted purities in the Borexino and KamLAND solar neutrino projects

	CTF of Borexino [20–22]	Borexino goals [19]	KamLAND [23]	KamLAND goals [23]
^{14}C	2×10^{-18} g/g	$\sim 10^{-18}$ g/g	No data	
^{238}U	$<4.8 \times 10^{-16}$ g/g	$\sim 10^{-16}$ g/g (1 μBq/m^3)	3.5×10^{-18} g/g	$\sim 10^{-16}$ g/g
^{232}Th	$<8.4 \times 10^{-16}$ g/g	$\sim 10^{-16}$ g/g	5.2×10^{-17} g/g	$\sim 10^{-16}$ g/g
^{40}K	$\leq 10^{-15}$ g/g	$\sim 10^{-18}$ g/g	2.7×10^{-16} g/g	$\leq 10^{-18}$ g/g
^{210}Pb	<500 μBq/t	~ 1 μBq/m^3	$\simeq 10^{-20}$ g/g	5×10^{-25} g/g (1 μBq/m^3)
^{85}Kr	<600 μBq/t	~ 1 μBq/m^3	0.7 Bq/m^3	1 μBq/m^3
^{39}Ar	<800 μBq/t	~ 1 μBq/m^3		
^{222}Rn	$(3.5 \pm 1.4) \times 10^{-16}$ g/g (~ 3 μBq/m^3)	$\sim 10^{-16}$ g/g	0.03 μBq/m^3	1 μBq/m^3

inside the scintillator, the corresponding charge is calculated:

$$\Delta Q_i = A E_{e_i} f(k_B, E_e) f_R(r_i). \qquad (3)$$

The total mean collected charge is defined when the gamma is discarded by the EG code, summing individual deposits:

$$Q_\gamma = \sum \Delta Q_i.$$

The weighted position is assigned to the final

Table 3. Comparison of the main features of the CTF, Borexino, and the proposed detector (some data for the KamLAND detector are shown for comparison; because of the higher threshold (400 keV), the energy and spatial resolutions are not estimated for KamLAND)

Parameter	CTF	Borexino	KamLAND (solar ν project)	Proposed detector
Geometrical coverage [%]	21	30	34	≅100
Light yield [p.e./MeV]	360	400	320	1800
Light yield per PMT for the event at the detector's center μ_0 [p.e./MeV]	3.6	0.25	≥0.25	2.25
Energy resolution at 200 keV [keV] $\left(\sim \frac{1}{\sqrt{\text{Light yield}}}\right)$	27	26		10.5
Threshold [keV]	250	250	400	170
Muon veto PMTs	16	200		50
Number of PMTs	100	2200	1325 (17 in.) + 554 (20 in.)	800
Total natural K content in the PMTs [g]	8	176		64
Distance between the PMTs and detector's center [cm]	330	675	825	440
Spatial resolution at 200 keV [cm] $\left(\sim \left\langle \frac{1}{\sqrt{N_{\text{hit}}}} \right\rangle \cong 1/\sqrt{N_{\text{PM}}(1-e^{-0.2\mu_0})}\right)$	20	45		8

gamma:

$$x_w = \frac{\sum \Delta Q_i x_i}{\sum \Delta Q_i}, \qquad (4)$$

where ΔQ_i and x_i are the charge deposited for the ith electron at the position $\{x_i, y_i, z_i\}$. The same rule is applied to the y_w and z_w coordinates.

In the next step, a random charge is generated according to the normal distribution with a mean value of $Q = \sum \Delta Q$ and with variance $\sigma_Q = \sqrt{(1+\overline{v}_1)Q}$. Finally, the radial reconstruction is simulated taking into account the energy dependence of the reconstruction precision. It is assumed that the reconstruction precision is defined by the number of PMTs fired in an event and that the reconstruction precision does not depend on the position. These two facts were confirmed by measurements with an artificial radon source inserted in the CTF-I and CTF-II detectors [22]. The reconstruction precision for the radon events can be obtained either by direct measurement with a source or by fitting the distribution of the radon events. The mean number of channels fired for an event with an energy E at the detector's center is

$$\langle N \rangle = N_{\text{PMT}}(1 - e^{-\mu_0}), \qquad (5)$$

where μ_0 is the mean number of photoelectrons (p.e.) registered by one PMT in the event and N_{PMT} is the total number of PMTs. If we assume that the reconstruction precision is defined by the mean number of fired channels, then the reconstruction precision is

$$\sigma_R(E) = \sigma_R(E_{\text{ref}})\sqrt{\frac{\langle N(E_{\text{ref}})\rangle}{\langle N(E)\rangle}}, \qquad (6)$$

where $\sigma_R(E_{\text{ref}})$ is the spatial resolution for a monoenergetic source with energy E_{ref}. We used as a reference the values obtained with the CTF-I detector with a ^{214}Po source: $\sigma_R(0.751\ \text{keV}) = 12.3 \pm 0.04$ cm [22].

We expect less than 1 event/d due to the internal background in 10 t of scintillator in the energy window 170–250 keV. The better energy and spatial resolutions of the detector will permit us to improve the α/β discrimination capability in comparison to the CTF. The very low energy threshold together with better energy and spatial resolutions will allow us as well to improve the selection of the sequential decays from the radioactive chains. More details on the large-volume detector energy and spatial resolutions can be found in [17, 25, 30].

5. NEUTRINO SIGNALS

In the calculations, we used SSM fluxes given by the standard solar model [31], neutrino energy spectra from [32–34], and survival probabilities for the LMA

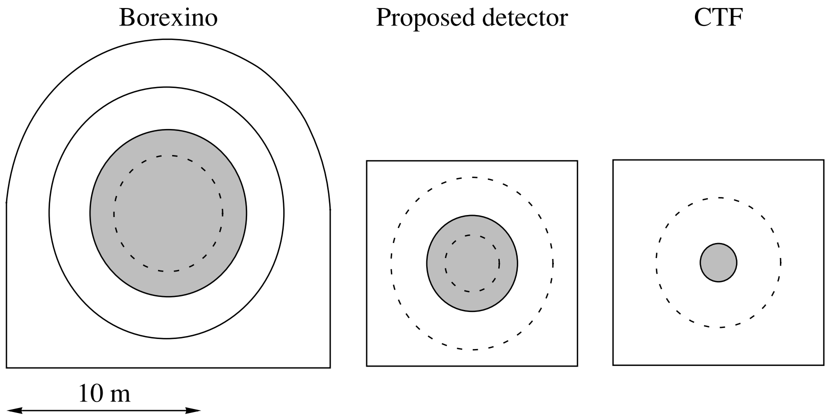

Fig. 1. Comparison of the geometry of the Borexino, CTF, and proposed detectors. The inner vessel with scintillator is shown with a gray color. The dashed line inside the inner vessel defines the fiducial volume; the outer layer protects the fiducial volume from the external gammas. PMTs are uniformly distributed over the surface shown with a solid line on the Borexino drawing and with a dashed line on the two others.

solar neutrino scenario from [35]. Signal shapes were convolved with the detectors' response function using the model described in [17].

The expected *pp*-neutrino count for the LMA solar neutrino oscillation scenario is listed in Table 4 for different thresholds (defined by ^{14}C content). The sensitivity was estimated with the MC method as described in [17].

The expected rates are listed in Table 4. The neutral current channel for the neutrinos of nonelectron flavors are taken into account in the calculations. Other neutrino sources also have nonnegligible contributions to the total signal in this energy window. The main source, besides the *pp*, is ^{7}Be neutrinos with a flat spectrum (see Fig. 2).

Table 4. The effect of the ^{14}C in the scintillator on the sensitivity of the detector to the SSM *pp* neutrinos (in the LMA MSW scenario) (the data correspond to the detector mass of 10 t and 1 yr of data taking; energy in keV)

^{14}C, g/g	2×10^{-18}	10^{-19}	10^{-20}	10^{-21}
Threshold (set at $\sqrt{\text{bkg}} = \text{eff}$)	172 (40)	152	108	0
Threshold (set at $2\sqrt{\text{bkg}} = \text{eff}$)	178	163	140	0
Energy interval	172–250	150–250	150–250	150–250
^{14}C events	1500	5383	538	54
Internal background	228	287	287	287
pp (LMA)	412	705	705	705
Total ν (LMA)	668	1035	1035	1035

We find out that the total neutrino flux will be measured with 7.5% (1σ) relative precision. Possible systematic errors due to the unknown shape of the background are not included in the estimate. We assume that the MC simulation can reproduce the form of the background and that only the total normalization of this shape is unknown. This assumption is reasonable because of the quite narrow signal window, where the background is dominated by the slowly varying continuous spectrum of the soft part of the gamma spectra of radioactive impurities.

6. IMPROVEMENT OF THE DETECTOR PERFORMANCE

The performance of the detector can be improved by using any of the following ideas:

Use of specially designed photomultipliers providing better quantum efficiency. The basic idea is the "recycling" of the incoming photons. Various optical arrangements have been used to improve light absorption by letting incoming light interact with the photocathode material more than once (see, e.g., [36]). This idea has been revived in recent works [37, 38], where the authors reported a significant increase in the quantum efficiency, up to a factor of 2. There are also indications supporting the possibility of creating a photocathode with very high quantum efficiency using a material doped with nanoparticles [39].

Use of beta/gamma discrimination techniques. The use of a different topology of the pointlike beta events and the spatially distributed gamma events can provide an opportunity to discriminate between beta- and gamma-induced signals with high efficiency. This method exploits the superior resolutions of the detector.

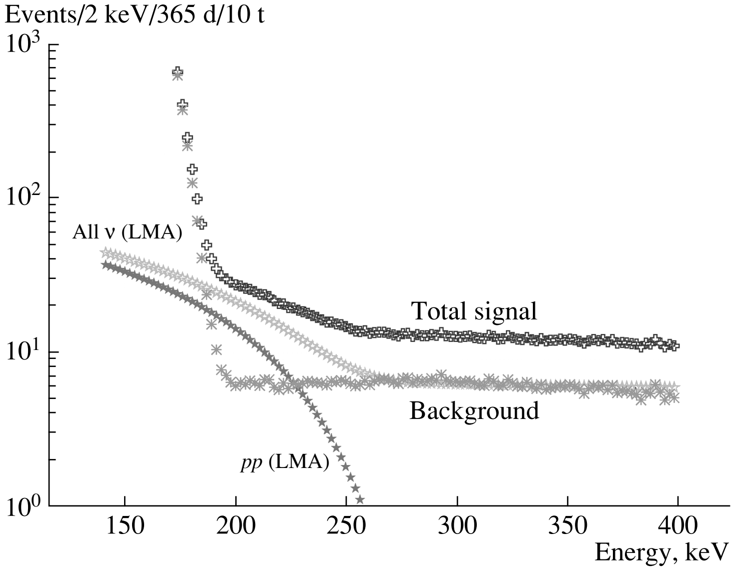

Fig. 2. Signal and background shape for the SSM neutrino fluxes in the LMA MSW solution. The ^{14}C content is 2×10^{-18} g/g. The concentrations of the main contributors to the background are listed in Table 2. The detector mass is 10 t. The resolution is calculated with the assumption of 100% geometrical coverage using CTF-I light output for the liquid scintillator (i.e., 1800 p.e./MeV) and is assumed to be $1/\sqrt{N_{\mathrm{p.e.}}}$. The shown signals correspond to 1 yr of data taking.

Choice of organic scintillator with lower content of ^{14}C. There are indications that the content of ^{14}C can be much smaller than that measured with the CTF-I detector, namely, of the order of 10^{-21} g/g [40]. In this case, the ^{14}C contribution to the background can be significantly reduced, and this will lead to an improvement in the detector's characteristics.

7. CONCLUSIONS

It is shown that a high-energy resolution detector with the radiopurity levels necessary for the operation of Borexino, as well as the solar neutrino project of KamLAND, will be sensitive to solar *pp* neutrinos. This project can compete with other existing proposals (see Table 1).

ACKNOWLEDGMENTS

This work would have been impossible without the support from the INFN sez. di Milano. We would like to thank Prof. G. Bellini and Dr. G. Ranucci for their continuous interest in our job. We would like to thank all the colleagues from the Borexino Collaboration for the pleasure of working together. Special thanks go to R. Ford for the careful reading of the manuscript.

REFERENCES

1. K. Eguchi *et al.* (KamLAND Collab.), Phys. Rev. Lett. **90**, 021802 (2003).
2. A. Bandyopadhyay, S. Choubey, R. Gandhi, *et al.*, Phys. Lett. B **559**, 121 (2003).
3. E. Calabresu, G. Fiorentini, and M. Lissia, astro-ph/9602045.
4. J. N. Bahcall, in *Proceedings of the 2nd International Workshop on Low-Energy Solar Neutrinos (LowNu2), Tokyo, 2000*, Ed. by Y. Suzuki (World Sci., Singapore, 2001).
5. S. Turck-Chieze, in *Proceedings of the International Workshop on Low-Energy Solar Neutrinos (LowNu-2003)*, Paris, 2003, http://cdfinfo.in2p3.fr/LowNu2003/.
6. R. S. Raghavan, in *Abstracts of Papers of LENS Meeting at LNGS, Assergi, 1998*; M. Fujiwara *et al.*, nucl-ex/0006006.
7. R. S. Raghavan, in *Proceedings of the International Workshop on Low-Energy Solar Neutrinos (LowNu-2003), Paris, 2003*, http://cdfinfo.in2p3.fr/LowNu2003/.
8. H. V. Klapdor-Kleingrothaus, Nucl. Phys. B (Proc. Suppl.) **100**, 350 (2001); W. Hofmann and G. Heusser, in *Proceedings of the International Workshop on Low-Energy Solar Neutrinos (LowNu-2003), Paris, 2003*, http://cdfinfo.in2p3.fr/LowNu2003/.
9. R. Lanou, in *Proceedings of the International Workshop on Low-Energy Solar Neutrinos (LowNu-2003), Paris, 2003*, http://cdfinfo.in2p3.fr/LowNu2003/.
10. M. Nakahata, in *Proceedings of the International Workshop on Low-Energy Solar Neutrinos (LowNu-2003), Paris, 2003*, http://cdfinfo.in2p3.fr/LowNu2003/.

11. A. Sarrat (on behalf of the HELLAZ Collab.), Nucl. Phys. B (Proc. Suppl.) **95**, 177 (2001).
12. H. Ejiri, in *Proceedings of the 2nd International Workshop on Low-Energy Solar Neutrinos (LowNu2), Tokyo, 2000*, Ed. by Y. Suzuki (World Sci., Singapore, 2001); http://www-sk.icrr.u-tokyo.ac.jp/neutlowe/2/transparency/index.html.
13. C. Broggini, in *Proceedings of the 2nd International Workshop on Low-Energy Solar Neutrinos (LowNu2), Tokyo, 2000*, Ed. by Y. Suzuki (World Sci., Singapore, 2001).
14. D. N. McKinsey and J. M. Doyle, astro-ph/9907314.
15. J. N. Abdurashitov *et al.*, Phys. Rev. C **60**, 055801 (1999).
16. W. Hampel *et al.*, Phys. Lett. B **447**, 127 (1999).
17. O. Yu. Smirnov, O. A. Zaimidoroga, and A. V. Derbin, Yad. Fiz. **66**, 741 (2003) [Phys. At. Nucl. **66**, 712 (2003)].
18. C. Arpesella *et al.*, *Borexino at Gran Sasso, Proposal for a Real Time Detector for Low-Energy Solar Neutrino*, Ed. by G. Bellini *et al.* (Dept. of Physics, Univ. of Milano, 1991), Vol. 1.
19. G. Alimonti *et al.*, Astropart. Phys. **16**, 205 (2002).
20. C. Arpesella *et al.*, Astropart. Phys. **18**, 1 (2002).
21. G. Alimonti *et al.*, Nucl. Instrum. Methods Phys. Res. A **406**, 411 (1998).
22. G. Alimonti *et al.*, Astropart. Phys. **8**, 141 (1998).
23. Y. Kishimoto, in *Proceedings of the International Workshop on Low-Energy Solar Neutrinos (LowNu-2003), Paris, 2003*, http://cdfinfo.in2p3.fr/LowNu2003/.
24. G. Alimonti *et al.*, Phys. Lett. B **422**, 349 (1998).
25. O. Ju. Smirnov, *Borexino Internal Note 02/27/07* (2002), http://borex.lngs.infn.it/people/smirnov.
26. G. Ranucci *et al.*, Nucl. Instrum. Methods Phys. Res. A **333**, 553 (1993).
27. W. R. Nelson, H. Hirayama, and D. W. O. Rogers, *The EGS4 Code System,* SLAC-265 (1985).
28. M. N. Peron, private communication.
29. S. Bonetti, private communication.
30. O. Ju. Smirnov, Instrum. Exp. Tech. **46**, 327 (2003).
31. J. N. Bahcall, H. Pinsonneault, and S. Basu, astro-ph/0010346.
32. J. N. Bahcall and R. K. Ulrich, Rev. Mod. Phys. **60**, 297 (1988).
33. J. N. Bahcall, E. Lisi, D. E. Alburger, *et al.*, Phys. Rev. C **54**, 411 (1996).
34. J. N. Bahcall, Phys. Rev. C **56**, 3391 (1997).
35. J. N. Bahcall, P. I. Krastev, and A. Yu. Smirnov, Phys. Rev. D **58**, 096016 (1998).
36. W. D. Gunter, Jr., G. R. Grant, and S. A. Shaw, Appl. Opt. **9** (2), 251 (1970).
37. S. Harmer, S. Hallensleben, and P. D. Townsend, Nucl. Instrum. Methods Phys. Res. B **166–167**, 798 (2000).
38. S. Hallensleben, S. Harmer, and P. D. Townsend, Opt. Commun. **180**, 89 (2000).
39. I. E. Protsenko, V. N. Samoilov, and O. A. Zaimidoroga, RF Patent No. 2002107248, priority from 22/03/2002.
40. E. Resconi, PhD Thesis (Università degli Studi di Genova, 2001); S. Schoenert, private communication.

Physics of Atomic Nuclei, Vol. 67, No. 11, 2004, pp. 2073–2079. Translated from Yadernaya Fizika, Vol. 67, No. 11, 2004, pp. 2094–2100.

New Method for Calculating the Potential Energy of Deformed Nuclei within the Liquid-Drop Model

R. S. Kurmanov[1)] **and G. I. Kosenko**[*]

Omsk State University, pr. Mira 55A, Omsk, 644077 Russia

Received July 22, 2003; in final form, December 16, 2003

Abstract—The method that we previously developed for going over from double volume integrals to double surface integrals in calculating the Coulomb energy of nuclei that have a sharp surface is generalized to the case of nuclei where the range of nuclear forces is finite and where the nuclear surface is diffuse. New formulas for calculating the Coulomb and the nuclear energy of deformed nuclei are obtained within this approach. For a spherically symmetric nucleus, in which case there is an analytic solution to the problem in question, the results are compared with those that are quoted in the literature, and it is shown that the respective results coincide identically. A differential formulation of the method developed previously by Krappe, Nix, and Sierk for going over from double volume integrals to double surface integrals is proposed here on the basis of the present approach. © *2004 MAIK "Nauka/Interperiodica"*.

The liquid-drop model [1, 2] has been extensively used so far to calculate the potential energy of a deformed nucleus. Instead of the liquid-drop model involving a sharp nuclear boundary [3], a more realistic model, that which employs a diffuse surface [4, 5], has been applied ever more frequently in recent years. Within the liquid-drop model, the potential energy of a nucleus includes the Coulomb, the nuclear, and the rotational component, each of these being dependent on the nuclear shape. In [6], a new formula was derived for calculating the Coulomb energy within the liquid-drop model involving a sharp boundary. In order to find the Coulomb energy, it is necessary to calculate a double volume integral. A new regular method that was different from that used in [4, 7, 8] was developed in [6] for reducing double volume integrals to double surface integrals for an arbitrary integrand. Within this approach, the integrand in the resulting double surface integral is simpler than its counterpart in [7]. In the present study, the method constructed in [6] is applied to calculating the potential energy within the liquid-drop model involving a diffuse boundary. Our main objective is to obtain formulas for calculating the potential energy of a nucleus—namely, its Coulomb and nuclear components—with allowance for a finite range of nuclear forces and the diffuseness of the nuclear surface.

1. DESCRIPTION OF THE FORMALISM

Let us briefly recall the fundamentals of the method used. The problem at hand is to go over from double volume integrals to double surface integrals,

$$\int dV dV' \rho(\sigma) = \int (d\mathbf{S} \cdot d\mathbf{S}') f(\sigma), \qquad (1)$$

where $\rho(\sigma)$ is a volume integrand ($\sigma = |\mathbf{r} - \mathbf{r}'|$) and $f(\sigma)$ is the respective surface integrand.

Mathematically, the problem is formulated as follows: for a known function $\rho(\sigma)$, it is necessary to find the function $f(\sigma)$. The method is based on the fact that, by using Gauss' integral theorem for a gradient, one can recast the right-hand side of (1) into the form

$$\int (d\mathbf{S} \cdot d\mathbf{S}') f(\sigma) = \int dV' (d\mathbf{S} \cdot \mathrm{grad}_{\mathbf{r}'}) f(\sigma). \qquad (2)$$

Applying Gauss' integral theorem for the divergence of a vector, we obtain

$$\int dV' (d\mathbf{S} \cdot \mathrm{grad}_{\mathbf{r}'}) f(\sigma) \qquad (3)$$
$$= \int dV dV' \mathrm{div}_{\mathbf{r}} \mathrm{grad}_{\mathbf{r}'} f(\sigma).$$

We note that the integrand on the right-hand side of this relation is the scalar product of two nabla operators that differentiate an unknown function with respect to the different variables. Since the relation in (3) must be satisfied for an arbitrary volume of integration, the integrand on the left-hand side of Eq. (1) must be equal to the integrand on the right-hand side of Eq. (3); that is,

$$\mathrm{div}_{\mathbf{r}} \mathrm{grad}_{\mathbf{r}'} f(|\mathbf{r} - \mathbf{r}'|) = \rho(|\mathbf{r} - \mathbf{r}'|). \qquad (4)$$

[1)] Omsk State Railway Transport University, pr. Marksa 35, Omsk, 644046 Russia. e-mail: `kurmanovrs@mail.ru`

[*] e-mail: `kosenko@phys.omsu.omskreg.ru`

Going over from the vector variables $\mathbf{r}$ and $\mathbf{r}'$, with respect to which one must perform differentiation, to the vector $\boldsymbol{\sigma} = \mathbf{r} - \mathbf{r}'$, we obtain the Laplacian of the sought function

$$\mathrm{div}_{\mathbf{r}}\mathrm{grad}_{\mathbf{r}'} f(|\mathbf{r}-\mathbf{r}'|) = -\Delta_{\boldsymbol{\sigma}} f(\sigma). \qquad (5)$$

This function must be equal to an "electrostatic" potential. We recall that, in electrostatics, such an equation is known as Poisson's equation

$$-\Delta_{\boldsymbol{\sigma}} f(\sigma) = \rho(\sigma), \qquad (6)$$

where $\rho(\sigma)$ plays the role of an arbitrary "charge" distribution. By way of example, we present Poisson's equation for a pointlike charge (that is, that which has a delta-function distribution):

$$-\Delta_{\boldsymbol{\sigma}} \frac{1}{\sigma} = 4\pi\delta(\boldsymbol{\sigma}).$$

This expression can be used to calculate the integral

$$\int (d\mathbf{S}\cdot d\mathbf{S}')\frac{1}{\sigma} = \int dV dV' \left(-\Delta_{\boldsymbol{\sigma}}\frac{1}{\sigma}\right) \qquad (7)$$

$$= \int dV dV' \cdot 4\pi\delta(\boldsymbol{\sigma}) = \frac{16\pi^2 R_0^3}{3},$$

where R_0 is the radius of a spherical nucleus. In the following, we will often use the result of this integration.

In deriving expression (6), we did not assume spherical symmetry. We now consider that the "charge" distribution $\rho(\sigma)$ in (6) is spherically symmetric, in which case the "potential" $f(\sigma)$ must have the same symmetry. Going over to spherical coordinates, we obtain a second-order differential equation for the sought function; that is,

$$-\frac{1}{\sigma^2}\frac{d}{d\sigma}\left[\sigma^2 \frac{d}{d\sigma} f(\sigma)\right] = \rho(\sigma). \qquad (8)$$

Upon the substitution

$$f(\sigma) = \frac{u(\sigma)}{\sigma}, \qquad (9)$$

Eq. (8) takes the form

$$-\frac{1}{\sigma}\frac{d^2}{d\sigma^2}u(\sigma) = \rho(\sigma). \qquad (10)$$

Upon integration, we find a general solution to Eq. (10) in the form

$$u(\sigma) = R(\sigma) + C_1\sigma + C_2 \qquad (11)$$

or

$$f(\sigma) = \frac{R(\sigma)}{\sigma} + C_1 + \frac{C_2}{\sigma},$$

where $R(\sigma)$ is the result of a double integration of the density $\rho(\sigma)$ and C_2 is an integration constant that can be determined from the condition requiring that the function $f(\sigma)$ be regular at the origin. Since the integral of a constant on the right-hand side of (1) is equal to zero, $C_1 = 0$ (if one substitutes $f(\sigma) = C_1$ into (6), then $\rho(\sigma) \equiv 0$).

Thus, we have found the surface function for a given volume function and can now go over from a double volume integral to the respective double surface integral. Further, we apply our method to calculating the Coulomb and the nuclear energy within the model of the nucleus where the range of nuclear forces is finite and where the surface of the nucleus is diffuse [4, 5, 8]. We recall that, apart from a constant that depends on the choice of reference level, the potential energy of the nucleus is given by

$$E_{\mathrm{pot}} = E_n + E_{\mathrm{C}}^{(0)}(B_{\mathrm{C}}^{\mathrm{sharp}} + \Delta B_{\mathrm{C}}) + E_R B_R,$$

where E_n is the nuclear energy, $E_{\mathrm{C}}^{(0)} = 3Z^2e^2/(5R_0)$ is the Coulomb energy of a uniformly charged spherical nucleus of radius $R_0 = r_0 A^{1/3}$, and $E_R B_R$ is the rotational energy (we do not consider it below).

In [6], where the authors considered the Coulomb energy of a nucleus that has a sharp surface, the expression obtained for the quantity $B_{\mathrm{C}}^{\mathrm{sharp}}$ has the form {see formula (16) in [6]}

$$B_{\mathrm{C}}^{\mathrm{sharp}} = -\frac{15}{64\pi^2 R_0^5}\int (d\mathbf{S}\cdot d\mathbf{S}')\sigma. \qquad (12)$$

We now write the Coulomb correction that takes into account the diffuseness of the nuclear surface and represent the nuclear energy in terms of double volume integrals according to the definitions adopted in [5]. We have

$$\Delta B_{\mathrm{C}} = -\frac{15}{64\pi^2 R_0^5}\int \left(\frac{\sigma}{a_c} + 2\right)\frac{e^{-\sigma/a_c}}{\sigma} dV dV', \qquad (13)$$

$$E_n = -\frac{c_s A^{2/3}}{8\pi^2 R_0^2 a^3}\int \left(\frac{\sigma}{a} - 2\right)\frac{e^{-\sigma/a}}{\sigma} dV dV', \qquad (14)$$

where c_s, a_c, and a are the constants specified in [5].

Further, we apply our method to determining the integrands $f(\sigma)$ in the surface integral in (1) for the following integrands $\rho(\sigma)$ in the volume integrals: the exponential function $\exp(-\varkappa\sigma)$ and the Yukawa function $\exp(-\varkappa\sigma)/\sigma$.

The resulting formulas for going over from the double volume integrals to double surface integrals are given immediately below (for the derivation of the integrands, see Section 3). For the Yukawa function, we have

$$\int dV dV' \frac{e^{-\varkappa\sigma}}{\sigma} = \frac{16\pi^2 R_0^3}{3\varkappa^2} \qquad (15)$$

$$-\frac{1}{\varkappa^2}\int(d\mathbf{S}\cdot d\mathbf{S}')\frac{e^{-\varkappa\sigma}}{\sigma},$$

where we have introduced the notation $\varkappa = 1/a$. For the exponential function, the respective result is

$$\int dVdV'e^{-\varkappa\sigma} = \frac{1}{\varkappa^3}\int(d\mathbf{S}\cdot d\mathbf{S}') \tag{16}$$
$$\times\left[\frac{2}{\sigma}-\frac{e^{-\varkappa\sigma}}{\sigma}(\varkappa\sigma+2)\right] = \frac{1}{\varkappa^3}\int(d\mathbf{S}\cdot d\mathbf{S}')\frac{2}{\sigma}$$
$$-\frac{1}{\varkappa^3}\int(d\mathbf{S}\cdot d\mathbf{S}')\frac{e^{-\varkappa\sigma}}{\sigma}(\varkappa\sigma+2).$$

Taking into account (7) and integrating the first term on the right-hand side of (16), we immediately obtain the constant that is analogous to that in expression (15):

$$\int dVdV'e^{-\varkappa\sigma} = \frac{32\pi^2R_0^3}{3\varkappa^3} \tag{17}$$
$$-\frac{1}{\varkappa^3}\int(d\mathbf{S}\cdot d\mathbf{S}')\frac{e^{-\varkappa\sigma}}{\sigma}(\varkappa\sigma+2).$$

This is the transformation formula for the exponential function.

The integrands in the integrals on the two sides of Eq. (15) prove to be identical, so that the transformation reduces to the inclusion of an additional constant term. In the case of Eq. (17), the situation is different since the integrand becomes more complicated: a Yukawa function additionally arises, which leads to a singularity at the origin, so that a correct integration is required. We note that the transformation formula (17) for the exponential function can be obtained from the corresponding formula (15) for the Yukawa potential by means of a mere differentiation with respect to the parameter $\varkappa$.

Let us finally consider the expressions for the Coulomb and the nuclear energy. We recast expression (13) for the correction to the Coulomb energy into the form

$$-\frac{64\pi^2R_0^5}{15}\Delta B_{\mathrm{C}} = 2\int dVdV'\frac{e^{-\sigma/a_c}}{\sigma} \tag{18}$$
$$+\frac{1}{a_c}\int dVdV'e^{-\sigma/a_c}$$

and make the substitution $1/a_c = \varkappa$. With the aid of expressions (15) and (17), we can then reduce the right-hand side of (18) to the form

$$2\left[\frac{16\pi^2R_0^3}{3\varkappa^2}-\frac{1}{\varkappa^2}\int(d\mathbf{S}\cdot d\mathbf{S}')\frac{e^{-\varkappa\sigma}}{\sigma}\right] \tag{19}$$
$$+\varkappa\left[\frac{32\pi^2R_0^3}{3\varkappa^3}-\frac{1}{\varkappa^3}\int(d\mathbf{S}\cdot d\mathbf{S}')\frac{e^{-\varkappa\sigma}}{\sigma}(\varkappa\sigma+2)\right].$$

Upon simplifying (19) and returning to the notation $\varkappa = 1/a_c$, we finally obtain

$$-\frac{64\pi^2R_0^5}{15}\Delta B_{\mathrm{C}} = \frac{64\pi^2R_0^3a_c^2}{3} \tag{20}$$
$$-a_c\int(d\mathbf{S}\cdot d\mathbf{S}')e^{-\sigma/a_c}-4a_c^2\int(d\mathbf{S}\cdot d\mathbf{S}')\frac{e^{-\sigma/a_c}}{\sigma}.$$

Here, there is neither simplification nor complication of the integrand in relation to the integrand in the original volume integral. Moreover, we obtained a less cumbersome expression than in [5]. If, however, one performs integration in (20), there arises a singularity for $\sigma \to 0$ in the second integral. We isolate this singularity by adding unity to and subtracting unity from the exponential function. This yields

$$\int(d\mathbf{S}\cdot d\mathbf{S}')\frac{1}{\sigma}(e^{-\sigma/a_c}-1+1) \tag{21}$$
$$=\int(d\mathbf{S}\cdot d\mathbf{S}')\frac{1}{\sigma}(e^{-\sigma/a_c}-1)+\int(d\mathbf{S}\cdot d\mathbf{S}')\frac{1}{\sigma}.$$

Substituting relation (21) into (20) and using the representation in (7), we find for ΔB_{C} that

$$-\frac{64\pi^2R_0^5}{15}\Delta B_{\mathrm{C}} = -a_c\int(d\mathbf{S}\cdot d\mathbf{S}')e^{-\sigma/a_c} \tag{22}$$
$$-4a_c^2\int(d\mathbf{S}\cdot d\mathbf{S}')\frac{1}{\sigma}(e^{-\sigma/a_c}-1).$$

In performing integration analytically, one can now see that, in the second integral, the integrand is finite for $\sigma \to 0$. Moreover, the procedure of subtracting from and adding to the respective integrand the two terms in the expansion of $e^{-\sigma/a_c}$ that follow unity makes it possible to arrive at a new expression for the Coulomb energy. Taking into account expressions (12) and (22) for $B_{\mathrm{C}}^{\mathrm{sharp}}$ and ΔB_{C}, respectively, we can obtain the following expression for B_{C}:

$$B_{\mathrm{C}}\frac{32\pi^2R_0^5}{15} = (B_{\mathrm{C}}^{\mathrm{sharp}}+\Delta B_{\mathrm{C}})\frac{32\pi^2R_0^5}{15} \tag{23}$$
$$=\frac{1}{2}\int(d\mathbf{S}\cdot d\mathbf{S}')\sigma+\frac{a_c}{2}\int(d\mathbf{S}\cdot d\mathbf{S}')e^{-\sigma/a_c}$$
$$+2a_c^2\int(d\mathbf{S}\cdot d\mathbf{S}')\frac{1}{\sigma}\left(e^{-\sigma/a_c}-\left[1-\frac{\sigma}{a_c}+\frac{\sigma^2}{2a_c^2}\right]\right).$$

Here, we have considered that, by virtue of (1) and (3), $\int(d\mathbf{S}\cdot d\mathbf{S}')\cdot 2a_c = 0$. In the last integral on the right-hand side of (23), the convergence of the integrand in the limit $\sigma \to 0$ is of order σ^2, this rendering the accuracy of a numerical integration higher than in (22).

A similar analysis can be performed for the nuclear component of the energy. As a result, we arrive at

$$E_n\frac{8\pi^2R_0^2a^3}{c_sA^{2/3}} = 2\int dVdV'\frac{e^{-\sigma/a}}{\sigma} \tag{24}$$

Computational formulas obtained within a new formalism along with the respective formulas from [5]

New approach	Old approach
$\oint\oint(d\mathbf{S}\cdot d\mathbf{S}')f(\sigma)$	$\oint\oint(d\mathbf{S}\cdot\boldsymbol{\sigma})(d\mathbf{S}'\cdot\boldsymbol{\sigma})g(\sigma)$
$f(\sigma)$	$g(\sigma)$
$B_{\rm C}$	
$-\frac{15}{64\pi^2R_0^5}\sigma$	$-\frac{5}{64\pi^2\sigma R_0^5}$
$\Delta B_{\rm C}$	
$\frac{15a_c}{64\pi^2R_0^5}\frac{1}{y_c}[-4+e^{-y_c}(y_c+4)]$	$\frac{15}{32\pi^2a_cR_0^5}\frac{1}{y_c^4}\left[2y_c^2-5+e^{-y_c}\left(\frac{1}{2}y_c^2+3y_c+5\right)\right]$
$E_n/E_s^{(0)}$	
$\frac{1}{8\pi^2R_0^2a^2}e^{-y_n}$	$\frac{1}{8\pi^2R_0^2a^4}\frac{1}{y_n^4}[2-e^{-y_n}(y_n^2+2y_n+2)]$

Note: Here, we present the general expressions for the calculated functionals in the upper part of the table and the expressions for the integrands in the new and the old ([5]) version in the lower part of the table. The notation used here for the respective quantities is spelled out in the Appendix.

$$-\frac{1}{a}\int dV dV' e^{-\sigma/a}.$$

Making the substitution $1/a=\varkappa$ and employing relations (15) and (17), we obtain

$$2\left[\frac{16\pi^2R_0^3}{3\varkappa^2}-\frac{1}{\varkappa^2}\int(d\mathbf{S}\cdot d\mathbf{S}')\frac{e^{-\varkappa\sigma}}{\sigma}\right] \tag{25}$$
$$-\varkappa\left[\frac{32\pi^2R_0^3}{3\varkappa^3}-\frac{1}{\varkappa^3}\int(d\mathbf{S}\cdot d\mathbf{S}')\frac{e^{-\varkappa\sigma}}{\sigma}(\varkappa\sigma+2)\right].$$

Upon the transition to the former notation and simplification, we have

$$E_n\frac{8\pi^2R_0^2a^2}{c_sA^{2/3}}=\int(d\mathbf{S}\cdot d\mathbf{S}')e^{-\sigma/a}. \tag{26}$$

Surprisingly, it is the nuclear component where the simplification is the most pronounced: only the integral of an exponential function is calculated. Apart from a constant factor, the same result can be obtained from expression (15) if one multiplies it by $\varkappa^2$ and then differentiates the product with respect to $\varkappa$. For the sake of comparison, we mention similar formulas obtained within traditional approaches [4, 7, 8] and presented in [5] (see also table). It can be seen that our surface functions are much simpler. The particular case of the calculation of the Coulomb and the nuclear energy for a spherically symmetric nucleus was also tested on the basis of our formulas, which were compared with the corresponding expressions from [4, 8]. The results of a direct analytic calculation proved to be coincident.

2. COULOMB AND NUCLEAR ENERGIES OF A SPHERICALLY SYMMETRIC NUCLEUS HAVING A DIFFUSE SURFACE

Let us now consider the case of a spherical nucleus—this case admits an analytic integration. In expression (20) for the correction to the Coulomb energy and in expression (26) for the nuclear energy, one must calculate integrals of the same type. We begin by considering the expression for the nuclear energy. First, we go over to the system of spherical coordinates; that is,

$$\int(d\mathbf{S}\cdot d\mathbf{S}')e^{-\sigma/a} \tag{27}$$
$$=R_0^4\int\cos\vartheta\exp\left(-\frac{2R_0\sin(\vartheta/2)}{a}\right)\sin\vartheta d\vartheta d\varphi d\Omega',$$

where ϑ is the angle between the normals to the surface elements $d\mathbf{S}$ and $d\mathbf{S}'$, their scalar product yielding $\cos\vartheta$. The solid-angle element $d\Omega$ corresponding to $d\mathbf{S}$ is written in terms of spherical coordinates; $d\Omega'$ corresponds to $d\mathbf{S}'$. In order to obtain the expression for the exponent in the integrand on the right-hand side of (27), it was considered that the angle between the vectors $\mathbf{r}$ and $\mathbf{r}'$ is identical to the angle between the surface elements (ϑ) and that the moduli of the vectors $\mathbf{r}$ and $\mathbf{r}'$ are equal to the radius R_0 of the spherical nucleus being considered. Integration with respect to φ and Ω' can be performed immediately; the result is $8\pi^2$. Performing integration with respect to ϑ from zero to π, we finally obtain

$$\int(d\mathbf{S}\cdot d\mathbf{S}')e^{-\sigma/a}=16\pi^2R_0^3a\left\{\frac{a}{2R_0}\right. \tag{28}$$
$$\left.-\frac{3a^3}{2R_0^3}+e^{-2R_0/a}\left(1+\frac{5a}{2R_0}+\frac{3a^2}{R_0^2}+\frac{3a^3}{2R_0^3}\right)\right\}.$$

Upon the substitution of this expression into (26), we obtain for E_n a formula that coincides with formula (8) from [4] {or with formula (17) from [5]}; that is,

$$E_n^{(0)} = E_s^{(0)}\left\{1 - \frac{3a^2}{R_0^2} + \left(\frac{R_0}{a} + 1\right)\right. \tag{29}$$
$$\left.\times\left(2 + \frac{3a}{R_0} + \frac{3a^2}{R_0^2}\right)e^{-2R_0/a}\right\},$$

where $E_s^{(0)} = c_s A^{2/3}$. Further, we consider expression (20) for the correction to the Coulomb energy. Here, we must additionally integrate a Yukawa function. As above, we go over to the system of spherical coordinates,

$$\int (d\mathbf{S}\cdot d\mathbf{S}')\frac{e^{-\sigma/a_c}}{\sigma} = R_0^4 \tag{30}$$
$$\times\int \exp\left(-\frac{2R_0\sin(\vartheta/2)}{a_c}\right)\frac{\sin\vartheta\cos\vartheta}{2R_0\sin(\vartheta/2)}d\Omega' d\vartheta d\varphi.$$

Performing integration in a way similar to that employed in (27), we obtain

$$\int (d\mathbf{S}\cdot d\mathbf{S}')\frac{e^{-\sigma/a_c}}{\sigma} \tag{31}$$
$$= 8\pi^2 R_0^2 a_c\left\{e^{-2R_0/a_c}\left(1 + \frac{a_c}{R_0}\right)^2 + 1 - \frac{a_c^2}{R_0^2}\right\}.$$

This expression and relation (28) can easily be verified by performing differentiation with respect to the parameter a. Taking into account the equality

$$\frac{d}{da}\int (d\mathbf{S}\cdot d\mathbf{S}')\frac{e^{-\sigma/a}}{\sigma} = \int (d\mathbf{S}\cdot d\mathbf{S}')\frac{e^{-\sigma/a}}{a^2}$$

and differentiating the right-hand side of (31), we obtain the expression on the right-hand side of (28). After the substitution of expressions (28) and (31) into (20) and some simple algebra, we obtain a formula that, apart from a difference in notation (a_c here instead of a), is coincident with formula (4.12) in [8]:

$$\Delta E_{\mathrm{C}}^{(0)} = E_{\mathrm{C}}^{(0)}\Delta B_{\mathrm{C}} = -\frac{3Z^2e^2a_c^2}{R_0^3} \tag{32}$$
$$\times\left\{1 - \frac{15}{8}\left(\frac{a_c}{R_0}\right) + \frac{21}{8}\left(\frac{a_c}{R_0}\right)^2\right.$$
$$-\frac{3}{4}e^{-2R_0/a_c}\left[1 + \frac{9}{2}\left(\frac{a_c}{R_0}\right) + 7\left(\frac{a_c}{R_0}\right)^2\right.$$
$$\left.\left. + \frac{7}{2}\left(\frac{a_c}{R_0}\right)^3\right]\right\}.$$

3. CALCULATION OF INTEGRANDS IN SURFACE INTEGRALS

Let us consider in greater detail the derivation of the integrand $f(\sigma)$ in the surface integral in (1). We assume that the function $\rho(\sigma) = e^{-\varkappa\sigma}$ appears in the integrand of the volume integral. In Eq. (10), we make the change of variable $\xi = \varkappa\sigma$ and the change of function $u(\xi) = U(\xi)/\varkappa^3$, whereupon we obtain the differential equation

$$U''(\xi) = -\xi e^{-\xi}.$$

By integrating this equation by parts two times, we arrive at

$$U(\xi) = -e^{-\xi}(\xi + 2) + C_1\varkappa^3\sigma + C_2\varkappa^3. \tag{33}$$

The constants of integration are chosen in such a way that it would be convenient to associate the result with formula (11). For the result of a double integration of $\rho(\sigma)$, we generally have [see (11) and the text below]

$$R(\sigma) = -e^{-\xi}(\xi + 2)/\varkappa^3$$

or

$$f(\sigma) = -e^{-\varkappa\sigma}(\varkappa\sigma + 2)/(\varkappa^3\sigma) + C_1 + C_2/\sigma.$$

In the case of a Coulomb potential, the constants were set to zero [6]. This follows from the requirement that the integrand be regular at the origin. In the case being considered, this requirement leads to the values of $C_1 = 0$ and $C_2 = 2/\varkappa^3$.

Further, we consider the case of a Yukawa potential, $\rho(\sigma) = e^{-\varkappa\sigma}/\sigma$. The equation for the free-particle Green's function is well known in scattering theory [9]. Our problem is similar to the Green's function problem for a particle of negative energy. In this case, a Yukawa potential plays the role of the Green's function. Upon setting $\boldsymbol{\sigma} = \mathbf{r} - \mathbf{r}'$, we have

$$-\frac{1}{4\pi}(\Delta_{\boldsymbol{\sigma}} + k^2)\frac{e^{ik\sigma}}{\sigma} = \delta(\boldsymbol{\sigma}). \tag{34}$$

At $k = i\varkappa$, we obtain

$$-\frac{1}{4\pi}(\Delta_{\boldsymbol{\sigma}} - \varkappa^2)\frac{e^{-\varkappa\sigma}}{\sigma} = \delta(\boldsymbol{\sigma}). \tag{35}$$

We will now use this equation to obtain a relation between the volume integral of the Yukawa function and the corresponding surface integral. We begin by transforming a double surface integral into a double volume integral in a way similar to that employed in (2) and (3). This yields

$$\int (d\mathbf{S}\cdot d\mathbf{S}')\frac{e^{-\varkappa\sigma}}{\sigma} = -\int dV dV'\Delta_{\boldsymbol{\sigma}}\left(\frac{e^{-\varkappa\sigma}}{\sigma}\right)$$
$$= \int dV dV'\left(4\pi\delta(\boldsymbol{\sigma}) - \varkappa^2\frac{e^{-\varkappa\sigma}}{\sigma}\right)$$
$$= 4\pi\int dV - \varkappa^2\int dV dV'\frac{e^{-\varkappa\sigma}}{\sigma}$$
$$= 4\pi\frac{4\pi R_0^3}{3} - \varkappa^2\int dV dV'\frac{e^{-\varkappa\sigma}}{\sigma},$$

whence, we obtain

$$\int dV dV' \frac{e^{-\varkappa\sigma}}{\sigma} \tag{36}$$
$$= \frac{16\pi^2 R_0^3}{3\varkappa^2} - \frac{1}{\varkappa^2}\int (d\mathbf{S}\cdot d\mathbf{S}')\frac{e^{-\varkappa\sigma}}{\sigma}.$$

4. DIFFERENTIAL FORMULATION OF THE STANDARD METHOD

A general method for going over from double volume to double surface integrals was described in [8]. This method, which is based on the Fourier transformation of relevant integrands, is disadvantageous in that it involves calculating integrals of oscillating functions, this strongly complicating the derivation of surface functions. Our approach reduces the problem of going over from double volume to double surface integrals to solving a partial differential equation.

In order to demonstrate the efficiency of our approach, we derive here the differential equation that corresponds to the method described in [8]. Solving this equation must yield the known functions given in [5].

Let us write the original integral equation for $g(\sigma)$:

$$\int dV dV' \rho(\sigma) = \int (d\mathbf{S}\cdot\boldsymbol{\sigma})(d\mathbf{S}'\cdot\boldsymbol{\sigma}) g(\sigma). \tag{37}$$

Mathematically, the problem is formulated as follows: it is necessary to find a differential equation that the function $g(\sigma)$ satisfies. By applying Gauss' divergence theorem two times, we obtain the partial differential equation

$$\frac{\partial^2}{\partial x_i \partial x_j'}(g(\sigma)\sigma_i\sigma_j) = \rho(\sigma). \tag{38}$$

Upon going over from differentiation with respect to the coordinates $\mathbf{r}$ and $\mathbf{r}'$ to differentiation with respect to σ and taking into account spherical symmetry, we obtain

$$\sigma^2 g'' + 8\sigma g' + 12 g = -\rho(\sigma). \tag{39}$$

Further, we substitute the functions g_1, g_2, and g_3 {see formulas (A4)–(A6) in [5]} into (39). Specifically, they are given by

$$g_1(\sigma) = -\frac{5}{64\pi^2\sigma R_0^5}, \tag{40}$$

$$g_2(\sigma) = \frac{15}{32\pi^2 a_c R_0^5}\frac{1}{y_c^4} \tag{41}$$
$$\times [2y_c - 5 + e^{-y_c}(y_c^2/2 + 3y_c + 5)],$$

$$g_3(\sigma) = -\frac{1}{8\pi^2 a^4 R_0^2}\frac{1}{y_n^4} \tag{42}$$
$$\times [2 - e^{-y_n}(y_n^2 + 2y_n + 2)],$$

where $y_c = \sigma/a_c$ and $y_n = \sigma/a$. After some simple but cumbersome calculations, we determine the volume functions $\rho(\sigma)$ appearing in the volume integrals in [5]. We have

$$\rho_1(\sigma) = \frac{15}{32\pi^2\sigma R_0^5}$$

for g_1 {formula (12) in [5]},

$$\rho_2(\sigma) = \frac{15}{32\pi^2 R_0^5}\left[1 + \frac{\sigma}{2a_c}\right]\frac{e^{-\sigma/a_c}}{\sigma}$$

for g_2 {formula (19) in [5]}, and

$$\rho_3(\sigma) = \frac{1}{8\pi^2 R_0^2 a^3}\left(2 - \frac{\sigma}{a}\right)\frac{e^{-\sigma/a}}{\sigma}$$

for g_3 {formula (15) in [5]}.

Equation (39) can be recast into a more elegant form. For this, we make the substitution $g(\sigma) = \psi(\sigma)f(\sigma)$ on the left-hand side of Eq. (39). Upon differentiation, we obtain

$$\sigma^2\psi f'' + f'(2\sigma^2\psi' + 8\sigma\psi)$$
$$+ f(12\sigma\psi + 8\sigma\psi' + \sigma^2\psi'') = -\rho(\sigma).$$

We require that the coefficient of f' vanish; that is,

$$2\sigma^2\psi' + 8\sigma\psi = 0.$$

Integrating this equation, we obtain $\psi = \sigma^{-4}C$, where C is an integration constant. Making this substitution, one can easily see that the coefficient of f also vanishes. Equation (39) now reduces to the equation $C\sigma^{-2}f'' = -\rho(\sigma)$. Setting $f(\sigma)C \equiv f(\sigma)$, we arrive at

$$f'' = -\sigma^2\rho(\sigma). \tag{43}$$

After the above transformations, we can see that, within the method developed in [8], the procedure of finding surface functions becomes as simple as that in our approach.

5. CONCLUSION

In the present study, the method proposed for calculating the Coulomb energy of a nucleus in the case of a sharp surface has been generalized to nuclei with a diffuse surface. New computational formulas have been derived for the diffuseness-induced correction to the Coulomb energy and for the nuclear component of the potential energy of a nucleus. These formulas have been tested by considering the particular case of a spherical nucleus. In this study, it has also been shown how, by using the Fourier transformation, the known integral approach [8] can be reduced to a differential approach similar to that which we have developed.

ACKNOWLEDGMENTS

We are grateful to G.D. Adeev for permanent support of our study and interest in it; his constructive criticism contributed greatly to improving the final version of the article. Special thanks are also due to Dr. A.J. Sierk for interest in the topic of our present activities and for valuable comments concerning our preceding article. The participation of L.A. Litnevsky in discussions on some special issues is gratefully acknowledged.

APPENDIX

Integrals for Axisymmetric Forms

We denote by $\rho(z)$ the profile function whose rotation about the symmetry axis z specifies the nuclear shape. Writing relevant surface integrals in terms of polar coordinates and considering that we are dealing with axisymmetric nuclear shapes, we have

$$\oint\oint(d\mathbf{S}\cdot d\mathbf{S}')f(\sigma)$$

$$= 2\pi\int\limits_{z_{\min}}^{z_{\max}} dz \int\limits_{z'_{\min}}^{z'_{\max}} dz' \int\limits_{0}^{2\pi} d\phi\Big\{\rho(z)\rho(z')\cos\phi$$

$$+ \rho(z)\frac{d\rho(z)}{dz}\rho(z')\frac{d\rho(z')}{dz'}\Big\}f(\{\rho^2(z)+\rho^2(z')$$

$$-2\rho(z)\rho(z')\cos\phi+(z-z')^2\}^{1/2}).$$

The surface functions $f(\sigma)$ correspond to the expressions quoted in the table. For the sake of comparison, the analogous functions for the surface integrals from [5] are also given in the table. The notation $y_c = \sigma/a_c$ and $y_n = \sigma/a$ is used there for the sake of brevity.

REFERENCES

1. Ya. I. Frenkel, Zh. Éksp. Teor. Fiz. **9**, 641 (1939); Phys. Rev. **55**, 987 (1939).
2. N. Bohr and J. A. Wheeler, Phys. Rev. **56**, 426 (1939).
3. W. D. Myers and W. J. Swiatecki, Ark. Fys. **36**, 343 (1967).
4. H. J. Krappe, J. R. Nix, and A. J. Sierk, Phys. Rev. C **20**, 992 (1979).
5. A. J. Sierk, Phys. Rev. C **33**, 2039 (1986).
6. R. S. Kurmanov, G. I. Kosenko, and G. D. Adeev, Yad. Fiz. **63**, 1978 (2000) [Phys. At. Nucl. **63**, 1885 (2000)].
7. K. T. R. Davies and A. J. Sierk, J. Comput. Phys. **18**, 311 (1975).
8. K. T. R. Davies and J. R. Nix, Phys. Rev. C **14**, 1977 (1976).
9. A. G. Sitenko, *Lectures in Scattering Theory* (Vishcha Shkola, Kiev, 1971; Pergamon, Oxford, 1971).

Translated by A. Isaakyan

Physics of Atomic Nuclei, Vol. 67, No. 11, 2004, pp. 2080–2094. Translated from Yadernaya Fizika, Vol. 67, No. 11, 2004, pp. 2101–2115.

NUCLEI
Theory

Theoretical Investigation of the Angular-Momentum Dependence of the Mean Fission Lifetime of Excited Nuclei

I. I. Gontchar, N. A. Ponomarenko, V. V. Turkin, and L. A. Litnevsky

Omsk State Railway Transport University, pr. Marksa 35, Omsk, 644046 Russia

Received June 16, 2003; in final form, November 4, 2003

Abstract—Mean fission lifetimes of nuclei excited to energies of 80 to 400 MeV were recently measured at the GANIL accelerator by the crystal-blocking technique. Those experiments served as a motivation for us to perform systematic calculations of the time distributions of fission events and the mean fission lifetimes versus the angular momentum, the initial excitation energy, and the fissility of a primary excited nucleus. The mean fission lifetimes are given as a function of the angular momentum L. The calculations were performed within the refined version of the combined dynamical–statistical model. It turned out that, if the height of the fission barrier at $L = 0$ is sizably greater than the neutron binding energy, the L dependence of the mean fission lifetimes has a resonance character. Such behavior of the mean fission lifetimes $\langle t_f \rangle$ is obtained both from statistical calculations and from a dynamical simulation of the fission process with allowance for friction. It is shown that the maximum in the L dependence of $\langle t_f \rangle$ is due to the fission of nuclei that lost a considerable part of the initial excitation energy through the emission of neutrons. The majority of the calculations were performed for ^{190}Pt at an initial excitation energy of 150 MeV. It is shown that the resonance behavior disappears with increasing fissility, but that it survives over a broad range of initial excitation energies. Systematic experimental studies are required for confirming or disproving our theoretical predictions. *© 2004 MAIK "Nauka/Interperiodica"*.

1. INTRODUCTION

The time of any physical process (or the lifetime of any physical system in an excited state) is one of the most important features of the process or the system being considered. The fission of excited nuclei is hardly an exception in this respect.

Although available experimental methods for studying the fission lifetimes of excited nuclei are quite diverse (for an overview of these methods and of the results that they produce, the interested reader is referred to the article of Hilscher and Rossner [1]), a full pattern of the results obtained in these realms to date is rather fragmentary and contradictory. Most frequently, some "typical" or "characteristic" fission lifetimes are extracted from data on the mean multiplicities of prescission neutrons and photons. As a rule, researchers do not address the problem of studying fission lifetimes as such. For one reason or another, it is tacitly assumed that these lifetimes are of interest only because they carry information about the dissipative properties of nuclear matter.

Only the studies reported in [2] stand out in this respect. There, the crystal-blocking technique [3] was used to perform systematic measurements of mean fission lifetimes of protoactinium, uranium, and neptunium isotopes excited to energies less than 15 MeV. According to those studies, the mean fission lifetime of a specific nuclear species is a monotonically decreasing function of excitation energy. This behavior can easily be understood on the basis of simple statistical considerations: the larger the phase-space domain accessible to the decaying system, the faster the decay process.

In a number of studies, Hilscher, Newton, and Heind and their coauthors (see the review articles quoted in [1, 4]) extracted, from data on the mean multiplicities of prescission neutrons, the fission lifetimes of nuclei excited to 50–200 MeV. These systematic data were obtained in heavy-ion reactions. It turned out that the fission lifetimes found in this way are about 6×10^{-20} s and that they are weakly dependent on the charge number for $Z = 70$–110 compound nuclei. We are unaware of data on the fission lifetimes of highly excited nuclei formed in reactions involving light particles (that is, at low angular momenta). Moreover, fission lifetimes extracted from the multiplicity of prescission neutrons do not contain information about fission that occurred after the emission of a considerable number of neutrons (see the discussion on this issue in [5, 6] and in Section 3 below).

It can be expected, however, that this gap in our knowledge of fission lifetimes will be filled upon further applying the method that is based on combining the crystal-blocking technique with deep-inelastic-scattering reactions and which was developed by Morjean and his coauthors at GANIL [7, 8].

With an eye to this possible development of the experimental situation, we will pursue the goal of establishing the most general regularities in the evolution of the mean fission lifetime of an excited nucleus as a function of its angular momentum L, excitation energy E^*, and fissility Z^2/A, relying on the present-day models of the fission process. To the best of our knowledge, such an attempt is being undertaken for the first time. In addition, we are going to study the effect of nuclear dissipation on mean fission lifetimes.

In the present study, we demonstrate how the mean fission lifetime $\langle t_f \rangle$ of an excited nucleus depends on its angular momentum and how the inclusion of nuclear friction affects this dependence. The dependences $\langle t_f \rangle (E^*)$ and $\langle t_f \rangle (Z^2/A)$ will be discussed in forthcoming publications.

The ensuing exposition is organized as follows. In Section 2, we briefly discuss modifications introduced in our model, which was described in detail in a number of articles (see, for example, [5, 9, 10]). In Section 3, we present the results of our calculations for mean fission lifetimes, mean multiplicities of prescission neutrons, time distributions of fission events and of events involving the emission of prescission neutrons, and distributions of fission events with respect to the number of emitted neutrons. These calculations were performed for ^{190}Pt at the initial excitation energy of $E^*_{\text{init}} = 150$ MeV both in the statistical and in the dynamical mode. In Section 4, the results in question are analyzed and are interpreted in terms of the neutron and fission widths. In Section 5, we give mean fission lifetimes versus L that were calculated for ^{205}Pb and ^{235}U at $E^*_{\text{init}} = 150$ MeV, as well as for ^{190}Pt at different values of E^*_{init}. Section 6 is devoted to estimating statistical uncertainties in the calculation of mean fission lifetimes. In Section 7, we compare our results with their counterparts available in the literature and analyze the possibility of observing the predicted effect in reactions leading to the complete fusion of heavy ions. The conclusions drawn from our study are given in Section 8.

2. FORMULATION OF THE MODEL

Mean fission lifetimes are calculated here on the basis of a refined version of the combined dynamical—statistical model employed in [5, 9—11]. For the sake of definiteness, we use the abbreviations CDSM and CDSM1 for, respectively, the former and the modified version of the model. Since the CDSM version was described in detail in many articles, we will only touch here upon modifications to the model that are of importance for the present study. They are the following:

(i) An option that makes it possible to perform calculations with full Langevin equations (not reduced ones) is included in the CDSM version. This makes it possible, among other things, to take into account the dependence of the inertial parameter of collective motion on the deformation of the nucleus undergoing fission.

(ii) Universal dependences obtained in [12] (see Figs. 8 and 9 in that article) are used to calculate the coordinate-dependent inertial and friction parameters.

(iii) In addition to CDSM, where the potential energy U was calculated within the model of a liquid drop with a sharp boundary (U_{LDM}), an option that makes it possible to calculate the potential energy with allowance for the finiteness of the range of nuclear forces (U_{FRM}; see [13, 14] for details) is included in CDSM1. In the presence of the fission barrier B_f, the potential energy U_{FRM} was calculated by means of scaling; that is,

$$U_{\text{FRM}}(q, L) = U_{\text{LDM}}(q, L) \frac{B_{f,\text{MKP}}(L)}{B_{f,\text{LDM}}(L)}. \qquad (1)$$

In the absence of a barrier (for $B_{f,\text{LDM}}(L) < 0.01$ PMeV in the code used), the potential energy is not rescaled.

(iv) In calculating the width with respect to nuclear decay through a channel competing with fission, the dynamical branch of CDSM1 takes into account not only the neutron- and photon-emission widths (this was done within CDSM) but also the widths with respect to the emission of protons, deuterons, and alpha particles. Test calculations revealed that this modification does not lead to changes in observables beyond the statistical errors of the calculation.

In the present study, all of the calculations are performed with the deformation-dependent single-particle-level-density parameter $a(q)$ from [15]; that is,

$$a(q) = a_V A + a_S A^{2/3} B_S(q), \qquad (2)$$

where $a_V = 0.0685$ MeV^{-1}, $a_S = 4a_V$, and $B_S(q)$ is the dimensionless coefficient that determines the surface area of the nucleus being considered and which is normalized in such a way that it is equal to unity for a sphere.

The potential energy of a nucleus as a function of its deformation, $U_{\text{FRM}}(q)$, was calculated on the basis of the procedure that was described in detail in [16], whereupon the result was scaled according to (1). Thus, fission barriers here correspond to the finite-range model (FRM) [17].

A dynamical simulation of the fission process was performed on the basis of full Langevin equations.

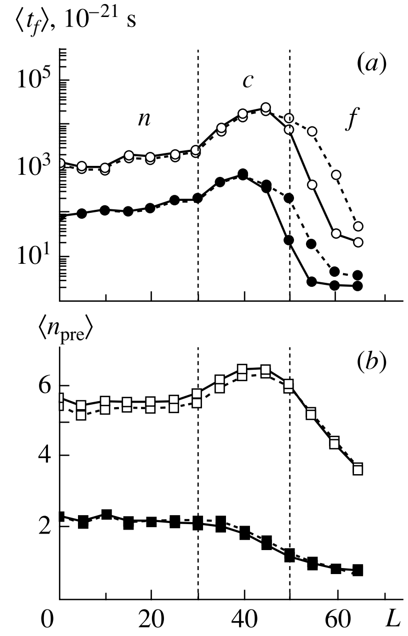

Fig. 1. (*a*) Mean fission lifetime and (*b*) mean multiplicity of prescission neutrons versus angular momentum for ^{190}Pt at the initial excitation energy of $E^*_{\rm init} = 150$ MeV. The calculations were performed in the (closed symbols) statistical and (open symbols) dynamical modes. The dotted lines represent the mean fission lifetimes and the mean multiplicities of prescission neutrons in all fission events, irrespective of how the nucleonic composition of the nucleus changed as the result of emission, while the solid lines are their counterparts in fission events where the charge number of the nucleus did not change. The partition into the segments n, c, and f reflects the dominance of one decay mode or another [neutron emission (n) or fission (f)], but the choice of its boundaries involves some degree of arbitrariness. There is a strong competition between these channels within the segment c.

The inertial and friction parameters, which are necessary for this, were calculated by approximate formulas that reproduce the results presented in Figs. 8 and 9 in [12]. These formulas provide a good approximation to the inertial parameter calculated on the basis of the Werner–Wheeler model [18] and the friction parameter corresponding to one-body dissipation from [19]. They are given by

$$M(q) = 8.56 M_{\rm CN} \left[-1 + 0.285 \exp\left(-\frac{q - q_{\rm qs}}{0.1575} \right) + 1.153 \exp\left(-\frac{q - q_{\rm qs}}{424} \right) \right], \tag{3}$$

$$\eta_{\rm OBD}(q) = 0.635 \hbar A^{4/3} \left[1 + 3.37 \exp\left(-\frac{q - q_{\rm qs}}{0.08997} \right) + 5.07 \exp\left(-\frac{q - q_{\rm qs}}{0.3848} \right) \right], \tag{4}$$

where q is the deformation parameter, which is equal to half the distance between the centers of mass of would-be fragments in units of the radius of a sphere having the same volume; $q_{\rm qs} = 0.375$; and $M_{\rm CN} = A m_n R_0^2$.

The calculations that produce the results quoted in the present article were performed both in the dynamical mode (that is, with the aid of Langevin equations) and in the statistical mode, in which case the rate of fission was calculated by the Bohr–Wheeler formula. The particle-emission widths were calculated identically in these two cases.

3. RESULTS OF THE CALCULATIONS FOR ^{190}Pt AT A PRIMARY EXCITATION ENERGY OF 150 MeV

In this section, we everywhere present the results of our calculations for a ^{190}Pt nucleus of excitation energy 150 MeV. This choice of initial excited nucleus (the term "compound nucleus" is inappropriate here) was motivated by the following considerations. As will be seen from the ensuing analysis, mean fission lifetimes depend greatly on the relationship between the fission-barrier height B_f and the neutron binding energy B_n. As the angular momentum of a ^{190}Pt nucleus changes from 0 to 60, all three cases of this relationship—that is, $B_f > B_n$, $B_f \approx B_n$, and $B_f < B_n$—are realized. Concurrently, the fission probability changes from a few percent to unity. About 10^4 fission trajectories were obtained in each of the calculations quoted below.

The mean fission lifetimes $\langle t_f \rangle(L)$ and the mean prescission-neutron multiplicities $\langle n_{\rm pre} \rangle(L)$ obtained from our calculations are displayed in Fig. 1. The results of the statistical calculation are shown by closed symbols, while the values obtained from a dynamical simulation are represented by open symbols. The solid lines represent the L dependences of the above quantities for fission events where the charge number did not change, while the dotted lines correspond to their counterparts averaged over all fission events, irrespective of how the nucleonic composition changed as the result of emission.

First, one can see from Fig. 1*b* that the solid and dotted lines for mean prescission-neutron multiplicities are virtually coincident over the entire range of L values under study. For mean fission lifetimes in Fig. 1*a*, they are indistinguishable within the range from zero value of the angular momentum to its value corresponding to the mean-fission-lifetime maximum, being significantly different only at high angular momenta. In order to explain qualitatively the unexpected resonance behavior of mean fission lifetimes, it is therefore sufficient to analyze the dependence $\langle t_f\rangle(L)$ for fission events where the charge number of the nucleus involved does not change (that is, solid curves), and we will discuss only such events in this article below.

Second, Fig. 1*a* shows that the dependences $\langle t_f\rangle(L)$ have the same shape for both regimes—the statistical and the dynamical one—differing only quantitatively. The mean-fission-lifetime value calculated dynamically exceeds its statistical counterpart by one to two orders of magnitude. This result is quite natural since dissipation moderates the fission process.

Third, the L dependence of the mean fission lifetime in Fig. 1*a* is nonmonotonic. It first ascends (region n), reaches a maximum (region c), and descends (region f) only at high angular momenta.

Finally, one can see from Fig. 1*b* that the $\langle n_{\text{pre}}\rangle$ values obtained from the dynamical calculation (open boxes) are approximately three times as great as the respective statistical results (closed boxes). This seems to confirm that it is legitimate to employ $\langle n_{\text{pre}}\rangle$ as a "clock" measuring fission lifetimes. However, the statistical values of $\langle n_{\text{pre}}\rangle$ do not show any sign of a resonance behavior, which is inherent in the dynamical values of $\langle n_{\text{pre}}\rangle$ in Fig. 1*b* and in the mean fission lifetimes in Fig. 1*a*. Thus, not only does the inclusion of friction increase the absolute values of $\langle n_{\text{pre}}\rangle$, but this also changes the form of the angular-momentum dependence of this quantity.

The mean value and the variance provide an adequate characterization of a distribution if it is close to a normal distribution. We will now consider the distributions of the quantities whose mean values were the subject of the above discussion.

Figure 2 shows the time distributions of fission events and events involving prescission-neutron emission. In this figure, each histogram is normalized to 100%. There are many panels in Fig. 2, but this ensures the clearest representation of the distributions. The left and right panels display the results of statistical and dynamical calculations, respectively. The first two rows of the panels in the horizontal direction correspond to zero angular momentum; the next two rows and the last two ones represent the results for $L = 40$ and $L = 60$, respectively. These angular-momentum values were chosen in such a way as to demonstrate how the events in the regions n, c, and f in Fig. 1 are distributed in time. For each value of the angular momentum L, the time distribution $f_{n_{\text{pre}}}(t) = \Delta n_{\text{pre}}/(\langle n_{\text{pre}}\rangle \Delta t)$ of events involving prescission-neutron emission is contrasted against the time distribution $f_{N_f}(t) = \Delta N_f/(N_f \Delta t)$ of fission events that was obtained in the same calculation. For $L = 0$ and $L = 40$, the distributions of fission events extend in time one to two orders of magnitude farther. The same is true for the mean values of the corresponding times (they are shown in the histograms by vertical straight lines). Only at $L = 60$ do the distributions $f_{N_f}(t)$ and $f_{n_{\text{pre}}}(t)$ become similar to each other, the mean times taking values on the same order of magnitude. The conclusion suggested by this was already formulated in [6] for the example of ^{235}U fission at $E^* = 80$ MeV: only in some individual cases can one extract mean fission lifetimes from the mean times of neutron emission; in general, data on $\langle n_{\text{pre}}\rangle$ yield the most probable times. This conclusion was drawn long ago in [5] from a

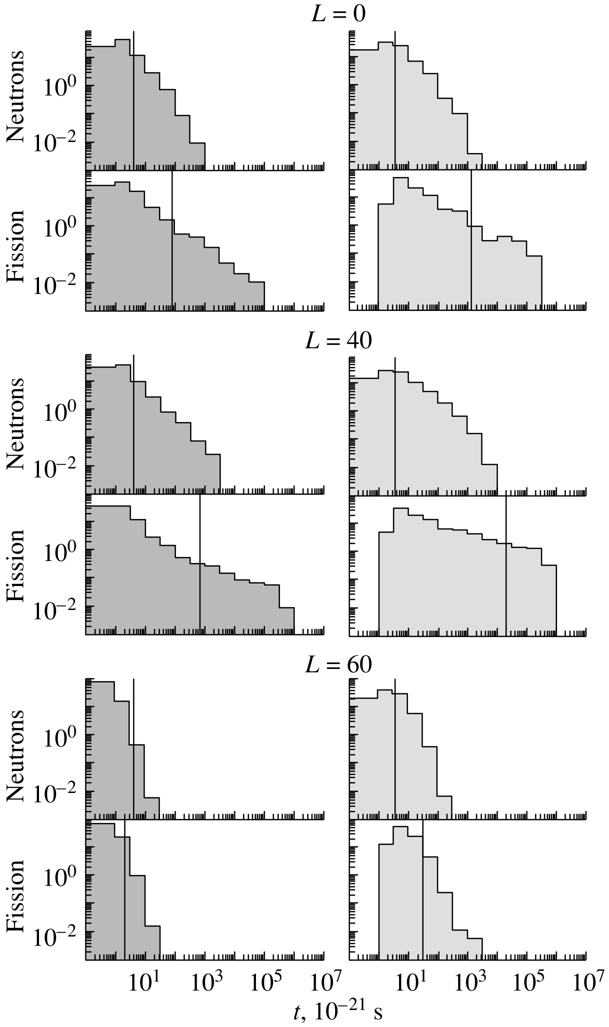

Fig. 2. Time distributions of events involving prescission-neutron emission and of fission events according to our calculations in the (left panels) statistical and (right panels) dynamical modes at $L = 0$, 40, and 60 for ^{190}Pt at $E^*_{\text{init}} = 150$ MeV. The vertical lines indicate the values of the mean fission lifetimes and of the mean times of prescission-neutron emission.

comparison with experimental data, without presenting the distributions $f_{n_{\rm pre}}(t)$ and the calculated mean neutron times.

The distributions in Fig. 2 are highly dissimilar to Gaussian distributions, this especially concerning $f_{N_f}(t)$ at $L = 0$ and 40. The mean fission lifetimes for these distributions are shifted to the region of large values and, as a matter of fact, are determined by long-lived tails, which are the most appropriate object for investigation by the crystal-blocking method (see [20, 21]). Thus, unique information about the shape of $f_{N_f}(t)$ can be obtained by studying, with the aid of prescission neutrons and with the aid of the crystal-blocking method, fission lifetimes of excited nuclei obtained in the same reaction.

In Fig. 2, $f_{N_f}(t)$ has an especially long-lived tail at $L = 40$, this concerning both the statistical and the dynamical results. It is precisely this tail (long-lived fission component according to the terminology adopted in [20–22]) that leads to the emergence of the maximum for $\langle t_f\rangle(L)$ in Fig. 1*a*.

Concluding the discussion of the data in Fig. 2, we note that the dynamical long-lived components in the distributions $f_{N_f}(t)$ are much greater than their statistical counterparts. One can see this at $L = 0$ and $L = 40$ most clearly. This is the way in which friction manifests itself via moderating the fission process.

Let us now consider the distributions of fission events with respect to the number of emitted prefission neutrons (so-called "chances of fission"). They are displayed in Fig. 3. In order to avoid encumbering the figures, we have only given there even chances. As in Fig. 1, closed symbols represent the results of statistical calculations (Fig. 3*a*), while open symbols stand for the results obtained from a dynamical simulation (Fig. 3*b*). For each mode, we present the distributions in question for the angular-momentum values of $L = 0$, 40, and 60.

The distributions obtained from the statistical calculation (Fig. 3*a*) have nothing in common with Gaussian distributions: for each chance, the fission probability is lower than that for the preceding chance. This is not so only at $L = 40$, in which case the fission probabilities at $n_{\rm pre} = 8$, 10, and 12 take approximately the same value. This "multichance tail" of the distribution does not affect $\langle n_{\rm pre}\rangle$: partial fission probabilities are as low as 2% at high values of $n_{\rm pre}$, and emission-free (first-chance) fission is dominant at all values of L. Moreover, the fraction of events involving first-chance fission increases monotonically with increasing L. It is precisely this circumstance that leads to a monotonically descending character of the dependence $\langle n_{\rm pre}\rangle(L)$ in Fig. 1*b*.

The distributions obtained from a dynamical simulation have a totally different shape (see Fig. 3*b*). The moderating effect of friction leads to an almost complete disappearance of emission-free fission, with the result that the distributions in question become closer in shape to conventional Gaussian distributions. Also, the maximum of $\langle n_{\rm pre}\rangle(L)$ in Fig. 1*b* becomes understandable: at $L = 40$, the distribution in Fig. 3*b* develops a pronounced "shoulder" for $n_{\rm pre} = 8$ and 10. For such a multichance fission, the fission probability is very high in the case being considered: it is about 15%.

Completing our discussion of the data in Fig. 3, we would like to emphasize that the tail in the distribution for the static regime and the shoulder in the distribution for the dynamical regime arise at the same value of $L = 40$, which is the value at which mean fission lifetimes develop maxima in Fig. 1*a*. Postponing a detailed discussion on this correlation until the next section, we will now address the problem of assessing the degree to which the mean fission lifetime is close to the characteristic fission lifetime, which can be extracted from the mean multiplicity of prescission neutrons.

In order to answer this question, we consider the data in Fig. 4. This figure displays the same fission lifetimes as in Fig. 1*a* (circles). They are contrasted against (squares) the characteristic fission lifetimes that were obtained by multiplying the mean times of prescission-neutron emission (see the vertical lines in Fig. 2) by the mean multiplicities of prescission neutrons. As always, the results of the statistical and dynamical calculations are represented by, respectively, closed and open symbols. The characteristic fission lifetimes found with the aid of mean prescission-neutron multiplicities are shown by boxes; they are seen to be much shorter than the mean fission lifetimes (circles) both in the statistical and in the dynamical calculation. This distinction is maximal at $L \approx 40$, reaching three orders of magnitude in the region of the peak of $\langle t_f\rangle(L)$ in Fig. 4*b*. Only in the range of L between about 50 and 60 do the characteristic fission lifetimes approach the mean fission lifetimes.

Preliminary conclusions of our present consideration can be summarized as follows. Mean fission lifetimes calculated at various values of the angular momentum of ^{190}Pt at an initial excitation energy of 150 MeV reveal an unexpected maximum at $L \approx 40$. This maximum appears both in the statistical and in the dynamical calculation. The presence of a pronounced long-lived component in the time distributions of fission events corresponds to it. The observable $\langle n_{\rm pre}\rangle$, which is used more extensively, behaves differently in the statistical and in the dynamical calculation as a function of the angular momentum: as

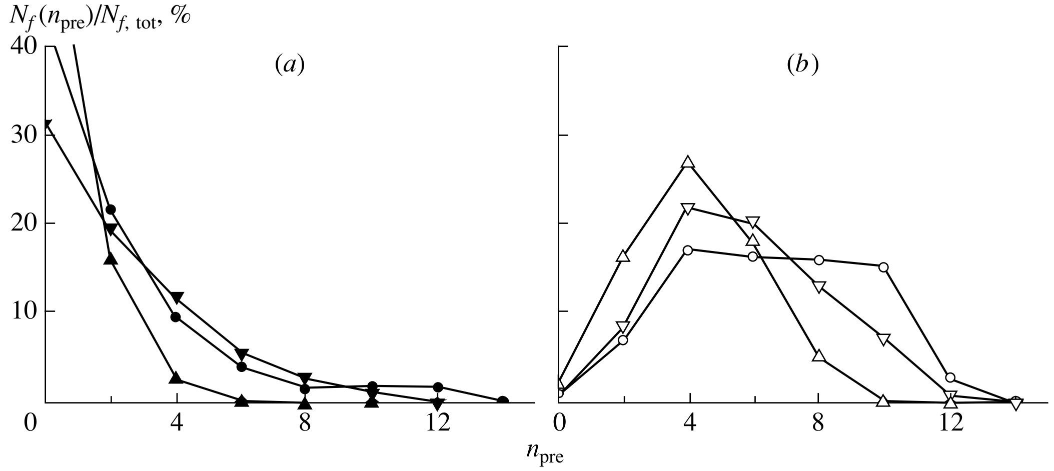

Fig. 3. Distributions of fission events with respect to the number of emitted prescission neutrons according to the calculations in the (a) statistical and (b) dynamical modes at the angular-momentum values of $L =$ (closed and open inverted triangles) 0, (closed and open circles) 40, and (closed and open triangles) 60 for ^{190}Pt at $E^*_{\text{init}} = 150$ MeV.

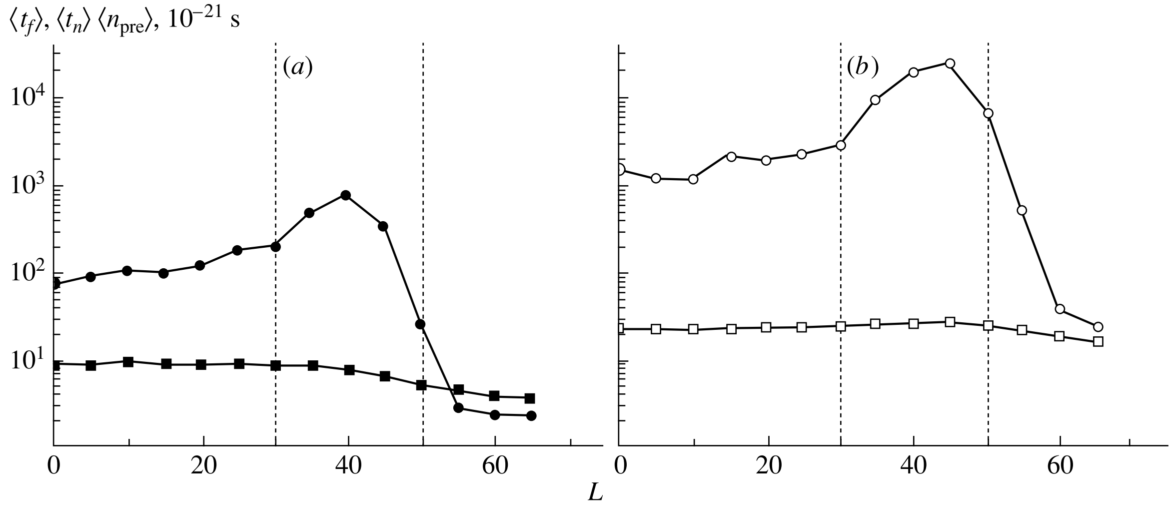

Fig. 4. Angular-momentum dependences of (closed and open circles) mean fission lifetimes and (closed and open boxes) characteristic fission lifetimes obtained by multiplying the mean time of prescission-neutron emission by the mean prescission-neutron multiplicity for ^{190}Pt at $E^*_{\text{init}} = 150$ MeV. The calculations were performed in the (a) statistical and (b) dynamical modes.

the angular momentum increases, it decreases monotonically in the former case and reveals a maximum at $L \approx 40$ in the latter case. The time distributions of events involving prescission-neutron emission are concentrated within a much shorter time interval than the time distributions of fission events.

These results are of interest in their own right and call for experimental tests. We emphasize that even the generally accepted statistical model predicts mean fission lifetimes $\langle t_f\rangle(L)$ having a maximum at $L \approx 40$ and the presence of a significant long-lived component of fission. This prediction does not change qualitatively upon taking into account the dynamics of the fission process, but its quantitative effect may be very large. We think that the potential of present-day experiments is sufficient for verifying this theoretical prediction. But the problem is that a direct measurement of fission lifetimes of highly excited nuclei by the crystal-blocking technique is not thought to be interesting for some reason.

4. ANALYSIS OF THE RESULTS

On the basis of general considerations, we know that the rate of fission of an excited system depends on its excitation energy, on the height of the fission barrier, and on the viscosity of nuclear matter. The higher the excitation energy, the higher the rate at which the system decays and, accordingly, the shorter the decay time. The higher the fission barrier and (or) the higher the viscosity, the lower the decay rate and the longer the decay time (here, we do not discuss the mode of anomalously low viscosity [23], in which case the fission rate is proportional to the coefficient of friction).

Guided by these general ideas, one could expect that, with increasing angular momentum, mean fission lifetimes would decrease because of the decrease in the fission-barrier height B_f. However, the results presented in the preceding section are at odds with this expectation, raising some questions. We begin by explaining why mean fission times displayed in Fig. 1*a* versus the angular momentum of the nucleus undergoing fission reach a maximum.

4.1. Statistical Calculations

Since the mean fission lifetimes obtained from dynamical and statistical calculations behave similarly in Fig. 1*a* and since it is easier to analyze the behavior of the lifetimes following from statistical calculations, we begin by considering precisely this case. Naturally, such an analysis must rely on the decay widths for the corresponding channels. They determine the one-step decay time τ_{dec}, which characterizes one competition event. It takes the same value for all channels, admitting an approximate representation $\tau_{\text{dec}} = \hbar/(\Gamma_f + \Gamma_n)$ since the remaining widths (Γ_p, Γ_d, Γ_γ, Γ_α) are negligible in the case being considered.

The widths in which we are interested are shown in Fig. 5. The neutron, fission, and total widths are represented by boxes, circles, and diamonds, respectively. As everywhere above, the results of the statistical and dynamical calculations are represented by, respectively, closed and open symbols. As to the neutron widths, they are identical in both regimes and were calculated in the Weisskopf–Ewing approximation. The statistical fission widths were calculated by the Bohr–Wheeler formula. As the dynamical fission widths, we displayed quasistationary widths obtained on the basis of a modified Kramers formula, which differs from the Bohr–Wheeler formula by the presence of a factor dependent on the friction parameter (the corresponding formulas are given, for example, in the review articles of Gontchar [5] and Fröbrich and Gontchar [10]).

We have already seen in Fig. 3 that our calculations involve emission fission, sometimes after the emission of 8 to 12 neutrons. In Fig. 5, we therefore show not only the widths for the primary nucleus ^{190}Pt at the initial excitation energy of $E^*_{\text{init}} = 150$ MeV (Figs. 5*a*, 5*b*) but also those for ^{186}Pt at $E^* = 110$ MeV (Figs. 5*c*, 5*d*), ^{182}Pt at $E^* = 70$ MeV (Figs. 5*e*, 5*f*), and ^{178}Pt at $E^* = 30$ MeV (Figs. 5*g*, 5*h*). The partition into the segments n, c, and f is identical here to that in Fig. 1.

With increasing L, the neutron widths decrease in all cases. Qualitatively, this is explained by the fact that the rotational component of the effective potential energy increases, which leads to a decrease in the internal excitation energies. On the contrary, the fission widths increase with increasing L. The reason is that the fission barrier becomes lower. The total widths depend on L rather weakly; however, they decrease fast as one goes over from ^{190}Pt to ^{186}Pt and further to ^{178}Pt. This effect is due to the fact that each emitted neutron carries away about 10 MeV of energy rather than due to the change in the nucleonic composition as such. Accordingly, the internal excitation energy E^* at which fission occurs becomes markedly less than its initial value E^*_{init}. Thus, a key to understanding the dependence $\langle t_f\rangle(L)$ in Fig. 1*a* must be sought in the distribution of fission events with respect to the number of emitted prescission neutrons (see Fig. 3).

Figure 5 (left panels) shows that the fission width is much less than the neutron width within the segment n, but that, on the contrary, $\Gamma_f > \Gamma_n$ within the segment f. Such relationships between the widths are determined by the neutron binding energy B_n and the fission-barrier height B_f: in our case, we have $B_f > B_n$ within the segment n and $B_f < B_n$ within the segment f.

For $L < 30$—that is, within the segment n—we have $\Gamma_f \ll \Gamma_n$, so that the one-step decay time is $\tau_{\text{dec}} \approx \hbar/\Gamma_n$. Thus, it is the neutron width (and not the fission one) that determines the time of decay (through the fission channel inclusive) at low angular momenta. The fission probability at each cascade step, $\Pi_f \approx \Gamma_f/\Gamma_n$, is low in this case, but it increases with increasing angular momentum. Owing to this, the emission-fission probability also increases. It is this circumstance that explains the slow increase in the mean fission lifetime for $L < 30$ in Fig. 1*a*. In other words, the behavior of $\langle t_f\rangle(L)$ reflects the inclusion of higher fission chances when this occurs at lower values of E^*. It turns out that the decrease in B_f owing to an increase in L at fixed A leads to a decrease in E^* at the instant of fission owing to an increase in the emission-fission probability.

For $L > 50$—that is, within the segment f—$\Gamma_f > \Gamma_n$ (see Fig. 5). Accordingly, the one-step decay time is $\tau_{\text{dec}} \approx \hbar/\Gamma_f$. It is precisely the case in which the behavior of the mean fission time in Fig. 1*a* is identical to that which was expected on the basis of the most general considerations: as the fission barrier becomes lower, $\langle t_f\rangle(L)$ decreases. However, the decrease in

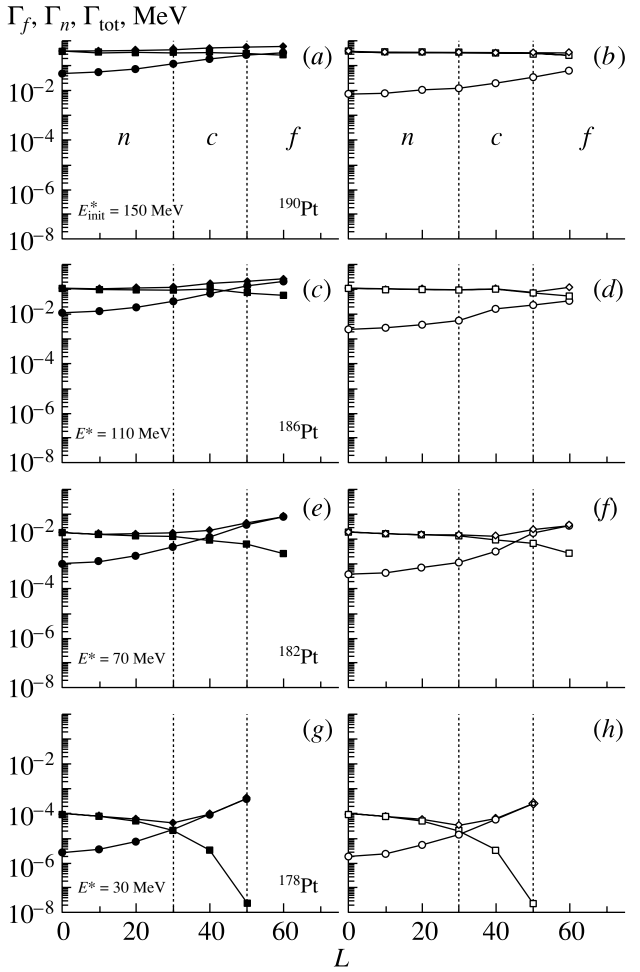

Fig. 5. Angular momentum dependences of the (boxes) neutron, (circles) fission, and (diamonds) total widths according to the calculations in the (left panels) statistical and (right panels) dynamical modes for ^{190}Pt at $E^*_{\text{init}} = 150$ MeV, ^{186}Pt at $E^* = 110$ MeV, ^{182}Pt at $E^* = 70$ MeV, and ^{178}Pt at $E^* = 30$ MeV.

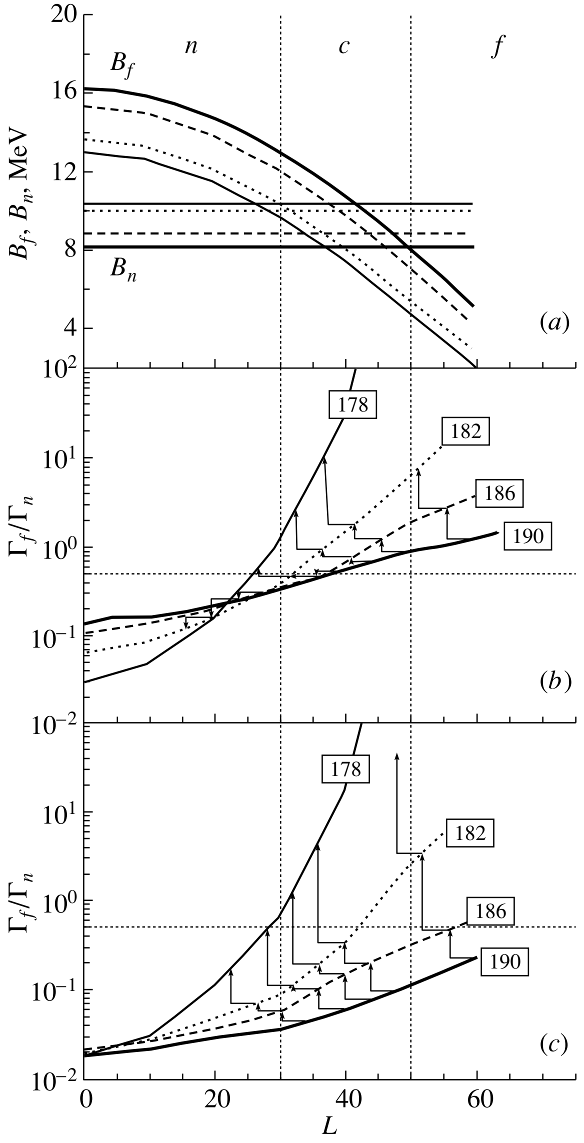

Fig. 6. Angular-momentum dependences of (a) the neutron binding energy B_n and the fission-barrier height B_f and (b, c) the ratio of the fission width Γ_f to the neutron width Γ_n for (thick solid curves) ^{190}Pt, (dashed curves) ^{186}Pt, (dotted curves) ^{182}Pt, and (thin solid curves) ^{178}Pt. The excitation energies of the various isotopes are identical to those in Fig. 5. The fission widths were calculated by (b) the statistical Bohr–Wheeler formula and (c) a modified Kramers formula with allowance for dissipation.

the one-step decay time is not the only (or even the main) reason for this. The main effect here is that the emission-fission probability decreases—that is, high chances become inoperative (see Fig. 3).

It is clear that, at intermediate values of the angular momentum, $30 < L < 50$ (segment c in Figs. 1 and 5), a slow increase in $\langle t_f \rangle(L)$ is expected to give way to a decrease. Instead, the mean fission lifetimes increase sharply, revealing some kind of resonance behavior. This is because the values of B_f and B_n approach each other, and so therefore do the neutron and fission widths. The latter have already been seen in Fig. 5 as well.

In order to obtain deeper insight into this resonance behavior of the mean fission lifetimes, we present, in Fig. 6, the angular-momentum dependences of the fission-barrier heights and of the neutron-binding energies, as well as of the ratios Γ_f/Γ_n. The partition into the segments n, c, and f here is identical to that above. As in Fig. 5, four curves are given for each quantity. They correspond to four platinum isotopes undergoing fission in the course of competition with neutron emission.

Let us consider Fig. 6b. The neutron-emission process is indicated there by the arrows. In our model, each neutron carries away an angular momentum of unity. In order to find, for example, that point on the curve for ^{186}Pt at which the primary nucleus ^{190}Pt will occur after the emission of four neutrons, one must therefore move first to the left by four units along the angular momentum axis and then upward or downward up to the intersection with the curve representing the ratio Γ_f/Γ_n for ^{186}Pt.

From Fig. 6*b*, one can see that, within the segment *c*, the ratio Γ_f/Γ_n for the primary isotope ^{190}Pt is close to unity. If, at the same time, it had an angular momentum of about 40, the ratio Γ_f/Γ_n for it would undergo virtually no changes upon the emission of eight or even twelve neutrons. In view of this, the nucleus in question may undergo fission with a sizable probability after emitting a large number of neutrons and, hence, after losing a considerable part of the initial excitation energy. It is this circumstance that determines the "resonance" value of the angular momentum L. Since the one-step decay time increases exponentially with decreasing excitation energy, even a small fraction of such "cold"-fission events has a strong effect on mean fission lifetimes.

Thus, we have qualitatively explained why, in the statistical calculation, the mean fission lifetime as a function of angular momentum has a distinct maximum in Fig. 1*a*: an approximate equality of Γ_f and Γ_n and a slow variation of Γ_f/Γ_n are responsible for this. Under these two conditions, there arises a strong competition between neutron emission and fission, with the result that higher chances of fission of a nucleus whose initial excitation was rather high come into play, so that it can therefore undergo cold fission. We have also been able to disclose factors that determine the resonance value of L. This is some kind of a bifurcation point, and a value of $\Gamma_f/\Gamma_n \approx 0.5$ for the primary nucleus corresponds to it. For $\Gamma_f/\Gamma_n < 0.5$ (see Fig. 6*b*), neutron emission leads to a substantial decrease in the partial fission probability (the arrows beginning on the curve for ^{190}Pt at $L = 28$ lead downward). Owing to this, high-chance fission becomes less probable, while the mean fission lifetimes become shorter than at the maximum of $\langle t_f\rangle(L)$.

If $\Gamma_f/\Gamma_n > 1$ for the primary isotope, then neutron emission leads to a sharp increase in the partial fission probability (the arrows beginning on the curve for ^{190}Pt at $L = 60$ lead sharply upward). In view of this, high-chance fission becomes impossible, while the mean fission lifetimes become much shorter than at the maximum of $\langle t_f\rangle(L)$.

The ratio Γ_f/Γ_n can be roughly estimated on the basis of the formula $\Gamma_f/\Gamma_n \approx \exp[(B_n - B_f)/T]$, according to which the equality of the widths and a strong competition between the channels must arise when the fission-barrier height B_f is equal to the neutron binding energy B_n [20]. A comparison of the data in Figs. 6*a* and 6*b* reveals that this equality is not precise even in a statistical calculation. The resulting distinction is due to the use of a deformation-dependent single-particle-level-density parameter in our calculations. With allowance for this circumstance, the equality of the widths reduces to the equality of the entropies in the fission and neutron channels; that is,

$$\Gamma_f/\Gamma_n \approx \exp\left\{2\sqrt{a_{\mathrm{qs}}(E^* - B_n)} - 2\sqrt{a_{\mathrm{sd}}(E^* - B_f)}\right\}. \qquad (5)$$

Nonetheless, arguments based on the relationship between the quantities B_n and B_f can still be helpful in qualitatively predicting the evolution of $\langle t_f\rangle(L)$.

4.2. Dynamical Calculations

The regularities found for the mean fission lifetimes obtained from statistical calculations are qualitatively preserved to a considerable extent for their counterparts deduced from a dynamical simulation. The quantitative difference for fission lifetimes and prescission-neutron multiplicities is significant (see Fig. 1*a*), but it is quite understandable. The main distinction between a dynamical and a statistical calculation is associated with the inclusion of dissipation in the former. The fission process then proceeds more slowly—in particular, the quasistationary fission width at the same values of A, L, and E^* is much less that its statistical counterpart (see Fig. 5). Naturally, this delay hinders nuclear fission without neutron emission (there is virtually no first-chance fission in Fig. 3*b*). At the same time, the partial probability of fission after the emission of a large number of neutrons increases. Owing to this, the nucleus involved becomes cooler, with the result that the mean fission lifetimes prove to be much longer in the dynamical than in the statistical calculation.

From Fig. 1*a*, one can see that the dependence $\langle t_f\rangle(L)$ obtained from a dynamical simulation develops a maximum at $L \approx 45$. At the same value of the angular momentum, there also arises a maximum in the dependence $\langle n_{\mathrm{pre}}\rangle(L)$ in Fig. 1*b*.

In order to obtain deeper insight into the mechanism responsible for the emergence of these maxima, we will consider the data in Fig. 6*c*, which is similar to Fig. 6*b*. As before, the arrows indicate the evolution of Γ_f/Γ_n due to neutron emission. By way of example, we indicate that, as neutrons are emitted from a ^{190}Pt nucleus having the angular momentum of $L = 40$, the width ratio changes from 0.06 to 0.1 up to ^{182}Pt. On

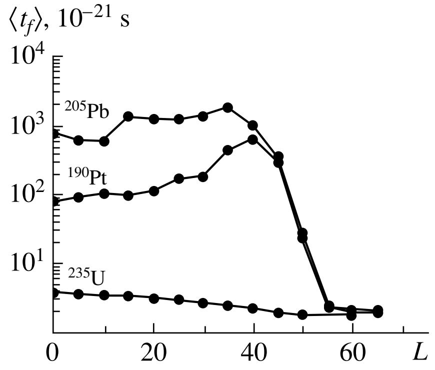

Fig. 7. Dependences $\langle t_f\rangle(L)$ for ^{205}Pb, ^{190}Pt, and ^{235}U at $E^*_{\rm init} = 150$ MeV according to calculations in the statistical mode.

the other hand, it increases up to 0.5 upon going over from this isotope to ^{178}Pt. It is this circumstance that leads to the appearance of a pronounced long-lived component in the time distribution of fission events in Fig. 2 (see the distribution of fission events that was obtained from a dynamical calculation at $L = 40$). This component owes its existence to fission after the emission of eight to twelve neutrons (see Fig. 3*b*).

Having analyzed the results of both statistical and dynamical calculations, we arrive at the conclusion that an approximate equality of the neutron and fission widths at the last stages of the cascade is a general condition for the emergence of a peak in the dependence $\langle t_f\rangle(L)$. A slow variation of Γ_f/Γ_n in the course of neutron emission at the first stages of the cascade must precede fulfillment of this condition. As to the condition of an approximate equality of the neutron and fission widths for a primary excited nucleus, it is of secondary importance and is not necessary.

5. RESULTS OF ADDITIONAL CALCULATIONS

The above consideration raises the question of whether a "resonance" behavior of mean fission lifetimes versus the angular momentum is a general phenomenon. Further, there arises the question of specifying the situations in which it is natural to expect this phenomenon and the situations in which it cannot occur. The analysis performed in the preceding section makes it possible to give an answer to these questions at a semiquantitative level.

For nuclei where the fission-barrier height at zero angular momentum is greater than the neutron binding energy, $B_{f0} > B_n$, the dependence $\langle t_f\rangle(L)$ must have a resonance shape, as in Figs. 1*a* and 1*b*. For nuclei where $B_{f0} \approx B_n$, mean fission times must first increase moderately with increasing angular momentum and then decrease sharply (it can be said that there remains only a right half of the peak). For nuclei where $B_{f0} < B_n$, mean fission times are expected to decrease monotonically with increasing angular momentum. Upon taking friction into account, this pattern is shifted entirely toward higher angular-momentum values.

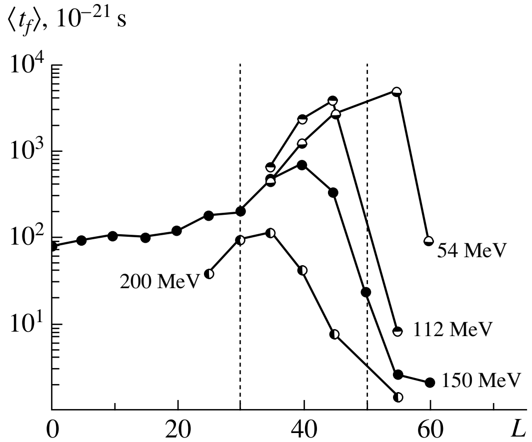

Fig. 8. Mean fission time as a function of the angular momentum for ^{190}Pt at the initial-excitation-energy values of $E^*_{\rm init} = 54$, 112, 150, and 200 MeV (statistical calculation).

In order to verify these predictions, we have calculated $\langle t_f\rangle(L)$ for ^{205}Pb ($B_{f0} = 12.78$ MeV, $B_n = 5.83$ MeV) and ^{235}U ($B_{f0} = 4.89$ MeV, $B_n = 5.33$ MeV) at $E^*_{\rm init} = 150$ MeV in the statistical mode. The results of these calculations are displayed in Fig. 7. Also given there for the sake of comparison is the dependence $\langle t_f\rangle(L)$ that was obtained for ^{190}Pt ($B_{f0} = 16.23$ MeV, $B_n = 8.16$ MeV) and which was already shown in Fig. 1*a*.

For uranium, $B_{f0} < B_n$; in the course of neutron emission, B_f decreases, while B_n increases. Since, in addition, B_f decreases with increasing L, the situation where the fission-barrier height is equal to the neutron-binding energy cannot arise here. For this reason, the respective mean fission lifetime in Fig. 7 decreases monotonically with increasing angular momentum. The mean fission lifetimes themselves prove to be very short; they are close to characteristic times that are extracted from mean multiplicities of prescission neutrons. However, this result is valid only in the case of a statistical calculation—the presence of friction can change the situation drastically (for a detailed discussion of this issue, the interested reader is referred to [22]).

Let us now proceed to discuss the results for ^{205}Pb. We chose this nuclear species because the mean fission lifetimes for it were measured by the crystal-blocking technique at GANIL [8]. For it,

B_{f0} is much less than that for platinum, although the condition $B_{f0} > B_n$ is satisfied. It seems that the fission process must proceed faster in the case of a lower barrier. However, this is so only in the absence of the competing neutron-emission channel. For ^{205}Pb at $L = 0$, we have $B_{f0} - B_n \approx 5$ MeV even after the emission of a single neutron, while, for ^{190}Pt, $B_{f0} - B_n \approx 8$ MeV. Therefore, the neutron and the fission channel compete more strongly for ^{205}Pb than for ^{190}Pt. Accordingly, the mean fission lifetimes for lead prove to be very long, and the peak in the dependence $\langle t_f \rangle(L)$ for it is very broad and is less distinct than that for platinum.

We will now address the question of how the resonance behavior of $\langle t_f \rangle(L)$ changes in response to a change in the excitation energy of the primary nucleus. For this purpose, we have performed statistical calculations for ^{190}Pt at $E^*_{\text{init}} = 200$, 112, and 54 MeV. The dependences obtained from these calculations are displayed in Fig. 8, along with our main curve representing $\langle t_f \rangle(L)$ at $E^*_{\text{init}} = 150$ MeV. From this figure, it can be seen that the resonance behavior of $\langle t_f \rangle(L)$ is observed for all energy values at which the calculations were performed. With increasing E^*_{init}, the height of the peak of $\langle t_f \rangle(L)$ decreases: an increase in the excitation energy enhances the decay process. The evolution of the height and the position of the maximum in response to a change in the excitation energy will be discussed in a separate publication.

6. STATISTICAL UNCERTAINTIES OF THE SIMULATION

In our model, we use stochastic equations and the Monte Carlo method. Therefore, values that we obtain from the calculations (simulation) suffer from statistical fluctuations. In view of this, it is necessary to estimate the statistical uncertainties in calculating observables. The commonly known formulas for the relative statistical uncertainties in the mean values $\langle y \rangle$ and in the variances $\langle \sigma_y^2 \rangle$ of a random variable y (see, for example, [24]),

$$\varepsilon_{\langle y \rangle} = \frac{\sigma_y}{\langle y \rangle \sqrt{N}}, \tag{6a}$$

$$\varepsilon_{\sigma_y^2} = \sqrt{\frac{8}{N}}, \tag{6b}$$

where N is the number of events, are applicable only to random variables whose distributions are Gaussian or are close to a Gaussian distribution. The time distributions of fission events (see Fig. 2) have nothing in common with Gaussian distributions. The same is true for the results obtained from statistical calculations for the distributions of fission events with respect to the number of emitted neutrons (see Fig. 3*a*). In view of this, it seems rather difficult to derive, for a statistical calculation, analytic estimates of the statistical uncertainties in mean fission lifetimes and in mean prescission-neutron multiplicities.

In order to sidestep this difficulty, we performed several times the same dynamical calculation, changing the time step of the simulation, Δt. The results obtained in this way for the Δt dependences of some observables are given in Fig. 9. As a representative set for this figure, we chose mean fission lifetimes (Fig. 9*a*), the fission probabilities P_f (Fig. 9*b*), and the mean prescission-neutron multiplicities $\langle n_{\text{pre}} \rangle$ (Fig. 9*c*), the last two quantities being well known from the literature (see, for example, [1, 4, 5, 10]). The horizontal lines indicate the values obtained for the corresponding quantities upon averaging them over the simulation step in the range (0.009–0.040) × 10^{-21} s. Within this range of Δt values, none of the three quantities being considered is a function of the simulation step, all of them only undergoing statistical fluctuations. From Fig. 9, one can see that these fluctuations are about 20% for the mean fission lifetimes and that they are much smaller for the fission probabilities and mean prescission-neutron multiplicities.

Since the mean fission lifetimes, P_f, and $\langle n_{\text{pre}} \rangle$ feature no functional dependence on the simulation step, an attempt can be made to treat values obtained for these observables at different Δt as a series of results of direct measurements:

$$\varepsilon_y = \Delta y / \langle y \rangle. \tag{7}$$

Here, the mean value $\langle y \rangle$ and the absolute error Δy of n "direct measurements" are calculated by the standard formulas

$$\langle y \rangle = \frac{1}{n} \sum_{i=1}^{n} y_i, \quad \Delta y = \left[\frac{1}{n-1} \sum_{i=1}^{n} (y_i - \langle y \rangle)^2 \right]^{1/2}. \tag{8}$$

In order to verify whether this approach is appropriate, we have calculated the errors ε_{P_f} in the fission probabilities and the errors $\varepsilon_{\langle n_{\text{pre}} \rangle}$ in the mean prescission-neutron multiplicity by two methods. The first method consists in employing formula (6a) to calculate $\varepsilon_{\langle n_{\text{pre}} \rangle}$ and the obvious formula $\varepsilon_{P_f} = 1/\sqrt{N}$ to calculate ε_{P_f}. The second method consists in using formulas (7) and (8) for the results of the above "direct measurements." Since, in a dynamical calculation, the distribution of events with respect to the number of emitted neutrons is close to a Gaussian distribution (see Fig. 3*b*), it is quite legitimate to use formula (6a) to calculate $\varepsilon_{\langle n_{\rm pre}\rangle}$.

The error values obtained by these two methods were in agreement and were 1% for P_f and 0.4% for $\langle n_{\rm pre}\rangle$ in the case of 10^4 fission events. On this basis, we estimated the statistical error in the mean fission lifetimes, for which formulas (6) are inapplicable, as the errors of the direct measurements—that is, by formulas (7) and (8). It turned out that, in the case being considered, $\varepsilon_{\langle t_f\rangle} = 12\%$; that is, the mean fission lifetime is a quantity that suffers from fluctuations much more considerably than P_f and $\langle n_{\rm pre}\rangle$, which are studied traditionally.

7. COMPARISON WITH OTHER STUDIES

Our study has some drawbacks. For example, we performed our calculations on the basis of a one-dimensional version, despite the fact that, within the last three to seven years, there appeared a large number of theoretical studies where the combined dynamical–statistical model [9, 11] was generalized to the case of two [25, 26] or three [27, 28] degrees of freedom of a nucleus undergoing fission. Such a generalization is a considerable advancement toward obtaining deeper insights into the fission process. For example, it enables one to calculate the mass–energy distribution of fission fragments, this being impossible in principle within the combined dynamical–statistical model, which is one-dimensional.

We deliberately employed the simplest one-dimensional version of the model for the following reasons. First, the machine time required for performing calculations based on full Langevin equations increases fast with increasing number of degrees of freedom that are taken into account. The volume of calculations that must be performed to find out how the mean fission lifetime depends on the angular momentum is extremely large. The reason is that the statistical errors in mean fission lifetimes obtained from a Monte Carlo simulation are an order of magnitude greater than the errors in fission probabilities. Second, the problem of the angular-momentum dependence of the mean fission lifetime, $\langle t_f\rangle(L)$, has not yet received adequate theoretical study. Therefore, even a derivation of basic regularities is a significant advancement here; as to the details, they can be further refined. We note that, as a matter of fact, we obtain the total distributions of fission events with respect to fission times—that is, this information is much wider than the set of mean-fission-lifetime values. In performing multidimensional calculations for such complicated distributions from the outset—that is, without having any idea of evolution in response to variations in L—one can go astray. Anyway, we are unaware of theoretical studies where mean fission lifetimes and time distributions of fission events were studied systematically, at least within a statistical model.

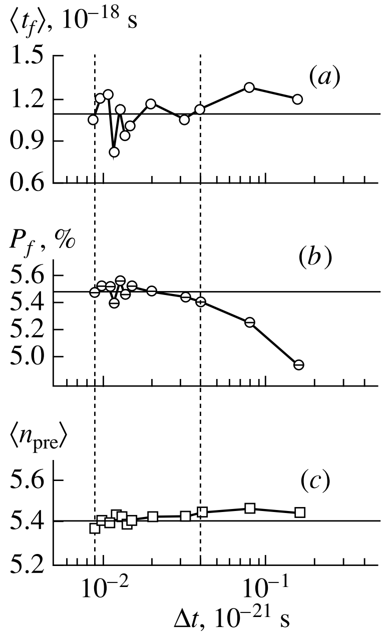

Fig. 9. Dependences of the mean fission lifetimes $\langle t_f\rangle$, the fission probabilities P_f, and the mean prescission-neutron multiplicities $\langle n_{\rm pre}\rangle$ on the dynamical-simulation step. For these quantities, the horizontal lines indicate the values averaged over the simulation step in the range $(0.009\text{–}0.040) \times 10^{-21}$ s. The calculations were performed for a ^{190}Pt nucleus at $E^*_{\rm init} = 150$ MeV in the dynamical mode.

Yet another drawback of our study is that it disregards shell corrections to the entropy. Of course, they can be safely disregarded for a nucleus whose initial excitation energy is 150 MeV. However, the excitation energy of a nucleus that undergoes fission after the emission of eight to twelve neutrons (multichance fission) sometimes becomes as low as 20 or 30 MeV, in which case shell corrections can play a significant role. Their inclusion in dynamical calculations is the subject of future investigations. However, we conjecture that the main features in the dependence $\langle t_f\rangle(L)$ that were found on the basis of the one-dimensional macroscopic model in the CDSM version will survive upon taking into account multidimensional and microscopic effects.

The problem of the time distributions of fission events has a long and complicated history. As far back as the 1980s, the authors of [20, 21] reported on measurements of the fission lifetimes of compound nuclei in the mercury–francium region that were obtained in reactions of complete heavy-ion fusion and which were characterized by initial excitation energies in the range $E^*_{\rm init} = 40$–80 MeV. In those experiments, performed by means of the crystal-blocking technique, $Z = 6$–9 nuclei were used as projectiles. The authors of those articles concluded, among other things, that there exists a long-lived fission component characterized by the fraction χ_L of fission events that corresponds to times in excess of some value t_L. It is determined by special features of an experiment and was set to 10^{-16} or 3×10^{-17} s in the studies being discussed.

The appearance of the long-lived component was explained in [20] by fission events that arise at the last stage of the evaporation cascade, where $B_f \approx B_n$. In [21], the magnitude and the projectile-energy dependence of the quantity χ_L was described on the basis of the statistical model that takes into account shell corrections and pairing effects. In the calculations performed in [29], it was shown, however, that macroscopic statistical effects—namely, the equality of the fission-barrier height and the neutron-binding energy—play a decisive role in the emergence of the long-lived fission component. The results of those calculations were in fairly good agreement with experimental data reported in [20, 21] (see Table 1 in the review article of Gontchar [5]).

Unfortunately, the results reported in [20, 21] were neither confirmed nor disproved in the literature. However, the filling of the blocking minimum could be rather strongly affected, as was justifiably indicated in [7], by neutron emission from fission fragments if the speed of compound nuclei was modest. It seems that this effect was disregarded by the authors of [20, 21] in processing primary experimental data.

Measurements of fission lifetimes by means of the crystal-blocking technique were resumed at GANIL after a lapse of many years. Those studies were based on the use of high-mass-transfer reactions and inverse kinematics, and their results were partly published in [7]; there, the dependence of mean fission lifetimes on the initial excitation energy $E^*_{\rm init}$ was explored for excited uranium nuclei. The fact that the angular momentum of the nucleus undergoing fission was rather poorly known in that experiment gave a primary impetus to our present investigation. We were able to reveal (see Fig. 7) that, for uranium, the dependence $\langle t_f \rangle(L)$ is rather weak, so that an uncertainty in the value of L is not expected to affect the results reported in [7].

The calculation of mean fission lifetimes that was aimed at a comparison with those experimental data was performed in [6] on the basis of the two-dimensional version of our model (a detailed description of this version, also known as CDSM2, was given in [25]). The experimental value of the mean fission lifetime for ^{235}U ($E^*_{\rm init} = 80$ MeV), 5×10^{-18} s, was reproduced in that calculation by using a reduced one-body dissipation and a level-density parameter depending on the deformation much more weakly than that in the present study above.

In [27, 28], where the authors generalized the combined dynamical–statistical model to the case of three degrees of freedom, one can find the results of respective calculations for mean fission lifetimes. In [27], where use was made of the total one-body viscosity, the calculated value of this quantity was 305×10^{-21} s^{-1} for the (99 MeV) ^{12}C + ^{194}Pt reaction leading to the formation of ^{206}Po at $E^*_{\rm init} = 76.6$ MeV. It is difficult to compare this result directly with one of the results obtained in the present study: a fusion reaction produces a broad distribution with respect to angular momenta, while fission events occur predominantly at L values such that $B_f > B_n$. However, about 10 to 20% of long-lived fission events occurring within 3×10^{-17} s or even within longer times were experimentally revealed in [21] for the similar (90–110 MeV) ^{19}F + ^{173}Ta reaction leading to the formation of ^{200}Pb at initial excitation energies in the range $E^*_{\rm init} = 57$–76 MeV. The statistical calculations (that is, calculations that disregard friction) that were performed in [21] reproduced that experimental result. For the above fraction of long-lived fission events, mean fission times must also be about 10^{-17} s. It is rather strange that the result of the calculation in [27], where friction was taken into account, was two orders of magnitude less.

At GANIL, Morjean and his colleagues [8], who used the crystal-blocking technique, measured mean fission lifetimes for lead nuclei that had rather low angular momenta and excitation energies in the range 150–400 MeV. The resulting values of $\langle t_f \rangle$ at $E^*_{\rm init} = 150$ MeV proved to be within the range $(6$–$20) \times 10^{-19}$ s. Our results for ^{205}Pb fall within this range (see Fig. 7). Of course, this agreement is accidental, since friction is completely ignored in our calculation. However, the fact that the mean fission lifetime obtained from our calculation is on the same order of magnitude as the experimental value deserves particular attention.

Here, we approach most closely the third drawback of our study—the absence of a direct comparison with experimental data. This is due to the following two factors. First, our present investigation was not aimed at reproducing available experimental data or at making predictions for specific experiments. Our objective was to find out how mean fission lifetimes must depend on a parameter that controls the relationship between the neutron and the fission width. The angular momentum of a fissile nucleus can play the role of such a parameter, and we considered here

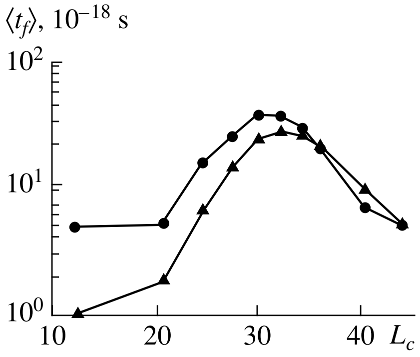

Fig. 10. Mean fission lifetime as a function of the critical angular momentum L_c according to calculations performed in the statistical mode for the fusion reaction ^{19}F + ^{181}Ta $\rightarrow$ ^{200}Pb at projectile energies in the range between 86 and 110 MeV: (closed circles) mean fission times obtained with the angular-momentum distribution of compound nuclei that was calculated according to formulas (45)–(49) from [5] and (closed triangles) respective results found with the L_c value from the preceding calculation and with $\delta L = 0.1$.

the angular-momentum dependence of mean fission times.

Second, there are simply no experimental data on the angular-momentum dependence of mean fission lifetimes in the literature. Such data could be obtained by measuring, with the aid of the crystal-blocking technique, mean fission lifetimes of nuclei obtained upon the complete fusion of heavy ions. Of course, a resonance dependence can be less pronounced in such reactions, since compound nuclei have a broad angular-momentum distribution. For above-barrier collision energies, this distribution can be reliably calculated, for example, on the basis of the surface-friction model with allowance for thermal fluctuations [10]. The corresponding transmission factor is well approximated by a Fermi function that is determined by two parameters, the critical angular momentum L_c and the diffuseness parameter δL. The values of these parameters that were obtained within the aforementioned model are fairly well approximated by the formulas that can be found, for example, in [5, 9] (for a more detailed discussion on the quality of this approximation, the interested reader is referred to the review article of Gontchar [5]).

In Fig. 10, we display an example of the L_c dependence of the mean fission lifetime for the reaction ^{19}F + ^{181}Ta $\rightarrow$ ^{200}Pb. Both calculations represented in this figure are purely statistical; of these, one relied on the diffuse distribution that was obtained by formulas (45)–(49) from [5], while the other employed the L_c value from the preceding calculation and the value of $\delta L = 0.1$. In this way, we demonstrate the effect of the diffuseness of the angular-momentum distribution of compound nuclei on the results of the calculations for mean fission times.

From Fig. 10, one can see that, as before, the mean fission time changes nonmonotonically. In response to the change in L_c from the minimum value for which the calculation was performed to the value that corresponds to the longest mean fission lifetime, the mean fission lifetime itself increases approximately by one order of magnitude. This is even greater than the variation in Fig. 1*a*.

Thus, a nonmonotonic angular-momentum dependence of mean fission lifetimes in complete-fusion reactions must manifest itself as a dependence on the projectile energy, to which L_c is related, and this effect is quite observable.

8. CONCLUSIONS

The main results of our study can be formulated as follows:

(i) On the basis of a modified version of the combined dynamical–statistical model, CDSM1, we have calculated the time distributions of fission events and of events involving prescission-neutron emission. These calculations have been performed for ^{190}Pt nuclei having angular momenta in the range $L = 0$–60 and the initial excitation energy of $E^*_{\rm init} = 150$ MeV both in the statistical (that is, without allowance for dissipation) and in the dynamical (with allowance for dissipation) mode.

(ii) It turns out that the angular-momentum dependence is not monotonically decreasing, in contrast to what might have been expected on the basis of general considerations; instead, it has a resonance-like shape. The dependence $\langle t_f \rangle(L)$ develops a maximum both in statistical and in dynamical calculations.

(iii) This maximum is due to a strong competition between the neutron-emission and fission channels, which arises under the condition that the width ratio Γ_f/Γ_n changes slowly in the process of emission at the initial stages of deexcitation.

(iv) An approximate equality of the fission and emission widths at the end of the emission chain is the second condition necessary for the emergence of a maximum in mean fission lifetimes. In a statistical calculation, this condition is satisfied at the beginning of the deexcitation process as well. In a dynamical calculation, however, mean fission lifetimes develop a maximum under the condition $\Gamma_f \ll \Gamma_n$ at initial stages of the cascade.

(v) The values of mean fission lifetimes considerably exceed characteristic fission times that can be obtained by multiplying the mean time of prescission-neutron emission by their mean multiplicity for $L \leq 50$.

(vi) The calculations performed for ^{205}Pb and ^{235}U nuclei at the same excitation energy of 150 MeV and for ^{190}Pt nuclei at different values of the initial excitation energy $E^*_{\rm init}$ have revealed that a resonance behavior of $\langle t_f \rangle(L)$ is an effect common to all nuclei in which $B_f(L=0) > B_n$.

(vii) In complete-fusion reactions, where there arise broad angular-momentum distributions of compound nuclei, a resonance behavior of mean fission times versus the critical value of the angular momentum survives. The respective maximum is not less pronounced than that in the case of fixed L.

(viii) Our theoretical investigations were motivated by recent experiments at GANIL where mean fission lifetimes were measured by means of the crystal-blocking technique. We hope that systematic measurements of mean fission lifetimes will be continued, since our present knowledge of this important feature of the fission process is incomplete; meanwhile, the theory predicts a nontrivial shape of the dependence $\langle t_f \rangle(L)$—in particular, the presence of a maximum as high as one order of magnitude. We would like to recall that, in the 1980s, the observation of three to five prescission neutrons instead of two, which were predicted by the statistical model, generated a new line of research in fission and heavy-ion physics (for details on this subject, see the review articles of Hilscher and Rossner [1] and Newton [4]), and investigations along this line have been continued so far [25, 27, 28, 30–34].

REFERENCES

1. D. Hilscher and H. Rossner, Ann. Phys. (Paris) **17**, 471 (1992).
2. D. O. Eremenko *et al.,* Yad. Fiz. **61**, 773 (1998) [Phys. At. Nucl. **61**, 695 (1998)].
3. S. A. Karamyan, Yu. V. Melikov, and A. F. Tulinov, Fiz. Élem. Chastits At. Yadra **4**, 456 (1973) [Sov. J. Part. Nucl. **4**, 196 (1973)].
4. J. O. Newton, Fiz. Élem. Chastits At. Yadra **21**, 821 (1990) [Sov. J. Part. Nucl. **21**, 349 (1990)].
5. I. I. Gontchar, Fiz. Élem. Chastits At. Yadra **26**, 932 (1995) [Phys. Part. Nucl. **26**, 394 (1995)].
6. I. Gontchar, M. Morjean, and S. Basnary, Europhys. Lett. **57**, 355 (2002).
7. F. Goldenbaum *et al.,* Phys. Rev. Lett. **82**, 5012 (1999).
8. M. Morjean, private communication (2003).
9. I. I. Gontchar, L. A. Litnevsky, and P. Fröbrich, Comput. Phys. Commun. **107**, 223 (1997).
10. P. Fröbrich and I. I. Gontchar, Phys. Rep. **292**, 131 (1998).
11. P. Fröbrich, I. I. Gontchar, and N. D. Mavlitov, Nucl. Phys. A **556**, 281 (1993).
12. J. Bartel *et al.,* Z. Phys. A **354**, 59 (1996).
13. H. J. Krappe, J. R. Nix, and A. J. Sierk, Phys. Rev. C **20**, 992 (1979).
14. A. J. Sierk, Phys. Rev. C **33**, 2039 (1986).
15. J. Toke and W. J. Swiatecki, Nucl. Phys. A **372**, 141 (1981).
16. I. Gontchar, P. Fröbrich, and N. I. Pischasov, Phys. Rev. C **47**, 2228 (1993).
17. P. Moeller *et al.*, At. Data Nucl. Data Tables **59**, 185 (1995).
18. K. T. R. Davies, A. J. Sierk, and J. R. Nix, Phys. Rev. C **13**, 2385 (1976).
19. J. P. Blocki, H. Feldmeier, and W. J. Swiatecki, Nucl. Phys. A **459**, 145 (1986).
20. J. U. Andersen *et al.*, K. Dan. Vidensk Selsk. Mat. Fys. Medd. **40** (7) (1980).
21. J. S. Forster *et al.*, Nucl. Phys. A **464**, 497 (1987).
22. Yu. A. Lazarev, I. I. Gontchar, and N. D. Mavlitov, Phys. Rev. Lett. **70**, 1220 (1993).
23. H. A. Kramers, Physica **7**, 284 (1940).
24. M. G. Kendall and A. Stuart, *The Advanced Theory of Statistics*, 4th ed. (Griffin, London, 1977; Nauka, Moscow, 1966).
25. I. I. Gonchar *et al.,* Yad. Fiz. **63**, 1778 (2000) [Phys. At. Nucl. **63**, 1688 (2000)].
26. W. Wagner *et al.*, Yad. Fiz. **65**, 1438 (2002) [Phys. At. Nucl. **65**, 1403 (2002)].
27. A. V. Karpov *et al.*, Phys. Rev. C **63**, 054610 (2001).
28. P. N. Nadtochy, G. D. Adeev, and A. V. Karpov, Phys. Rev. C **65**, 064615 (2002).
29. I. I. Gontchar, Yu. A. Lazarev, and N. D. Mavlitov, *Heavy-Ion Physics*, Sci. Report 1989/1990, E7-91-75, Joint Inst. Nucl. Res. (Dubna, 1991), pp. 70, 72.
30. A. Gargi Chaudhuri and Santanu Pal, Phys. Rev. C **65**, 054612 (2002).
31. K. Mahata *et al.,* Nucl. Phys. A **720**, 209 (2003).
32. G. Rudolf and A. Kelić, Nucl. Phys. A **679**, 251 (2001).
33. L. Donadille *et al.,* Nucl. Phys. A **656**, 259 (1999).
34. K. Pomorski *et al.,* Nucl. Phys. A **679**, 25 (2000).

Translated by A. Isaakyan

Physics of Atomic Nuclei, Vol. 67, No. 11, 2004, pp. 2095–2100. Translated from Yadernaya Fizika, Vol. 67, No. 11, 2004, pp. 2116–2122.
Original Russian Text Copyright © 2004 by Kurilin.

ELEMENTARY PARTICLES AND FIELDS
Theory

Leptonic Decays of the W Boson in a Strong Electromagnetic Field

A. V. Kurilin[*]

Moscow State Open Pedagogical University, Verkhnyaya Radishchevskaya ul. 16–18, Moscow, 109004 Russia

Received October 14, 2003

Abstract—The probability of W-boson decay into a lepton and a neutrino, $W^{\pm} \to \ell^{\pm}\bar{\nu}_{\ell}$, in a strong electromagnetic field is calculated. On the basis of the method for deriving exact solutions to relativistic wave equations for charged particles, an exact analytic expression is obtained for the partial decay width $\Gamma(\varkappa) = \Gamma(W^{\pm} \to \ell^{\pm}\bar{\nu}_{\ell})$ at an arbitrary value of the external-field-strength parameter $\varkappa = eM_W^{-3}\sqrt{-(F_{\mu\nu}q^{\nu})^2}$. It is found that, in the region of comparatively weak fields ($\varkappa \ll 1$), field-induced corrections to the standard decay width of the W boson in a vacuum are about a few percent. As the external-field-strength parameter is increased, the partial width with respect to W-boson decay through the channel in question, $\Gamma(\varkappa)$, first decreases, the absolute minimum of $\Gamma_{\min} = 0.926\Gamma(0)$ being reached at $\varkappa = 0.6116$. A further increase in the external-field strength leads to a monotonic growth of the decay width of the W boson. In superstrong fields ($\varkappa \gg 1$), the partial width with respect to W boson decay is greater than the corresponding partial width $\Gamma^{(0)}(W^{\pm} \to \ell^{\pm}\bar{\nu}_{\ell})$ in a vacuum by a factor of a few tens. *© 2004 MAIK “Nauka/Interperiodica”.*

1. INTRODUCTION

Presently, the Standard Model of electroweak interactions is the basis of our knowledge in the realms of elementary-particle physics. Many compelling pieces of evidence according to which the Standard Model describes correctly lepton and quark-interaction processes, which occur via the exchange of intermediate vector $W^{\pm}$ and Z^0 bosons, have been obtained over the past decade. The majority of experiments currently performed at the LEP and SLC electron–positron colliders are devoted to studying the properties of these particles, which mediate weak interactions [1]. Concurrently, the properties of W bosons are being investigated at the Tevatron proton–antiproton accelerator. The accuracy reached in those experiments makes it possible to test the predictions of the Standard Model at the level of radiative corrections. For example, the upgrade of the LEP electron–positron collider, which is now referred to as LEP-2, enabled physicists working at CERN to observe, for the first time, the double production of W bosons, $e^+e^- \to W^+W^-$ [2]. This reaction provides one of the most promising tools for precisely determining the W-boson mass ($M_W = 80.423 \pm 0.039$ GeV) and width ($\Gamma_W = 2.12 \pm 0.04$ GeV) [3]. Even at present, the errors in experimentally measuring the cross section $\sigma(e^+e^- \to W^+W^-)$ are as small as about one percent, whence it follows that theorists must calculate a number of $O(\alpha)$ radiative corrections to the tree diagrams for this process or radiative corrections of a still higher order. It should be noted that, because of W-boson instability, one actually has to deal with the more complicated multiparticle reaction $e^+e^- \to W^+W^- \to 4f$, where f stands for the fermion products of W-boson decay. Therefore, it is very difficult to perform an exact analytic calculation of all radiative corrections to the cross section for this process, and this will hardly be done in the near future.

In this connection, it is reasonable to discuss alternative methods for studying the properties of intermediate vector bosons. In this study, we aim at calculating the effect of strong electromagnetic fields on the leptonic mode of W-boson decay. The electromagnetic interactions of these particles, which are mediators of weak interactions, are the subject of special investigations [4]. The point is that the general form of the Lagrangian describing electromagnetic γWW interactions and satisfying the requirements of C and P invariance has not yet been obtained experimentally. From the theoretical point of view, it is quite admissible to extend the Standard Model by including in it new-physics effects that would generalize the minimal γWW vertex via the introduction of two dimensionless parameters k_γ and λ_γ [5],

$$\begin{aligned}\mathcal{L}_{\gamma WW} = -iek_\gamma F^{\mu\nu}W_\mu^+W_\nu^- \quad (1)\\ - ieW_{\mu\nu}^+W^{-\mu}A^\nu + ieW_{\mu\nu}^-W^{+\mu}A^\nu\\ + ie(\lambda_\gamma/M_W^2)W_{\mu\alpha}^+W^{-\mu\beta}F_\beta^\alpha,\end{aligned}$$

where $W_{\mu\nu}^{\pm} = \partial_\mu W_\nu^{\pm} - \partial_\nu W_\mu^{\pm}$, $F_{\mu\nu} = \partial_\mu A_\nu - \partial_\nu A_\mu$, and A^ν is the 4-potential of the electromagnetic field

---

[*] e-mail: `kurilin@mail.ru`

being considered. In the Standard Model of electroweak interactions due to Glashow, Weinberg, and Salam, these parameters have the following values at the tree level: $k_\gamma = 1$ and $\lambda_\gamma = 0$. A precise experimental verification of these conditions must be performed by studying the reaction $e^+e^- \to W^+W^-$. However, this problem has yet to be solved conclusively.

In view of the aforesaid, the approach to studying the gauge structure of W-boson electromagnetic interactions on the basis of an analysis of W-boson decays in an external field is of particular interest. In the present study, we calculate the probability of the reaction $W \to \ell\bar{\nu}_\ell$ and the changes that this reaction induces in the total decay width Γ_W, relying on the method that employs exact solutions to relativistic wave equations. It should be noted that precise measurements of the decay width of the W bosons are of great interest both for theorists and for experimentalists. This is because all processes associated with the production of these particles at electron–positron colliders are investigated by analyzing the leptonic or hadronic products of W-boson decays. In addition, the W-boson width is used as one of the parameters that form a basis for calculating radiative corrections to electroweak processes occurring at energies in the vicinity of the W resonance; therefore, it is of paramount importance to have precise theoretical predictions for the width Γ_W.

One-loop radiative corrections to the decay width of the W boson have already been calculated in the literature. In the approximation of massless fermions, they were obtained in a number of studies [6–11]. In that case, the main contribution comes from strong-interaction effects (about 4% with respect to the initial value of Γ_W) [12–14], whereas the corrections from electroweak processes are quite modest. It is noteworthy that new-physics phenomena (supersymmetry and so on) also make rather small contributions (see, for example, [15]). This is also corroborated by the calculations of the W-boson decay width within the two Higgs doublet model [16].

At the same time, the possibility of studying the properties of the W bosons via changing external conditions under which their production occurs has not yet been explored. In high-energy physics, the method of channeling relativistic particles through single crystals, in which case the momenta of such particles are directed along the crystal axes and planes formed by the regular set of crystal-lattice atoms [17], has been known for a long time. The electric fields generated by the axes and planes of single crystals can reach formidable values (above 10^{10} V/m), extending over macroscopic distances. This changes substantially the physics of all processes in an external field in relation to the analogous phenomena in a vacuum. Thus, single crystals prove to be a unique testing ground where one can study reactions that become possible in the presence of a strong external electromagnetic field.

2. PROBABILITY OF W-BOSON DECAY IN AN EXTERNAL FIELD

In the leading order of perturbation theory, the matrix element for the reaction of W-boson decay to a lepton ℓ and a neutrino $\bar{\nu}_\ell$ is given by

$$S_{fi} = \frac{ig}{2\sqrt{2}} \int d^4x \bar{\Psi}_\ell(x,p)\gamma^\mu(1+\gamma^5) \times \nu_\ell^c(x,p')W_\mu(x,q). \tag{2}$$

Here, an external electromagnetic field is included through a specific choice of wave functions for the charged lepton ℓ and the W boson: $\Psi_\ell(x,p)$ and $W_\mu(x,q)$, respectively. Within this approach, one goes beyond ordinary perturbation theory, taking into account nonlinear and nonperturbative effects of an external field in the probability of the reaction under consideration. The explicit form of the wave functions for charged particles in an external field can be obtained by solving the corresponding differential equations that are determined by the Standard Model Lagrangian (see, for example [4, 18]). In the present study, we restrict our consideration to the case of a so-called crossed field, whose strength tensor satisfies the relations

$$F_{\mu\nu}F^{\mu\nu} = F_{\mu\nu}\tilde{F}^{\mu\nu} = 0. \tag{3}$$

Investigation of quantum processes in a crossed field is the simplest way to analyze the transformations of elementary particles in electromagnetic fields of arbitrary configuration. This is because all formulas obtained in the semiclassical approximation for the probabilities of processes that occur in a crossed field are also applicable to describing analogous processes in arbitrary constant electromagnetic fields. Thus, the crossed-field model appears to be the most universal in the region of relatively weak fields. At the same time, the wave functions for charged particles in a crossed field have the simplest form, and this renders relevant mathematical calculations much less cumbersome. In our case, the W-boson and the lepton (ℓ) wave function are expressed in terms of the external-crossed-field strength tensor $F_{\mu\nu} = \partial_\mu A_\nu - \partial_\nu A_\mu$ as

$$\Psi_\ell(x,p) = \exp\left[-ipx - \frac{ie(pa)}{2(pFa)}(x^\mu F_{\mu\lambda}a^\lambda)^2 - \frac{ie^2}{6(pFa)}(x^\mu F_{\mu\lambda}a^\lambda)^3\right] \tag{4}$$

$$\times \left\{1 - \frac{e(xFa)}{4(pFa)}(F_{\mu\lambda}\gamma^\mu\gamma^\lambda)\right\}\frac{u(p)}{\sqrt{2p_0V}},$$

$$W_\mu(x,q) = \exp\left[-iqx - \frac{ie(qa)}{2(qFa)}(x^\mu F_{\mu\lambda}a^\lambda)^2 \right. \quad (5)$$
$$\left. - \frac{ie^2}{6(qFa)}(x^\mu F_{\mu\lambda}a^\lambda)^3\right]\left\{g_{\mu\nu} - \frac{e(xFa)}{(qFa)}F_{\mu\nu}\right.$$
$$\left. + \frac{e^2(xFa)^2}{2(qFa)^2}(F_{\mu\lambda}a^\lambda)(F_{\nu\sigma}a^\sigma)\right\}\frac{v^\nu(q)}{\sqrt{2q_0V}}.$$

The spin component of these wave functions, which are normalized to the three-dimensional volume V of the space, is determined by the Dirac bispinor $u(p)$ and the W-boson polarization 4-vector $v^\nu(q)$. Concurrently, it is assumed that the external-electromagnetic-field potential $A_\mu(x)$ is taken in the gauge

$$A_\mu(x) = -a_\mu(x^\alpha F_{\alpha\beta}a^\beta), \quad (6)$$

where the unit constant 4-vector a_μ satisfies the conditions

$$a_\mu a^\mu = -1, \quad (7)$$
$$F_{\mu\nu} = (a_\mu F_{\nu\lambda} - a_\nu F_{\mu\lambda})a^\lambda.$$

Let us substitute the lepton and W-boson wave functions (4) and (5) into expression (2) for the S-matrix element and integrate $|S_{fi}|^2$ over the lepton and neutrino phase spaces. After some simple but cumbersome algebra, we obtain

$$\Gamma(W \to \ell\bar{\nu}_\ell|\varkappa) = \frac{g^2M_W}{48\pi^2} \quad (8)$$
$$\times \int\limits_0^1 du\left\{\left[1 - \frac{m_\ell^2 + m_\nu^2}{2M_W^2} - \frac{(m_\ell^2 - m_\nu^2)^2}{2M_W^4}\right]\Phi_1(z)\right.$$
$$- 2\varkappa^{2/3}\left(\frac{u}{1-u}\right)^{1/3}$$
$$\left.\times\left[1 - 2u + 2u^2 + \frac{m_\ell^2 + m_\nu^2}{2M_W^2}\right]\Phi'(z)\right\}.$$

The partial decay width of the W boson can be expressed in terms of the special mathematical functions $\Phi'(z)$ and $\Phi_1(z)$ (see Appendix), which depend on the argument

$$z = \frac{m_\ell^2 u + m_\nu^2(1-u) - M_W^2 u(1-u)}{M_W^2[\varkappa u^2(1-u)]^{2/3}}. \quad (9)$$

In the semiclassical approximation, the external-electromagnetic-field strength tensor appears in expression (8) for the partial decay width only in combination with the W-boson energy–momentum 4-vector q^μ via the dimensionless parameter

$$\varkappa = \frac{e}{M_W^3}\sqrt{-(F_{\mu\nu}q^\nu)^2}. \quad (10)$$

The values of the parameter $\varkappa$ have a crucial effect on the W-boson width in an external field. From formula (8), one can see that, in the presence of an external electromagnetic environment, the rate of the reaction $W \to \ell\bar{\nu}_\ell$ becomes a dynamical characteristic that depends not only on the W-boson energy but also on external conditions under which this decay occurs. Therefore, we can no longer treat the W-boson width $\Gamma(W \to \ell\bar{\nu}_\ell)$ as a constant since, in an external field, it becomes a function of the parameter $\varkappa\,[\Gamma(\varkappa)]$.

Let us now consider asymptotic estimates of this function for various values of the external-electromagnetic-field strength. In the region of relatively weak fields that satisfy the constraint $\varkappa \ll m_\ell/M_W$, the partial decay width of the W boson can be written as the sum of two terms; of these, one is coincident with the decay width in a vacuum, while the other is the correction induced by the electromagnetic-field effect:

$$\Gamma(W \to \ell\bar{\nu}_\ell|\varkappa) = \Gamma^{(0)}(W \to \ell\bar{\nu}_\ell) + \Delta\Gamma(\varkappa). \quad (11)$$

The quantity $\Gamma^{(0)}(W \to \ell\bar{\nu}_\ell)$ is well known in the literature (see, for example, [2]). In the leading order of perturbation theory in the electroweak coupling constant g, it is given by

$$\Gamma^{(0)}(W \to \ell\bar{\nu}_\ell) = \frac{g^2M_W}{48\pi} \quad (12)$$
$$\times\sqrt{\left[1 - \left(\frac{m_\ell + m_\nu}{M_W}\right)^2\right]\left[1 - \left(\frac{m_\ell - m_\nu}{M_W}\right)^2\right]}$$
$$\times\left[1 - \frac{m_\ell^2 + m_\nu^2}{2M_W^2} - \frac{(m_\ell^2 - m_\nu^2)^2}{2M_W^4}\right].$$

As for the other term in expression (11) for the partial decay width, $\Delta\Gamma(\varkappa)$, its value depends nontrivially on the lepton and neutrino masses. In the case where the neutrino mass can be disregarded ($m_\nu = 0$), the effect of an external field on $\Delta\Gamma(\varkappa)$ is described by the relation

$$\Delta\Gamma(\varkappa) = -\frac{g^2M_W}{48\pi}\frac{4}{3}\varkappa^2\left[1 - \frac{13}{2}\left(\frac{m_\ell}{M_W}\right)^2\right. \quad (13)$$
$$\left. + 16\left(\frac{m_\ell}{M_W}\right)^4 - \frac{51}{4}\left(\frac{m_\ell}{M_W}\right)^6\right].$$

This expression is the second term in the asymptotic expansion of the integral representation (8) for $\varkappa \to 0$. Here, the entire dependence on the lepton mass m_ℓ is taken into account exactly, while the terms proportional to m_ν are discarded. The role of the effects induced by a nonzero neutrino mass is noticeable only in the region of very weak fields, $\varkappa \ll (m_\nu/M_W)^3$, in

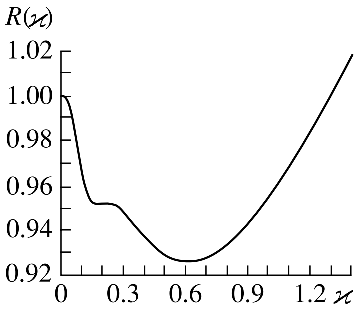

Fig. 1. Relative variations in the leptonic-decay width of the W boson in weak electromagnetic fields.

which case the expression for the field-induced correction $\Delta\Gamma(\varkappa)$ develops a characteristic oscillating term that modifies expression (13) as follows:

$$\Delta\Gamma(\varkappa) = \frac{g^2 M_W}{48\pi}\left[\frac{32}{\sqrt{6}}\varkappa\left(\frac{m_\nu}{M_W}\right)^3 \times \cos\left(\frac{\sqrt{3}}{8\varkappa}\frac{M_W}{m_\nu}\right) - \frac{4}{3}\varkappa^2\right]. \tag{14}$$

From the estimates obtained above, it can be seen that weak electromagnetic fields have virtually no effect on the decay width of the W boson—that is, the corrections to the probability of the decay $W \to \ell\bar{\nu}_\ell$ in a vacuum are within the errors of present-day experiments. However, this pessimistic conclusion is valid only for $\varkappa \ll m_\ell/M_W$. In the region of rather strong electromagnetic fields, the effects discussed here appear to be significant.

In view of this, we consider another limiting case, that of $\varkappa \gg m_\ell/M_W$. This relationship between the parameters makes it possible to disregard the lepton masses against the W-boson mass. The relative error of this approach does not exceed the level of corrections that are proportional to the ratio of the masses of these particles; that is,

$$\delta_\ell = \frac{m_\ell}{M_W} < 10^{-2}, \qquad \delta_\nu = \frac{m_\nu}{M_W} < 10^{-4}. \tag{15}$$

By using the approximation $\delta_\ell = \delta_\nu = 0$, one can calculate analytically the W-boson decay width at any arbitrarily large value of the external-field-strength parameter $\varkappa$. The total result of our calculations is expressed in terms of the so-called Gi function and its derivative (see Appendix). In order to render the ensuing exposition clearer, it is convenient to introduce the normalized partial decay width $R(\varkappa)$ that is defined as the ratio of the decay width (8) in an external field to the analogous quantity in a vacuum; that is,

$$R(\varkappa) = \frac{\Gamma(W \to \ell\bar{\nu}_\ell|\varkappa)}{\Gamma^{(0)}(W \to \ell\bar{\nu}_\ell)}. \tag{16}$$

For the normalization factor, we chose the W-boson decay width (12) calculated at zero lepton and neutrino masses:

$$\Gamma^{(0)}(W \to \ell\bar{\nu}_\ell) \simeq \frac{G_{\rm F} M_W^3}{6\pi\sqrt{2}} = 0.227\ \text{GeV}. \tag{17}$$

The ultimate formula determining the effect of electromagnetic fields on the leptonic modes of W-boson decay then takes the form

$$R(\varkappa) = \frac{4\pi}{81y}(19 - 2y^3)Gi'(y) - \frac{2\pi y}{81}(11 + 2y^3)Gi(y) + \frac{1}{81}(103 + 4y^3), \tag{18}$$

where the argument of the Gi functions is related to the parameter $\varkappa$ by the equation $y = \varkappa^{-2/3}$. This expression is very convenient for computer calculations of the rate of W-boson decay in an external field. The results of the present numerical analysis, which was based on the Mathematica system, are displayed in Fig. 1. The graph there represents the quantity R (16) as a function of the electromagnetic-field strength ($\varkappa$). One can see that, as the parameter $\varkappa$ increases, the partial decay width of the W boson gradually decreases. In the intermediate region $\delta_\ell \ll \varkappa \ll 1$, this decay width is well described by the asymptotic formula

$$\Gamma(W \to \ell\bar{\nu}_\ell) = \frac{g^2 M_W}{48\pi}\left(1 - \frac{8}{3}\varkappa^2 - \frac{304}{3}\varkappa^4 - \frac{4}{\sqrt{3}}\frac{\delta_\ell^3}{\varkappa}\right). \tag{19}$$

It is noteworthy that the numerical coefficient of the first correction to the W-boson decay width in a vacuum, $(8/3)\varkappa^2$, is precisely two times as great as the analogous coefficient of $\varkappa^2$ in the region $\varkappa \ll \delta_\ell$ [see (13), (14)]. This indicates that the partial decay width of the W boson in an external field takes a minimum value in the region around $\varkappa \sim 1$. A computer calculation shows that the quantity $R(\varkappa)$ reaches the absolute minimum of $R_{\min} = 0.926$ at $\varkappa_{\min} = 0.6116$. Thus, we can state that, in weak fields, the deviation of the partial decay width of the W boson from that in a vacuum does not exceed 7.4%. A further increase in the external-field strength leads to a monotonic growth of the probability of W-boson decay, so that, at $\varkappa > 1.3$, the decays to a lepton and a neutrino occur faster than those in a vacuum ($R(\varkappa) > 1$). In this region of relatively strong fields, the mean lifetime of the W boson decreases sizably, which is illustrated by the graph in Fig. 2. One can see that, even at $\varkappa = 7$, the dynamical width of the W boson becomes two times larger than the static vacuum value in (12). In superstrong fields ($\varkappa \gg 1$), the partial decay width of the W boson can be estimated with the aid of the

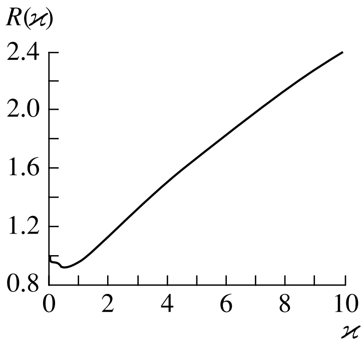

Fig. 2. Effect of strong electromagnetic fields on the leptonic mode of W-boson decay.

asymptotic expression

$$\Gamma(W \to \ell\bar{\nu}_\ell) = \frac{g^2 M_W}{48\pi} \times \left\{ \frac{38}{243}\Gamma(2/3)(3\varkappa)^{2/3} + \frac{1}{3} + \frac{8}{81}\frac{\Gamma(1/3)}{(3\varkappa)^{2/3}} \right\}. \tag{20}$$

3. CONCLUSION

The effect of strong electromagnetic fields on the leptonic mode of W-boson decay has been investigated. We have revealed that, in an external field, the partial width with respect to the decay $W \to \ell\bar{\nu}_\ell$ is a nonmonotonic function of the field-strength parameter $\varkappa$ (10). In particular, there is a domain of field-strength values where the decays of the W boson occur somewhat more slowly than those in a vacuum. This fact has a significant effect on the total decay width of the W boson, since, in the approximation of massless leptons and quarks, this width is known to be related to the partial width with respect to the leptonic decays considered here by the equation

$$\Gamma_W \simeq (N_\ell + N_q N_c)\Gamma(W \to \ell\bar{\nu}_\ell) = 12\Gamma(W \to \ell\bar{\nu}_\ell), \tag{21}$$

where $N_\ell = N_q = 3$ are the numbers of the lepton and quark generations and $N_c = 3$ is the total number of color quarks. Thus, one can state that, in relatively weak electromagnetic fields, the maximum deviation of the total width of the W boson from its vacuum value Γ_W is 7%. As for the region of strong fields ($\varkappa \geq 1$), a stable trend toward an increase in the rate of W-boson decays is observed here, which reduces their lifetime to a still greater extent.

It is noteworthy that a similar nonmonotonic dependence on the external-field-strength parameter is observed in the decay of the scalar pion to a lepton pair, $\pi \to \ell\bar{\nu}_\ell$ [19]. This circumstance is explained by the similarity of kinematical conditions under which the decays of massive charged particles proceed in a crossed field and by the fact that the reactions $W \to \ell\bar{\nu}_\ell$ and $\pi \to \ell\bar{\nu}_\ell$ are both energetically allowed; therefore, they are possible even in the absence of external fields. At the same time, it should be noted that the electromagnetic interactions of the W bosons are much more complicated than the interactions of scalar pions, this leading to a number of interesting phenomena.

It is well known (see, for example, [20]) that the energy spectrum of W bosons in a superstrong electromagnetic field involves the so-called tachyon mode, which is due to their anomalous magnetic moment $\Delta\mu_W = ek_\gamma/2M_W$. This results in that the W-boson vacuum becomes unstable within perturbation theory, so that there arises, in superstrong fields, the possibility of a phase transition to a new ground state, this phase transition being accompanied by the restoration of $SU(2)$ symmetry, which is spontaneously broken under ordinary conditions [21–24]. The trend toward the rearrangement of the W-boson vacuum manifests itself in a singular behavior of many physical quantities in the vicinity of the critical external-field-strength value of $F_{\text{cr}} = M_W^2/e \simeq 1.093 \times 10^{24}$ G. For example, the anomalous magnetic moment of Dirac neutrinos that is due to the virtual production of W bosons has a logarithmic singularity in a superstrong field for $F = \sqrt{F_{\mu\nu}F^{\mu\nu}/2} \to F_{\text{cr}}$ [25]. Unfortunately, the crossed-field model, which was used in the present study, is inadequate to the problem of calculating the behavior of the W-boson decay width at external-field strengths close to the critical value F_{cr}. In order to solve this problem, it is necessary to go beyond the semiclassical approximation (3) and to employ more complicated wave functions for charged particles. At any rate, it seems that this problem is of particular interest and that it deserves a dedicated investigation.

Yet another interesting result obtained in the present study is that which concerns the effect of a nonzero mass of Dirac neutrinos on the W-boson decay width in weak electromagnetic fields. In the case of $m_\nu \neq 0$, it has been found that the correction $\Delta\Gamma(\varkappa)$ to the vacuum decay width develops a nontrivial oscillating term (14), which can serve as some kind of indication that massive neutrinos exist. It should be noted that oscillations of the probabilities of quantum processes in an external field emerge for a number of reactions allowed in a vacuum if the participant particles have a nonzero rest mass. For example, similar oscillations arise in the cross section for the process $\gamma e \to W\nu_e$ if the respective calculations take into account effects of a nonzero neutrino mass [26].

APPENDIX

In the present study, we have employed special mathematical functions generically termed Airy functions. A somewhat different notation is used for Airy functions in the physical and in the mathematical literature. Mathematicians describe Airy functions with the aid of the symbols $Ai(z)$, $Bi(z)$, and $Gi(z)$, which are related to our notation as follows:

$$\Phi(z) = \pi Ai(z), \qquad \Phi'(z) = \pi Ai'(z), \tag{A.1}$$

$$\Phi_1(z) = \pi^2 \Big[Ai(z)Gi'(z) - Ai'(z)Gi(z) \Big]. \tag{A.2}$$

Airy functions are particular solutions to the second-order linear differential equations

$$Ai''(z) - zAi(z) = 0, \tag{A.3}$$
$$Gi''(z) - zGi(z) = -1/\pi.$$

These solutions can be represented in the form of improper integrals of trigonometric functions,

$$Ai(z) = \frac{1}{\pi} \int\limits_0^\infty dt \cos(zt + t^3/3), \tag{A.4}$$

$$Gi(z) = \frac{1}{\pi} \int\limits_0^\infty dt \sin(zt + t^3/3). \tag{A.5}$$

The properties of Airy functions are well known, and a compendium of these properties can be found in mathematical handbooks (see, for example, [27]).

REFERENCES

1. Z. Kunszt, W. J. Stirling, *et al.*, in *Physics at LEP-2,* Ed. by G. Altarelli, T. Sjöstrand, and F. Zwirner, CERN Report 96-01, Vol. 1, p. 141; hep-ph/9602352.
2. W. Beenakker, F. A. Berends, *et al.*, in *Physics at LEP-2,* Ed. by G. Altarelli, T. Sjöstrand, and F. Zwirner, CERN Report 96-01, Vol. 1, p. 81; hep-ph/9602351.
3. K. Hagiwara *et al.* (Particle Data Group), Phys. Rev. D **66**, 01001 (2002).
4. A. V. Kurilin, Nuovo Cimento A **112**, 977 (1999); hep-ph/0210194.
5. K. Hagiwara *et al.*, Nucl. Phys. B **282**, 253 (1987).
6. W. J. Marciano and A. Sirlin, Phys. Rev. D **8**, 3612 (1973); W. J. Marciano and D. Wyler, Z. Phys. C **3**, 181 (1979); D. Albert, W. J. Marciano, D. Wyler, and Z. Parsa, Nucl. Phys. B **166**, 460 (1980).
7. K. Inoue, A. Kakuto, H. Komatsu, and S. Takeshita, Prog. Theor. Phys. **64**, 1008 (1980).
8. M. Consoli, S. L. Presti, and L. Maiani, Nucl. Phys. B **223**, 474 (1983).
9. D. Yu. Bardin, S. Riemann, and T. Riemann, Z. Phys. C **32**, 121 (1986).
10. F. Jegerlehner, Z. Phys. C **32**, 425 (1986); **38**, 519 (E) (1988).
11. J. W. Jun and C. Jue, Mod. Phys. Lett. A **6**, 2767 (1991).
12. A. Denner and T. Sack, Z. Phys. C **46**, 653 (1990); A. Denner, Fortschr. Phys. **41**, 307 (1993).
13. T. H. Chang, K. J. F. Gaemers, and W. L. van Neerven, Nucl. Phys. B **202**, 407 (1982).
14. T. Alvarez, A. Leites, and J. Terron, Nucl. Phys. B **301**, 1 (1988).
15. J. Rosner, M. Worah, and T. Takeuchi, Phys. Rev. D **49**, 1363 (1994).
16. D.-S. Shin, Nucl. Phys. B **449**, 69 (1995).
17. S. P. Moller, CERN Report 94-05.
18. A. V. Kurilin, Yad. Fiz. **57**, 1129 (1994) [Phys. At. Nucl. **57**, 1066 (1994)]; Int. J. Mod. Phys. A **9**, 4581 (1994).
19. V. I. Ritus and A. I. Nikishov, *Quantum Electrodynamics of Phenomena in Strong Fields,* Tr. FIAN SSSR **111** (1979); V. I. Ritus, Zh. Éksp. Teor. Fiz. **56**, 986 (1969); V. R. Khalilov, Yu. I. Klimenko, O. S. Pavlova, and É. Yu. Klimenko, Yad. Fiz. **41**, 756 (1985) [Sov. J. Nucl. Phys. **41**, 482 (1985)].
20. N. K. Nielsen and P. Olesen, Nucl. Phys. B **144**, 376 (1978).
21. A. Salam and J. Strathdee, Nucl. Phys. B **90**, 203 (1975).
22. S. G. Matinyan and G. K. Savvidi, Yad. Fiz. **25**, 218 (1977) [Sov. J. Nucl. Phys. **25**, 118 (1977)]; I. A. Batalin, S. G. Matinyan, and G. K. Savvidi, Yad. Fiz. **26**, 407 (1977) [Sov. J. Nucl. Phys. **26**, 214 (1977)]; S. G. Matinyan and G. K. Savvidy, Nucl. Phys. B **134**, 539 (1978); G. K. Savvidy, Phys. Lett. B **71B**, 133 (1977).
23. V. V. Skalozub, Yad. Fiz. **21**, 1337 (1975) [Sov. J. Nucl. Phys. **21**, 690 (1975)]; **28**, 228 (1978) [Sov. J. Nucl. Phys. **28**, 113 (1978)]; **35**, 782 (1982) [Sov. J. Nucl. Phys. **35**, 453 (1982)].
24. J. Ambjørn and P. Olesen, Phys. Lett. B **218**, 67 (1989); Nucl. Phys. B **315**, 606 (1989); **330**, 193 (1990).
25. A. V. Borisov, V. Ch. Zhukovskiĭ, A. V. Kurilin, and A. I. Ternov, Yad. Fiz. **41**, 743 (1985) [Sov. J. Nucl. Phys. **41**, 473 (1985)].
26. V. Ch. Zhukovskiĭ and A. V. Kurilin, Yad. Fiz. **48**, 179 (1988) [Sov. J. Nucl. Phys. **48**, 114 (1988)].
27. M. Abramowitz and I. A. Stegun, *Handbook of Mathematical Functions* (Dover, New York, 1965, 1971; Nauka, Moscow, 1979).

Translated by A. Isaakyan

Physics of Atomic Nuclei, Vol. 67, No. 11, 2004, pp. 2101–2106. From Yadernaya Fizika, Vol. 67, No. 11, 2004, pp. 2123–2128.
Original English Text Copyright © 2004 by Kaczmarczyk.

ELEMENTARY PARTICLES AND FIELDS
Theory

Simple Numerical Method of Computing the Probabilities of Angular Momentum $\mathbf{J}_\nu$ Occurring among Possible Vectors $\mathbf{J}$ Resulting from n Angular Momentum $\mathbf{j}_\mu$ Summation ($\mu = 1$–n)*

M. Kaczmarczyk

Division of Nuclear Physics, University of Lodz, Lodz, Poland

Received February 7, 2003; in final form, November 19, 2003

Abstract—A relatively simple numerical method of summing angular momentum vectors with maintaining space quantization rules of each summed angular momentum has been presented. The method enables the calculation of the values of probability $p(\mathbf{J}_\nu)$ of finding a definite angular momentum $\mathbf{J}_\nu$ among all vectors $\mathbf{J}$ being the results of quantum summation of n angular momentum vectors $\mathbf{j}_\mu$ ($\mu = 1$–n). It may be used, e.g., in the calculations of angular momentum of many-particle states. The significance of the paper is connected with the possibility of taking into account, in a simple way, the angular momentum conservation principle for a system which consists of an arbitrary number of excitons. *© 2004 MAIK "Nauka/Interperiodica".*

1. INTRODUCTION

The angular momentum $\mathbf{j}$ is the nucleon's quantum characteristic in the potential well according to the shell model.[1]

In the compound nucleus excitation process, e.g., as a result of slow neutron capture, various nucleon configurations are realized. According to the formalism of the semiclassical approach [1], we consider the target nucleus as a potential well with single-particle levels occupied by nucleons up to the Fermi level. After the capture of a slow neutron with kinetic energy T lower than the neutron binding energy S_n, the composite nucleus is excited to the energy $U \approx S_n$. The initial configuration of the composite nucleus is the single-particle one ($1p0h$) as long as the captured neutron does not collide first with some of the target nucleons. The probability of collisions is higher than the probability for neutron escape from the nucleus, and, as a rule, the $2p1h$ configuration is obtained as a result of the energy exchange in the two-body residual interaction. A sequence of two-body interactions between nucleons moving in an averaged potential well leads to redistributions of the excitation energy U among nucleons. In the semiclassical model [1], based on the description of the composite nucleus excitation, according to the exciton model [2], it has been accepted to characterize the configuration type adequately to the number of i particles raised over the target nucleus Fermi level and of $i-1$ holes under this level. As an example, one of the possible configurations is the configuration $ip(i-1)h$, where i is contained in the range 1–k; k is called the complexity of the nuclear structure and denotes the maximum number of particles which may be raised above the Fermi level. A suitable expression for k is found in [1].

The complexity of k values for particular nuclei excited as a result of slow neutron capture is determined by the energy conservation principle, the Pauli exclusion rule, and the presence of energy gaps separating nucleon shells in the potential well. The configuration $ip(i-1)h$ can be realized in many ways, as a result of possible creation of a large number of subconfigurations (each with i particles and $i-1$ holes), in the nucleus excitation process. The subconfigurations of the configuration $ip(i-1)h$ for defined excitation energy U arise, because particles and holes (excitons) may be located in the potential well on different single-particle levels with different quantum characteristics. However, these subconfigurations (for configuration $ip(i-1)h$) are not equivalent to one another because excitons with different angular momentum values $\mathbf{j}_\mu$ participate in them.

One can expect that considering the angular momentum conservation principle and using it in exci-

---

*This article was submitted by the author in English.

[1] In this paper, it has been assumed that, e.g., the symbol $\mathbf{j} = 5/2$ represents the vector of the angular momentum, which has length equal to $\sqrt{\frac{5}{2}(\frac{5}{2}+1)}\hbar$, where 5/2 denotes the maximum value of the quantum magnetic number, describing the maximum angular momentum projection on the quantization axis. According to the quantization rule, vector $\mathbf{j} = 5/2$ can assume $2j+1$ (e.g., six) orientations towards the given axis. The symbol j denotes the angular momentum quantum number.

tation analysis of i particles and $i-1$ holes in the potential well will limit, to a large extent, the number of possible subconfigurations for each configuration with i particles over the Fermi level.

There exists a need for working out a method for the calculation of reduction coefficients for the whole numbers of subconfigurations, which are specific for every configuration with i particles and $i-1$ holes. These reduction coefficients allow one to bring these numbers to such values which result not only from the energy conservation principle but also from the angular momentum conservation principle. This requirement refers to every one of the possible configurations $ip(i-1)h$, where $i = 1–k$.

This paper presents a proposal for calculation of the probabilities of the angular momentum vector $\mathbf{J}_\nu$ occurring among possible $\mathbf{J}$ vectors, which are the result of many angular momentum $\mathbf{j}_\mu$ summation. It is worth noting that the presented numerical method provides a way of relatively simply calculating $p(\mathbf{J}_\nu)$ probability values. We can demonstrate this with a few simple examples. The calculation of $p(\mathbf{J}_\nu)$ is essential, e.g., in shell-model calculations; however, associated methods are not presented separately. Moreover, adoption of the basic formulas found in a selected academic handbook [3] is not efficient.

It seems that the considered problem may have a significance for agreeing upon neutron resonance density values ρ_{cal} calculated on the base of the semiclassical model with resonance level density ρ_{exp} values determined in an experimental way.

In this place, we want to note distinctly that the nuclear model [1] used for calculation of subconfiguration numbers as based on the exciton model [2] assumes that particles and holes occupy equally spaced single-particle levels separately in the nuclear potential well (equidistant spacing model). So, in such a concept, the Pauli principle is fulfilled automatically.

2. THE SUMMATION OF TWO ANGULAR MOMENTA $\mathbf{j}_1$ AND $\mathbf{j}_2$ TO THE $\mathbf{J}_\nu$ VALUES WITHOUT NECESSITY OF USING CLEBSCH–GORDAN COEFFICIENTS

Below, we have explained the rules of calculating probabilities $p(\mathbf{J}_\nu)$ of angular momentum $\mathbf{J}_\nu$ occurring in a set of vectors $\mathbf{J}$ resulting from summation of two angular momenta $\mathbf{j}_1$ and $\mathbf{j}_2$ when, e.g., $\mathbf{j}_1 = 5/2$ and $\mathbf{j}_2 = 2$.

According to the expectations of quantum mechanics, vectors $\mathbf{j}_1$ and $\mathbf{j}_2$ may assume, respectively, $2j_1 + 1$ and $2j_2 + 1$ orientations, relative to the quantization axis. For the considered case, these are the numbers 6 and 5. Table 1 contains the presentation of magnetic quantum numbers for angular momenta $\mathbf{j}_1$ and $\mathbf{j}_2$ in the analyzed case.

As a result of summing magnetic numbers presented in Table 1, we obtain a collection of 30 magnetic numbers of angular momenta resulting from the summation. Being ordered, the collection of these 30 elements is written below:

$$\begin{array}{cccccccccc}
9/2 & 7/2 & 5/2 & 3/2 & 1/2 & -1/2 & -3/2 & -5/2 & -7/2 & -9/2 \\
 & 7/2 & 5/2 & 3/2 & 1/2 & -1/2 & -3/2 & -5/2 & -7/2 & \\
 & & 5/2 & 3/2 & 1/2 & -1/2 & -3/2 & -5/2 & & \\
 & & & 3/2 & 1/2 & -1/2 & -3/2 & & & \\
 & & & & 1/2 & -1/2 & & & &
\end{array}$$

As we can easily see on the basis of the above presentation, in the written set of 30 numbers, there exist groups of angular momentum magnetic numbers which are adequate for angular momenta: $\mathbf{J}_1 = 9/2$, $\mathbf{J}_2 = 7/2$, $\mathbf{J}_3 = 5/2$, $\mathbf{J}_4 = 3/2$, $\mathbf{J}_5 = 1/2$, resulting from summation.

Assuming that each set of quantum configurations is equally probable, we can calculate the probability $p(\mathbf{J}_\nu)$ of angular momentum $\mathbf{J}_\nu$ occurrence on the basis of the formula

$$p(\mathbf{J}_\nu) = \frac{r_\nu}{N}. \qquad (1)$$

In (1), r_ν denotes the frequency of angular momentum occurrence (i.e., the number of magnetic numbers for angular momentum $\mathbf{J}_\nu$), whereas N denotes the total number of all possible projections of all vectors $\mathbf{J}$ which arise as summation results. In the analyzed case, $N = 30$.

We should note that, in the analyzed case (and always when only two angular momenta are being summed), the so-called multiplication factors $\eta_{\mathbf{J}_\nu}$ of angular momenta $\mathbf{J}_\nu$ occurrence are equal to one.

In Table 2, we have the presentation of vector summation results when $\mathbf{j}_1 = 5/2$ and $\mathbf{j}_2 = 2$.

Table 1. The presentation of magnetic quantum numbers m_j for angular momenta $\mathbf{j}_1 = 5/2$ and $\mathbf{j}_2 = 2$

$\mathbf{j}_1 = 5/2$	$\mathbf{j}_2 = 2$
5/2	2
3/2	1
1/2	0
−1/2	−1
−3/2	−2
−5/2	

Table 2. The presentation of two-vector summation results when $\mathbf{j}_1 = 5/2$ and $\mathbf{j}_2 = 2$ and of the appropriate $p(\mathbf{J}_\nu)$ values

$\mathbf{J}_\nu$	$\eta_{\mathbf{J}_\nu}$	$2J_\nu + 1$	$r_\nu = \eta_{\mathbf{J}_\nu}(2J_\nu + 1)$	$p(\mathbf{J}_\nu)$
1/2	1	2	2	2/30
3/2	1	4	4	4/30
5/2	1	6	6	6/30
7/2	1	8	8	8/30
9/2	1	10	10	10/30

On the basis of the data collected in Table 2, formula (1) can be written in the form

$$p(\mathbf{J}_\nu) = \frac{\eta_{\mathbf{J}_\nu}(2J_\nu + 1)}{\sum\limits_{J_\nu} \eta_{\mathbf{J}_\nu}(2J_\nu + 1)}. \quad (2)$$

Taking into consideration the presented method, the $p(\mathbf{J}_\nu)$ values have been calculated for summing a few other angular momenta $\mathbf{j}_1$ and $\mathbf{j}_2$; they are presented in Table 3.

In formula (2), the summation comprises the values $|j_1 - j_2| \le J \le |j_1 + j_2|$ with a unit step.

The results $p(\mathbf{J}_\nu)$ presented in Table 3, calculated according to the method proposed in this paper, are in full agreement with the obtained values if we use Clebsch–Gordan coefficients [4].

The great ease in calculating $p(\mathbf{J}_\nu)$ probabilities in the case of two angular momentum summation with the method proposed in this paper, compared to the generally recognized and accepted method using Clebsch–Gordan coefficients, makes the method encouraging and worth extending to n angular momentum summation.

Table 3. The presentation of $p(\mathbf{J}_\nu)$ probability values in a few other cases of two angular momentum $\mathbf{j}_1 + \mathbf{j}_2$ summation

	$\mathbf{J}_\nu$	$p(\mathbf{J}_\nu)$
$\mathbf{j}_1 = 1/2$	0	1/4
$\mathbf{j}_2 = 1/2$	1	3/4
$\mathbf{j}_1 = 1$	0	1/9
$\mathbf{j}_2 = 1$	1	3/9
	2	5/9
$\mathbf{j}_1 = 1$	1/2	1/3
$\mathbf{j}_2 = 1/2$	3/2	2/3

2.1. Angular Momentum Statistical Coefficient g

It is worth noting that formula (2) for the case of only two ($n = 2$) angular momentum summation $\mathbf{j}_1 + \mathbf{j}_2$ can be written in the form

$$p(\mathbf{J}) = (2J + 1) \Big/ \sum_{J=|j_1 - j_2|}^{J=j_1+j_2} (2J + 1). \quad (3)$$

However, as $n = 2$, the equality

$$\sum_{J=|j_1 - j_2|}^{J=j_1+j_2} (2J + 1) = (2j_1 + 1)(2j_2 + 1) \quad (4)$$

holds, so in the case when the quantum number of $\mathbf{j}_1$ angular momentum $j_1 = s = 1/2$ (e.g., quantum number of neutron spin) and $j_2 = I_x$, where I_x is the quantum number of target nucleus spin $\mathbf{I}_x$, e.g., in resonance s-wave neutron capture reactions, formula (3) has the form

$$g = p(\mathbf{J}) = \frac{(2J + 1)}{2(2I_x + 1)}. \quad (5)$$

This is a known nuclear physics formula for the so-called statistical angular momentum coefficient. It enables calculating the probability of resonance state creation with spin $\mathbf{J}$, as a result of s-wave neutron (spin $\mathbf{s} = 1/2$) interaction with the target nucleus, which has spin $\mathbf{I}_x$.

3. EXPANDING THE ACCEPTED METHOD OF $p(\mathbf{J}_\nu)$ PROBABILITY CALCULATION TO THE CASE OF SUMMING ANY NUMBER n OF ANGULAR MOMENTA

3.1. The Summation of Four Angular Momenta $\mathbf{j}_\mu$

Presented in Section 2, the way of $p(\mathbf{J}_\nu)$ probability calculation (the example when only two angular momenta being summed) can be successfully applied to any number n of angular momenta. As an example of summing n vectors when $n > 2$, consider the case when $n = 4$. Let $\mathbf{j}_1 = 5/2$, $\mathbf{j}_2 = 3/2$, $\mathbf{j}_3 = 1/2$, and $\mathbf{j}_4 = 1/2$. Table 4 presents the adequate magnetic quantum numbers suitable for the above-mentioned angular momenta $\mathbf{j}_\mu$.

There are 14 elements in Table 4. As a result of summing foursomes of numbers, written in Table 4, we obtain 96 magnetic numbers M characteristic of the resulting angular momenta $\mathbf{J}_\nu$. These are the following magnetic numbers M presented in the chart below, obtained as results of four angular momentum summation:

$$\begin{array}{cccccccccccccccccc}
5 & 4 & 3 & 2 & 1 & 0 & 4 & 3 & 2 & 1 & 0 & -1 & 3 & 2 & 1 & 0 & -1 & -2 \\
2 & 1 & 0 & -1 & -2 & -3 \\
4 & 3 & 2 & 1 & 0 & -1 & 3 & 2 & 1 & 0 & -1 & -2 & 2 & 1 & 0 & -1 & -2 & -3 \\
1 & 0 & -1 & -2 & -3 & -4 \\
4 & 3 & 2 & 1 & 0 & -1 & 3 & 2 & 1 & 0 & -1 & -2 & 2 & 1 & 0 & -1 & -2 & -3 \\
1 & 0 & -1 & -2 & -3 & -4 \\
3 & 2 & 1 & 0 & -1 & -2 & 2 & 1 & 0 & -1 & -2 & -3 & 1 & 0 & -1 & -2 & -3 & -4 \\
0 & -1 & -2 & -3 & -4 & -5
\end{array}$$

Among the above M values, we can see groups of magnetic numbers for angular momenta: $\mathbf{J}_\nu = 5$, 4, 3, 2, 1, 0. There are all $N = 96$ magnetic numbers obtained in the summation process.

In the presently analyzed case ($n = 4$), we can note that the multiplication factors $\eta_{\mathbf{J}_\nu}$ of vectors $\mathbf{J}_\nu$ are not units, as this was in the case when only two angular momenta $\mathbf{j}_1 + \mathbf{j}_2$ were summed.

Table 5 presents the results of calculations for the analyzed case.

Figure 1 presents the distribution of the frequencies r_ν of angular momentum $\mathbf{J}_\nu$ occurrence (for data in Table 5).

3.2. The Rule of Finding $\mathbf{J}_{min}$ and $\mathbf{J}_{max}$ When Many Angular Momenta $\mathbf{j}_\mu$ Are Summed

While determining the maximum angular momentum value $\mathbf{J}_{\max}$ occurring among $\mathbf{J}$ vectors which result from n angular momentum $\mathbf{j}_\mu$ summation is not difficult (quantum number $J_{\max}$ of vector $\mathbf{J}_{\max}$ is $J_{\max} = \sum_{\mu=1}^{n} j_\mu$), the rule of determining quantum number $J_{\min}$ is not directly obvious. It has been noted that

$$\text{(i) if } j_{\max} \leq \sum j_{\mu,\text{ remaining}}, \text{ then } J_{\min} = 0,$$

$$\text{or if } n \text{ is odd, } J_{\min} = 1/2;$$

$$\text{(ii) if } j_{\max} > \sum j_{\mu,\text{ remaining}}, \text{ then}$$

$$J_{\min} = j_{\max} - \sum j_{\mu,\text{ remaining}}.$$

As is seen on the basis of the above consideration, in the case of many angular momentum $\mathbf{j}_\mu$ summation, especially for high values of n number (determining the number of summed vectors), there may

Table 4. The list of adequate magnetic quantum numbers m_j suitable for four angular momenta: $\mathbf{j}_1 = 5/2$, $\mathbf{j}_2 = 3/2$, $\mathbf{j}_3 = 1/2$, and $\mathbf{j}_4 = 1/2$

$\mathbf{j}_1 = 5/2$	$\mathbf{j}_2 = 3/2$	$\mathbf{j}_3 = 1/2$	$\mathbf{j}_4 = 1/2$
5/2	3/2	1/2	1/2
3/2	1/2	−1/2	−1/2
1/2	−1/2		
−1/2	−3/2		
−3/2			
−5/2			

Table 5. The list of $p(\mathbf{J}_\nu)$ values calculated for four angular momentum summation (in the example analyzed in Table 4 and in the chart)

$\mathbf{J}_\nu$	$\eta_{\mathbf{J}_\nu}$	$2J_\nu + 1$	$r_\nu = \eta_{\mathbf{J}_\nu}(2J_\nu + 1)$	$p(\mathbf{J}_\nu)$
5	1	11	11	11/96
4	3	9	27	27/96
3	4	7	28	28/96
2	4	5	20	20/96
1	3	3	9	9/96
0	1	1	1	1/96
			$N = 96$	1

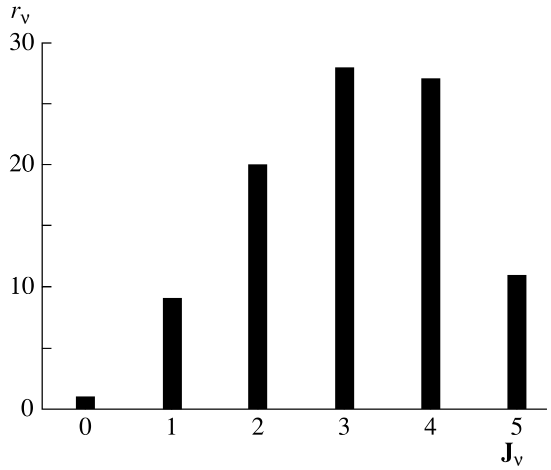

Fig. 1. The distribution of vectors $\mathbf{J}_\nu$ occurrence frequencies, resulting from summation of four angular momenta: $\mathbf{j}_1 = 5/2$, $\mathbf{j}_2 = 3/2$, $\mathbf{j}_3 = 1/2$, and $\mathbf{j}_4 = 1/2$.

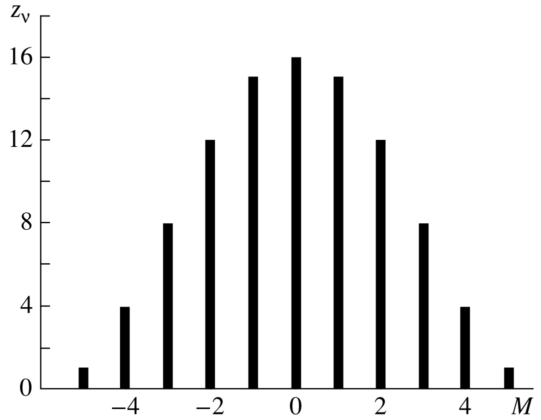

Fig. 2. The distribution of particular M values in a set of 96 magnetic numbers in the analyzed case of summation of four angular momenta: $\mathbf{j}_1 = 5/2$, $\mathbf{j}_2 = 3/2$, $\mathbf{j}_3 = 1/2$, and $\mathbf{j}_4 = 1/2$.

appear a difficulty in writing a computer procedure for searching for the groups of magnetic numbers characteristic of the determined vectors $\mathbf{J}_\nu$ and the multiplication factors $\eta_{\mathbf{J}_\nu}$.

Below, we present a modified version of the discussed calculation proposal of $p(\mathbf{J}_\nu)$ probabilities, which does not have this inconvenience and does not encounter the above-mentioned difficulty in preparing a proper algorithm of calculations.

3.3. Modified Way of Numerical Calculation of the Probabilities $p(\mathbf{J}_\nu)$ (Important because of Particular Simplicity of Calculations)

A modified way of $p(\mathbf{J}_\nu)$ calculation will be explained here using an example of four angular momentum summation: $\mathbf{j}_1 = 5/2$, $\mathbf{j}_2 = 3/2$, $\mathbf{j}_3 = 1/2$, and $\mathbf{j}_4 = 1/2$. The given vectors $\mathbf{j}_\mu$ are identical to those assumed for consideration in Section 3.1. Summation results of magnetic numbers m_j (included in Table 4) related to the above-mentioned angular momenta are presented in the chart (see Section 3.1) and these are all 96 possible values of quantum magnetic numbers M of angular momenta resulting from summation. Figure 2 presents the distribution of frequencies z_ν of the occurrence of particular M values in the collection of these 96 magnetic numbers.

We can easily notice that the multiplication factors $\eta_{\mathbf{J}_\nu}$ for vectors $\mathbf{J}_\nu$ resulting from summation in the analyzed case can be obtained by means of simple subtraction of $z_\nu(M)$ frequencies (see Fig. 2):

$$\eta_{\mathbf{J}=5} = z_\nu(M=5) - z_\nu(M=6) = 1 - 0 = 1,$$
$$\eta_{\mathbf{J}=4} = z_\nu(M=4) - z_\nu(M=5) = 4 - 1 = 3,$$
$$\eta_{\mathbf{J}=3} = z_\nu(M=3) - z_\nu(M=4) = 8 - 4 = 4,$$
$$\eta_{\mathbf{J}=2} = z_\nu(M=2) - z_\nu(M=3) = 12 - 8 = 4,$$
$$\eta_{\mathbf{J}=1} = z_\nu(M=1) - z_\nu(M=2) = 15 - 12 = 3,$$
$$\eta_{\mathbf{J}=0} = z_\nu(M=0) - z_\nu(M=1) = 16 - 15 = 1.$$

Thus, the obtained results $\eta_{\mathbf{J}_\nu}$ are identical to those presented in Table 5. A further procedure in $p(\mathbf{J}_\nu)$ calculation has already been explained in Section 3.1 (see Table 5).

On the basis of the above presentations, one can recognize that the proposed method of $p(\mathbf{J}_\nu)$ probability calculations, particularly in the version of this section, as being very simple and enabling any angular momentum number summation, is worth noting.

4. CONCLUSION

The equality of $p(\mathbf{J}_\nu)$ probability values obtained in this paper according to the proposed method with the values $p(\mathbf{J}_\nu)$ calculated by means of Clebsch–Gordan coefficients for the case of two angular momentum ($n = 2$) summation makes the starting point for expanding the method in cases where the number of summed vectors $n > 2$.

In particular, the variant of the method described in Section 3.3 is worth noting for the reason of foreseen ease in working out a computer procedure as compared to the proposal contained in Section 3.1.

Correctness of the presented method of n angular momentum summation is justified by the fact that one can find a basis on algebraic summation of values of $\mathbf{j}_\mu$ ($\mu = 1$–n) vector components, which are determined by quantum magnetic numbers m_j. Obtained as a result of summation, the quantum magnetic numbers M, which describe all resulting $\mathbf{J}_\nu$ vector components on the quantization axis, are then ordered to find multiplication factors $\eta_{\mathbf{J}_\nu}$ of angular momentum $\mathbf{J}_\nu$ occurrence in **J** vector group, where quantum number $J_{\rm min} \leq J \leq J_{\rm max}$.

To sum up, it is worth noting that, in [5, 6], there is given an empirical description of neutron resonance level density ρ, either as in [5] by finding the dependence of level density parameter a on k (see Introduction) and U (excitation energy) or as in [6] by fitting the given level density function ρ to the experimental (normalized) values of $\rho_{\rm exp}$. Now it seems that the summation method presented in this paper for any number of angular momentum vectors makes it possible to calculate values of neutron resonance level densities ρ by calculating the exciton subconfiguration numbers, which may be realized in the excitation process of the nucleus, for each configuration type $ip(i-1)h$, where $i = 1{-}k$.

The method of calculating the subconfiguration numbers may be based on Böhning's suggestion [7], which, however, in the form described there, does not take into consideration the angular momentum conservation principle. Applying this method [7] and taking into account the energy gaps in the nucleon level scheme, we have the possibility of obtaining quite interesting results for s-resonance level densities ρ [8]. It became possible after using in our calculations the function $R(J)$ given in [9], which describes the spin factor for neutron resonance level density. The results that we have obtained up to now for ρ are direct substantiation for the search for still other ways which could improve the suitable calculations of resonance level density. This means, for example, (i) a new analysis of the energy gap values for a wide region of nuclides, and (ii) numerical method research to consider the angular momentum conservation principle, based on the nucleon single-particle levels in a potential well and on their quantum characteristics. This numerical method is presented in the paper and suitable computational program is available on request.

ACKNOWLEDGMENTS

I wish to thank Prof. M. Przytula for formulation of the subject and Dr. L. Lason for participation in the solution of the problem. I gratefully acknowledge Prof. S. Giller and Dr. C. Gonera from the Division of Theoretical Physics for their kind explanations.

REFERENCES

1. M. Kaczmarczyk and M. Przytula, Z. Phys. A **323**, 465 (1986).
2. J. J. Griffin, Phys. Rev. Lett. **17**, 478 (1966).
3. A. Messiah, *Quantum Mechanics* (North-Holland, Amsterdam, 1962), Vol. II, p. 566.
4. E. U. Condon and G. H. Shortley, *The Theory of Atomic Spectra* (Cambridge Univ. Press, Cambridge, 1963), p. 76.
5. M. Kaczmarczyk, J. Phys. G **26**, 253 (2000).
6. M. Kaczmarczyk and M. Przytula, Phys. At. Nucl. **63**, 758 (2000).
7. M. Böhning, Nucl. Phys. A **152**, 529 (1970).
8. M. Kaczmarczyk (in press).
9. D. Ryckbosch and E. Van Camp, Nucl. Phys. A **469**, 106 (1987).